



Delft University of Technology

## Boundary Layer Separation Diagnostics and Control

Michelis, Theodoros

### DOI

[10.4233/uuid:f5ecca35-71f6-4c99-92e8-a3004113fa53](https://doi.org/10.4233/uuid:f5ecca35-71f6-4c99-92e8-a3004113fa53)

### Publication date

2017

### Document Version

Final published version

### Citation (APA)

Michelis, T. (2017). *Boundary Layer Separation: Diagnostics and Control*. [Dissertation (TU Delft), Delft University of Technology]. <https://doi.org/10.4233/uuid:f5ecca35-71f6-4c99-92e8-a3004113fa53>

### Important note

To cite this publication, please use the final published version (if applicable).  
Please check the document version above.

### Copyright

Other than for strictly personal use, it is not permitted to download, forward or distribute the text or part of it, without the consent of the author(s) and/or copyright holder(s), unless the work is under an open content license such as Creative Commons.

### Takedown policy

Please contact us and provide details if you believe this document breaches copyrights.  
We will remove access to the work immediately and investigate your claim.



**Boundary Layer Separation**  
DIAGNOSTICS AND CONTROL

Theodoros MICHELIS



# **Boundary Layer Separation**

DIAGNOSTICS AND CONTROL

**Theodoros MICHELIS**



# **Boundary Layer Separation**

DIAGNOSTICS AND CONTROL

## **Proefschrift**

ter verkrijging van de graad van doctor  
aan de Technische Universiteit Delft,  
op gezag van de Rector Magnificus prof. ir. K.C.A.M. Luyben,  
voorzitter van het College voor Promoties,  
in het openbaar te verdedigen op  
Maandag 25 September 2017 om 10:00 uur

door

**Theodoros MICHELIS**

Master of Science in Aerospace Engineering,  
Delft University of Technology, Delft, the Netherlands,  
geboren te Cholargos, Athene, Griekenland.

Dit proefschrift is goedgekeurd door de

promotor: Prof. Dr. F. Scarano  
tweede promotor: Prof. Dr. S. Yarusevych  
copromotor: Dr. M. Kotsonis

Samenstelling promotiecommissie:

Rector Magnificus	voorzitter
Prof. dr. F. Scarano	Technische Universiteit Delft
Prof. dr. S. Yarusevych	University of Waterloo, Canada
Dr. M. Kotsonis	Technische Universiteit Delft

*Onafhankelijke leden:*

Prof. Dr. H. Alfredsson	KTH Royal Institute of Technology, Sweden
Prof. Dr. M. Gaster	City University of London, United Kingdom
Dr.-Ing. O. Marxen	University of Surrey, United Kingdom
Prof. Dr. D. Casalino	Technische Universiteit Delft

*Reservelid:*

Prof. Dr.-Ing. S. Hickel,	Technische Universiteit Delft
---------------------------	-------------------------------



Keywords: Boundary layer separation, DBD plasma actuators

Cover: View of the Vertical Tunnel inverse contraction from the working section, prior to its removal due to refurbishments in 2017.

ISBN 978-94-92516-82-4

Copyright © 2017 by Theodoros Michelis (TU Delft Open Access)

Printed by Rijnja Repro, Delft

An electronic version of this dissertation is freely available at  
<http://repository.tudelft.nl/>.

*Ἐξειδίκευση εἶναι ἡ διέξοδος τῆς ἀγνοίας πρὸς μίαν κατεύθυνσιν.*

*Ἐμμανουήλ Ροῖδης*

*Specialisation is the recourse of oblivion towards a certain direction.*

Emmanuel Rhoides

# PREFACE

ONE of the shortcomings of a document such as this thesis is the inability of the author to adequately convey the full story regarding how its pages ended up being written. Arguably, a separate survey would be required to cover this four-year-long material, hence, I shall restrict myself to the obvious, stating that “they were written on a computer under the influence of not-so-high quality caffeine”. On a more personal note, however, I would like to grasp this opportunity and thank a few dramatis personae who, at different extents, contributed to the aggregation of experiences, knowledge, emotions, and perky memories, in the head of Theo.

To begin with, I would like to acknowledge the members of my doctorate committee as a whole, for investing their time in reading this document in order to pose valuable questions and suggest improvements. In the end, I believe we have opened several new routes to lengthy and fruitful discussions.

Gratitude to my promotor, Fulvio Scarano for his endless energy and enthusiasm for research, that others in his position would have lost. His greatest achievement is, often, overlooked: everyone can simply address him as “Fulvio”.

Special thanks to my second promotor, Serhiy Yarusevych, for his humorous and, during conferences, alcoholic guidance in the world of laminar separation bubbles. Our collaboration has been both instructive and entertaining. He provided me the opportunity of visiting Canada for the first time, where I was charmingly introduced to his doctorate slaves, John Kurelek and Jeff McClure, with whom I spent intriguing times both near and far of laboratory equipment.

I am greatly indebted to my supervisor and friend, Marios Kotsonis. His attitude, enthusiasm and interest should serve as an example to everyone. His spontaneity, colourful language and unsurpassed clarity of thought have proven to be significantly more lubricative in research (and life) than the extra virgin olive oil we have been, rather miserably, trying to sell.

This brings me to a well-known chapter in the aerodynamics department, namely Giuseppe Correale. He is the colleague and friend who first introduced me to plasma actuators and smoked mozzarella. Our discussions have probably been some of the most elaborate scatology the laboratory walls ever had to endure. This challenging rhetoric that I, daily, greatly miss, was the most appropriate for coming up with new ideas for research progress and spectacular equipment failure.

Having spent significant time in the low-speed laboratory, I had the chance to annoy the local technicians, Stefan Bernardy and Leo Molenwijk. They have both been of great help during my experimental campaigns and are admired for their capability of keeping a very busy lab functional and tidy. Our discussions regarding soaring and island vacations have been a pleasant note to the daily routine.

I would like to thank all my colleagues in the doctorate room for contributing to the nice environment within which we all strived to achieve our goals, while

collectively ignoring to water the office plants. Namely Henri, Martin, Hao-Hua, Zeno, Tiago, Alberto, Liesbeth, Wouter, Jan, Paul, Qing-Qing, Wouter, Weibo, Shaafi, Rakesh, Mustafa, Stefan, Varun, and Yi. Extra credits go to the textbook sarcasm of Beppe Caridi and to the knowledge of Ilya Popov regarding the dark corners of physics. Jacopo Serpieri is acknowledged for his excellent humour and for accompanying me in the two weirdest taxi rides I ever experienced, both in the same evening. The efforts of Koen Groot for concealing my inadequacies in Dutch language by assisting in the necessary translations are greatly appreciated.

I would like to thank my flatmate, neighbour, colleague and friend, Valeria Gentile for reminding myself, my supervisor and a few of my aforementioned colleagues for how “disgaaasting” we all are and how she “ate us all”. Her unorthodox support in the weirdest of situations is dearly remembered.

I am grateful to the backbone of the aerodynamics department, Colette Russo, who facilitated many processes and without whom internal bureaucracy would undeniably lead to increased murder and suicide rates amongst students and staff.

Cheers to my colleagues in the aeroacoustics department, Daniele Ragni and Francesco Avallone for providing limitless entertainment during coffee time in their office. Credits to Riccardo Pereira for our discussions regarding the dead ends of life, always accompanied by a twist of hilarious word abuse and implied meanings.

To my dearest friends who cannot be alphabetically sorted, George and George. They and their families have been a constant source of inspiration, fun and relaxation for a very long time. I could not have asked for a better set of childhood memories which, to this day, drive a lot of my decisions. As I write these lines, we have unexpectedly lost a valuable and beloved member of the Syros team who is, already, greatly missed. Yet, as he would agree, I am confident that the best is still to come. I wish you both all the best.

I am indebted to my companion Egle Kalonaityte. She wholeheartedly decided to fulfil numerous roles in my life and has been the person who has, by far, been supporting me the most during the past few years abroad, perhaps without even realising. Her honesty and care are very rare elements indeed.

Hereby, I must express my gratitude and love towards my parents, Konstantinos and Eliza, and grandparents, Theodoros, Anastasia, Dimitris and Lola. I shall never be able to return what they have done for me. The final word is reserved for my brother, Dimitris, who, regardless of the geographical distances that separate us, has always been the person closest to me.

20th April 2017  
Flight from Athens to Amsterdam  
Theodoros Michelis

# CONTENTS

<b>Preface</b>	<b>vii</b>
<b>Summary</b>	<b>xiii</b>
<b>Samenvatting</b>	<b>xv</b>
<b>1 Introduction</b>	<b>1</b>
1.1 The Phenomenon of Flow Separation . . . . .	2
1.2 Fundamental Principles . . . . .	3
1.2.1 Navier-Stokes Equations . . . . .	3
1.2.2 The Boundary Layer . . . . .	4
1.2.3 Boundary Layer Transition . . . . .	4
1.2.4 Boundary Layer Separation . . . . .	5
1.3 Special Cases of Separation . . . . .	6
1.3.1 Laminar Separation Bubbles . . . . .	6
1.3.2 Separation on Elongated Bluff Bodies . . . . .	8
1.3.3 Separation on Wall-Bounded Cylinders . . . . .	9
1.4 Separation Control . . . . .	10
1.5 Active Control for Flow Diagnostics . . . . .	11
1.6 Motivation, Objectives and Thesis Outline . . . . .	12
<b>2 Methodology</b>	<b>15</b>
2.1 Experimental Techniques . . . . .	16
2.1.1 Wind Tunnel Facilities . . . . .	16
2.1.2 Particle Image Velocimetry . . . . .	16
2.1.3 Dielectric Barrier Discharge Plasma Actuators . . . . .	19
2.2 Post-Processing Methodology . . . . .	22
2.2.1 Linear Stability Theory . . . . .	22
2.2.2 Proper Orthogonal Decomposition . . . . .	24
2.2.3 Wavelet Analysis . . . . .	26
2.3 Uncertainty Quantification . . . . .	26
<b>3 Impulsively Forced Laminar Separation Bubbles</b>	<b>29</b>
3.1 Background . . . . .	30
3.2 Description of Experiments . . . . .	32
3.2.1 Flow and Model Configuration . . . . .	32
3.2.2 Impulsive Forcing . . . . .	34
3.2.3 Data Acquisition . . . . .	35
3.3 Post-Processing Methodology . . . . .	36
3.3.1 Notation and Scaling . . . . .	36
3.3.2 Linear Stability Analysis . . . . .	37

3.4	The Unforced LSB . . . . .	38
3.4.1	Steady State Features . . . . .	38
3.4.2	Proper Orthogonal Decomposition. . . . .	40
3.4.3	Spectral Content and Stability Characteristics . . . . .	41
3.5	The Forced LSB . . . . .	43
3.5.1	Temporal Response to Impulse . . . . .	44
3.5.2	Quasi-Steady Spatial Stability . . . . .	48
3.5.3	Disturbance Characteristics . . . . .	51
3.5.4	Onset of Shear Layer Breakdown . . . . .	57
3.6	Concluding Remarks . . . . .	58
<b>4</b>	<b>Spanwise Deformation in Laminar Separation Bubbles</b>	<b>61</b>
4.1	Background . . . . .	62
4.2	Description of Experiments . . . . .	63
4.2.1	Flow and Model Configuration. . . . .	63
4.2.2	Data Acquisition . . . . .	64
4.3	Baseline LSB . . . . .	65
4.3.1	Steady State Features . . . . .	65
4.3.2	Spatio-Temporal Characteristics. . . . .	67
4.4	Origin of Spanwise Vortex Deformation . . . . .	70
4.4.1	Boundary Layer Upstream of the LSB . . . . .	70
4.4.2	Linear Stability Analysis . . . . .	71
4.4.3	Two-Dimensional Impulsive Forcing . . . . .	74
4.4.4	Mechanism of Initial Spanwise Vortex Deformation . . . . .	74
4.5	Concluding Remarks . . . . .	78
<b>5</b>	<b>Spanwise Structures in Airfoil Laminar Separation</b>	<b>81</b>
5.1	Background . . . . .	82
5.2	Description of Experiments . . . . .	82
5.3	Data Analysis and Discussion . . . . .	84
5.3.1	The Unforced Bubble. . . . .	84
5.3.2	The Forced Bubble . . . . .	89
5.4	Concluding Remarks . . . . .	91
<b>6</b>	<b>Bluff Body Separation Control with a Cylinder</b>	<b>93</b>
6.1	Background . . . . .	94
6.2	Description of Experiments . . . . .	95
6.2.1	Flow and Model Configuration. . . . .	95
6.2.2	Data Acquisition . . . . .	96
6.3	Data Analysis and Discussion . . . . .	96
6.3.1	Baseline Flow . . . . .	96
6.3.2	Steady State Features . . . . .	98
6.3.3	Spectral Analysis . . . . .	100
6.3.4	Proper Orthogonal Decomposition. . . . .	102
6.3.5	Wake and Vortex Dynamics . . . . .	105
6.4	Concluding Remarks . . . . .	106

---

<b>7</b>	<b>Hybrid Separation Control on a Truck Mirror</b>	<b>109</b>
7.1	Background . . . . .	110
7.2	Description of Experiments . . . . .	110
7.3	Data Analysis and Discussion . . . . .	112
7.3.1	Baseline Flow . . . . .	112
7.3.2	Controlled Flow. . . . .	113
7.3.3	Power Considerations. . . . .	117
7.4	Concluding Remarks . . . . .	117
<b>8</b>	<b>Conclusions and Recommendations</b>	<b>119</b>
8.1	On Laminar Separation Bubbles. . . . .	120
8.2	On Bluff Body Passive Separation Control . . . . .	121
8.3	On Hybrid Separation Control. . . . .	122
	<b>Bibliography</b>	<b>123</b>
	<b>Scientific Contributions</b>	<b>135</b>
	<b>Biographical Note</b>	<b>137</b>



# SUMMARY

THE RESEARCH presented in this thesis focuses on boundary layer separation and, more specifically, on the related physical mechanisms, such as laminar to turbulent transition, with a vision towards effective separation control. The work is divided in three parts, each corresponding to a different separation scenario. The supporting data is experimental, obtained by means of particle image velocimetry.

The first and major part regards the phenomenon of laminar separation bubbles. The spatial and temporal response characteristics of a flat plate laminar separation bubble to impulsive forcing are first investigated in order to shed light on the processes of flapping and bursting. The impulsive disturbance is introduced two-dimensionally with a dielectric barrier discharge plasma actuator. The disturbance develops into a wave packet that causes rapid shrinkage of the bubble in both upstream and downstream directions. This is followed by bubble bursting, during which the bubble elongates significantly, while vortex shedding strength in the aft portion of the bubble is reduced. Duration of the recovery of the bubble to its unperturbed state is independent of the forcing amplitude. At the same time, linear stability analysis shows that the growth rate and the frequency of the most unstable mode decreases for increasing forcing amplitude. Throughout recovery, growth rates are directly proportional to the shape factor, indicating that bursting and flapping mechanisms are driven by altered stability characteristics due to variations in incoming disturbances. It is found that the stability of the flow changes only when disturbances interact with the shear layer breakdown and reattachment processes, supporting the notion of a closed feedback loop.

Three-dimensional features in the aft part of the same flat plate laminar separation bubble are explored via tomographic particle image velocimetry. Measurements on the unforced bubble reveal a staggered distribution of spanwise vortices in the rollup region. The location of staggering persists throughout measurements with a ratio of streamwise to spanwise wavelengths of approximately 1:2. Moreover, linear stability analysis predicts that the fundamental two-dimensional and oblique modes develop with comparable amplification factors until separation promotes the two-dimensional mode. It is suggested that the cause of this topology is the interaction of two oblique waves with opposite angles, creating spanwise modulation which is amplified by the separation bubble. Impulsively forcing the boundary layer mitigates the expression of oblique growth.

The development of a laminar separation bubble on the suction side of an airfoil under natural and forced conditions is also considered, in both streamwise and spanwise planes. Statistical analysis of the unforced bubble reveals a rapid growth of velocity fluctuations, typical of rigorous shedding and transition to turbulence on laminar separation bubbles. Spectral analysis corroborates linear stability analysis predictions regarding the band of unstable frequencies. In turn, proper orthogonal

decomposition analysis on the spanwise plane indicates that, while dominant modes are coherent and monochromatic, they develop three-dimensional amplitude and shape modulation in the spanwise direction. This behaviour persists under natural, unforced conditions within an otherwise strongly two-dimensional baseline flow. Forcing is applied two-dimensionally and periodically by the plasma actuator upstream of the mean separation point. Actuation forces the shedding process to lock onto a single mode, while the coherency in the spanwise plane increases considerably. Nevertheless, distinct spanwise deformation of the dominant structures persists in the forced case.

The second part considers the combination of the problems of bluff body leading edge separation and a wall-bounded cylinder. More specifically, the leading edge separation from an elongated bluff body is controlled by means of a passive cylinder that imposes a local pressure gradient on the flow. The cylinder is placed at three different wall-normal positions and two streamwise positions, upstream and downstream of the bluff body leading edge. The streamwise position of the cylinder is found to significantly affect the mean flow topology and the vortex shedding dynamics of both the cylinder and the bluff body separation bubble. When the cylinder is positioned upstream of the bluff body leading edge, cylinder shedding locks on the same frequency as the bluff body separation shedding, while bubble flapping is not significantly affected. Instead, moving the cylinder downstream eliminates the separation bubble. Proper orthogonal decomposition captures the separation and cylinder shedding dynamics demonstrating that when the cylinder is placed near the wall, flapping modes dominate over the cylinder shedding modes.

The third part of the research is an exploratory study that couples advantages of passive and active flow control schemes on a full scale transport truck side mirror. A slim guide vane is employed for redirecting high momentum flow towards the mirror wake region. In turn, leading edge separation from the guide vane is reduced or eliminated by means of a plasma actuator. The measurements show that at  $-5^\circ$  windward conditions, the guide vane is, on its own, capable of recovering significant momentum with respect to the uncontrolled case. No measurable improvement is observed by operating the plasma actuator. In contrast, at  $5^\circ$  leeward conditions, the guide vane results in momentum deficit. Actuation eliminates separation, leading to a momentum gain with respect to the uncontrolled scenario.

# SAMENVATTING

HET IN DEZE THESIS gepresenteerde onderzoek focust op de loslating van grenslagen en, in specifiekere zin, op de gerelateerde fysische mechanismes, zoals laminaire naar turbulente transitie, met als visie het effectief controleren van loslating. Het werk is in 3 gedeeltes opgesplitst, elk gerelateerd aan een ander loslatingsscenario. De onderbouwende data is experimenteel, vergaard door middel van Particle Image Velocimetry.

Het eerste en voornaamste gedeelte beschouwt het laminaire loslatingsblaas fenomeen. De respons karakteristieken van laminaire loslatingsblazen op een vlakke plaat in de ruimte en tijd onderhevig aan impulsieve forcering worden eerst onderzocht om inzicht te bieden in de processen als flappen en barsten. De impulsieve tweedimensionale verstoring is geïntroduceerd met een diëlectische barrière ontlading plasma actuator. De verstoring ontwikkelt zich tot een golf pakket dat de blaas doet krimpen in beide de stroomopwaartse en stroomafwaartse richtingen. Dit wordt gevolgd door het barsten van de blaas, gedurende welke de blaas zich significant verlengt, terwijl de sterkte waarmee wervels worden afgeschud in de achterste regio van de blaas vermindert. De herstelduur van de blaas tot de onverstoorde staat is onafhankelijk van de amplitude van de forcering. Gedurende het herstel is de groei direct proportioneel aan de vormfactor, welk aangeeft dat de barst- en flapmechanismes gedreven worden door aangepaste stabiliteitskarakteristieken door variaties in inkomende verstoringen. De stabiliteit van de stroming is ontdekt alleen te veranderen als de verstoringen interacteren met de ineenstorting- en herbevestigingsprocessen van de schuiflaag, dat de notie van een gesloten terugkoppelingslus onderbouwt.

Driedimensionale kenmerken in het achterste gedeelte van dezelfde laminaire loslatingsblaas op de vlakke plaat zijn onderzocht met tomographic particle image velocimetry. Metingen van de ongeforceerde blaas onthullen een zigzagpatroon van spanwijze wervels in de regio waar wervelingen oprollen. Het zigzagpatroon volhardt gedurende de metingen en heeft een ratio van stroomwijze en spanwijze golflengtes van ongeveer 1:2. Bovendien voorspelt lineaire stabiliteitsanalyse dat de fundamentele tweedimensionale en schuine modes met vergelijkbare amplificatie factoren ontwikkelen totdat loslating de tweedimensionale modes promoot. De oorzaak van deze topologie is de interactie van twee schuine golven met tegengestelde hoeken, dat spanwijze modulatie creëert, welk door de loslatingsblaas wordt geamplificeerd. Het impulsief forceren van de grenslaag matigt de groei van schuine golven.

De ontwikkeling van een laminaire loslatingsblaas op de bovenrug van een vleugelprofiel in natuurlijke en geforceerde condities is ook beschouwd, in beide stroomwijze en spanwijze vlakken. De statistische analyse van de ongeforceerde blaas onthult een snelle groei van snelheidsfluctuaties, die typisch zijn voor rigoureuze afschudding van wervels en transitie naar turbulentie van laminaire loslatingsblazen. De spectrale analyse bekrachtigt voorspellingen door lineaire stabiliteitsanalyse met betrekking

tot de band van instabiele frequenties. Hoofdcomponentenanalyse in het spanwijze vlak toont aan dat de dominante modes een driedimensionale amplitude en vorm modulatie in de spanwijze richting ontwikkelen, ook al zijn de modes coherent en monochromatisch. Dit gedrag volhardt onder natuurlijke, ongeforceerde omstandigheden in een anders sterk tweedimensionale basis stroming. De forcering is toegepast op een tweedimensionale manier en periodiek in de tijd door de plasma actuator welk stroomopwaarts is geplaatst ten opzichte van het gemiddelde loslatingspunt. Activering forceert het afschudproces zich te vergrendelen aan een enkelvoudige mode, terwijl de coherentie in het spanwijze vlak aanzienlijk toeneemt. Desalniettemin volhardt de uitgesproken spanwijze vervorming van de dominante structuren in het geval van toegepaste forcering.

Het tweede gedeelte beschouwt de combinatie van de problemen van aanvalsboordloslating op stompe lichamen en een cilinder begrensd door een wand. De aanvalsboordloslating van een lang stomp lichaam is bestuurd door middel van een passieve cilinder die een lokaal drukgradiënt oplegt aan de stroming. The cilinder is geplaatst op drie posities ten opzichte van de wand en twee stroomwijze posities, stroomopwaarts en stroomafwaarts van het aanvalsboord van het stompe lichaam. De stroomwijze positie van de cilinder heeft een significante invloed op de topologie van de gemiddelde stroming en de wervelafschudding dynamica van beide de cilinder en de loslatingsblaas op het stompe lichaam. Als de cilinder stroomopwaarts van het aanvalsboord van het stompe lichaam wordt geplaatst, vergrendelt de wervelafschudding zich aan dezelfde frequentie als de afschudding van de loslating op het stompe lichaam, terwijl het flappen van de loslatingsblaas niet significant beïnvloed wordt. Als de cilinder stroomafwaarts wordt geplaatst, wordt de loslatingsblaas geëlimineerd. Hoofdcomponentenanalyse vangt de loslating en cilinder afschuddynamica, wat demonstreert dat als de cilinder dichtbij de wand geplaatst wordt, de flapping modes over de cilinder afschud modes domineren.

Het derde gedeelte van het onderzoek is een verkennende studie die de voordelen van passieve en actieve stromingscontrole schema's koppelt voor een zijspiegel van een transport vrachtwagen op volledige schaal. Een dunne geleideschoep is gebruikt om de hoge momentum stroming om te leiden naar het zog van de spiegel. Beurtelings wordt de aanvalsboordloslating van de geleideschoep gereduceerd of geëlimineerd door middel van een plasma actuator. De metingen tonen aan dat, bij  $-5^\circ$  naar de wind gerichte condities, de geleideschoep, op zichzelf, in staat is momentum significant te herstellen vergeleken met het ongecontroleerde geval. Daarentegen, bij  $5^\circ$  onder de wind gerichte condities, zorgt de geleideschoep voor een momentum tekort. Actuatie elimineert loslating, dat een winst in momentum oplevert ten opzichte van het ongecontroleerde scenario.

# 1

## INTRODUCTION

*The first chapter of this thesis is dedicated to introducing a few fundamental principles and concepts regarding boundary layer separation and its control. Through this introduction, a few open questions are presented that form the basis of this thesis and formulate its objectives.*

## 1.1. THE PHENOMENON OF FLOW SEPARATION

SEPARATED flows are a very common phenomenon and are encountered in a multitude of situations where a body is immersed in a fluid. In simple terms, separation occurs when a fluid in relative motion with respect to an object cannot follow the contour of the body. This behaviour is primarily caused by pressure variation along the body surface. As evident from figure 1.1, separation results in the manifestation of complex flow dynamics such as unstable shear layers, large scale vortex shedding and wake interactions.

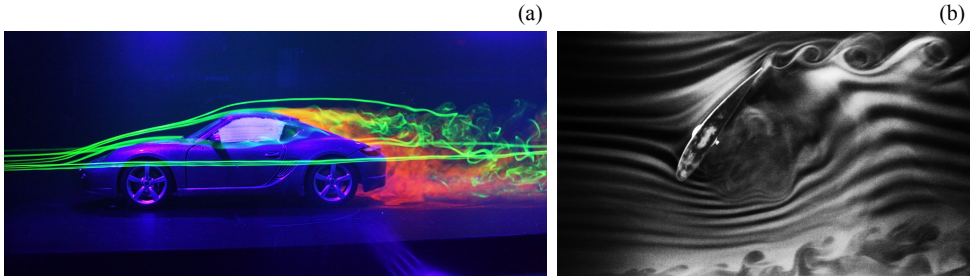


FIGURE 1.1: Examples demonstrating the complexity of flow separation. (a) Separation in the aft part of a road vehicle (photo courtesy of Rob Bulmahn). (b) Separation on a NACA 4412 airfoil in negative angle of attack (visualisation by Smart Blade GmbH).

Flow separation and the associated flow dynamics have significant implications regardless of the application at hand. For example, in the ground transportation industry, separated flows are related to increased drag and, therefore, raise fuel consumption. In turn, separation on aircraft airfoils and wings is responsible for loss of lift, commonly termed as *stall*, thus, posing both a performance and a severe safety issue. Apart from vehicles, separation is relevant in engines and energy production, affecting the performance and efficiency of turbomachine and wind turbine blades. In addition, since separation is a dynamic phenomenon involving major temporal variation of aerodynamic forces, it is relevant when considering structural loads and fatigue. Typical examples include wind turbine towers and blades, bridge platforms and suspension cables, electricity pylons and skyscrapers.

Although the aforementioned examples identify separation as a problem, its effect on lift and drag can also be used advantageously. For instance, aircraft utilise spoilers for manoeuvring and altitude control. At the same time, high performance road vehicles are often equipped with air brakes to achieve greater deceleration. Similarly, separation on parachutes creates drag forces necessary for safe landing of spacecraft either when exploring other planets or when returning to earth.

The above considerations indicate the requirement of manipulating the flow in line with the application of interest in order to eliminate, promote or control the phenomenon of flow separation. On the whole, effective separation control demands understanding the physical processes that lead to separation and which define its phenomenology. This notion forms the motivational grounds on which the research presented in this thesis is based upon.

## 1.2. FUNDAMENTAL PRINCIPLES

THIS SECTION concentrates on some fundamental concepts of fluid mechanics, namely the boundary layer, boundary layer transition and boundary layer separation. Since the aforementioned phenomena are highly relevant for any application involving a fluid flow, they have been the focus of considerable research. In addition, they form the basis on which other complex phenomena manifest. Understanding the governing mechanisms of the latter is a major part of contemporary experimental and numerical investigations.

### 1.2.1. NAVIER-STOKES EQUATIONS

The motion of a fluid is governed by the conservation laws of mass, momentum and energy. These are expressed as a system of non-linear differential equations, requiring initial and boundary conditions for their solution. These equations are fundamental for the science of fluid mechanics and are known as the *Navier-Stokes* equations, named after Claude-Louis Navier and George Gabriel Stokes who independently derived them. For isothermal and incompressible conditions the Navier-Stokes equations reduce to the following system in Cartesian coordinates:

$$\nabla \cdot \mathbf{u} = 0, \quad (1.1a)$$

$$\frac{\partial \mathbf{u}}{\partial t} + (\mathbf{u} \cdot \nabla) \mathbf{u} = \mathbf{F} - \nabla p + \nu \nabla^2 \mathbf{u}. \quad (1.1b)$$

Derivation of this system may be found in the books of Schlichting & Gersten [150] and White [176]. Equations 1.1a and 1.1b represent conservation of mass and momentum, respectively. The momentum equation terms represent acceleration ( $\partial \mathbf{u} / \partial t$ ), convection ( $\mathbf{u} \cdot \nabla \mathbf{u}$ ), pressure gradient ( $\nabla p$ ) and body forces ( $\mathbf{F}$ ). Together, the mass and momentum conservation expressions constitute a system of four equations with four unknowns, the latter being the three components of velocity ( $u, v, w$ ) and pressure ( $p$ ), assuming the body forces ( $F_x, F_y, F_z$ ) are known. The aforementioned system of equations can be rewritten in tensor notation yielding,

$$\frac{\partial u_i}{\partial x_i} = 0, \quad (1.2a)$$

$$\frac{\partial u_i}{\partial t} + u_j \frac{\partial u_i}{\partial x_j} = F_i - \frac{\partial p}{\partial x_i} + \nu \frac{\partial^2 u_i}{\partial x_j \partial x_j}. \quad (1.2b)$$

The four unknown parameters can be decomposed into a mean and fluctuating component, often expressed as

$$u_i = \bar{u}_i + u'_i, \quad p = \bar{p} + p'. \quad (1.3)$$

The above constitute the Reynolds decomposition and can be substituted in equations 1.2a and 1.2b, yielding the Reynolds-Averaged Navier-Stokes (RANS) equations:

$$\frac{\partial \bar{u}_i}{\partial x_i} = 0, \quad (1.4a)$$

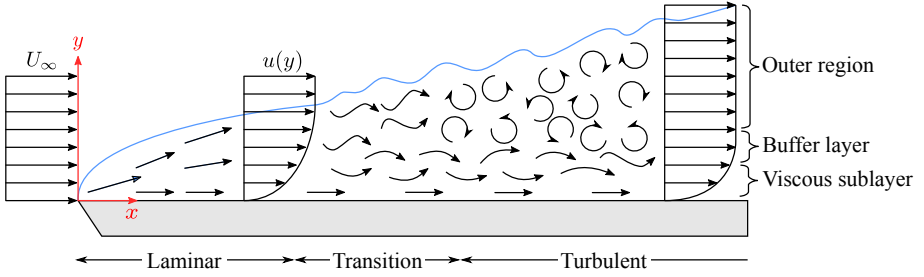


FIGURE 1.2: Schematic of a boundary layer laminar to turbulent transition.

$$\frac{\partial \bar{u}_i}{\partial t} + \bar{u}_j \frac{\partial \bar{u}_i}{\partial x_j} = F_i - \frac{\partial \bar{p}}{\partial x_i} + \nu \frac{\partial^2 \bar{u}_i}{\partial x_j \partial x_j} - \frac{\partial \overline{u'_i u'_j}}{\partial x_j}. \quad (1.4b)$$

Evidently, the RANS equations are time-averaged, with an additional term representing the Reynolds stress tensor  $(\partial \overline{u'_i u'_j} / \partial x_j)$ . In an experimental framework, the RANS equations can be used for estimating the mean pressure gradient when the time-average velocity field is known, e.g. through particle image velocimetry measurements (see section 2.1.2). It follows that time-averaging of multiple measurement realisations approximates steady state conditions, thus, the acceleration term  $(\partial \bar{u}_i / \partial t)$  may be neglected.

### 1.2.2. THE BOUNDARY LAYER

One of the greatest breakthroughs in the field of fluid mechanics was the definition of the boundary layer by Ludwig Prandtl [131]. When a fluid is in contact with a solid surface, intermolecular interactions cause the fluid to adhere to the surface while flow in its vicinity is retarded via viscous forces. Consequently, the fluid velocity on the surface is equal to zero (*no-slip* condition), while at infinite distance it is equal to the free stream velocity ( $U_\infty$ ). The opposite is true for the shear stress ( $\tau$ ), i.e. it peaks on the surface and is zero at infinite distance from it. This information can be used as boundary conditions for the solution of the Navier-Stokes equations. In addition, the latter can be further simplified as the flow outside the boundary layer may be assumed inviscid without significantly affecting the results. Depending on the ratio between inertial and viscous forces, referred to as the *Reynolds number*, a boundary layer may be *laminar* or *turbulent* (figure 1.2). A laminar boundary layer is characterised by straight, smooth flow. In contrast, a turbulent boundary layer exhibits chaotic behaviour involving rotating flow structures of various scales.

### 1.2.3. BOUNDARY LAYER TRANSITION

*Transition* is the process through which laminar flow breaks down to turbulence. The very existence of such a process implies that transition is a phenomenon directly related to stability of laminar flows. As Morkovin *et al.* [121] describe, several roadmaps can be identified that lead to turbulence in boundary layers. Regardless of the specific roadmap, transition begins through the process of *receptivity*. The

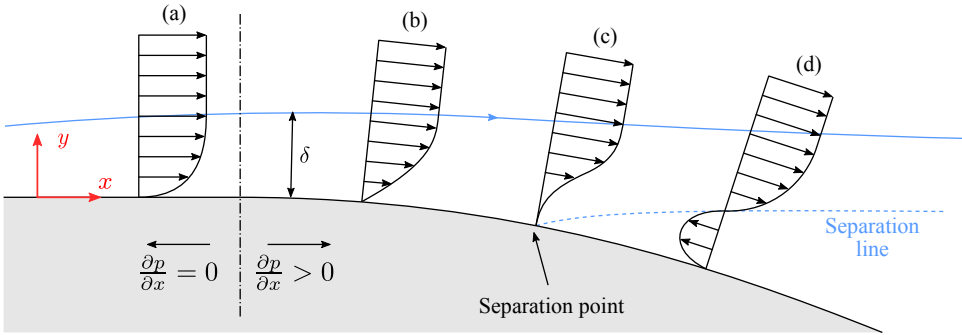


FIGURE 1.3: Schematic of boundary layer separation.

latter is responsible for introducing disturbances into the boundary layer in the form of periodic or unsteady fluctuations. In addition, receptivity determines the initial amplitude that the aforementioned fluctuations acquire prior to growth and turbulent breakdown. In depth reviews of receptivity mechanisms are given by Kozlov & Ryzhov [82], Kachanov [67] and Saric *et al.* [143].

There is a multitude of disturbances that can be identified such as acoustic, thermal, vibrational, wall roughness and turbulence intensity in the free stream flow. In addition, an important role is played by the pressure gradient that may amplify or dampen disturbances to a certain degree depending on whether it is adverse or favourable, respectively. During transition, according to the mean flow characteristics and the disturbance amplitude, instabilities manifest which may develop either independently or simultaneously [143]. With reference to Morkovin's path to transition [121], low amplitude disturbances are characterised by primary modal growth. In general, the latter is weak, two-dimensional and manifests over a significant streamwise extent, e.g. Tollmien-Schlichting waves [5]. In contrast, within environments of moderate disturbance amplitude, non-linear secondary modes set in, characterised by rapid disturbance growth, resulting in three-dimensional interactions and breakdown to turbulence. In this work, low amplitude disturbance environments are considered, in which primary growth is described by linear stability analysis (see section 2.2.1).

#### 1.2.4. BOUNDARY LAYER SEPARATION

Viscosity is responsible for the formation of a boundary layer. At the same time, it draws kinetic energy from the boundary layer, converting it to thermal energy via intermolecular friction. Consequently, the boundary layer decelerates, i.e. there is momentum loss. A schematic of a separating boundary layer is provided in figure 1.3. With reference to the momentum balance equation 1.1b, imposing an adverse pressure gradient further reduces the local boundary layer rate of change of momentum. Consequently, boundary layer profiles become less full and, often, inflected. Eventually, if the adverse pressure gradient exceeds the local rate of change

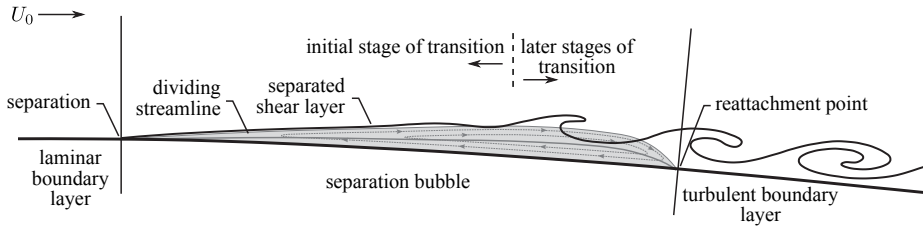


FIGURE 1.4: Typical features of a laminar separation bubble. Courtesy of J. Kurelek, University of Waterloo, Canada [84].

of momentum, the boundary detaches from the surface, i.e. *boundary layer separation* occurs. Boundary layer separation is accompanied by partial reversal of both velocity and wall-shear profiles.

Since no mass flux exchange occurs along the separation line, the latter constitutes a boundary in terms of streamfunction. In turn, flow in the separated region is characterised by low velocity and high pressure. Therefore, when considering applications such as aircraft and road vehicles, a separated region causes loss of lift and a significant increase in pressure drag.

Depending on the state of the boundary layer, separation may be laminar or turbulent. Under the same adverse pressure gradient, due to the higher momentum carried by the turbulent structure of a turbulent boundary layer, the latter can propagate further downstream without separating with respect to the equivalent laminar boundary layer. In both cases, separation is a dynamic phenomenon, with a variety of instabilities developing along the separation line (e.g. Kelving-Helmholtz [91]). In convective flow scenarios, these instabilities give rise to the formation of large scale vortical structures which manifest as periodic vortex shedding (see, for example, chapter 3).

### 1.3. SPECIAL CASES OF SEPARATION

**S**IGNIFICANT variety of boundary layer separation conditions and the ensuing phenomenology depending on the application is available in literature [e.g. 162]. Hereby, three cases of separation are considered, namely laminar separation bubbles, separation on elongated bluff bodies and separation on wall-bounded cylinders.

#### 1.3.1. LAMINAR SEPARATION BUBBLES

When laminar boundary layers separate under the influence of an adverse pressure gradient, the separated shear layer undergoes laminar to turbulent transition. The latter increases momentum exchange between the inner and outer parts of the shear layer. If the momentum exchange is adequate for counteracting the adverse pressure gradient, reattachment is observed. Therefore, in the time-average sense, a wall-bounded closed recirculation region forms, namely a *laminar separation bubble* or LSB [47]. A schematic of this phenomenology is provided in figure 1.4.

Due to the requirement of a laminar boundary layer state at the separation

location, this phenomenon is usually observed at low to moderate Reynolds numbers [21, 99, 122], typical in applications such as glider or unmanned aerial vehicle wings and turbomachine blades. The transition process associated with LSBs is highly susceptible to environmental disturbances and the resulting separated shear layers are inherently unstable. As a result, changes in background disturbances can lead to unwanted impact on aerodynamic performance such as stalling, loss of lift, increase of drag and tonal noise emission [133]. Due to these implications, numerous studies have been performed to investigate and predict LSB dynamic properties and stability characteristics [38, 49, 173]. Although applications primarily involve aerofoils, LSBs driven by adverse pressure gradient on semi-infinite flat plates exhibit the relevant fundamental effects and have been used as a suitable experimentation and computation platform [e.g. 47, 108].

In the laminar part of the LSB, flow is considered two-dimensional and parallel. If, in addition, low amplitude perturbations in the flow are assumed, it is possible to apply linear stability theory for estimating the most amplified unstable mode frequency (see section 2.2.1). Häggmark *et al.* [54], Rist & Maucher [140] and Marxen & Rist [108] demonstrated that LST applied to the mean baseline flow can successfully reproduce experimental and numerical stability observations. It is generally accepted that disturbances developing in an LSB are initially convectively amplified via a Kelvin-Helmholtz instability mechanism, similar to free shear layers [59, 104, 173]. Inviscid inflectional and Göertler type instability mechanisms have been proposed by Diwan & Ramesh [35] and Marxen *et al.* [107], respectively. Furthermore, Theofilis *et al.* [171] conjectured a self-exciting, globally unstable process in a disturbance-free numerical environment. In practice, convective amplification of disturbances in the separated shear layer leads to the formation of initially two-dimensional vortical structures which manifest as coherent vortex shedding [55, 66, 83, 155]. Once the aforementioned vortical structures reach the aft part of the LSB, they undergo three-dimensional breakdown, the underlying mechanism of which is the subject of ongoing investigations such as the ones presented in chapters 4 and 5.

As Marxen *et al.* [106] summarise, at least three types of instability leading to three-dimensionality of the bubble rollup can be identified. The first type refers to primary global instability and is typically of low frequency and spanwise scale of the order of the bubble recirculation size. For such an instability to develop, reverse flow below 10% is sufficient [170]. The second type considers secondary instabilities which are absolute and related to vortex shedding. They can be either elliptic, causing spanwise deformation of vortex cores, or hyperbolic, active in the braid region between consecutive vortices. Their spanwise scale is comparable to the diameter of the shed vortices while their frequency is both fundamental and subharmonic. Though it is still debated whether the braid instability is of hyperbolic nature, evidence exists that the aforementioned instabilities are simultaneously in action [e.g. 66, 106, 109]. Finally, the third type refers to highly localised instabilities of very small scale. They occur in cases of strong shear and have been shown to play a role in the formation of hairpin vortices in transitional boundary layers [6].

Laminar separation bubbles are often classified as *short* or *long* based on their absolute length or whether their influence on pressure distribution is global or local

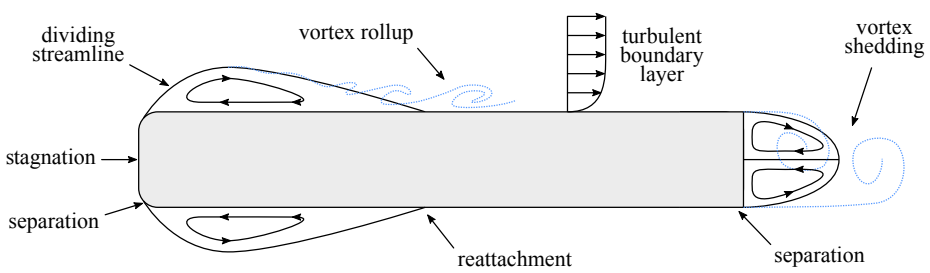


FIGURE 1.5: Flow topology about a symmetric elongated bluff body.

[47, 127, 167]. A detailed overview of the associated bubble characteristics is given by Marxen & Henningson [103]. Pauley *et al.* [128] noted that long separation bubbles with laminar reattachment do not exhibit vortex shedding. In contrast, the long separation bubbles of Gaster [47] and Marxen & Henningson [103] exhibit laminar to turbulent transition and turbulent reattachment. However, they fail to reattach as early as short separation bubbles. Marxen & Henningson [103] point out that, contrary to short bubbles, vortex roll-up in long bubbles occurs further downstream of the transition location.

Under certain conditions involving minor flow variations, a short separation bubble may significantly elongate, a dynamic process termed *bursting* that has been associated with aerofoil stall by Sandham [142]. It should be noted that bursting and elongation do not necessarily imply that the LSB acquires long bubble characteristics. The mechanism of bursting in terms of boundary layer stability is extensively treated in chapter 3.

### 1.3.2. SEPARATION ON ELONGATED BLUFF BODIES

Elongated and symmetric bluff bodies are distinguished by both leading and trailing edge separation if the Reynolds number rises above a certain critical value. This flow scenario is relevant for applications such as transport truck trailers. If the body is of sufficient length, the separated flow at the leading edge reattaches forming a closed recirculation region. The reattachment process is similar to the one described in the previous section regarding laminar separation bubbles and involves vortex roll-up and shedding [60, 169]. The boundary layer developing after reattachment is turbulent and once again separates when flow reaches the trailing edge of the bluff body. Trailing edge separation is accompanied by coherent vortex shedding whose frequency is dependent on the bluff body length and thickness [60]. A schematic of the phenomenology is shown in figure 1.5.

The leading edge separation bubble exhibits significant dynamic behaviour. It is known to be substantially affected by free stream turbulence intensity. More specifically, the bubble size is reduced as turbulence levels increase [57, 85, 86]. This effect is due to the increased perturbation amplitude shifting the transition location and, thus, momentum exchange due to mixing further upstream. Furthermore, the separation bubble is dependent on the leading edge geometry. An increase in leading

edge curvature leads to stronger adverse pressure gradient and, thus, to an overall larger bubble. Therefore, the bubble size for increasing adverse pressure gradient is determined by the competing effects of the separation angle increase and the corresponding mixing enhancement brought by earlier transition [85, 86].

Vortices that form on the leading edge separated shear layer due to inviscid instabilities shed downstream and impinge on the wall affecting the location of the reattachment point [181]. In addition to this regular vortex shedding, a large scale, low frequency unsteady fluctuation of the separation bubble has been observed, that is accompanied by a flapping motion of the shear layer in the vicinity of the separation line [23, 74, 181]. This fluctuation, often referred to as *flapping*, is considered to be a characteristic of two-dimensional separation bubbles as it has been observed in leading edge separation [75], backwards facing steps [39] and laminar separation bubble [186] conditions.

Several theories have been proposed in order to explain the occurrence of flapping. Eaton & Johnston [39] suggest that the motion is caused by an instantaneous imbalance between the entrainment rate from the recirculation zone and the re-injection close to the reattachment line. Tafti & Vanka [166] ascribe the fluctuation to the enlargement and shrinkage of the separation bubble, with enlargement due to unsteady mass increase within the bubble and shrinkage due to the dispersion of fluid in the spanwise direction. Finally, Yang & Voke [181] indicate the presence of a secondary vortex shedding phenomenon where large bubbles form, either directly or by merging of smaller bubbles, the presence of which affects the shear layer dynamics. The work presented in chapter 3 suggests that flapping as well as laminar separation bubble bursting are due to the same mean flow deformation mechanism. The latter consists of a feedback loop that causes stability changes thus affecting the reattachment process, in line with the argumentation of Marxen & Rist [108].

### 1.3.3. SEPARATION ON WALL-BOUNDED CYLINDERS

A geometric arrangement that has received significant attention due to its relevance in industrial applications such as cooling pipes is a wall-bounded cylinder (figure 1.6). The flow dynamics around a cylinder in proximity to a solid surface are notably different than in the case where the cylinder is isolated. The wall inhibits normal velocities and at the same time offers a surface along which a boundary layer develops. The pressure field imposed by the wall on the cylinder results in asymmetry in the strength of the Kármán shedding, shifting the cylinder's front stagnation point towards the wall. As a consequence, a mean lift force acts on the cylinder, directed away from the wall [7]. The shift of the cylinder stagnation point and the production of lift result in the displacement of the cylinder wake away from the wall, increasing its base pressure and, thus, reduce its drag.

Numerous experimental and numerical studies investigated the effect of gap to diameter ratio on the cylinder vortex shedding process [11, 141, 145, 168]. All demonstrated the existence of a critical gap to diameter ratio below which regular vortex shedding is suppressed. The value of  $G/D_{\text{crit}}$  is typically in the range  $0.2 < G/D_{\text{crit}} < 0.5$  and is greatly dependent on the character and thickness of the wall boundary layer in the absence of the cylinder. There is a distinct difference in

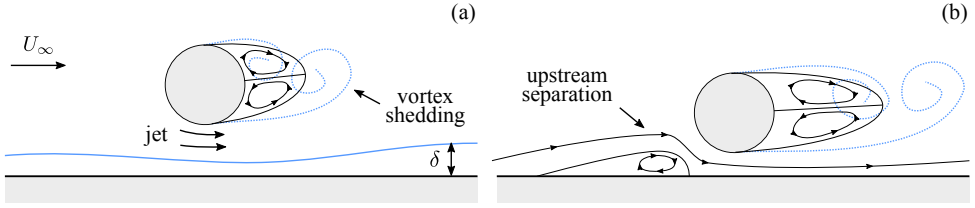


FIGURE 1.6: Schematic of a wall-bounded cylinder flow topology. (a) Cylinder in moderate distance from the wall. (b) Cylinder in close proximity to the wall.

the wake dynamics when the cylinder is placed outside or within the boundary layer, i.e. when there is an inflow velocity gradient [93, 145]. In the first case, there is weak coupling between the shear layer and the approaching boundary layer, thus, vortex shedding occurs close to the cylinder. In contrast, when the cylinder is immersed in the boundary layer, strong coupling is observed that suppresses regular vortex shedding, forcing both separation shear layers to stretch.

Cessation of vortex shedding has also been observed when boundary layer growth is eliminated by means of a moving wall. Nishino & Roberts [125] performed stability analysis in such a scenario and concluded that the dominant instability mechanism in the near cylinder wake changes from absolutely unstable to convectively unstable as  $G/D$  is reduced below its critical value. Therefore, the presence of a wall eliminates the necessary symmetry for the absolutely unstable Kármán shedding to occur.

Finally, when the cylinder is located at close proximity to the wall (figure 1.6b), it imposes an adverse pressure gradient in the upstream direction. Consequently, a separation bubble forms on the wall surface, upstream of the cylinder [98, 132]. As the distance between the cylinder and the wall is further reduced, this upstream separation bubble increases in size and flow is forced over the cylinder, limiting the velocity of the gap jet.

As discussed further in this chapter, the wall-bounded cylinder problem can be combined with the leading edge separation on bluff bodies presented in the previous section. The resulting flow topology poses a complex wake interaction and is extensively analysed in chapter 6.

## 1.4. SEPARATION CONTROL

IMPROVING aerodynamic performance or developing an aerodynamic application dictates that air flow must be appropriately manipulated. The methods used to do so are termed *flow control* methods. They vary based on the required goal, physical mechanism of interaction with the flow as well as on their technical implementation. Typical examples of flow control goals are separation control, lift increase, drag reduction and noise suppression. An introduction to the fundamental flow control concepts and techniques is outlined in the work of Gad-El-Hak [45, 46]. Hereby, a few techniques are discussed, focusing on separation control.

Separation control revolves around manipulation of terms in the momentum part of the Navier-Stokes equation (equation 1.1b). Therefore, separation control methods

may rely on vorticity generation, mass and momentum addition or removal as well as alteration of transition characteristics. These methods may be carried out using either *passive* or *active* strategies.

Passive strategies rely on fixed devices that do not require energy expenditure for their operation. In general, passive devices are simple, reliable and can greatly influence the flow. Their lack of adaptability implies that they can perform only within a limited range of conditions, therefore, they often present disadvantages such as parasitic drag. A typical example of a passive device for separation control are vortex generators. They are commonly found in aircraft wings and promote mixing in order to eliminate laminar separation or for preventing trailing edge separation at higher angles of attack [96]. In turn, guide vanes and flaps directly affect the pressure gradient, reducing its adversity [90]. Golf balls famously feature indentations that increase surface roughness, promoting early transition thus shifting the separation point downstream reducing drag [111].

On the other hand, active strategies require a certain degree of energy investment and often involve increased complexity and cost. However, they offer a larger degree of control authority as they are adaptable to different flow conditions or may just be simply switched off. Active devices can, in addition, be included in open-loop or feedback-loop control schemes, further classifying them in non-reactive and reactive, respectively. Blowing and suction are typical active separation control methods that create a wall-normal velocity component, affecting the mass and momentum transfer in the boundary layer to which they are applied.

When considering moderation of transition characteristics for separation control with an active strategy, the interaction of the device with the flow may be periodic or unsteady. This type of approach has been proven successful for leading edge separation control on airfoils as well as for the manipulation of vortex shedding from bluff bodies using devices such as zero net mass flux synthetic jets [51] and vibrating ribbons [76]. A category of devices called *plasma actuators* has received significant attention due to their fast response and excellent control on the amplitude and frequency of operation [79]. This implies that actuation can be targeted to specific instability modes such as Tollmien-Schlichting instability waves. Plasma actuators are further discussed in section 2.1.3.

## 1.5. ACTIVE CONTROL FOR FLOW DIAGNOSTICS

SUCCESSFUL active flow control techniques consist of tailored interaction with the flow at hand. In many cases this interaction involves the introduction of controlled disturbances, thus, available active flow control devices constitute suitable tools for flow diagnostics. More specifically, monitoring the spatial and temporal development of artificial perturbations and their effect on the flow field can provide clues regarding pertinent mechanisms. This holds particularly true for transitional flow scenarios where the respective boundary layers are receptive to external perturbations. For instance, dominant stability mechanisms in laminar separation bubbles have been investigated by periodically oscillating wires [87], impulsive blowing [173] as well as plasma actuators [114]. Furthermore, plasma actuators have been recently employed to investigate cross-flow instability on swept wings [158].

## 1.6. MOTIVATION, OBJECTIVES AND THESIS OUTLINE

THE RESEARCH presented in the chapters of this thesis is related to different separation scenarios derived from the cases described in section 1.3. It involves understanding the underlying mechanisms of each with a vision of successful separation control. The latter is projected to fuel economy and aerodynamic efficiency in sectors such as transportation and energy. The majority of this work is carried out experimentally and is divided in three parts.

The first part regards the phenomenon of laminar separation bubbles. As mentioned in section 1.2.4, turbulent boundary layers can sustain a more adverse pressure gradient without separating with respect to laminar boundary layers. For this reason they are, in general, preferred in industrial applications. However, due to their turbulent nature, they significantly increase skin friction. Efforts are, thus, made for sustaining laminar boundary layers for the longest possible extent as, for instance, in natural laminar airfoils [154]. The development of laminar separation bubbles under mild adverse pressure gradients poses a significant shortcoming as they are inherently unstable and may burst, causing abrupt loss of lift and increase in drag. Currently, design approaches aim at preventing laminar separation bubbles from developing rather than controlling them, partly due to the limited understanding of pertinent processes such as bursting, flapping and reattachment. This part of the research aims to provide insight into the aforementioned mechanisms. Herein, a DBD plasma actuator is used as a diagnostic tool introducing known perturbations. The following objectives are, therefore, formulated:

- Investigation on the origin of bursting and flapping by assessing temporal stability variations in response to controlled incoming disturbances.
- Assessment of the influence of streamwise and oblique boundary layer modes on the onset of three-dimensional features in the reattachment region.
- Characterisation of the effect of continuous forcing on the formation of spanwise structures in the reattachment of airfoil laminar separation bubbles.

The second part of this study is motivated by the transportation truck industry, focusing on improving the fuel efficiency of European type transport trucks. This is materialised as the *CONVENIENT* project, a joint effort between industries funded by the European commission under FP7-TRANSPORT. The presented research regards aerodynamics of the side view mirrors with respect to their position relative to the cabin. This problem is approximated as the combination of elongated bluff body leading edge separation and the wall-bounded cylinder cases, introduced in sections 1.3.2 and 1.3.3, respectively. Apart from industrial, the resulting flow topology is of fundamental fluid mechanics interest as the combination of the two canonical cases gives rise to the formation of complex separation and wake interactions. With these considerations in mind, the focus points of this part of the research are:

- Assessment of the flow topology for different locations of the cylinder with respect to the leading edge of the bluff body.

- Evaluation of the flow dynamics of the cylinder shedding with respect to its distance from the bluff body surface.
- Characterisation of the interaction of the cylinder wake and the bluff body separation bubble.

The third and final part of this work is an exploratory study coupling advantages of passive and active flow control strategies discussed in section 1.4. Similar to the second part of the research, the application tackled is that of a transport truck side view mirror. However, in this case, a full-scale DAF-XF production mirror is considered. The primary interest is not reducing the absolute value of the mirror drag but to condition its wake width. This is expected to have significant impact on the whole truck drag, given the length of the trailer on which the mirror wake expands. In addition, a reduced wake size improves flow conditions for any additional controlling devices located further downstream. The proposed hybrid control scheme employs a passive guide vane and an active plasma actuator. The guide vane prevents early separation on the surface of the mirror while accelerating flow for filling part of the mirror wake. In turn, leading edge separation from the guide vane itself is controlled by the plasma actuator.

This thesis is organised as follows. Chapter 2 introduces data acquisition techniques as well as methods of post-processing. In chapter 3, the temporal response of the laminar separation bubble to impulsive forcing is presented. In turn, chapter 4 focuses on the emergence and development of oblique modes whose interactions promote distinct three-dimensional topology in the bubble reattachment region. Chapter 5 treats the spanwise feature comparison between a natural and a continuously forced LSB on a NACA 0018 airfoil. The combined problem of the elongated bluff body and the wall-bounded cylinder is treated in chapter 6 while results of the hybrid flow control study are discussed in chapter 7. Finally, chapter 8 is dedicated to discussion of conclusions presented in the previous chapters as well as to suggestions for future research on the topic.



# 2

## METHODOLOGY

*The work presented in this thesis is mainly derived from experimental data. As such, a concise description of the facilities and experimental procedures is hereby provided. Of course, data acquisition on its own is hardly adequate for drawing conclusions regarding the observed phenomena. Hence, this chapter additionally includes theoretical background of the applied data post-processing techniques.*

## 2.1. EXPERIMENTAL TECHNIQUES

**E**XPERIMENTS require appropriate facilities and flow measurement techniques. For an introduction in flow measurement techniques, the reader is referred to the book of Tropea *et al.* [172]. Hereby, only the facilities, techniques and ancillary methods relevant to the studies presented are discussed.

### 2.1.1. WIND TUNNEL FACILITIES

The experimental campaigns presented in this thesis have been carried out in three different wind tunnel facilities. The first two, namely the W-tunnel and the Open Jet Facility (OJF) are part of the TU-Delft Aerodynamics department. The third facility is located in the Mechanical and Mechatronics Engineering department of the University of Waterloo in Canada. Both the W-tunnel and the OJF are of the open-loop and open-jet type. However, they differ in terms of exit cross-sectional area and, consequently, of the scale of experiments that can be performed. Two square cross-sections are available for the W-tunnel, with an area of  $0.4 \times 0.4\text{m}^2$  and  $0.5 \times 0.5\text{m}^2$ , respectively. The maximum achieved free stream velocity is approximately 25m/s with corresponding turbulence intensity ( $U'_{\text{rms}}/\bar{U}$ ) of approximately 0.3%. In turn, the OJF is a large scale wind tunnel whose exit is octagonal, spanning  $2.85 \times 2.85\text{m}^2$ . The maximum achievable free stream velocity is approximately 35m/s with turbulence intensity of 0.5%. Finally, the facility of the University of Waterloo is closed-loop with a square  $0.61 \times 0.61\text{m}^2$  working section, maximum free stream velocity of 32m/s and free stream turbulence below 0.1%.

### 2.1.2. PARTICLE IMAGE VELOCIMETRY

Particle Image Velocimetry (PIV) is the main flow measurement technique used throughout the experimental campaigns described in the present thesis. PIV has been extensively treated and validated and is currently one of the most common techniques for velocity measurements. Excellent overviews may be found in the books of Raffel *et al.* [134] and Adrian & Westerweel [1]. The primary reason behind the popularity of PIV is that it is an optical technique and, therefore, is considered non-intrusive. In addition, from a single realisation, it can provide either two- or three-dimensional velocity vector fields within a plane or a volume. Namely, this corresponds to planar/stereoscopic or tomographic PIV, respectively.

PIV measurements rely on the introduction of seeding particles in the flow and determining the average velocity of a small particle group. The ideal seeding particles are capable of following the flow without exhibiting significant inertial effects or altering the natural flow development. For low Reynolds numbers, vaporising water-glycol mixture produces droplets of approximately  $1\mu\text{m}$  diameter, a spectacle closely resembling disco smoke release. In cases of high Reynolds number flows where compressible effects dominate, solid seeding particles are preferred such as titanium dioxide powder.

Illumination of the region of interest is achieved by means of a green pulsed laser system ( $\lambda \approx 530\text{nm}$ ). Light scattered from the particles is captured by means of digital cameras. Image acquisition may be performed in either low-speed or time-resolved manner. Although low-speed PIV does not provide temporal resolution

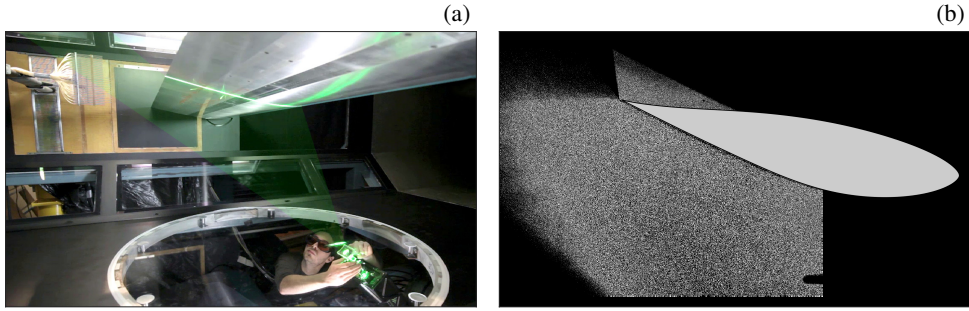


FIGURE 2.1: (a) An experimentalist with protective eye wear setting up a planar PIV experiment. (b) A typical raw recording from the same experiment demonstrating seeding particle illumination from the laser beam.

in measurements, the illumination intensity achieved by the laser is typically an order of magnitude higher than in time-resolved PIV. Consequently, the size of the illuminated plane or volume can be larger.

In planar PIV configurations, the laser beam is transformed into a sheet by means of spherical and cylindrical lenses (figure 2.1a). Typically, the laser sheet is approximately 1mm thick. Cameras are directed normal to and focused on the illuminated plane. In the recorded images, such as the one shown in figure 2.1b, light scattered from the particles is represented by high intensity pixels. Spatial calibration is performed with a template that bears markers at known locations.

For each representative time instant, two images are recorded, separated by a time difference,  $\Delta t$ , that is significantly smaller than the relevant flow time scales. The average particle displacement,  $D(\mathbf{x}, \Delta t)$ , for this time interval is expressed by

$$D(\mathbf{x}, \Delta t) = \int_0^{\Delta t} \mathbf{u}(\mathbf{x}, t) dt. \quad (2.1)$$

Estimation of  $D(\mathbf{x}, \Delta t)$  is a statistical process that begins by subdividing the two recorded frames into interrogation windows. Let  $I_1$  and  $I_2$  be the intensity of corresponding interrogation windows from each frame, respectively, whose size is  $l \times m$  pixels.  $I_2$  may now be used as a sliding template for estimating normalised cross-correlation with  $I_1$ , expressed by

$$C(\Delta x, \Delta y) = \sum_{\Delta x=1}^l \sum_{\Delta y=1}^m \frac{I_1(x, y) - \bar{I}_1}{\sigma_{I_1(x, y)}} \cdot \frac{I_2(x + \Delta x, y + \Delta y) - \bar{I}_2}{\sigma_{I_2(x + \Delta x, y + \Delta y)}}. \quad (2.2)$$

Here,  $\Delta x$  and  $\Delta y$  are the sliding displacements of  $I_2$  with respect to  $I_1$ , while  $\sigma$  signifies estimation of standard deviation for intensity normalisation. The values of  $\Delta x$  and  $\Delta y$  for which  $C$  is maximised define the average particle displacement for this interrogation window. They are introduced in the  $D(\mathbf{x})$  term of equation 2.1 and, since  $\Delta t$  is known, the velocity vector,  $\mathbf{u}(\mathbf{x})$ , is established. This process is

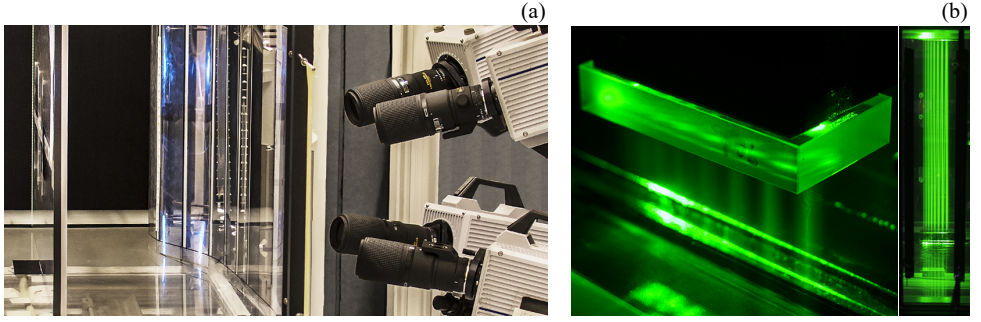


FIGURE 2.2: (a) Typical tomographic PIV setup with cameras arranged in a rectangle. (b) Mirror detail and resulting laser beam in a multi-pass light amplification configuration.

repeated for the remaining interrogation windows for obtaining the velocity vector field for the entire field of view.

The tomographic PIV technique [40] is, in essence, the scaling up of the aforementioned workflow in order to obtain a three dimensional vector field within a volume. The first requirement is, therefore, that illumination is volumetric, formally achieved by expanding the laser beam by means of spherical lenses. In order to determine the location of particles in space, a minimum of three cameras is required, imaging from different angles (figure 2.2a). Scheimpflug adapters [22, 148] are employed to ensure that all camera lenses are focused on the same plane. Spatial calibration is then performed in two iterations. First, a physical calibration template is inserted in the field of view, whose surface marks are in known relative locations. Second, seeding particles are introduced, whose position is determined via optical triangulation. The self-calibration procedure [177] is subsequently followed in order to re-iterate on the first volume calibration estimate.

Similarly to the planar configuration, for each measurement realisation, two frames are recorded per camera with time separation of  $\Delta t$ . The volume calibration and the corresponding camera frames are then used for volume reconstruction, a process that locates particles in space and returns two volumes of  $l \times m \times n$  voxels, containing a three-dimensional representation of the scattered light intensity. Although there are several methods for achieving volume reconstruction [146], for the present work, the Simultaneous Implementation of Multiplicative Algebraic Reconstruction Technique (SMART) [4] is used. Increasing the number of cameras is crucial for reducing the number of ghost particles in the reconstructed volume [41]. Three-dimensional interrogation windows are now defined and cross-correlation is performed in three-dimensions by adding a third spatial component ( $z, \Delta z$ ) to equation 2.2, yielding

$$C(\Delta x, \Delta y, \Delta z) = \sum_{\Delta x=1}^l \sum_{\Delta y=1}^m \sum_{\Delta z=1}^n \frac{I_1(x, y, z) - \bar{I}_1}{\sigma_{I_1(x, y, z)}} \cdot \frac{I_2(x + \Delta x, y + \Delta y, z + \Delta z) - \bar{I}_2}{\sigma_{I_2(x + \Delta x, y + \Delta y, z + \Delta z)}}. \quad (2.3)$$

Once three-dimensional displacement is estimated, the full three-dimensional velocity field is obtained within the reconstructed volume by means of equation 2.1.

As mentioned earlier, one of the shortcomings of tomographic PIV, particularly for time-resolved measurements, is the limited illumination intensity. This is first due to the light being expanded to a volume rather than a sheet and, secondly, due to the increase of lens aperture ( $f_{\#}$ ) for increasing depth of field. Illumination may be improved with the multi-pass light amplification technique [50, 151]. The laser beam is first expanded and collimated with spherical lenses. Subsequently, it is reflected multiple times across the volume of interest by means of two opposing mirrors. The relative angle between the mirrors must be such that the angle of reflection decreases as the beam travels downwards between the mirrors. Eventually, the reflection angle reverses and the beam once again travels through the illuminated volume and exits the mirror pair. A photograph demonstrating the resulting illumination is shown in figure 2.2b. Finally, knife edges are used in order to remove regions affected by light attenuation at the edges of the beam and, thus, sharpen the volume boundaries.

### 2.1.3. DIELECTRIC BARRIER DISCHARGE PLASMA ACTUATORS

The term *plasma* was first used for referring to ionised gases by Langmuir [88]. Plasma is often considered as the fourth state of matter, characterised by charge equilibrium. In essence, this means it is a gaseous entity consisting of free-floating charged species, such as electrons, anions, cations etc. The very presence of such species renders the plasma volume electrically conductive and greatly responsive to electromagnetic fields. An in-depth review of plasma physics may be found in the work of Fridman [44].

Creating and maintaining a plasma discharge requires expenditure of energy such that ionisation overcomes recombination processes. Commonly, this is done by applying an electric field across a gas volume by means of opposing electrodes, driven by either DC or AC voltage. Depending on several factors such as temperature, pressure and chemical consistency, a breakdown voltage is defined, often of the order of several kV for air. If this value is exceeded by the applied electrical field, electrical breakdown ensues, followed by the formation of plasma arcs, photon emission and flow of current between electrodes. In the specific case of air in standard temperature and pressure, such a process leads to the formation of non-thermal plasma (cold plasma). It is characterised by incomplete ionisation and lack of thermal equilibrium, with most of the energy stored in the free electrons, thus its overall temperature is relatively low [180].

The enveloping of one of the two electrodes by an electrical insulation (dielectric barrier) causes charge accumulation on the barrier surface. Consequently, filamentary microdischarges form, also known as *streamers* [77]. They affect capacitance and locally reverse the electrical field, thus, eliminate themselves. This implies that when a dielectric barrier is present, continuous discharge requires application of variable voltage, either in alternating or pulsating form. Application of DC voltage is possible by replacing the dielectric barrier with a resistive barrier [89].

In the context of aerodynamics, the most typical configuration of DBD actuators is shown in figure 2.3. It consists of two asymmetrically positioned electrodes,

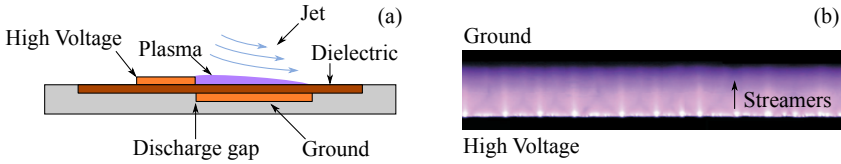


FIGURE 2.3: (a) Typical cross-section of an asymmetric AC-DBD plasma actuator. (b) Top-view photograph of a discharge exhibiting the DBD purple glow.

separated by a dielectric layer. When operating the actuator with AC voltage (AC-DBD actuator), heavy ions such as  $O^+$ ,  $O^-$  and  $N^+$  are driven by the electric field back and forth as the AC polarity reverses. This results in momentum exchange with air surrounding the plasma volume through ion-neutral collisions. In addition, the electrode asymmetry implies that the electric field and, consequently, the discharge are also asymmetric. As a result, the momentum exchange during the two AC half-cycles is not the same, but exhibits directionality from the exposed to the covered electrode. This *body force* gives rise to a weak jet, parallel to the wall, whose velocity is typically less than 10m/s [120].

Variation of the actuator voltage in pulsating mode is conducted by means of nanosecond pulses (ns-DBD actuator). The main mechanism of actuation is, however, very different from the AC-DBD actuators, due to time scale differences. The nanosecond discharge causes a fast, localised temperature rise [31, 164]. This results in an adiabatic expansion of the gas and the formation of a weak sonic wave within a few microseconds after the discharge. Due to the small time-scales related to these phenomena, the flow is incapable of reacting. However, after a few milliseconds, the heated gas volume starts expanding as a consequence of non-adiabatic diffusion of energy deposited in the gas during the discharge. In addition, this is followed by local viscosity gradients. At the same millisecond time scale, a body force is also induced, albeit of lower magnitude than the AC-DBD scenario [100].

Since DBD plasma actuators are electrical devices, they have no moving parts, hence, do not increase mechanical complexity. At the same time, they have a very fast and controllable response in terms of amplitude and frequency within their operating limits. In addition, their thickness is of the order of a few micrometers, depending on the dielectric and electrode material as well as on the manufacturing method. Consequently, they have minimal impact on skin and pressure drag as they do not affect the shape of the geometry on which they are attached. The above considerations, render DBD plasma actuators excellent candidates for aerodynamic flow control. Indeed, they have been successfully used in efforts of transition control [53, 81] as well as separation control [100, 112]. An extensive overview of related studies is summarised in the reviews of Benard & Moreau [8], Corke *et al.* [28], Moreau [120] and Kotsonis [79].

Challenges remain for scaling control authority of DBD plasma actuators to high Reynolds number flows due to the relatively low momentum and energy deposition. Consequently, they are more suitable for cases where the receptivity of transitional

boundary layers can be exploited, such as leading edge separation. Nonetheless, due to the aforementioned precision in their operation regarding frequency and amplitude, they present a valuable tool for transitional flow diagnostics. More specifically, the response of flow to artificially introduced perturbations provides insight to the underlying mechanisms. Such endeavours have, for example, been carried out for investigating swept wing crossflow instability [157] and stability of laminar separation bubbles [182]. The latter topic constitutes a major part of this work and is further discussed in chapters 3, 4 and 5.

The actuator selected throughout the studies presented in this thesis is the AC-DBD. The reason behind this choice is that, contrary to the thermal deposition of the ns-DBD [30], the exerted body force is easier to determine experimentally. Consequently, the body force is directly identified as a source term in the Navier-Stokes equations 1.1b. Instead, the ns-DBD actuation effect representation in the same equation is less straightforward due to its interaction with both viscosity and source terms. The induced body force is expressed in terms of momentum coefficient ( $C_\mu$ ), as formulated by Amitay *et al.* [3],

$$C_\mu = \frac{\bar{\mathbf{I}}}{\frac{1}{2}\rho_0 U_0^2 l}. \quad (2.4)$$

Here, the time-averaged momentum per unit length,  $\bar{\mathbf{I}}$ , is normalised by the fluid density,  $\rho_0$ , the square of the free stream velocity,  $U_0$ , and the length of the plasma actuator,  $l$ . For estimating  $\bar{\mathbf{I}}$  at each voltage, PIV measurements are carried out with the actuator operating continuously at a given carrier frequency,  $f_c$ .  $\bar{\mathbf{I}}$  is then calculated as described by Kotsonis *et al.* [80], through application of the momentum balance equation,

$$\bar{\mathbf{I}} = \oint_s \rho_0 \bar{\mathbf{u}} (\bar{\mathbf{u}} \cdot \hat{\mathbf{n}}) dS, \quad (2.5)$$

to the appropriate control volume,  $S$ , assuming uniform pressure distribution. Both the topology of the jet and the value of  $C_\mu$  are dependent on the external flow to which the actuator is exposed [130], thus, for characterisation purposes, quiescent conditions are chosen. Since the described momentum coefficient is calculated based on continuous operation of the actuator, it pertains to the mechanical power of actuation. Hence, when the actuator is operated in a modulated manner, the momentum transferred to the flow at each burst can be extracted by simply multiplying the relevant momentum coefficient by the duty cycle and the ratio of carrier to modulation frequency.

An exemplary flow field during continuous operation of an actuator along with momentum coefficient for several peak to peak voltages is shown in figure 2.4. Evidently, the largest contribution in forcing originates from the momentum exchange along the  $x$ -direction ( $C_{\mu_x}$ ). As fluid is displaced by the jet, a secondary effect is observed in the region of the discharge gap ( $x = 0$ ). As a result, thrust along the  $y$ -direction is generated towards the wall, signified by negative momentum coefficient ( $C_{\mu_y}$ ). Although the magnitude of momentum coefficient is proportional to the voltage,  $C_{\mu_y}$  is significantly lower than  $C_{\mu_x}$ . Therefore, for the remainder of this document,  $C_\mu \approx C_{\mu_x}$  is used as an indicator of actuator strength.

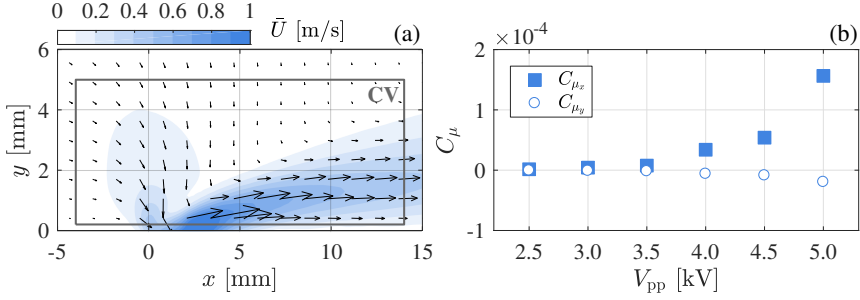


FIGURE 2.4: (a) Time-averaged velocity field in quiescent conditions demonstrating the effect of actuation in continuous operation (5kV, 5kHz). The control volume boundary for momentum coefficient estimation is indicated by a grey rectangle. (b) Momentum coefficient components as a function of applied voltage.

Assessment of the electrical power consumption of the actuator circuit, excluding the high voltage amplifier, is performed by measuring voltage difference and current on the ground electrode. The average power is, therefore, estimated through

$$\bar{P} = \frac{1}{T} \int_0^T V(t)I(t)dt, \quad (2.6)$$

where  $V(t)$  is voltage,  $I(t)$  is current and  $T$  is the measurement duration. Typically, the power consumption is of the order of tens of watts per meter of actuator length.

## 2.2. POST-PROCESSING METHODOLOGY

ONCE data acquisition has been completed, further analysis is necessary. Although it is not possible to exhaust all available methods, the most relevant are hereby discussed. Each post processing method can help draw different conclusions from the same dataset. For PIV data, analysis begins from velocity fields.

### 2.2.1. LINEAR STABILITY THEORY

Linear stability theory (LST) is applied in order to assess the stability characteristics of a given laminar boundary layer. The method applied in this work follows the description and terminology of Mack [101] and van Ingen [62].

In classical LST analysis, flow may be assumed locally parallel while disturbances are considered to be low-amplitude and wave-like. Consequently, they are expressed via the streamfunction,

$$\psi(x, y, z, t) = \varphi(y)e^{i(\alpha x + \beta z - \omega t)}, \quad (2.7)$$

where  $\varphi(y)$  is the perturbation eigenfunction,  $\alpha$  and  $\beta$  the complex streamwise and spanwise wavenumbers and  $\omega$  the respective wave real angular frequency. In turn, the wave angle is defined as the angle between the real part of the streamwise and

spanwise wave numbers,  $\vartheta = \tan^{-1}(\beta_r/\alpha_r)$ . Velocity fluctuations at the wall and at infinite distance from the wall are assumed to be zero, i.e.  $\mathbf{u}'(0) = \mathbf{u}'(\infty) = 0$ . It follows that the boundary conditions of the eigenfunction  $\varphi(y)$  in equation 2.7 are

$$\varphi(0) = \varphi'(0) = \varphi(\infty) = \varphi'(\infty) = 0.$$

The development of disturbances is governed by the Navier-Stokes equations. Therefore, equation 2.7 is substituted in equations 1.1a and 1.1b, which are then linearised and combined. This results in the formulation of the Orr-Sommerfeld equation,

$$\begin{aligned} (D_y^2 - \alpha^2 - \beta^2)^2 \varphi(y) &= \\ &= iRe [(\alpha\bar{u} + \beta\bar{w} - \omega)(D_y^2 - \alpha^2 - \beta^2) - \alpha D_y^2 \bar{u} - \beta D_y^2 \bar{w}] \varphi(y). \end{aligned} \quad (2.8)$$

Here,  $D_y$  represents the differential operator in the wall-normal direction, while  $\bar{u}(y)$  and  $\bar{w}(y)$  the time-averaged streamwise and spanwise velocity components, respectively. A detailed discussion on the derivation process may be found in the classical book of Schlichting & Gersten [150].

When the Orr-Sommerfeld equation is treated in spatial terms,  $\omega$  and  $\beta$  may be explicitly introduced, with  $\omega$  being real. Hence, an eigenvalue problem with respect to the streamwise wavenumber,  $\alpha$ , is posed, solved following the companion matrix technique proposed by Bridges & Morris [15]. The solution begins by expressing  $\varphi(y)$  as a finite and even Chebyshev series of length  $N$ ,

$$\varphi(y) = \frac{\alpha_0}{2} + \sum_{n=1}^N \alpha_n T_n(y). \quad (2.9)$$

Thus,  $\phi(y)$  is mapped on the Chebyshev domain, with limits  $y \in [-1, 1]$ . In turn, the second and fourth order derivative operators are expressed as Chebyshev derivative matrices,  $\mathbf{D}_2$  and  $\mathbf{D}_4$ , respectively. They are computed based on Chebyshev interpolants through the algorithms described by Weideman & Reddy [174]. The discretised Orr-Sommerfeld equation is, thus, rewritten as the following system of homogeneous equations,

$$[\mathbf{C}_0 \alpha^4 + \mathbf{C}_1 \alpha^3 + \mathbf{C}_2 \alpha^2 + \mathbf{C}_3 \alpha + \mathbf{C}_4] \mathbf{a} = 0. \quad (2.10)$$

The coefficients  $\mathbf{C}_{0..4}$  are square matrices of  $N \times N$  elements, defined as

$$\begin{aligned} \mathbf{C}_0 &= \mathbf{I}, \\ \mathbf{C}_1 &= iRe\bar{u}, \\ \mathbf{C}_2 &= 2\beta^2 \mathbf{I} - 2\mathbf{D}_2 + iRe(\beta\bar{w} - \omega \mathbf{I}), \\ \mathbf{C}_3 &= iRe(D_y^2 + \beta^2 - \mathbf{D}_2) \bar{u}, \\ \mathbf{C}_4 &= \mathbf{D}_4 - 2\beta^2 \mathbf{D}_2 + \beta^4 \mathbf{I} - iRe[\beta(\beta^2 - \mathbf{D}_2 + D_y^2) \bar{w} + (\mathbf{D}_2 - \beta^2 \mathbf{I}) \omega], \end{aligned}$$

where,  $\mathbf{I}$  is the identity matrix.

The eigenvalue spectrum of this system of equations consists of several root branches. A dominating root often does not belong to any of the aforementioned

branches and corresponds to the complex wavenumber of the most dominant wave,  $\alpha = \alpha_r + i\alpha_i$ . The latter is substituted in equation 2.7, yielding

$$\psi(y) = \varphi(y)e^{-(\alpha_i x + \beta_i z)} e^{i(\alpha_r x + \beta_r z - \omega t)}. \quad (2.11)$$

From the equation above it follows that the sign of the exponents  $\alpha_i$  and  $\beta_i$  determines whether the amplitude of disturbance grows ( $\alpha_i, \beta_i < 0$ ), decays ( $\alpha_i, \beta_i > 0$ ) or remains invariant ( $\alpha_i, \beta_i = 0$ ) along  $x$  and  $z$  spatial dimension, respectively.

In general, for flows where the free stream component or its derivatives along the  $z$  dimension are infinitesimally small,  $\beta_i$  is assumed zero, i.e. the disturbance amplitude does not vary with respect to  $z$ . Hence, the disturbance amplitude ratio from an arbitrary location  $x$  to  $x + dx$  may be expressed through equation 2.11 as

$$\frac{A + dA}{A} = \frac{e^{-\alpha_i(x+dx)}}{e^{-\alpha_i x}} = e^{-\alpha_i dx}. \quad (2.12)$$

The above is equivalent to

$$\ln(A + dA) - \ln(A) = d\ln(A) = -\alpha_i dx, \quad (2.13)$$

which, when integrated definitely, yields

$$n = \ln\left(\frac{A}{A_0}\right) = \int_{x_c}^x -\alpha_i dx, \quad (2.14)$$

with  $x_c$  being the critical location along  $x$  where a disturbance of amplitude  $A_0$  and frequency  $\omega$  first becomes unstable. Hereby,  $n$  is referred to as the *amplification factor*, whereas  $-\alpha_i$  and  $e^n$  as the *growth rate* and *amplification ratio*, respectively. Since the Orr-Sommerfeld equation is solved explicitly for a range of  $\omega$  at each  $x$ , a curve set of  $n$  as a function of  $x$  is obtained. The locus of the  $n(x, \omega)$  curve maxima,  $N(x)$ , is used as an indicator of transition. Typically, this is of the order of  $N = 9$ , however, the exact amplification factor for transition is dependent on perturbation factors such as free stream turbulence, surface roughness, noise etc.

### 2.2.2. PROPER ORTHOGONAL DECOMPOSITION

Proper Orthogonal Decomposition (POD) was introduced by Pearson [129] as Principal Component Analysis (PCA). It is a statistical method that utilises the orthogonal transformation in order to identify components of large variance. In essence, this facilitates low order approximation of high order systems using a number of relevant modes. In terms of fluid mechanics, POD has been extensively used for identification of coherent structures in laminar or turbulent flow conditions [9, 126]. Two flavours of POD are available, the classical *direct* method [27] and the *snapshot* method [161]. Here, only the second method shall be analysed as is the one utilised throughout this work.

First, a snapshot matrix is constructed, containing the temporally fluctuating components,  $\mathbf{u}'(t) = \mathbf{u}(t) - \bar{\mathbf{u}}$ , of the complete velocity field,  $\mathbf{u} = [u \ v \ w]^T$ . The

snapshot matrix rows and columns correspond to the value of  $\mathbf{u}'$  at each measurement location and time instant, respectively. Consequently, the snapshot matrix takes the form of,

$$\mathbf{S} = \begin{bmatrix} \mathbf{u}'(\mathbf{x}_1, t_1) & \mathbf{u}'(\mathbf{x}_1, t_2) & \cdots & \mathbf{u}'(\mathbf{x}_1, t_N) \\ \mathbf{u}'(\mathbf{x}_2, t_1) & \mathbf{u}'(\mathbf{x}_2, t_2) & \cdots & \mathbf{u}'(\mathbf{x}_2, t_N) \\ \vdots & \vdots & \ddots & \vdots \\ \mathbf{u}'(\mathbf{x}_M, t_1) & \mathbf{u}'(\mathbf{x}_M, t_2) & \cdots & \mathbf{u}'(\mathbf{x}_M, t_N) \end{bmatrix}, \quad (2.15)$$

where  $N$  and  $M$  are the number of snapshots and number of measurement locations per snapshot, respectively.

An eigenvalue problem may now be formulated, considering the autocovariance matrix of  $\mathbf{S}$ , that is  $\mathbf{R} = \mathbf{S}^T \mathbf{S}$ . It is expressed as,

$$\mathbf{R}\mathbf{a} = \lambda\mathbf{a}, \quad (2.16)$$

where  $\lambda$  and  $\mathbf{a}$  are the eigenvalues and temporal eigenfunctions, respectively. The latter assume the form of

$$\mathbf{a} = \begin{bmatrix} a^1(t_1) & a^2(t_1) & \cdots & a^N(t_1) \\ a^1(t_2) & a^2(t_2) & \cdots & a^N(t_2) \\ \vdots & \vdots & \ddots & \vdots \\ a^1(t_N) & a^2(t_N) & \cdots & a^N(t_N) \end{bmatrix}. \quad (2.17)$$

Each individual spatial POD mode  $\Phi^n$  can, therefore, be described by considering the associated temporal eigenfunctions  $a^n(t)$ , and is expressed as

$$\Phi^n(\mathbf{x}) = \sum_{i=1}^N a^n(t_i) \mathbf{u}'(\mathbf{x}, t_i). \quad (2.18)$$

The calculated eigenvalues ( $\lambda$ ) may provide an estimate of the energy related to each mode with respect to the total energy content of the fluctuating flow field,

$$E^n = \frac{\lambda^n}{\sum_{i=1}^N \lambda^i}. \quad (2.19)$$

$\Phi$  may, therefore, be sorted in order of decreasing  $\lambda$ . Hence, eigenfunctions with large eigenvalue represent the most dominant flow structures. A reduced order representation (denoted by the subscript ro) may, therefore, be achieved by summation of the time-averaged velocity field and a few selected spatial eigenfunctions by means of the following equation,

$$\mathbf{u}_{\text{ro}}(\mathbf{x}, t) = \bar{\mathbf{u}}(\mathbf{x}) + \sum_{n=1}^{N_{\text{ro}}} a^n(t) \Phi^n(\mathbf{x}). \quad (2.20)$$

An important note to be made is that POD analysis as described here is sensitive to the field of view within which it is applied. Consequently, the relative energy of each mode is also dependent on the selected field of view. Care must be, therefore, taken in order to capture all the relevant phenomena within the field of view.

### 2.2.3. WAVELET ANALYSIS

An in-depth overview of wavelet analysis may be found in the work of Daubechies [33], thus, only the essential concepts are hereby mentioned. The wavelet transform may be used where discrete Fourier analysis is inadequate, e.g. when investigating impulsive events or insufficient periodic repetitions of the signal of interest are available (see chapters 3 and 4).

For determining the spectral content of an arbitrary temporal signal,  $u(t)$ , a baseline wavelet function,  $\Psi$ , must first be chosen.  $\Psi$  must have a zero mean value and, in addition, it should be localised in both space and time. Throughout this work, the Morlet wavelet is selected, expressed as

$$\Psi = e^{(-t/c)^2} e^{i2\pi f_c t}. \quad (2.21)$$

In order to satisfy the admissibility condition described by Farge [42], the wavelet central frequency is selected to be  $2\pi f_c = 5\text{rad/s}$ , while the damping parameter is  $c = 2\text{s}$ . The convolution between the temporal signals of interest,  $F(t)$ , and the complex conjugate of  $\Psi$ , noted as  $\Psi^*$ , provide the wavelet coefficients,

$$\Gamma = \frac{s^{-1/2}}{\sqrt{2\pi f_a}} \int_{-\infty}^{\infty} \Psi^* \left( \frac{t-\tau}{s} \right) F(t) dt. \quad (2.22)$$

Here, the terms  $\tau$  and  $s$  represent the baseline wavelet translation and dilation scales, respectively. Unit power per scale is achieved by scaling the wavelet coefficients with  $\sqrt{2\pi f_a}$ , with  $f_a$  being the signal sampling frequency.

This analysis is not restricted to temporal signals. In fact, it may also be performed in space by substituting the temporal dimension,  $t$ , with a spatial dimension, e.g.  $x$  or  $z$ . In such case, the sampling frequency corresponds to the spatial resolution while the dilation scale takes the form of a wavelength.

## 2.3. UNCERTAINTY QUANTIFICATION

UNCERTAINTY in the experiments discussed in this document is mainly related to velocity uncertainty in PIV measurements. This may be caused by systematic and/or random errors. Systematic errors involve calibration errors as well as errors introduced by the available window interrogation algorithms [1]. On the other hand, random errors may, for instance, be caused by camera noise, out of plane motion of particle seeds, uneven illumination etc.

As discussed by Raffel *et al.* [134], errors in PIV measurements can generally be defined as the difference between real and measured values ( $u_{\text{real}} - u_{\text{meas}}$ ). Given that velocity is measured by means of particle displacement  $\Delta x$  at a given time interval  $\Delta t$ , the relative error in velocity,  $\varepsilon_u$ , is expressed as

$$\varepsilon_u = \frac{u_{\text{real}} - u_{\text{meas}}}{u_{\text{meas}}} = \sqrt{\left(\frac{\varepsilon_{\Delta x}}{\Delta x}\right)^2 + \left(\frac{\varepsilon_{\Delta t}}{\Delta t}\right)^2}, \quad (2.23)$$

where  $\varepsilon_{\Delta x}$  and  $\varepsilon_{\Delta t}$  are the errors on the measured displacement,  $\Delta x$ , and pulse separation,  $\Delta t$ , respectively. Typically, the value of  $\Delta t$  is higher than  $1\mu\text{s}$  and the

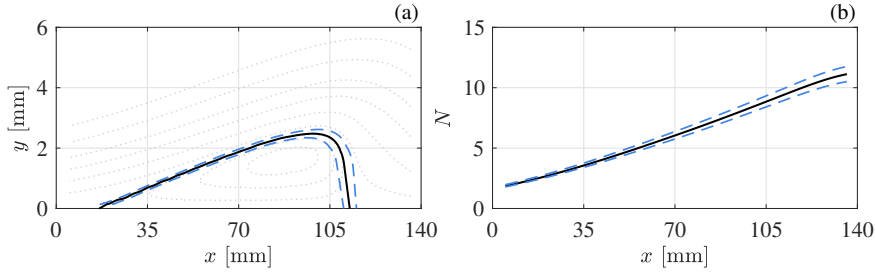


FIGURE 2.5: (a) Dividing streamline ( $\psi = 0$ ) of a laminar separation bubble. (b) Amplification factor along the length of the bubble. *Solid line*: estimates on the average flow field. *Dashed lines*: uncertainty limits.

error on the laser pulse separation is below one nanosecond. Consequently, the relative error on the time separation is below 0.1%. On the other hand, typical particle displacement is approximately 10 pixels with an uncertainty of the order of 0.1 pixels. Therefore, the relative error in the displacement is of the order of 1%, thus dominating the error of the measured velocity.

The above values are often utilised as an a priori indication of the measurement uncertainty. However, they do not always apply across different experiments or different regions within the same experiment. A representative example is the case of laminar separation bubbles where a strong shear layer divides the flow field into regions of high and low velocity. There are several methods with which uncertainty in PIV is formally estimated, the most prominent of which are discussed by Schiacchitano *et al.* [149]. All these methods take into account information such as raw images, correlation peaks and velocity vectors in order to quantify uncertainty.

For the purpose of this study, the correlation statistics method [178] is utilised, which incorporates errors such as particle disparity, camera noise and particle out of plane motion in a single error value. Through this approach, the error is estimated by mapping residual intensity differences from each pair of interrogation windows. More specifically, since the two interrogation windows do not perfectly match in terms of intensity, the correlation peak is asymmetric. This asymmetry is reflected in the shape of the correlation peak which is also asymmetric. The contribution of each pixel of the interrogation windows to the aforementioned asymmetry is associated with a standard deviation, hence, the local error. Performing the correlation statistics method to every interrogation window yields a velocity error field of the same size as the velocity field for each time instant.

To demonstrate how the velocity uncertainty is treated, a laminar separation bubble example is provided in figure 2.5a. Here, the solid line corresponds to the dividing streamline,  $\psi = 0$ , estimated on the time-averaged velocity field,  $\bar{u}$ . Adding and subtracting the uncertainty vector field from the time-averaged one ( $\bar{u} \pm \varepsilon_u$ ) provides the upper and lower limits within the velocity uncertainty. The dividing streamline is computed for each of these limits resulting in the dashed lines of figure 2.5a. In the same manner, the uncertainty is propagated to any further analysis

relying on velocity measurements such as the application of linear stability theory [118]. For instance, figure 2.5b depicts the amplification factor and its corresponding limits estimated on  $\bar{u}$  and  $\bar{u} \pm \varepsilon_u$ , respectively. Note that, when time-averaging, the estimated uncertainty is reduced in proportion to  $\sqrt{n_s}$ , where  $n_s$  is the number of samples [70]. Consequently, if no bias is present in the measurements, the upper and lower uncertainty limits converge for increasing number of averaging samples.

# 3

## IMPULSIVELY FORCED LAMINAR SEPARATION BUBBLES

*The work presented in this chapter investigates the response of laminar separation bubbles to impulsive forcing by assessing the attendant changes of flow dynamics and the underlying stability mechanism. Through the above, further insight is provided into both flapping and bursting mechanisms.*

---

MICHELIS, T., KOTSONIS. M. & YARUSEVYCH, S. 2017 Response of a laminar separation bubble to impulsive forcing. *Journal of Fluid Mechanics* **820**, 633-666.

MICHELIS, T. & KOTSONIS. M. 2016 Spatio-temporal response of a laminar separation bubble under impulsive forcing. *46th AIAA Fluid Dynamics Conference*.

### 3.1. BACKGROUND

GIVEN the relevance of laminar separation bubbles in terms of flow control for applications such as unmanned aerial vehicles and turbomachine blades, a considerable amount of studies has concentrated in understanding the underlying physics. Therefore, the evolution of disturbances and cascade of events on the separated shear layer is well documented. Marxen *et al.* [105] note that amplification of disturbances initiates in the laminar boundary layer, significantly upstream of the separation point. Prior to separation as well as in the laminar part of the LSB, flow is considered two-dimensional, thus linear stability theory (LST) may be applied successfully for prediction of unstable modes [54, 140].

The general consensus is that disturbances are convectively amplified via a Kelvin-Helmholtz instability mechanism [59]. Diwan & Ramesh [35] propose an instability of inflectional nature, whereas Marxen *et al.* [107] provide evidence of a Görtler type instability. On the other hand, as reported by Alam & Sandham [2], absolute instabilities may be prevalent in the case that reverse flow in the LSB lies between 15% and 20% of the local free stream velocity. Regardless of the instability path, amplification of disturbances through these mechanisms leads to shear layer rollup and the formation of vortical structures in the aft part of the LSB. Their dynamics constitute coherent vortex shedding [55, 66].

Whether numerical or experimental, most studies that investigate stability characteristics involve artificial forcing of the boundary layer with known perturbations at a location upstream of the separation point and describe the subsequent flow evolution. The most common type of forcing is sinusoidal and periodic at the most unstable frequency of the separated shear layer, usually identified through linear stability theory. This type of forcing has been introduced by various means including spanwise uniform wall oscillation [2, 107], externally imposed acoustic excitation [65, 184] as well as DBD plasma actuation [183].

Most of the past studies consider the response of the LSB to continuous forcing. Gaster & Grant [49] were the first to introduce an impulsive disturbance, exciting the full spectrum of instability modes, thus generating a wave packet through selective amplification. This method was subsequently used by Watmuff [173] and Diwan & Ramesh [35]. It must be noted that impulsive disturbances have, so far, been locally introduced at a single point, usually a pressure tap. Consequently, the emerging wave packets initially exhibit strong three-dimensional features, complicating the elucidation of the underlying physical mechanisms and application of LST. Indeed, non-linear evolution in the form of subharmonic resonance has been observed in locally introduced wave packets [25]. The present study, instead, focuses on two-dimensional spanwise-uniform impulsive disturbances.

Rist & Augustin [139] and Marxen & Rist [108] documented enhanced flow stabilisation with increasing forcing amplitudes. Additionally, they observed reduction of the LSB size from both upstream and downstream directions. Similarly to Dovgal *et al.* [38] and Boiko *et al.* [12], they suggested a feedback loop process to explain the bubble size reduction due to controlled disturbances. More specifically, a disturbance input alters the flow in the aft part of the bubble, resulting in a global change of pressure gradient due to viscous-inviscid interactions. This indirectly distorts the

mean flow at the upstream part of the bubble towards a more stable state, mitigating subsequent disturbance amplification, effectively leading to stabilisation. Marxen & Henningson [103] argued that, if irregular disturbances are present in the incoming flow, such as free stream turbulence in free flight or wind-tunnel experiments, the aforementioned feedback loop may explain the occurrence of an intermittent shear layer fluctuation associated with LSBs, often referred to as *flapping* [186]. Adding to this argumentation, significant reduction of the flapping behaviour due to artificial monochromatic forcing has been noted by Dovgal & Boiko [37] and Sandham [142], related to the locking of the bubble dynamics to modes of constant amplitude. Moreover, flow stabilisation due to the mean flow deformation under continuous forcing has recently been confirmed experimentally by Yarusevych & Kotsonis [183].

Laminar separation bubbles are often classified in literature as *short* or *long* based on their length or whether their influence on pressure distribution is global or local [47, 127, 167]. A detailed overview of the associated bubble characteristics is given by Marxen & Henningson [103]. Pauley *et al.* [128] noted that long separation bubbles with laminar reattachment do not exhibit formation of vortex shedding. In contrast, the long separation bubbles of Gaster [47] and Marxen & Henningson [103] exhibit laminar to turbulent transition and turbulent reattachment. However, they fail to reattach as early as short bubbles. Marxen & Henningson [103] note that, contrary to short separation bubbles, vortex roll-up in long bubbles occurs further downstream of the transition location. Under certain conditions involving minor flow variations, a short separation bubble may significantly elongate, a dynamic process termed *bursting* which has been associated with aerofoil stall [142]. It should be noted, however, that bursting and elongation do not necessarily imply that the LSB acquires long bubble characteristics. Although determining appropriate criteria for bubble bursting has been a recurrent topic [e.g. 35, 47, 103, 156], the development of a universal criterion has proven difficult, mainly due to the lack of sufficient understanding of the bursting process.

In an effort to characterise short and long bubbles, Gaster [47] initiated bursting by reducing the wind-tunnel speed, affecting pressure gradient and free stream turbulence. Following a different approach, Marxen & Henningson [103] induced bursting by eliminating or attenuating disturbances in their DNS boundary conditions. Both studies, therefore, relied on artificial reduction of the amplitude of disturbances in the separated shear layer. It must be noted here, that although this approach is technically straightforward in experimental and numerical frameworks, it does not correspond fully to the physical sequence of events preceding bubble bursting. The reason is the inability of these approaches to decouple the effect of local mean flow stability changes (i.e. mean flow deformation) and the effect of incoming perturbation amplitude, since the latter is varied. Nevertheless, based on these studies, a hypothesis can be formulated regarding global changes of the size of LSBs as a function of incoming disturbances which could lay the foundation for elucidating both the flapping and bursting mechanisms [103]. Namely, *the amplitude of flow perturbations entering the LSB defines the breakdown location which, in turn, defines the size of the LSB and the growth of the developing instabilities*. The evaluation of such a hypothesis in an experimental framework is the premise of the present study,

in reference to the numerical study of Marxen & Henningson [103].

The work presented in this chapter investigates the response of laminar separation bubbles to impulsive forcing by assessing the attendant changes of flow dynamics and the underlying stability mechanism. Through the above, further insight is provided into both flapping and bursting mechanisms. A laminar separation bubble is induced on a flat plate by an externally imposed adverse pressure gradient. Repetitive, two-dimensional, impulsive disturbances are introduced upstream of the location of LSB separation point by means of a dielectric barrier discharge (DBD) plasma actuator [28, 79, 183]. The premise of using impulsive, spanwise uniform, disturbances is twofold. Firstly, impulsive excitation features a broad spectral content, giving rise to the naturally pertinent instability modes through selective amplification. Secondly, for constant conditions (free stream velocity and turbulence levels) the inflow of the LSB experiences an elevated incoming disturbance amplitude only during the short duration of the impulse. At all other instants, the LSB experiences a natural level of incoming disturbances. Effectively, this enables monitoring mean flow deformation effects, following the wave packet convection, without altering the amplitude of incoming disturbances.

The evolution of the emerging wave packet and the response of the LSB are captured with time-resolved particle image velocimetry (PIV), demonstrating that bursting occurs shortly after the convection of the wave packet. Finally, linear stability theory is employed in order to relate pertinent changes in stability characteristics to the changes in LSB dynamics. Since the aforementioned studies involving linear stability theory analysis only consider stability characteristics of the mean flow [54, 108, 140], a necessity rises of investigating dynamic stability, for which quasi-steady assumptions may be made. LST in the spatial formulation is, therefore, applied on phase-averaged velocity fields within a forcing cycle in order to assess changes in stability characteristics from bursting until relaxation of the LSB.

## 3.2. DESCRIPTION OF EXPERIMENTS

### 3.2.1. FLOW AND MODEL CONFIGURATION

Experiments are carried out in the W-tunnel, described in section 2.1.1. An overview of the experimental setup is shown in figure 3.1. A 20mm thick, 500mm wide and 1000mm long Plexiglas<sup>®</sup> flat plate is inserted in the test section off-centre at a 30% distance from the floor for alleviating wind tunnel corner effects [144]. The flat plate leading edge is a modified super ellipse [97], enabling seamless curvature change and ensuring development of laminar boundary layer. A movable flap is positioned at the trailing edge of the flat plate and is deflected such as to localise the leading edge stagnation point on the upper side of the flat plate, eliminating possible unsteady separation effects. The pressure gradient on the flat plate surface is conditioned with the aid of a flexible, 1mm thick polycarbonate wall, positioned on the opposite side of the test section. The flexible wall shape is modified by adjustable screw struts, located at ten streamwise locations. A Cartesian coordinate system is defined such that  $\tilde{x} = 0$  lies 420mm from the leading edge of the flat plate,  $\tilde{y} = 0$  at its top surface and  $\tilde{z} = 0$  at its midspan.

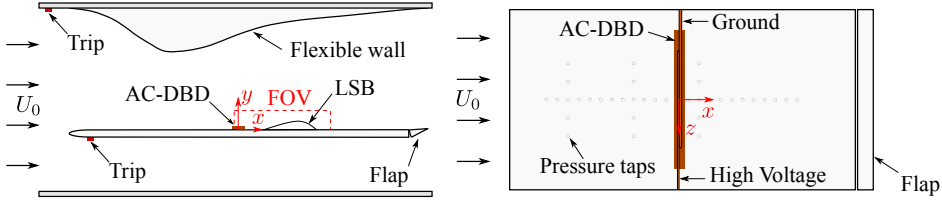


FIGURE 3.1: Schematic of the experimental setup.

The boundary layer on the lower side of the flat plate is tripped at a distance of 50mm from the leading edge by means of a 2mm thick zig-zag turbulator. This is done for eliminating possible fluctuations of a laminar boundary layer as well as for reducing the strength of shedding at the trailing edge flap. The same technique is applied at the upstream end of the flexible wall in order to avoid unsteady separation in the adverse pressure gradient region. Suppression of these effects was confirmed during preliminary studies by employing both tuft flow visualisation and PIV measurements. In addition, flowfield surveys with a stethoscope confirmed that the boundary layer does not re-laminarise in the favourable pressure gradient region.

The free stream velocity ( $\tilde{U}_0$ ) is set using a Pitot-static tube located 100mm upstream of the flat plate leading edge and is kept constant at 6.4m/s, with uncertainty lower than 2%. Hot-wire measurements, bandpass filtered between 0.1Hz and 1kHz, were used to estimate free stream turbulence intensity ( $\text{TI} = \tilde{U}'_{\text{rms}}/\tilde{U}_0$ ), determined to be under 0.2%.

The pressure distribution imposed by the flexible wall is measured by means of 36 pressure taps integrated in the flat plate (figure 3.1) and is expressed in terms of surface pressure coefficient ( $C_p$ ) defined as

$$C_p = \frac{\tilde{p} - \tilde{p}_\infty}{\frac{1}{2}\tilde{\rho}_0\tilde{U}_0^2}. \quad (3.1)$$

In the streamwise direction, pressure taps are located at the midspan ( $\tilde{z} = 0$ ) with 30mm spacing. Spanwise taps are spaced symmetrically with respect to the midspan at three streamwise locations;  $\tilde{x} = -260\text{mm}$ ,  $-80\text{mm}$  and  $100\text{mm}$ , with a spanwise spacing of 50mm. Pressure coefficient measurements are performed with a high accuracy multi-channel pressure scanner at an acquisition frequency of 0.1Hz and mean pressures are estimated from 150 samples at each location. The obtained mean  $C_p$  distribution is shown in figure 3.2. The presence of a pressure plateau in the streamwise surface pressure distribution (figure 3.2a) indicates the formation of a laminar separation bubble [185] in the interval between  $\tilde{x} \approx 30\text{mm}$  and  $\tilde{x} \approx 150\text{mm}$ . The presence of a laminar separation bubble is confirmed by tripping the boundary layer with a zig-zag turbulator placed at the leading edge of the flat plate. The resulting streamwise pressure distribution (figure 3.2a) shows that the turbulent boundary layer overcomes the adverse pressure gradient without separating and that  $C_p$  increases downstream without exhibiting the typical for laminar separation

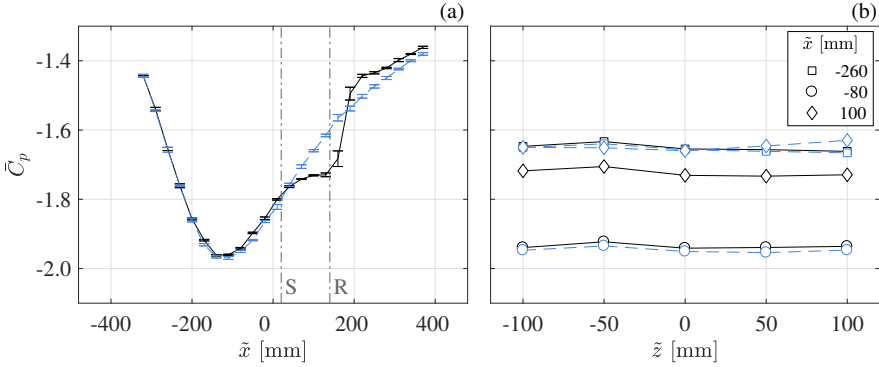


FIGURE 3.2:  $C_p$  distribution in (a) streamwise direction ( $\bar{z} = 0$ ) and (b) spanwise direction. *Solid lines*: clean flat plate conditions. *Dashed lines*: tripped boundary layer near the leading edge.

bubbles pressure plateau. Figure 3.2b demonstrates that both clean and tripped configurations produce uniform pressure distribution in the spanwise direction, ensuring essentially two-dimensional conditions in the time averaged sense.

### 3.2.2. IMPULSIVE FORCING

Controlled disturbances are introduced upstream of the LSB with the use of an AC-DBD plasma actuator (see section 2.1.3), located just upstream of the mean separation point (figure 3.1). For this study, the streamwise extent of the high voltage and ground electrodes are 2mm and 5mm, respectively. Both electrodes are painted on the surfaces using conductive silver coating and are less than  $10\mu\text{m}$  in thickness. The dielectric comprises of  $60\mu\text{m}$  thick *Kapton*<sup>®</sup> polyimide film whose thickness is significantly lower than the local boundary layer displacement thickness ( $\approx 5.5\text{mm}$ ). Preliminary studies have confirmed negligible influence on the bubble dynamics from the mechanical roughness associated with the actuator. The discharge gap is located at a distance of 420mm from the leading edge and serves as the origin of the reference system (figure 3.1).

The actuator is driven by a digitally controlled *TREK 20/20C* high voltage amplifier. The forcing signal is comprised by repetitive pulses as shown in figure 3.3. Each pulse is constructed by modulating the sinusoidal carrier signal ( $\tilde{f}_c = 5\text{kHz}$ ) with a square signal at significantly lower pulse frequency of  $\tilde{f}_p = 2\text{Hz}$ . The duty cycle of modulation is fixed at 0.2%, resulting in a pulse width of 1ms. The relevant hydrodynamic frequency associated with the primary shear layer instability and subsequent vortex shedding in the current LSB is approximately 130 Hz as will be shown in a later section. Respectively, the frequency associated with flapping is of the order of 10 Hz. With the carrier frequency exceeding any relevant hydrodynamic frequency by at least two orders of magnitude, each 1ms burst is essentially equivalent to a single impulsive perturbation. Furthermore, the frequency of the pulses ( $\tilde{f}_p = 2\text{Hz}$ ) is selected such that the bubble fully recovers to its unperturbed state between two consecutive pulses, which has been verified experimentally. Thus,

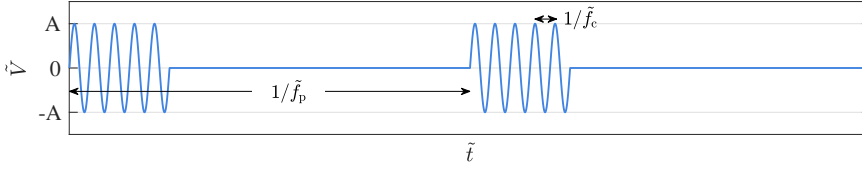


FIGURE 3.3: Sample of the DBD plasma actuator forcing signal of amplitude  $A$ . The sinusoidal signal at carrier frequency  $\tilde{f}_c = 5\text{kHz}$  is modulated with a square wave of pulse frequency  $\tilde{f}_p = 2\text{Hz}$ . Duty cycle is 0.2% leading to 1ms pulse width.

the perturbations introduced at such parameters represent a sequence of statistically independent impulses, facilitating phase-averaging of the flow measurements.

In order to assess the effect of the excitation amplitude on LSB topology and dynamics, several peak to peak voltage amplitudes are considered, between 2.5kV and 5kV. Characterisation of the forcing exerted on the fluid by the AC-DBD for the applied voltages is expressed in terms of momentum coefficient ( $C_\mu$ , equation 2.4). The described momentum coefficient is calculated based on continuous operation of the actuator and, as such, pertains to the mechanical power of the actuator. Since for the LSB control the actuator is operated in a modulated manner, the momentum transferred to the flow during each individual pulse can be extracted by simply multiplying the relevant momentum coefficient by the duty cycle.

The estimated  $C_\mu$  during continuous operation under quiescent conditions for each applied voltage and an exemplary velocity field are shown in figure 2.4. Evidently, the largest contribution in forcing originates from the momentum exchange along the  $x$ -axis ( $C_{\mu_x}$ ). As fluid is displaced by the jet, a secondary effect is observed in the region of the discharge gap ( $\tilde{x} = 0$ ). As a result, thrust along the  $y$ -axis is generated towards the wall, signified by negative momentum coefficient ( $C_{\mu_y}$ ). Although the magnitude of momentum coefficient is proportional to the voltage,  $C_{\mu_y}$  is significantly lower than  $C_{\mu_x}$  for all applied voltage amplitudes. For the remainder of the study,  $C_\mu \approx C_{\mu_x}$  is used as an indicator of actuator strength. It is important to note that the topology of the jet as well as the value of  $C_\mu$  are largely unchanged in the case of the relatively weak external flow encountered in this study [130].

### 3.2.3. DATA ACQUISITION

A time-resolved, two-component Particle Image Velocimetry (PIV) system is employed for investigating the flowfield in the  $x$ - $y$  plane as seen in figure 3.1. Illumination is performed by a *Quantronix Darwin Duo* laser system that delivers green light (532nm). The beam is transformed into a 1mm light sheet with the aid of an array of spherical and cylindrical lenses. Two *Photron FASTCAM SA1.1* cameras with  $1024 \times 1024$  pixels sensor resolution are used to image the illuminated region. Both are equipped with 200mm macro objectives set at an aperture of  $f/5.6$ . Particle seeding consists of vaporised water-glycol mixture droplets of  $1\mu\text{m}$  diameter. Acquisition frequencies ( $\tilde{f}_a$ ) at 250Hz, 500Hz and 2000Hz are selected for obtaining statistics and resolving high frequency phenomena accordingly. For each acquisition frequency,

10914 cropped image pairs ( $\Delta\tilde{t} = 60\mu\text{s}$ ) are recorded, resulting in total acquisition times of 43.7s, 21.8s and 5.5s, respectively. The image pairs are acquired and processed with *LaVision DaVis 8.3*. The magnification factor is  $M = 0.29$ , yielding a resolution of 14px/mm for each camera. Particle displacements are calculated by applying the multi-step interrogation algorithm [147] from an initial window of  $48 \times 48$  pixels to a final window of  $12 \times 12$  pixels with a 75% overlap between windows. The resulting vector spacing is 0.19mm in both  $x$  and  $y$  directions. The multi-step interrogation window sizes have been selected such that the final vector spacing matches the limit of spatial resolution determined via the method described by Kähler *et al.* [69]. Vector fields from the two cameras are stitched together to obtain a combined field of view of 131mm by 14mm.

For the experimental data presented in this work, uncertainty is quantified using the correlation statistics method [178]. The local error for instantaneous velocity measurements is estimated to be  $\varepsilon_u \approx 1\%$  in the free stream and  $\varepsilon_u \approx 10\%$  within the LSB. Maximum uncertainty is associated with the region of shear layer breakdown and reattachment. At this location, the uncertainty in the phase-averaged velocity fields is 3%, 5% and 8% for acquisition frequencies of 250Hz, 500Hz and 2000Hz, respectively. Since the majority of results discussed in the present study pertain to an acquisition frequency of  $\tilde{f}_a = 500\text{Hz}$ , the corresponding uncertainty is propagated through the analysis (see section 2.3) to yield uncertainty estimates for the location of the LSB dividing streamline ( $< 2.5\%$ ) and LST growth rates ( $< 3.5\%$ ).

Actuation and PIV measurements are digitally controlled and synchronised. The reference time  $\tilde{t}_0 = 0\text{s}$  is set at the moment when the actuator is activated. Subsequently, the camera shutter and laser pulse signals are used for establishing the time of the first measurement to within  $1\mu\text{s}$ .

### 3.3. POST-PROCESSING METHODOLOGY

#### 3.3.1. NOTATION AND SCALING

Throughout this report, dimensional quantities are noted by a tilde and are accompanied by the respective unit (e.g.  $\tilde{x}$  [mm]). For non-dimensional representation, measured and computed quantities are globally normalised with representative scaling parameters from the baseline unforced LSB. More specifically, all lengths are normalised with the displacement thickness at the separation point of the unforced LSB ( $\tilde{\delta}_{s_0}^* = 2.39\text{mm}$ ). Integral boundary layer parameters are estimated based on the numerical integration of the measured time-averaged velocity field. Velocities are non-dimensionalised with the local edge velocity at separation,  $\tilde{U}_{\infty_s} = 8.6\text{m/s}$ . These two scaling factors are employed for defining the Reynolds number as  $Re_{\tilde{\delta}_s^*} = \tilde{U}_{\infty_s} \tilde{\delta}_{s_0}^* / \tilde{\nu} = 1305$ . Furthermore, they are combined for frequency scaling in the form of a Strouhal number,  $St = \tilde{f} \tilde{\delta}_{s_0}^* / \tilde{U}_{\infty_s}$ . All non-dimensional quantities are denoted by their respective symbol (e.g.  $x = \tilde{x} / \tilde{\delta}_{s_0}^*$ ,  $u = \tilde{u} / \tilde{U}_{\infty_s}$ ). Time-averaged quantities are identified with an overbar (e.g.  $\bar{u}$ ), whereas temporal fluctuations are marked by a dash (e.g.  $u'$ ).

An additional scaling scheme is introduced for the comparison of forced and unforced cases. Accordingly, quantities are scaled with the respective time-averaged

value pertaining to the unforced LSB for each case. For example, the separation point,  $x_s$ , is scaled with the mean separation point of the unforced LSB,  $\bar{x}_{s_0}$ . All scaled primary (e.g. length) and derived (e.g. vorticity) quantities, are subsequently denoted by a hat (e.g.  $\hat{x} = x/\bar{x}_{s_0}$ ,  $\hat{\omega} = \omega/\bar{\omega}_{s_0}$ ).

As mentioned in section 3.2.2, the LSB is cyclically forced by pulses of frequency  $\tilde{f}_p = 2\text{Hz}$ . Therefore, a non-dimensional phase,  $\phi$ , is defined based on the pulse frequency and the time interval elapsed from the preceding pulse ( $\tilde{t}$ ), expressed as

$$\phi = \tilde{t}\tilde{f}_p. \quad (3.2)$$

Consequently,  $\phi = 0$  coincides with the moment of actuation, while  $\phi = 1$  occurs after a time interval of  $\tilde{t} = 1/\tilde{f}_p$ , at the moment prior to the next pulse initiation. Phase-averaged quantities are denoted with chevron brackets (e.g.  $\langle u \rangle$ ).

### 3.3.2. LINEAR STABILITY ANALYSIS

Similarly to earlier studies [54, 65, 108, 140, 183] the stability characteristics of the LSB mean flow field are investigated using linear stability theory (LST). The latter assumes local parallel flow and low amplitude wave-like disturbances. While these assumptions are approximations for separated flows such as the LSB at hand, the above studies have shown very good agreement between LST predictions and direct numerical simulation (DNS) or experimental data.

In classical LST analysis, the amplification of disturbances is governed by the Orr-Sommerfeld eigenvalue problem,

$$\begin{aligned} (D_y^2 - \alpha^2 - \beta^2)^2 \varphi(y) = \\ = iRe [(\alpha\bar{u} + \beta\bar{w} - \omega)(D_y^2 - \alpha^2 - \beta^2) - \alpha D_y^2 \bar{u} - \beta D_y^2 \bar{w}] \varphi(y). \end{aligned} \quad (3.3)$$

Here,  $\alpha$  and  $\beta$  are the complex streamwise and spanwise wavenumbers, respectively while  $\omega$  is the corresponding wave frequency. The problem is solved in spatial formulation, i.e. for real values of  $\omega$ . Please refer to section 2.2.1 for a detailed description of the solution process. For this study, two-dimensional flow is assumed and only streamwise disturbances are considered, therefore,  $\beta = 0$  and  $\bar{w} = 0$ .

The amplification factor,  $N$ , is expressed as,

$$N = \ln \left( \frac{\tilde{A}}{\tilde{A}_0} \right) = \int_{\tilde{x}_c}^{\tilde{x}} -\tilde{\alpha}_i d\tilde{x}, \quad (3.4)$$

with  $\tilde{x}_c$  being the critical streamwise location where a disturbance of amplitude  $\tilde{A}_0$  and frequency  $\omega$  first becomes unstable. Due to practical limitations of experimental techniques, it is not possible to directly measure minute amplitude of disturbances prior to their amplification above a given measurement noise level. This renders experimental determination of the critical point difficult. However, in the upstream part of the LSB,  $\alpha_i$  may be approximated by a second order polynomial (e.g. Jones *et al.* [65], cf. figure 11). As a result, it is possible to estimate  $x_c$  by extrapolating the fit curve to  $\alpha_i = 0$ . Hence, the amplification factor at the beginning of the imaged field of view is quantified, serving as a constant for the integration thereon.

Linear stability in temporally variable baseline flows may generally be treated following the formulation of Reynolds & Hussain [137], that reads

$$\begin{aligned} [(\alpha\bar{u} - \omega)(D_y^2 - k^2) - \alpha D_y^2 \bar{u}] \varphi(y) = \\ = -\frac{i}{Re}(D_y^2 - k^2)^2 \varphi(y) + ikD_y(s_{11} - s_{22}) + k(D_y^2 + k^2)s_{12}, \end{aligned} \quad (3.5)$$

where,  $k^2 = \alpha^2 + \beta^2$ . This formulation differs from the classical Orr-Sommerfeld eigenvalue problem, by the inclusion of Reynolds stress terms,  $s_{ij}$ .

It is well asserted that global flow modification in the region of the LSB is associated with rather low frequencies, e.g. changes experienced due to flapping or bursting [47, 103]. In contrast, the objective of LST is to describe the growth of instabilities of significantly higher frequencies, such as the pertinent Kelvin-Helmholtz modes developing in the separated shear layer. Due to this large timescale separation, LST modes essentially experience a quasi-steady baseline flow at a given time after the introduction of a pulse. Further discussion on the timescale separation is carried out in section 3.5.2. A quasi-steady assumption can, therefore, be made and LST calculations may be performed on phase-averaged velocity profiles, omitting Reynolds stress terms of equation 3.5, thus arriving to equation 3.3. This approach has been treated and discussed in past studies [e.g. 14, 71]. Finally, it should be stressed that non-linear effects cannot be predicted using LST, especially in the aft part of the LSB, where high amplitude three dimensional structures are dominant. Reliable stability estimates are, therefore, expected in the fore portion of the bubble, where the amplitude of disturbances is relatively low.

## 3.4. THE UNFORCED LSB

### 3.4.1. STEADY STATE FEATURES

Prior to the analysis of the spatio-temporal response of the bubble to the impulsive forcing, it is instructive to examine the behaviour pertaining to the natural, unforced flow serving as baseline in this study. Figure 3.4 depicts time-averaged and fluctuating fields of the unforced flow. Driven by the adverse pressure gradient, the flow separates and reattaches forming a closed, in the time-averaged sense, laminar separation bubble. The boundary of the LSB is defined by the mean dividing streamline, where the streamfunction  $\psi = 0$ . The mean separation and reattachment points are estimated at  $\bar{x}_s = 6.3$  and  $\bar{x}_r = 47.5$ , establishing a bubble length of  $\bar{l}_b = 41.2$ . The height of the bubble is defined as the point of the dividing streamline that is most distant from the wall,  $\bar{h} = 0.73$ , and is located at  $\bar{x}_h = 41.7$ . The maximum reverse flow observed within the bubble is of the order of 2% of the local free stream velocity, indicating development of only convective instabilities Gaster [48], Alam & Sandham [2] and Rist & Maucher [140].

Time-averaged streamwise velocity profiles scaled with the local freestream velocity ( $\tilde{U}_\infty$ ) are provided for several streamwise stations in figure 3.4a. These profiles are similar to the hyperbolic tangent approximations suggested by Dovgal *et al.* [38] as well as with hot-wire measured profiles rectified in proximity to the wall [35, 124, 173]. Similar to the studies of Gaster & Grant [49] and Marxen & Henningson

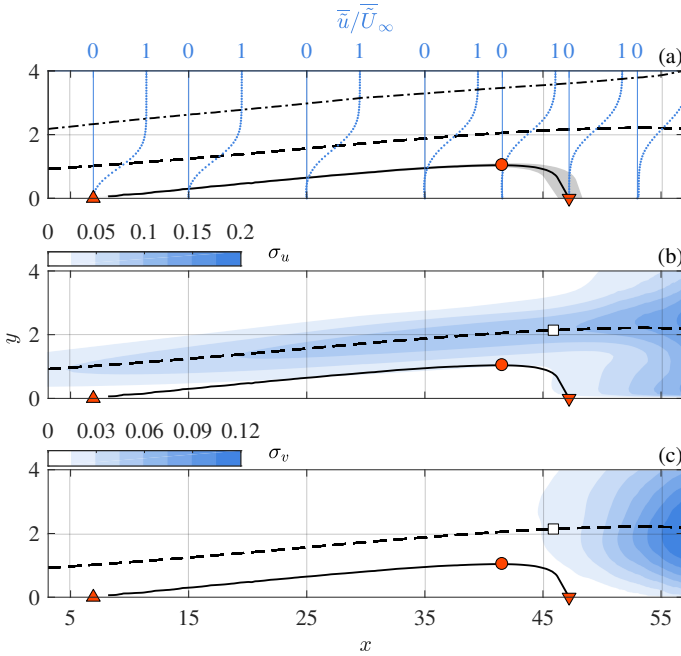


FIGURE 3.4: Unforced LSB. (a) Time-averaged streamwise velocity profiles, scaled with the local free stream velocity. (b) Streamwise velocity fluctuations. (c) Wall-normal velocity fluctuations. *Solid line*: dividing streamline, *dashed line*: displacement thickness, *dash-dotted line*:  $\delta_{99\%}$ .  $\Delta$ : separation point,  $\nabla$ : reattachment point,  $\circ$ : maximum height,  $\square$ : maximum shape factor. *Shaded region*: dividing streamline uncertainty limits for  $\tilde{f}_a = 500\text{Hz}$ .

[103], reattachment is turbulent, however, there is no correspondence with a fully developed turbulent velocity profile (log-law) in the downstream vicinity of the reattachment. Indeed, as Alam & Sandham [2] indicate, relaxation of the boundary layer to a fully turbulent equilibrium state may require several bubble lengths, well downstream of the current field of view.

Fluctuations in the velocity field are quantified by the standard deviation of the two velocity components,  $\sigma_u = \tilde{\sigma}_u/U_0$  and  $\sigma_v = \tilde{\sigma}_v/U_0$  (figures 3.4b and 3.4c). Two regions of increased fluctuation can be identified, the first extending along the displacement thickness, upstream of  $\bar{x}_h$ . In this region, small variations in the shear layer distance from the wall due to the flapping mechanism [186] result in substantial changes in the value of  $u$ . Flapping does not affect the wall-normal velocity to the same extent, thus this region is absent in the  $\sigma_v$  field. In contrast, the second region of elevated fluctuations is evident in both standard deviation fields downstream of  $\bar{x}_h$ . Here, fluctuations are attributed to coherent vortex shedding (figure 3.5) and the subsequent breakdown to turbulence. In both velocity components, the associated velocity fluctuations are concentrated about the displacement thickness, known to approximate the trajectory of the shed structures [13].

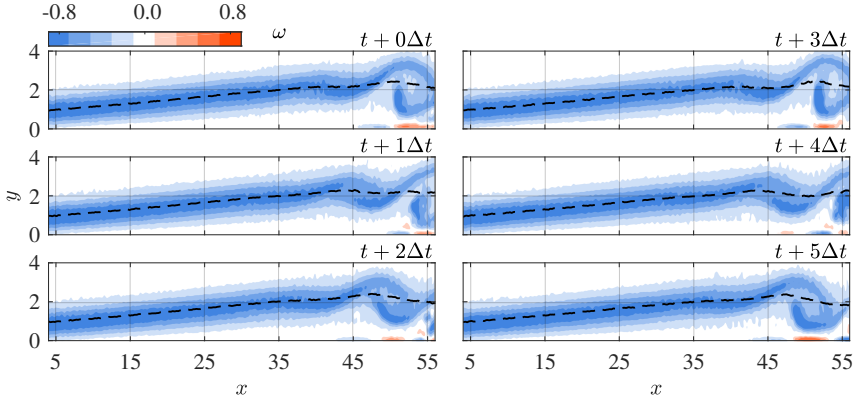


FIGURE 3.5: Instantaneous vorticity demonstrating coherent vortex shedding at timesteps separated by  $\Delta t = 5\tilde{f}_p/\tilde{f}_a$ , with  $\tilde{f}_a = 2\text{kHz}$ . *Dashed line*: displacement thickness ( $\delta^*$ ).

### 3.4.2. PROPER ORTHOGONAL DECOMPOSITION

Identification of coherent structures and data order reduction are performed via the snapshot POD method (see section 2.2.2). The fluctuations of the velocity field,  $\mathbf{u}'$ , are first decomposed to a set of eigenfunctions,  $\Phi$ . The latter are sorted in decreasing order of eigenvalue ( $\lambda$ ). Hence, eigenfunctions with large eigenvalue represent the most dominant flow structures. A reduced order representation (denoted by the subscript  $ro$ ) may, therefore, be achieved by summation of the time-averaged velocity field and few selected spatial eigenfunctions by means of

$$\mathbf{u}_{ro}(\mathbf{x}, t) = \bar{\mathbf{u}}(\mathbf{x}) + \sum_{n=1}^{N_{ro}} a^{(n)}(t)\Phi^{(n)}(\mathbf{x}), \quad (3.6)$$

where,  $a$  are the temporal coefficients, unique to each snapshot. The analysis shows that for both unforced and forced cases studied here, 85% of the total estimated modal energy is concentrated within the first four POD modes (figure 3.6a).

A preliminary study sought in identifying the underlying phenomena that each of the first four modes represent. In the unforced scenario,  $\Phi^{(1)}$  captures fluctuations of the shear layer attributed to the flapping behaviour. The following eigenfunctions,  $\Phi^{(2)}$  and  $\Phi^{(3)}$  represent the convective shedding of the LSB. Similar observations regarding the first three modes have been made by Lengani *et al.* [94]. When the bubble is forced (figure 3.6b-e),  $\Phi^{(1)}$  remains to be associated with the shear layer flapping while the second eigenfunction,  $\Phi^{(2)}$  represents the rapid shrinkage and recovery of the LSB shear layer that is further described in section 3.5.1. Shedding and convection of the introduced disturbance are simultaneously captured in  $\Phi^{(3)}$  and  $\Phi^{(4)}$ , as they assume the same frequency.

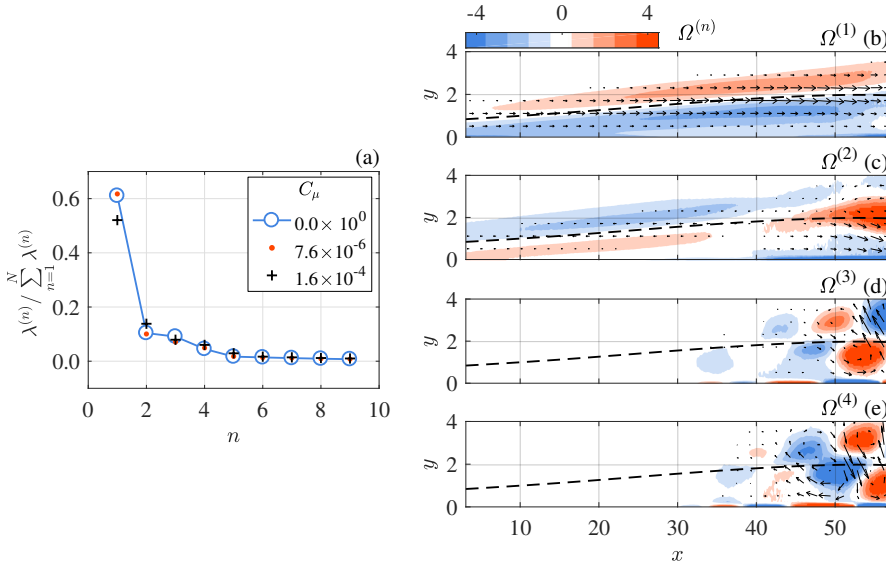


FIGURE 3.6: (a) Nine first POD eigenvalues for unforced and forced LSB. (b)-(e) Curl between the streamwise and wall-normal component of the first four eigenfunctions,  $\Omega^{(n)} = \nabla \times [\Phi_u^{(n)} \Phi_v^{(n)}]$  for  $C_\mu = 1.6 \times 10^{-4}$ . *Dashed line*: displacement thickness.

### 3.4.3. SPECTRAL CONTENT AND STABILITY CHARACTERISTICS

The global displacement of the separated shear layer in a LSB, i.e. flapping, is known to occur at significantly lower frequencies than the respective vortex rollup and shedding [55]. To access the spectral content of the shear layer flapping and vortex shedding of the unforced LSB, velocity measurements are performed at  $\tilde{f}_a = 250\text{Hz}$  and  $\tilde{f}_a = 2000\text{Hz}$ , respectively. The selection of reference locations is made based on results in figure 3.4. For assessing flapping, a temporal signal,  $u(t)$  is extracted at the streamwise location corresponding to the mean separation point,  $\bar{x}_s$ , and at wall normal location corresponding to  $\delta^*(\bar{x}_s)$ . Here, minimal vortex shedding signature is expected in the spectra. For characterising vortex shedding in the aft part of the bubble, a  $v(t)$  signal is sampled at the streamwise location of mean maximum height and wall-normal distance equal to the displacement thickness  $\delta^*(\bar{x}_h)$ .

Power spectral density is estimated via the Welch method [175] by dividing the corresponding temporal signal into 6 windows with 50% overlap. The resulting frequency resolution is  $St = 3.6 \times 10^{-5}$  and  $2.8 \times 10^{-4}$  (0.13Hz and 0.98Hz) for each of the two acquisition frequencies, respectively. The results shown in figure 3.7a suggest that flapping is comprised of a range of frequencies below  $St = 0.005$  (18Hz). The two peaks present in the vicinity of  $St \approx 0.005$  are attributed to aliasing from shedding signature and are approximately three orders of magnitude weaker than the highest point in the band. In contrast, shedding in the aft portion of the bubble produces a well defined, elevated spectral content situated between  $St = 0.022$  (80Hz) and  $St = 0.047$  (170Hz) (figure 3.7b). The dominant frequency is  $St = 0.038$  (136Hz),

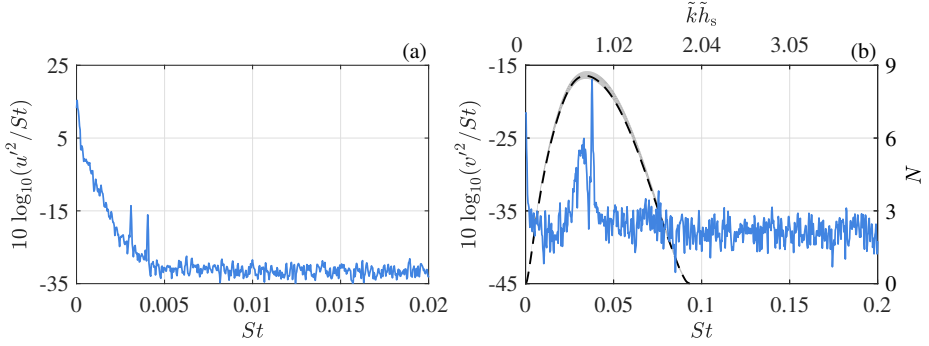


FIGURE 3.7: Power spectral density of the unforced LSB. (a)  $u(t)$  at  $x = \bar{x}_s$  and  $y = \delta^*(\bar{x}_s)$ ,  $\bar{f}_a = 250\text{Hz}$ . (b)  $v(t)$  at  $x = \bar{x}_h$  and  $y = \delta^*(\bar{x}_h)$ ,  $\bar{f}_a = 2000\text{Hz}$ . Dashed line:  $N$  factor at the same location. Shaded region:  $N$  factor uncertainty at  $\bar{f}_a = 500\text{Hz}$ .

with an order of magnitude higher spectral density than the rest of the band. The spectral content is also related to the dimensionless shedding parameter,  $\tilde{k}\tilde{h}_s$  [181]. Here,  $\tilde{k} = 2\pi\tilde{f}/\tilde{u}_{\text{infl}}$ , is the angular wave number, with  $\tilde{u}_{\text{infl}}$  being the inflection point velocity at  $\bar{x}_h$ , and  $\tilde{h}_s$  is the shear layer thickness, equal to the displacement thickness at the same location. For the dominant shedding frequency,  $\tilde{k}\tilde{h}_s = 0.78$ , lying well within the expected limits for Kelvin-Helmholtz instability,  $0 < \tilde{k}\tilde{h}_s < 1.2785$  [181] and in good agreement with other relevant studies, [e.g. 54, 160].

In addition to spectral measurements, LST analysis is instrumental for identifying the dynamic characteristics relevant to the growth of instabilities in the separated shear layer. For validation purposes, a comparison between spectral results and  $N$  factors computed from LST analysis is shown in figure 3.7b. It can be seen that the frequencies associated with maximum amplification factor are in excellent agreement with that of the dominant peak in the spectrum, both corresponding to  $St = 0.038$  (136Hz). The results of linear stability calculations performed on the time-averaged streamwise velocity field (figure 3.4a) are presented in figure 3.8a. It is evident that the growth rate of the most unstable frequency wave increases from  $St = 0.033$  (117Hz) in the vicinity of separation to a maximum  $St = 0.043$  (155Hz) near the mean maximum height ( $x = 42.3$ ). The corresponding amplification factor at this streamwise location is  $N = 7.2$ , comparable to the direct numerical simulations of Marxen *et al.* [107]. Moreover, LST calculations yield a convective speed of disturbances in the unforced LSB of approximately  $0.45\tilde{U}_0$ . This is in good agreement with observations on the propagation of coherent vortex shedding structures (figure 3.5).

Monkewitz & Huerre [119] suggested a scaling scheme for determining the occurrence of Kelvin-Helmholtz instability in free shear layers. Shear layers are characterized by an external and an internal velocity,  $U_e$  and  $U_i$ , respectively. Their difference,  $\Delta U = U_e - U_i$ , is used for calculating the vorticity thickness,  $\delta_w = \Delta U / (\partial \bar{u} / \partial y)_{\text{max}}$ . By including the dimensional frequency,  $\tilde{f}$ , and the average of the bounding velocities,  $\bar{U} = (U_e + U_i)/2$ , a dimensionless frequency is expressed as  $\omega^* = 0.25\delta_w(2\pi\tilde{f})/\bar{U}$ .

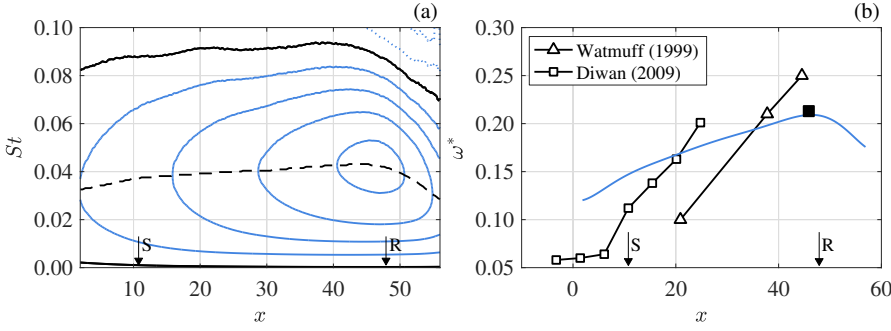


FIGURE 3.8: Unforced LSB stability diagram. (a) Non-dimensional growth rate,  $-\alpha_i = -\tilde{\alpha}_i \tilde{\delta}^*$  in steps of 0.1. *Solid lines*:  $-\alpha_i \geq 0$ , *dotted lines*:  $-\alpha_i < 0$ , *dashed line*: maximum  $-\alpha_i(x)$ . (b) Dimensionless frequency  $\omega^* = 0.25\delta_w(2\pi\tilde{f})/\tilde{U}$ . *Solid line*:  $\omega^*$  estimated on the most unstable LST frequency.  $\blacksquare$ :  $\omega^*$  with  $\tilde{f}$  derived from experimental velocity spectra at the maximum  $\delta^*$ . For comparing datasets, their  $x$  axis is scaled such that separation and reattachment locations match with the current experiment.

Monkewitz & Huerre [119] demonstrated that the range of frequencies for Kelvin-Helmholtz instability lies in the interval  $0.21 < \omega^* < 0.222$ . For the case of laminar separation bubbles, the internal velocity may be assumed negligible ( $U_i \approx 0$ ) while the external velocity is equal to the local freestream ( $U_i \approx U_\infty$ ). Since the distance of the bubble shear layer from the wall varies with respect to streamwise position, the aforementioned scaling is not valid unless the shear layer is at sufficient distance from the wall. Consequently, correspondence with the expected range ( $\omega^* \approx 0.21$ ) is mainly achieved in the region of the mean maximum height [e.g. 128, 159, 173].

Figure 3.8b depicts a comparison between  $\omega^*$  from the present results and the reporting of Watmuff [173] and Diwan & Ramesh [35]. The solid line corresponding to  $\omega^*$  estimated based on the local most unstable frequency (dashed line in figure 3.8a). Its maximum ( $\omega^* = 0.213$ ), agrees well with the estimate based on the dominant frequency in velocity spectra at the maximum  $\delta^*$  ( $\omega^* = 0.209$ ). Similar to the aforementioned references,  $\omega^*$  exhibits linear increase downstream of the separation point, confirming the inviscid nature of disturbance amplification [173]. The differences between the slopes of the linear portions of the three data sets are attributed to the substantially different bubble height to length ratio between the respective experiments

### 3.5. THE FORCED LSB

THE SEPARATION BUBBLE is subjected to impulsive forcing with amplitudes ranging from  $C_\mu = 1.5 \times 10^{-6}$  to  $C_\mu = 1.6 \times 10^{-4}$ . The pulses are repeated at a frequency of  $\tilde{f}_p = 2\text{Hz}$ . Sample temporal and phase-averaged streamwise velocity signals at the mean maximum height of the unforced LSB are provided in figure 3.9. The beginning of each cycle is marked by introduction of a pulse and is identified as the vertical grid line. The results illustrate the dynamic nature of the cycle, confirming that the transient completely subsides before the introduction of the

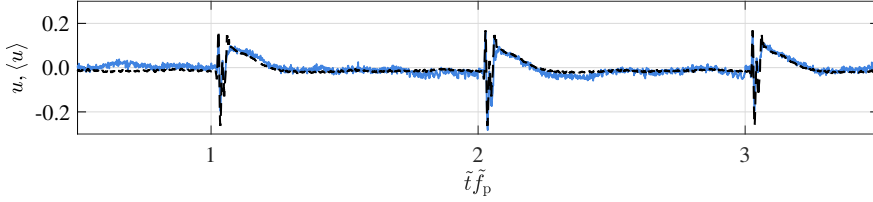


FIGURE 3.9: Sample of velocity signal at the location of maximum height,  $\bar{h}$ , for  $C_\mu = 1.6 \times 10^{-4}$ . The initiation of each forcing cycle is marked by the vertical grid lines. *Solid line*: raw velocity signal,  $u$ . *Dashed line*: phase-averaged velocity signal,  $\langle u \rangle$ .

next impulse. The strong cycle-to-cycle periodicity affirms the feasibility of phase-averaging for subsequent increase of statistical significance. Experimental limitations dictate that, for each acquisition frequency (250Hz, 500Hz and 2000Hz), the number of realisations available at each phase is 87, 43 and 10, respectively.

### 3.5.1. TEMPORAL RESPONSE TO IMPULSE

The pertinent features of the temporal response of the LSB to the impulsive forcing are captured by phase-averaged vorticity fields,  $\langle \omega \rangle = \langle \tilde{\omega} \rangle \delta_{s_0}^* / \tilde{U}_0$ , shown in figure 3.10. The forcing magnitude of the demonstrated sequence is  $C_\mu = 5.4 \times 10^{-5}$ , although the same general behaviour has been observed at all other forcing amplitudes. An overview of the topological changes of the separation bubble for all forcing amplitudes is achieved by tracing bounding properties of the LSB with respect to phase and is shown in figure 3.11. Specifically, the phase-averaged location of separation,  $\langle x_s \rangle$  and reattachment,  $\langle x_r \rangle$ , bubble length,  $\langle l \rangle = \langle x_r \rangle - \langle x_s \rangle$ , and maximum height,  $\langle h \rangle$  are shown in figure 3.11. For ease of comparison, these metrics are normalised by the corresponding parameters of the unforced LSB (thus are denoted with the hat symbol). At this point a note needs to be made considering the definition of the LSB boundaries. As seen in figure 3.10, for phases  $\phi < 0.08$ , the introduced vortical wave packet distorts the flow to a degree where a classical definition of LSB is no longer applicable. As such, the focus of the analysis is directed to phases greater than 0.08. In figure 3.11, the shaded area corresponds to phases at which the introduced disturbance advances within the field of view.

Shortly after the introduction of the pulse, a wave packet emerges, which develops into a set of co-rotating vortices that propagate downstream ( $0.036 < \phi < 0.052$ , figure 3.10). The convective nature of the developing disturbance confirms the aforementioned assumption that present LSB is globally stable based on the magnitude of maximum reverse flow of 2% [2, 48]. Once the developing wave packet convects past the streamwise location of the mean maximum height of the unforced case ( $\phi = 0.08$ ), the LSB undergoes rapid contraction with the separation and reattachment points shifting downstream and upstream, respectively, similar to the DNS observations of Rist & Maucher [140]. For forcing amplitudes exceeding  $C_\mu = 4.2 \times 10^{-6}$ , the LSB is completely eliminated ( $\phi = 0.096$ , figure 3.10). Complete elimination of the LSB is signified in figure 3.11 by discontinuities in the plots at phases close to  $\phi = 0.1$ .

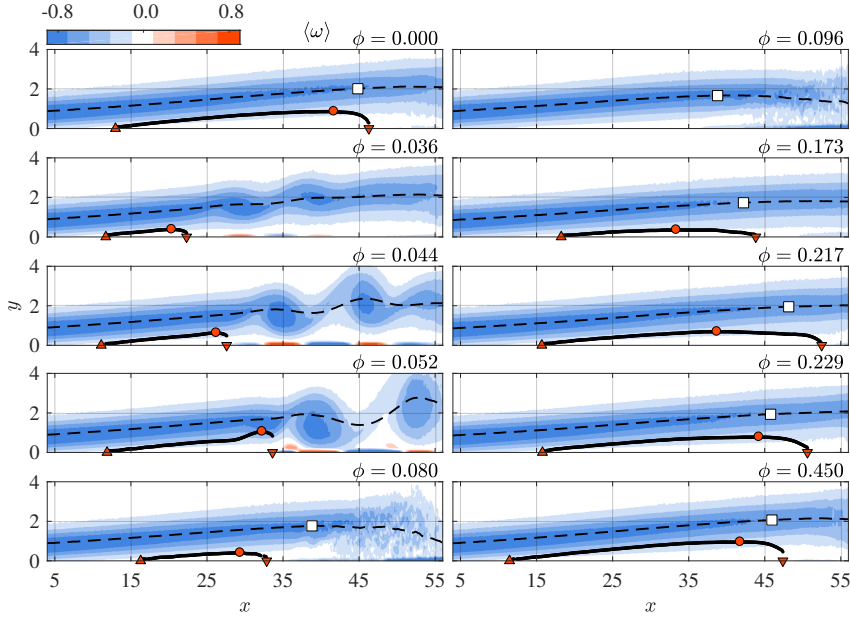


FIGURE 3.10: Phase-averaged vorticity within the forcing cycle for  $C_\mu = 5.4 \times 10^{-5}$ . *Solid line*: dividing streamline; *dashed line*: displacement thickness ( $\delta^*$ );  $\Delta$ : separation point;  $\nabla$ : reattachment point;  $\circ$ : maximum height;  $\square$ : location of maximum shape factor.

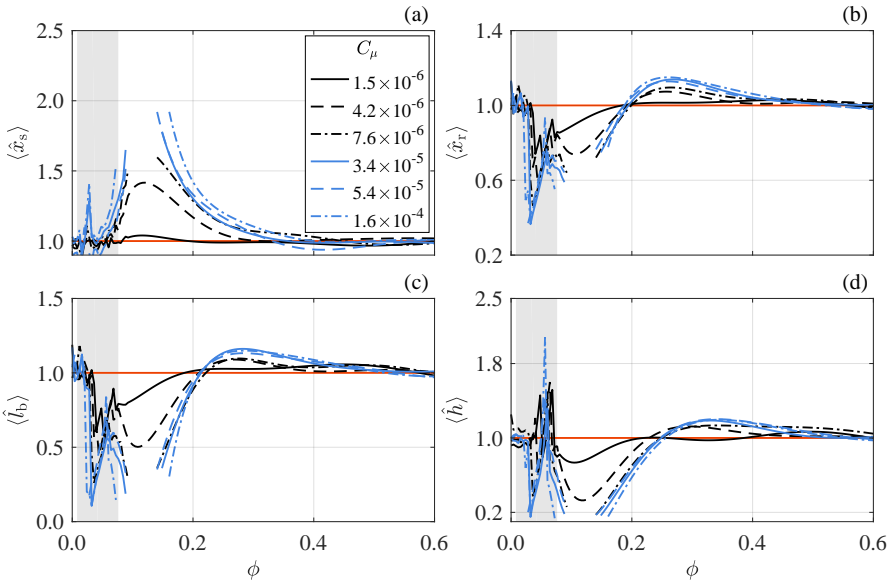


FIGURE 3.11: Evolution of phase-averaged (a) separation point; (b) reattachment point; (c) bubble length and; (d) maximum bubble height. All metrics are scaled with the respective unforced value. *Shaded region*: Interval during which the wave packet is within the field of view.

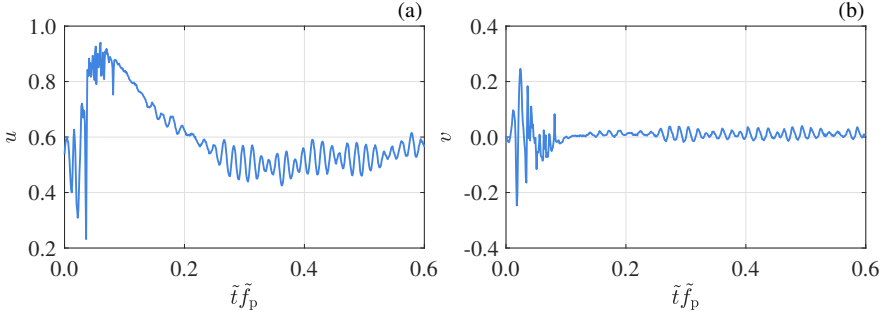


FIGURE 3.12: Velocity signals at  $x = 55$  and  $y = \bar{\delta}_0^*(55)$  for  $C_\mu = 5.4 \times 10^{-5}$ . (a) streamwise component,  $u$ . (b) wall-normal component,  $v$ .

Within the same range, the two lowest forcing amplitudes result in the reduction of LSB size, albeit not complete elimination. From this point, the LSB starts recovering, a process that is significantly slower than the contraction. Growth of the LSB is also occurring towards both upstream and downstream directions (figure 3.11).

During the recovery stage, the LSB elongates before contracting to its unperturbed state ( $\phi \approx 0.45$ , figure 3.10). The reattachment point shifts downstream, similar to the behaviour of the bursting process described by Gaster [47] and Marxen & Henningson [103]. This produces the overshoot in the reattachment location, bubble length and the maximum height seen in figures 3.11b, 3.11c, and 3.11d, respectively, within  $0.2 < \phi < 0.4$ . Bursting is accompanied by reduction of the vortex shedding strength. This is visualised in figure 3.12, which depicts instantaneous velocity traces probed at the aft part of the bubble. At the early stages of the bursting process, for a short time interval after the bubble elimination, no shedding traces are evident within the field of view ( $0.1 < \tilde{t}\tilde{f} < 0.15$ ). Shedding, however, quickly resumes as the bubble grows, albeit at a lower strength, until reattachment assumes its most downstream location ( $\phi \approx 0.25$ , figure 3.10). From this point, the bubble height increases further than its unforced value, an inertial effect that is a direct consequence of the vortex shedding strength reduction. More specifically, mass accumulation caused by the reverse flow is not balanced by sufficient mass entrainment in the aft portion through vortex shedding until breakdown has moved sufficiently upstream. After the latter occurs, the LSB finally recovers to its unperturbed state.

The dynamic cycle described here, including the bubble size reduction or elimination, is also observed in cases where laminar separation bubbles interact with controlled periodic wake disturbances [e.g. 159]. In addition, the separation bubble does not exhibit any features of long bubbles [103] throughout the forcing cycle, thus the elongation represents part of a dynamic process of a short bubble.

The LSB topology is dependent on the laminar to turbulent transition process as the latter governs momentum entrainment and leads to reattachment. It is therefore expected that variations in laminar to turbulent transition within the LSB shear layer are accompanied by evident changes in integral boundary layer length scales

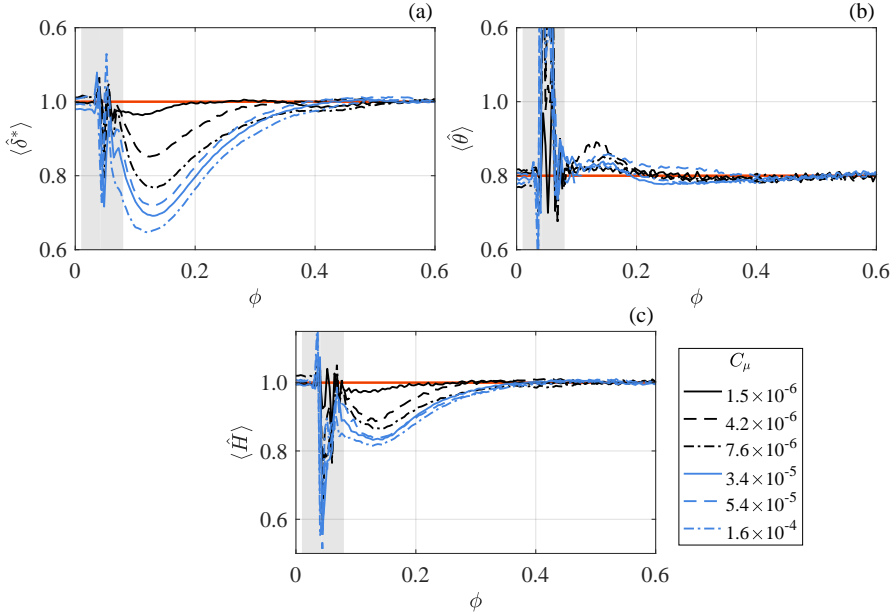


FIGURE 3.13: Evolution of phase-averaged boundary layer integral quantities scaled to the respective unforced value. Values are probed at the streamwise location of maximum height of the unforced LSB  $\bar{x}_{h_0}$  (a) Displacement thickness; (b) momentum thickness; (c) shape factor. *Shaded region*: Interval during which forced disturbance is within the field of view.

[62, 183]. The aforementioned quantities are estimated during the forcing cycle at the streamwise location of the unforced LSB mean maximum height and are shown in figure 3.13. It is evident that during bursting, increasing forcing amplitude results in decrease of displacement thickness ( $\delta^*$ ) and increase of momentum thickness ( $\theta$ ). Consequently, the shape factor ( $H = \delta^*/\theta$ ) decreases, signifying enhanced stabilisation of the boundary layer for increasing forcing amplitude, consistent with the documentations of Rist & Augustin [139] and Marxen & Rist [108].

Prior to the disturbance introduction ( $\phi = 0$ ), the location of maximum shape factor,  $H$ , is located in the upstream vicinity of the mean reattachment location (figures 3.13c and 3.10). This location corresponds well to the abrupt rise of wall-normal velocity fluctuations in the unforced bubble (figure 3.4), signifying the onset of the shear layer breakdown. Due to the low turbulence environment and the strongly inflectional profiles exhibited by the LSB, the breakdown and transition onset locations are in close proximity. As such, a first order estimation of the breakdown onset location can be derived based on the streamwise location where the shape factor is maximised. This is indicated by a square marker in figure 3.10. Shortly after the convection of the forced wave packet and the elimination of the LSB, the breakdown onset point swiftly shifts upstream by approximately  $12\tilde{\delta}_s^*$  ( $\phi = 0.08$  and  $0.096$ ). Here, the absence of reverse flow leads to temporary stabilisation, which, in turn, causes the breakdown onset point to shift downstream ( $\phi = 0.173$ ). This

downstream shift persists throughout the entire bursting process (figure 3.11). Given the observed behaviour, the phase at which the breakdown onset location is most downstream corresponds to the longest LSB ( $\phi \approx 0.25$ ), i.e. at the end of bursting (figure 3.11c). As gradual recovery ensues after maximum elongation, the breakdown onset point propagates upstream, reaching its unforced location at  $\phi \approx 0.5$ .

During the interval between the bubble elimination and the end of the bursting process, the LSB shedding strength is reduced (figure 3.12). This notion, in conjunction with the significant changes in the breakdown onset location implies that an impulsive disturbance significantly influences the stability characteristics of the LSB. Following the elimination of the reverse flow region, the temporary stabilisation leads to reduced growth rate of incoming disturbances, thus, transition to turbulence and the associated increase of wall-normal mixing are driven to occur farther downstream. Consequently, the separated shear layer fails to reattach as early as in the unforced scenario. It is important to stress here that the apparent stabilisation of the LSB is slightly different than the one observed by Gaster [47] and Marxen & Henningson [103] in their respective studies. While a combination of mean flow distortion and changing amplitude of incoming instabilities was at play in the aforementioned studies, the current investigation is performed with a non-changing incoming disturbance amplitude during the bubble bursting and recovery phase.

A final comment can be given on the characteristic timescales of the observed topological changes in the LSB. As indicated by  $\langle \hat{h} \rangle$  in figure 3.11d, increase of forcing amplitude results in faster elimination of the LSB as well as increase of the duration of reverse flow absence. Nonetheless, the phase at which the LSB recovers to its unperturbed state ( $\phi \approx 0.45$ ) seems to be independent of the forcing amplitude. This serves as an additional indication that while the rapid and significant changes imparted on the topology and shedding behaviour of the LSB are due to the initial effect of impulsive forcing, the recovery to the unperturbed state is driven by the global pressure gradient and the amplitude of the natural incoming disturbances, which are constant for all tested cases.

### 3.5.2. QUASI-STEADY SPATIAL STABILITY

According to the analysis carried out in section 3.3.2 (figure 3.8), LST predictions suggest that the most amplified instability mode in the unforced LSB manifests at a frequency of approximately  $St = 0.038$  (136Hz,  $\tilde{k}\tilde{h}_s = 0.78$ ). This is confirmed by the spectral content (figure 3.7) where the band of amplified frequencies ranges from  $St = 0.022$  (80Hz,  $\tilde{k}\tilde{h}_s = 0.62$ ) to  $St = 0.047$  (170Hz,  $\tilde{k}\tilde{h}_s = 0.96$ ). The results agree well with the findings of similar studies, e.g. Häggmark *et al.* [54],  $\tilde{k}\tilde{h}_s = 0.88$ , Yang & Voke [181],  $\tilde{k}\tilde{h}_s = 0.98$  and Simoni *et al.* [160],  $\tilde{k}\tilde{h}_s = 0.98$ . In addition, as demonstrated in section 3.5.1, the time interval from the disturbance introduction until full recovery of the LSB is approximately  $\delta\phi = 0.45$ , yielding an equivalent frequency of  $St = 1.2 \times 10^{-3}$  (4.4Hz). Due to this large separation of timescale between pertinent instability modes and global topology changes in the LSB, the forcing cycle may be treated as a quasi-steady process [14]. In this manner, statistical and stability properties at any given phase are considered independent of the rate of change of bubble characteristics.

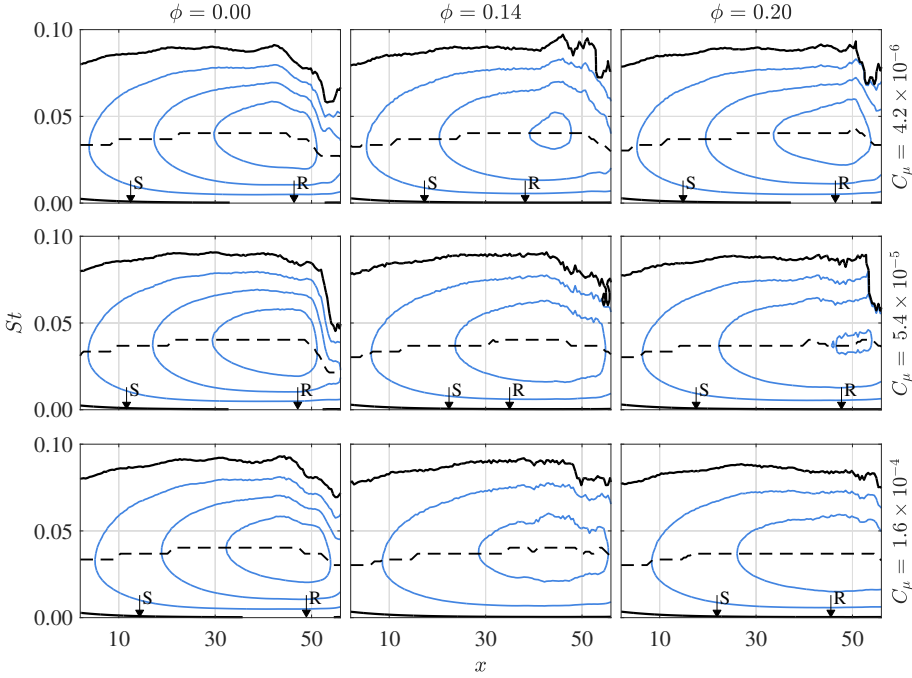


FIGURE 3.14: Stability diagrams for selected phases and forcing amplitudes. Iso-contours of non-dimensional growth rate,  $-\alpha_i = -\tilde{\alpha}_i \tilde{\delta}^*$ , in steps of 0.1. *Solid lines*:  $-\alpha_i \geq 0$ ; *dashed line*: frequency of the most unstable mode.

The assumption of quasi-steady behaviour allows performing LST analysis as formulated in section 3.3.2, using phase-averaged streamwise velocity fields. Contours of growth rates for three different forcing amplitudes and selected phases within the forcing cycle are shown in figure 3.14. For  $\phi = 0$ , the growth rate fields correspond to the unforced case (figure 3.4a). In the following column ( $\phi = 0.14$ ), the bubble attains its smallest size or is eliminated, depending on forcing amplitude. Evidently, the magnitude of the maximum growth rate decreases for increasing forcing amplitude, indicating increase of stability of the LSB, supporting observations made in section 3.5.1. Similar behaviour is observed for  $\phi = 0.20$ , during the recovery phase.

The trend of the maximum growth rate within the forcing cycle at the streamwise location of the unforced LSB mean maximum height,  $\bar{x}_{h_0}$ , and for different forcing amplitudes is shown in figure 3.15a. Here, with reference to figure 3.11, note that as the LSB recovers ( $\phi > 0.2$ ) growth rates increase. In addition, LST calculations indicate that the frequency of the most unstable mode at the same location (figure 3.15b) decreases with respect to its unforced LSB value during the bubble recovery phase ( $0.1 < \phi < 0.4$ ), with a minimum achieved at  $\phi \approx 0.25$ . This reduction, however, is relatively small ( $\approx 5\%$ ) compared to the respective reduction of growth rate ( $\approx 25\%$ ), agreeing well with observations of Marxen *et al.* [104].

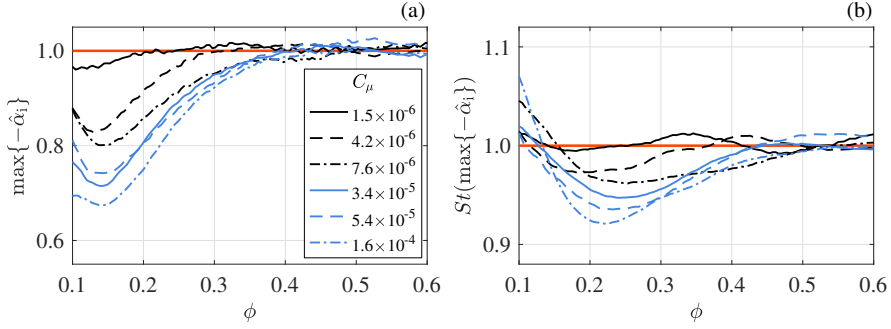


FIGURE 3.15: (a) Maximum growth rate and (b) most unstable frequency at  $\bar{x}_{h_0}$  for different forcing amplitudes as predicted by quasi-steady LST analysis. Quantities are normalised with the respective unforced values.

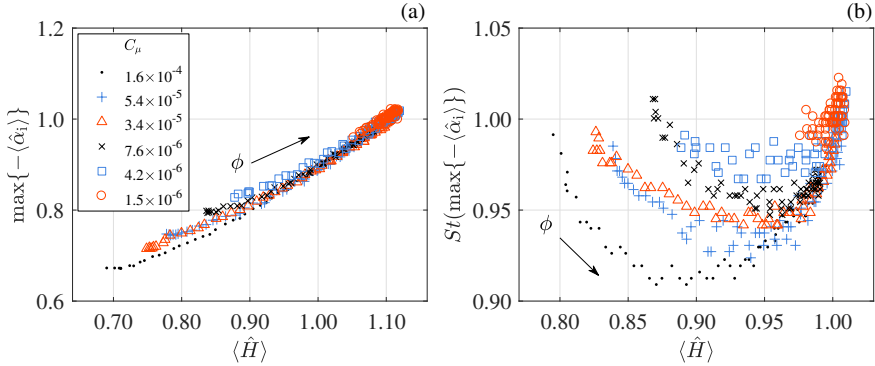


FIGURE 3.16: (a) Maximum growth rate and (b) most unstable frequency for different forcing amplitudes. Data are probed at  $\bar{x}_{h_0}$  and  $0.1 < \phi < 0.5$  as a function of the local shape factor. All quantities are normalised with the respective unforced values.

As evident by the previous discussion, the change in mean bubble size and topology has direct consequence on stability. Reduction of the bubble height and even complete elimination of the reverse flow region results in more stable flow in LST terms. Furthermore, the effect of impulsive forcing on the integral properties of the boundary layer, such as  $\delta^*$ ,  $\theta$  and  $H$ , appears to follow similar trend as the growth rate and frequency of most amplified mode (figure 3.13). The maximum growth rate as a function of the corresponding shape factor at  $\bar{x}_{h_0}$  are, therefore, shown in figure 3.16a for all phases during the recovery phase of the forcing cycle ( $0.1 < \phi < 0.5$ ) and all forcing amplitudes. For ease of comparison the values are scaled with the respective values pertaining to the unforced bubble.

It is apparent that all growth rates collapse on a monotonic, nearly-linear regression. This indicates strong correlation between stability of the LSB and integral characteristics of the boundary layer regardless of the forcing amplitude, as previously suggested in the works of LeBlanc *et al.* [92], van Ingen & Kotsonis [63] and Boutilier

& Yarusevych [13]. The implication of this notion for both flapping and bursting mechanisms is a consequence of altered stability characteristics due to the influence of incoming perturbations on the bubble topology. If the perturbations are of small amplitude and intermittent, as in the case of freestream disturbances, the LSB will react with mild shape factor and stability variations leading to the observation of the flapping phenomenon. In turn, introduction of a periodic disturbance at the most unstable frequency or impulsive forcing, of amplitude higher than environmental disturbances, may achieve reduction of flapping by pegging the stability characteristics, explaining the observations of Dovgal & Boiko [37]. In the extreme case of a high amplitude impulsive disturbance, the flow distorts to an extent that the LSB diminishes and by consequence stabilises considerably. As a result, the shear layer breakdown onset location is forced downstream (see figure 3.10), alleviating mixing benefits, and resulting in bubble bursting. This confirms the observations of Marxen & Henningson [103] regarding the bursting process based on simulations where the flow becomes more stable by decreasing the amplitude of numerical unsteady forcing.

Contrary to the growth rates, the frequency of the most unstable waves is not directly proportional to the shape factor but demonstrates a parabolic variation (figure 3.16b). In particular, the minimum value is achieved at  $\phi \approx 0.22$ . With reference to the trace of the bubble length and height shown in figures 3.11c and 3.11d, this coincides with the instant when these quantities temporarily assume their unforced value, followed by the elongation due to bursting. The extremum in the frequency variation with shape factor suggests a notable change in the boundary layer characteristics. Indeed, the inflection point in the displacement thickness can be observed at the same time instant ( $\phi \approx 0.22$ ) in figure 3.13a.

### 3.5.3. DISTURBANCE CHARACTERISTICS

The analysis performed in the preceding sections demonstrates the strong influence of the impulsive disturbance on the LSB dynamic topology and stability. It is, therefore, imperative to describe and quantify the disturbance evolution in order to close the interaction loop. Complementary to figure 3.10, contours of  $Q$ -criterion [61] are shown in figure 3.17 for  $0.026 < \phi < 0.046$ . A set of three co-rotating vortices, labelled  $V_p$ ,  $V_u$  and  $V_d$ , dominates the flow field, downstream of which there are traces of structures shed prior to the introduction of the impulse.  $V_p$  is the primary vortex produced due to the introduction of the pulse as it can be traced to the streamwise location of the actuator,  $x = 0$ , at  $\phi = 0$ .  $V_d$  is induced by  $V_p$  shortly after the impulse and becomes measurable when  $V_p$  has reached  $x \approx 15$ . A tertiary weaker vortex,  $V_u$ , emerges upstream of  $V_p$  closing the cascade. The streamwise distance between all three vortices is initially approximately  $9\delta_s^*$ , however, it gradually increases to  $12\delta_s^*$  between  $V_p$  and  $V_d$ , as  $V_d$  passes through the accelerated flow in the reattachment region. The process closely resembles the wave packet sequence observed by Watmuff [173]. For completing characterisation of this wave packet, analysis of its frequency, convective speed and growth rate is performed.

Due to the highly transient nature of events, assessment of the frequency characteristics of the disturbance cannot be performed via Fourier analysis. Instead, the wavelet transform is employed as described in section 2.2.3, on the phase-averaged

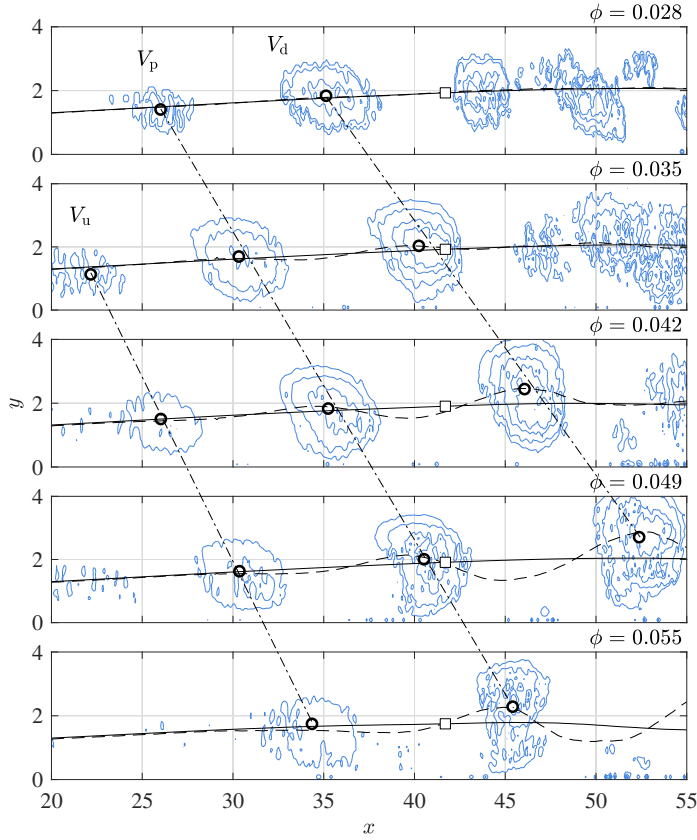


FIGURE 3.17:  $Q$ -criterion for  $C_\mu = 1.6 \times 10^{-4}$  at various phases. *Dashed lines*: displacement thickness. *Solid lines*: displacement thickness based on reconstruction with  $\Phi^{(1)}$  and  $\Phi^{(2)}$ . *Dash-dot lines*: connect the vortex centroids (indicated by circles) at different time instants. *Square marker*: location of probe used for extracting signal for wavelet analysis (figure 3.18).

vorticity signal. The disturbance is expected to affect the shape of the LSB as it convects, thus, the probe location where vorticity is extracted takes into account the deformation of the separated shear layer. Specifically, the probe's streamwise location is fixed to the location of mean maximum height of the unforced LSB, while the distance of the probe from the wall is set to the displacement thickness at the corresponding phase.

In order to reduce the uncertainty in the probe location due to the passing wave packet disturbance, displacement thickness is estimated on reduced order velocity fields, reconstructed by considering POD modes  $\Phi^{(1)}$  and  $\Phi^{(2)}$ . As demonstrated in section 3.4.2, these modes capture the overall motion of the bubble disregarding shedding as well as distortion of the shear layer due to the presence of the disturbance. A comparison between the displacement thickness calculated based on the full phase-averaged signal and the displacement thickness calculated on the reduced order

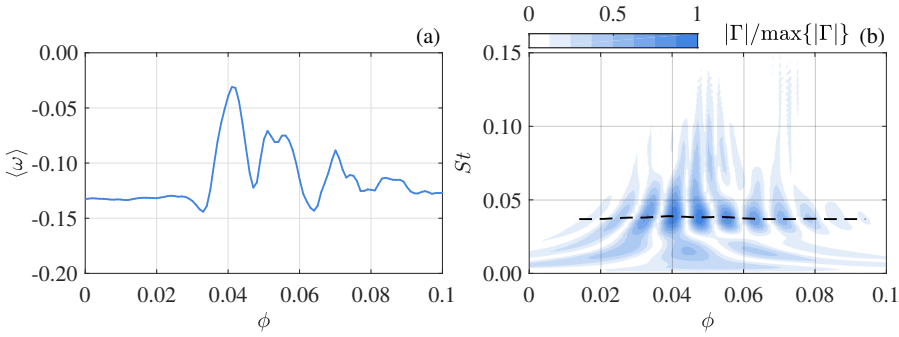


FIGURE 3.18: (a) Signal of phase-averaged vorticity at  $x = \bar{x}_h$  and  $y = \langle \delta_{ro}^* \rangle$  for  $C_\mu = 1.6 \times 10^{-4}$ . (b) Normalised wavelet coefficients. Dashed line: connects the maxima at each phase.

signal ( $\delta_{ro}^*$ ) is shown in figure 3.17. The location of the probe coinciding with the reduced order displacement thickness is indicated by the square marker. The extracted vorticity signal and the corresponding wavelet coefficients for forcing amplitude of  $C_\mu = 1.6 \times 10^{-4}$  are plotted in figure 3.18. Peaks in the wavelet coefficient field indicate that the dominant frequency assumed by the wave packet is approximately  $St = 0.037$  (134Hz), which agrees with the most amplified frequency of the unforced bubble, determined from velocity spectra and LST predictions at the same streamwise position (section 3.4.3). The introduced disturbance frequency remains approximately constant during all the phases for which it is detected.

Though it is possible to obtain an approximation of the disturbance convective speed by tracing the propagation of the vortex cores (figure 3.17), a more reliable approach is followed based on integrating the phase-averaged wall-normal velocity component along the  $y$ -direction. With this method, disturbance traces are detectable even at upstream locations where the structures are still too weak to be detected by vortex identification schemes. The result is shown on an  $x - \phi$  diagram in figure 3.19a, for the case corresponding to forcing amplitude of  $C_\mu = 1.6 \times 10^{-4}$ . Two distinct sets of convective ridges are identified. The first set is located in the interval  $0 < \phi < 0.08$ , spanning throughout the entire streamwise extent and pertaining to the passage of the three structures induced by the pulse ( $V_p$ ,  $V_d$  and  $V_u$ , figure 3.17). The second set of convective ridges ( $\phi > 0.2$  and  $x > 40$ ) is the signature of the coherent vortex shedding in the aft part of the LSB, re-established after the bursting process. Between these two regions in time ( $0.08 < \phi < 0.2$ ), elimination of the LSB takes place, followed by cessation of vortex shedding associated to the bursting process (see figure 3.12), therefore, no clear convective ridges are observed. The convective speed of the wave packet introduced by the impulsive forcing is directly related to the slope of the dominant convective ridge (marked by the dashed line in figure 3.19a). The convective speed is found to be largely independent of the forcing amplitude (figure 3.19b) with an average value of  $0.46\bar{U}_0$ , equal to estimations made on the unforced bubble. This is in good agreement with LST analysis predictions as well as the work of Rist & Maucher [140] and Pröbsting & Yarusevych [133].

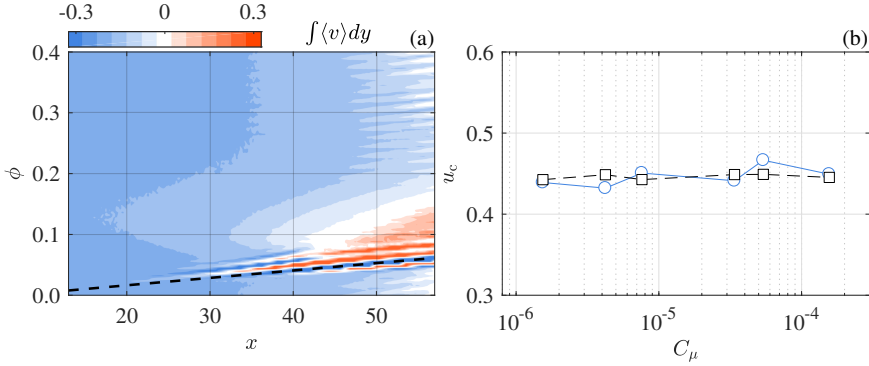


FIGURE 3.19: (a) Phase-streamwise location map of  $y$ -integral of wall-normal phase-averaged velocity ( $\int \langle v \rangle dy$ ) for  $C_\mu = 1.6 \times 10^{-4}$ . (b) Convective speed ( $u_c$ ) of forced disturbance for tested forcing amplitudes.  $\circ$ : Measurements and  $\square$ : corresponding LST predictions for the most unstable mode at  $St = 0.043$  (155Hz).

Figure 3.19a provides an additional confirmation that the wave packet is convectively, rather than globally unstable due to the lack of ridges with negative slope that would otherwise signify upstream propagation of disturbances in the vicinity of the wall. Additionally, it is noteworthy that although data extraction is performed on phase-averaged results, evident spatial and temporal coherence due to vortex shedding is observed in the aft portion of the bubble during recovery ( $\phi > 0.2$ ). At these phases, the artificial forcing wave packet has convected downstream and is no longer directly influencing the bubble dynamics. Consequently, the aforementioned spatio-temporal coherence indicates that bursting and the following recommencing onset of vortex shedding are associated with nearly constant time scales with respect to the impulse instant.

Given that incoming disturbances during this phase intervals are effectively random, it follows that the onset of vortex shedding in a LSB that has undergone bursting is deterministically synchronised with the bursting and recovery process. This effect is not evident in the sequence presented in figure 3.10. This can be attributed to the limited local resolution of PIV as well as insensitivity of the velocity curl to weak vortices. Nevertheless, the latter can be discerned in figure 3.19a due to the employed integration in the wall-normal direction.

Quantification of the growth of the introduced disturbance is based on the extraction of the phase-averaged wall-normal velocity fluctuating component,  $\langle v' \rangle = \langle v \rangle - \bar{v}$ , as it is not significantly affected by global shear layer fluctuation. Each of the three dominant vortical structures induced by the impulsive forcing (figure 3.17) features a region downstream its core where fluid is displaced towards the wall. The location where the unique local maximum magnitude of  $\langle v' \rangle$  is reached within such region is recorded for phases in the interval  $0.02 < \phi < 0.07$ , i.e. when the wave packet is within the FOV (figure 3.10). Figure 3.20a depicts the resulting values. The magnitude of  $\langle v' \rangle$  related to  $V_p$  increases as the vortex convects, reaching its peak at approximately the mean maximum height of the unforced LSB ( $x = 42$ ). A

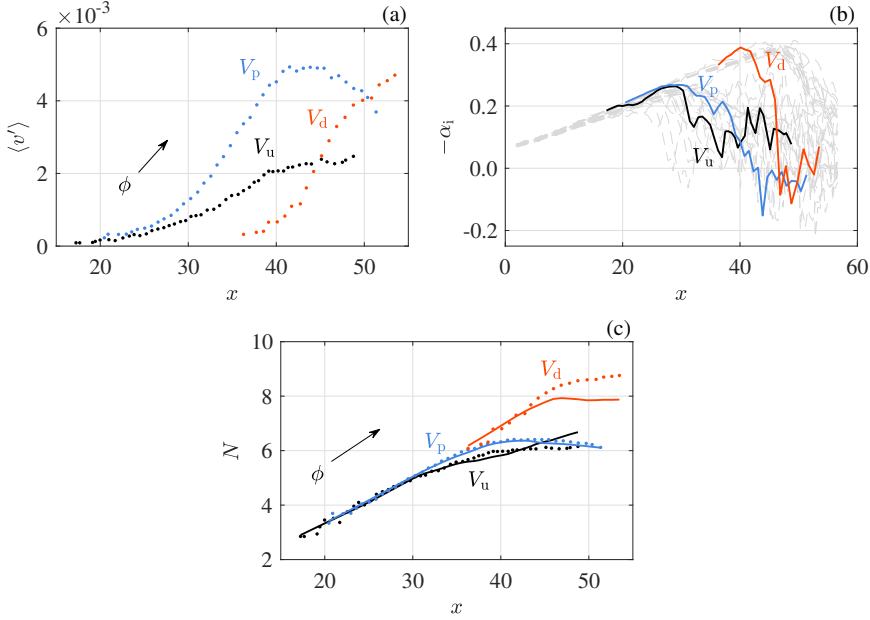


FIGURE 3.20: Quasi-steady LST analysis for the case of  $C_\mu = 1.6 \times 10^{-4}$  in the phase interval  $0.02 < \phi < 0.07$ . (a) *Points*: magnitude of wall-directed  $\langle v' \rangle$  due to forced wave packet. (b) *Dashed lines*: Non-dimensional growth rates ( $-\alpha_i = -\tilde{\alpha}_i \delta^*$ ) at the centre frequency determined by wavelet analysis. *Solid lines*: Composite  $\alpha_i$  based on the maximum  $\langle v' \rangle$  location at each phase. (c) *Points*:  $N$  factor calculated from  $\langle v' \rangle$ . *Solid lines*: composite  $N$  factor calculated from the composite  $\alpha_i$ .

similar process is observed farther downstream for the secondary vortex  $V_d$ , although the maximum point is not captured within the current field of view. In contrast, the weaker vortex  $V_u$  induces notably lower  $\langle v' \rangle$ .

Comparison of the experimentally measured growth of the three individuated vortices with quasi-steady LST is enabled by extracting LST growth rates at each phase for the frequency determined through wavelet analysis ( $St = 0.037$ , 134Hz), shown as dashed lines in figure 3.20b. It must be noted here, that as individual vortices convect through the LSB, they experience a changing base velocity profile due to the global reduction of bubble size (figure 3.10). As such, each vortex is traced at a given streamwise location for each phase.

A certain growth rate is predicted by LST for each pair of streamwise location and phase values. Consequently, a composite growth rate is obtained for each vortex by sliding through the phases and extracting the growth rate per streamwise location and phase where the measured  $\langle v' \rangle$  is locally maximised (i.e. at each phase and corresponding streamwise location, a point is selected from the respective dashed-line growth rate curve). The resulting composite growth rates correspond to the solid lines of figure 3.20b. A composite amplification factor,  $N_c$ , may, therefore, be estimated by integrating the composite growth rates (as per equation 3.4). Subsequently, amplification factors of the experimentally measured disturbances are derived from

the logarithmic part of the same equation by setting  $\tilde{A} = \langle \tilde{v}' \rangle$ . Defining  $\tilde{A}_0$  requires reformulating the left hand side of equation 3.4 as

$$\tilde{A}_0 = \frac{\tilde{A}}{e^{N_c}}, \quad (3.7)$$

and utilising the measured induced velocity and the aforementioned composite amplification factor at an arbitrary streamwise location ( $x = 30$  for  $V_{p,u}$  and  $x = 40$  for  $V_d$ ). The constraint for this location selection is that  $\langle v' \rangle$  be higher than the PIV measurement error ( $\varepsilon_v \approx 2\%$ ).

The two sets of growth factors are plotted in figure 3.20c, where point markers and solid lines correspond to measurements and quasi-steady LST, respectively. Agreement between the two methods is remarkable, even when the amplitude of the experimentally measured disturbance is higher than the conventionally accepted threshold of  $0.1\%U_0$  for LST [101, 136]. As discussed by Diwan & Ramesh [35], the success of LST estimations in LSBs is not fully understood. The good agreement between the two analyses shown here suggests that rather weak non-linear effects come into play for the investigated case, with little energy transferred between modes. This is traced to the impulsive nature of the forcing and the exciting of a single dominant mode, characterised by essentially constant frequency and convective speed within the bubble. The above is further enhanced by the strong two-dimensionality of the considered disturbance, pivoting on the inherent features of the plasma actuator [79]. Negligible non-linear interactions appear to take place in the case of the stronger vortex  $V_p$ , for which LST predictions collapse on experimental measurements for the whole streamwise extent. Contrary, for the cases of the induced  $V_d$  and  $V_u$  vortices, LST analysis diverts from measured  $N$  values at higher amplitudes, implying more substantial non-linear interactions.

It is important to note that, as the three identified vortices convect sequentially, they experience the base flow profiles at slightly different phases (figure 3.17). Nevertheless, it is evident that the amplification factor of the two advancing vortices ( $V_p$  and  $V_d$ ) increases with the same rate (i.e. slope) until approximately the mean maximum height of the unforced LSB (figure 3.20c). In contrast, the results for the trailing vortex ( $V_u$ ), which crosses the mean bubble last, indicate a notable change in growth rate slope, manifested as a ‘kink’ in the  $N$  factor curve, at  $x \approx 30$  (figure 3.20c). Following figure 3.17, vortex  $V_u$  is at this location at phase  $\phi \approx 0.05$ . Indeed, again with reference to figure 3.17, at that instant,  $V_d$  has reached the aft part of the separation bubble. This suggests that the stability characteristics of the separated shear layer remain largely invariant during the convection of the forced wave packet. It is only when the introduced disturbance first interacts with the reattachment region that stability characteristics of the bubble are affected. The above, further reconcile with the hypothesis of a closed-loop feedback between stability, breakdown onset location and amplification of incoming disturbances suggested by Marxen & Henningson [103].

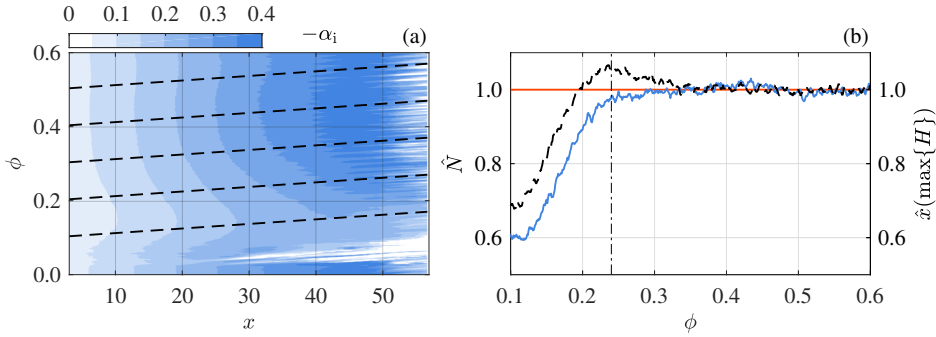


FIGURE 3.21: Quasi-steady LST analysis for the case of  $C_\mu = 1.6 \times 10^{-4}$ . (a) Growth rates ( $-\alpha_i = -\tilde{\alpha}_i \tilde{\delta}^*$ ) of mode with  $St = 0.043$  (155Hz), with respect to phase and streamwise location. *Dashed lines*: Loci of composite growth rates ( $-\alpha_{i_{\text{comp}}}$ ) for disturbances convecting at speed of  $0.46\tilde{U}_0$ . (b) *Dashed line*: Evolution of the measured streamwise location of maximum shape factor,  $\hat{x}(\max\{H\})$ ; *Solid line*: LST-predicted  $N$ -factor at the streamwise location of maximum shape factor calculated from  $\alpha_{i_{\text{comp}}}$ ; *Dash-dot line*: End of the bursting process ( $\phi \approx 0.24$ ).

### 3.5.4. ONSET OF SHEAR LAYER BREAKDOWN

Two essential features of the transitional dynamics and spatio-temporal evolution of the LSB emerge from the so-far presented analysis. These are the proportionality of the maximum growth rate to the shape factor irrespective of the incoming disturbance amplitude (section 3.5.2, figure 3.16) and the indication that stability characteristics are modified only when disturbances reach and interact with the reattachment region (section 3.5.3, figure 3.20). Both effects highlight the final stages of disturbance growth, turbulent breakdown and reattachment as the key element of the closed feedback loop, governing the flapping and bursting mechanisms.

In this section the temporal attributes of the transition process after convection of the forced disturbances are investigated. As discussed in section 3.5.1, for the unforced LSB the streamwise location where the shape factor is maximised may serve as a first order approximation of the onset of shear layer breakdown (figure 3.4). A critical amplification factor can be estimated at this streamwise position through LST, being equal to  $N_{\text{crit}} = 7.7$  (figure 3.8). In the forced LSB cases, at each phase, incoming disturbances perceive the LSB at a certain stability state. The latter is modified as a disturbance convects downstream due to the global topological changes induced by the bursting and subsequent recovery of the bubble. This behaviour is expressed by the growth rate of the most unstable mode calculated through quasi-steady LST analysis. This is visualised in the  $x - \phi$  plane by the contours of figure 3.21a. Evidently, any given disturbance convecting through the domain will experience a local growth rate corresponding to both the current streamwise location of the disturbance ( $x$ ) and phase ( $\phi$ ). Based on this observation and given the established nearly-constant convective speed of  $0.46\tilde{U}_0$  (figure 3.19), a composite growth rate,  $-\alpha_{i_{\text{comp}}}$ , can be constructed for a given disturbance entering the domain at phase  $\phi$ . The trajectories of such disturbances through the  $x - \phi$  plane (loci of  $-\alpha_{i_{\text{comp}}}$ ) are visualised by exemplary dashed lines in figure 3.21a, the slope of which

is equal to the convective speed. Composite growth rate curves are extracted only for disturbances entering after the propagation of the wave packet ( $\phi > 0.08$ ).

A comparison is now performed between LST predictions for breakdown onset and the experimental measurements. Direct estimations of the streamwise location where the shape factor is maximised (i.e. onset of breakdown) may be done from the phase-averaged velocity data (figure 3.10) and are marked by a dashed line in figure 3.21b. Additionally, integration of the composite growth rates (figure 3.21a) provides composite  $N$  factor curves,  $N_{\text{comp}}(x, \phi)$ , (as per equation 3.4). Subsequently, the value of  $N_{\text{comp}}$  is extracted for each phase at the  $x$ -location of maximum  $H$ . The result is traced by the solid line in figure 3.21 and is complementary to the observations analysed in section 3.5.1 and figure 3.10. It is evident that the convection of the initial forced wave packet over the aft portion of the bubble ( $\phi \approx 0.1$ ) is followed by a significant decrease in the amplification factor with respect to its unforced LSB value ( $\sim 0.55N_{\text{crit}}$ ). The flow is, therefore, becoming more stable, in line with the results of the analysis carried out in section 3.5.2.

### 3.6. CONCLUDING REMARKS

**A**N EXPERIMENTAL investigation of the spatial and temporal response of a laminar separation bubble to impulsive forcing is carried out by means of time-resolved PIV and linear stability theory. The LSB develops on a flat plate, driven by an imposed adverse pressure gradient at a Reynolds number based on the separation point displacement thickness of  $Re_{\delta_s^*} = 1305$ . The aim is providing insight into both flapping and bursting mechanisms of a short LSB by deterministically forcing the dynamics of the bubble. The selection of impulsive forcing allows excitation of natural modes through selective amplification [47] as well as further development of the flow in natural disturbance conditions. Introduction of disturbances is spanwise and two-dimensional, achieved by means of an AC-DBD plasma actuator, located just upstream of the mean separation point of the unforced LSB. The forcing amplitude spans over two orders of magnitude when expressed in terms of momentum coefficient and is varied by adjusting the DBD voltage. The forcing of the bubble with well-separated impulsive pulses facilitates phase-averaged analysis.

Following its introduction, the impulsive disturbance undergoes convective amplification as it propagates along the separated shear layer, evolving into a wave packet, similar to the results of Watmuff [173]. Once the latter has convected past the reattachment point, the LSB rapidly shrinks from both upstream and downstream sides. If the forcing amplitude is sufficiently high, the separation bubble is completely eliminated. This rapid process is followed by a gradual recovery in the bubble length similar to the bubble bursting process. Recovery to the unperturbed state is shown to be achieved at the same phase regardless of the forcing amplitude, further reconciling with the principle of impulsive forcing.

The timescale difference between pertinent instability modes derived from LST analysis and measured global topology changes of the LSB during the forcing cycle allows for treating the latter as a quasi-steady process [14]. Pivoting on this observation, LST calculations are performed on phase-averaged velocity fields. After the elimination of the LSB, the amplification rate and the frequency of the predicted

most unstable mode are found to decrease with increasing forcing amplitude. The same trend is followed by boundary layer integral quantities and, therefore, when the maximum growth rate is compared to the shape factor, the two quantities collapse on a monotonic linear regression for all forcing amplitudes. The aforementioned correlation confirms the conjecture that both flapping and bursting mechanisms are driven by altered stability characteristics due to the influence of incoming disturbances of different amplitude. Contrary to the growth rate, the frequency of the most unstable wave is not monotonic with respect to the shape factor but rather exhibits a parabolic relation.

Analysis of the wave packet produced by the impulse is performed for estimating frequency, convective speed and growth rate. The transient nature of the disturbance dictates the use of wavelet analysis for estimating the frequency of the wave packet. As expected, the frequency assumed is equal to the LSB shedding frequency, both from the comparison with velocity spectra and LST analysis of the unforced bubble. The convective speed is determined to be constant regardless of the forcing amplitude ( $0.46\tilde{U}_0$ ). Regarding the wave packet amplification, a remarkable agreement between measurements and LST is observed. The estimated growth of the vortices comprising the wave packet is shown to change once they start interacting with the breakdown region. This implies that stability changes ensue only when disturbances gain significant amplitudes and affect the flow in the aft portion of the separation bubble.

Variation of stability due to interactions of disturbances with the shear layer breakdown process stresses the necessity of investigating temporal attributes of the latter. The convection of the wave packet is followed by a significant reduction of the amplification factor, indicating flow stabilisation. At the same time, the breakdown onset location where the shape factor is maximised shifts upstream.

In conclusion, experimental evidence has been provided for coupling incoming disturbances with the LSB shear layer breakdown location and, consequently, with changes in stability characteristics towards flow stabilisation. This feedback loop serves as a ground for both flapping and bursting mechanisms and is paramount for active flow control realisation.



# 4

## SPANWISE DEFORMATION IN LAMINAR SEPARATION BUBBLES

*This chapter presents an experimental study carried out to investigate three dimensional features in the aft part of a flat plate laminar separation bubble. For promoting two-dimensional growth, the boundary layer is impulsively forced by means of a DBD plasma actuator. Time-resolved measurements reveal a staggered distribution of spanwise vortices in the rollup region. The observed topology is linked to a pair of oblique waves with opposite angles.*

---

MICHELIS, T., KOTSONIS. M. & YARUSEVYCH, S. 2017 On the origin of spanwise vortex deformations in laminar separation bubbles. *Journal of Fluid Mechanics* [**Under revision**].

MICHELIS, T. & KOTSONIS. M. 2016 Three dimensional breakdown of an impulsively forced laminar separation bubble. *APS Division of Fluid Dynamics Meeting Abstracts*.

## 4.1. BACKGROUND

VORTEX rollup in laminar separation bubbles at relatively low levels of free stream disturbances is generally regarded to be strongly two-dimensional [e.g. 73, 83, 123]. However, as Rist & Augustin [139] and Marxen *et al.* [106] have demonstrated through direct numerical simulations, introduction of oblique disturbances at moderate angles causes spanwise staggering of the rollup process. In the time-averaged sense, this results in a peak-valley distribution of the LSB boundaries. In addition, measurements performed by Burgmann *et al.* [18, 19], Burgmann & Schröder [20] and Wolf *et al.* [179] on a laminar separation bubble developing on an airfoil, demonstrate the occurrence of a group of c-shaped vortices downstream of the reattachment region. These vortices are found to have a staggered arrangement that persists in the wake of the airfoil, however, the mechanism responsible for the formation of these patterns remains unexplained.

Apart from instabilities active within the bubble itself, growth of disturbances in the laminar boundary layer upstream of the bubble must be considered since they may serve as an initial condition for the instabilities within an LSB [35]. Linear stability analysis carried out by Mack [101] on a flat plate boundary layer at Reynolds numbers based on streamwise distance from the leading edge below 1800, indicates that oblique growth may be more unstable than normal Tollmien-Schlichting (TS) waves for certain wavenumber vector angles. Indeed, the interaction between normal and oblique modes is responsible for the three-dimensional flow evolution in K-type [76], H-type [56] and oblique [72] transition.

A model of such an interaction has been proposed by Craik [32] and extended by Zelman & Maslennikova [187]. It considers the formation of a symmetric resonant triad between a two-dimensional TS wave and two oblique TS waves propagating at equal but opposite angles with respect to the flow. Notably, the streamwise wavenumber of the oblique pair is half of the TS streamwise wavenumber, thus, the interaction is often referred to as subharmonic. A resonance condition occurs when phase velocities of the aforementioned waves match. The emergence of subharmonic resonant waves has been demonstrated by several experimental studies [e.g. 29, 68] which consider attached flows. Nonetheless, they provide valuable insight for the present investigation.

In the majority of studies focusing on active instabilities in LSBs, the incoming boundary layer is forced upstream of the separation point. Forcing is often applied in the form of periodic perturbations. These are introduced in a two-dimensional fashion through wall oscillators [e.g. 2, 107], acoustic excitation [e.g. 65, 184] and plasma actuators [e.g. 114, 182]. The aforementioned type of forcing is continuous at a frequency equal to the fundamental frequency of the unstable boundary layer or LSB shedding.

An alternative forcing scheme, first suggested by Gaster & Grant [49], employs an impulsive disturbance that excites all instability modes, thus, generating a wave packet through selective amplification. Such a disturbance is experimentally introduced locally, e.g. through a pressure tap [35, 173]. The shortcoming of local introduction is strong non-parallel effects during the wave packet formation, thus, raising uncertainties regarding subsequent instability growth and its effect on the

separation bubble. Indeed, non-linear evolution in the form of subharmonic resonance has been observed experimentally in locally introduced wave packets by Cohen *et al.* [25]. Medeiros & Gaster [110], in turn, demonstrated the dependence of the non-linear evolution on the phase of the ripples within the wave packet. They concluded that subharmonic resonance alone is inadequate to fully justify the observed non-linearity, suggesting the presence of a yet unidentified mechanism of oblique mode production.

The present study is carried out towards an investigation of the three-dimensional deformation of coherent structures in the LSB and assessment of a possible link of the observed phenomena with the stability characteristics of the incoming boundary layer. An LSB is promoted on a flat plate subjected to an adverse pressure gradient, which has been shown to capture the fundamental characteristics of LSBs observed on aerofoil sections [47, 49]. To excite the primary instability mode, the flow is impulsively forced. In line with chapter 3, forcing is applied in a two-dimensional fashion by means of a spanwise-uniform dielectric barrier discharge (DBD) plasma actuator [28, 79], located upstream of the separation point, thus circumventing the shortcomings of localised point forcing discussed earlier. In addition, an essential feature of impulsive forcing is that, for fixed freestream velocity and turbulent intensity, the bubble experiences elevated disturbance levels only during the forcing impulse, otherwise being subjected to natural level of disturbances. Consequently, in contrast to continuous forcing, the flow evolution following the wave packet convection occurs without further conditioning the incoming disturbances.

The spatio-temporal flow development is characterised via time-resolved particle image velocimetry (PIV). Two-component planar PIV is used to capture the streamwise characteristics of the LSB, while tomographic PIV is employed for investigating the full three-dimensional velocity field in the roll-up region of the LSB. Upstream of the PIV field of view, the flow is assessed by means of numerical solution of the boundary layer equations, based on the measured pressure distribution. The combined numerical solution and experimentally measured mean flow forms the base for linear stability theory (LST) analysis. The performed analysis explores the link between the boundary layer stability characteristics and the ensuing development of coherent structures in the separated shear layer, and provides a handle for future control strategies.

## 4.2. DESCRIPTION OF EXPERIMENTS

THROUGHOUT this chapter, the notation conventions introduced in section 3.3.1 are followed. In addition, the notation  $(h, k)$  is used to denote instability modes, where  $h$  and  $k$  are integer multiples of the fundamental frequency ( $\tilde{f}_0$ ) and spanwise wavenumber ( $\beta_{r_0}$ ), respectively (see section 4.3.2). In addition, time is normalised by the fundamental shedding frequency, yielding  $\tau = \tilde{t}\tilde{f}_0$ . The time-averaged laminar separation bubble on the  $x - y$  plane coincides with the one presented in chapter 3.

### 4.2.1. FLOW AND MODEL CONFIGURATION

The same model and flow conditions discussed in section 3.2.1 are utilised (figure 4.1). The origin is defined with  $\tilde{x} = 0$  corresponding to the plasma actuator discharge

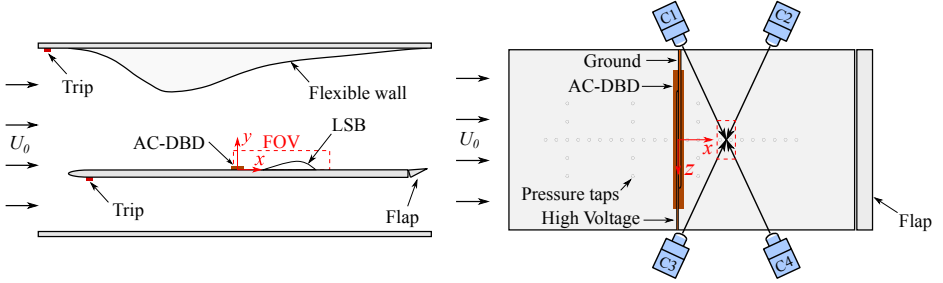


FIGURE 4.1: Schematic of the experimental setup. It is identical to the one shown in figure 3.1 with the exception of the four cameras used for tomographic PIV measurements.

gap, 420mm from the flat plate leading edge. In turn,  $\tilde{y} = 0$  lies on the flat plate top surface and  $\tilde{z} = 0$  at its midspan. For a free stream velocity of  $\tilde{U}_0 = 6.4\text{m/s}$  and turbulence intensity below 0.2%, the prescribed pressure gradient results in the formation of a laminar separation bubble between  $\tilde{x} = 30\text{mm}$  and  $\tilde{x} = 150\text{mm}$  (figure 3.2). Impulsive forcing is applied in the form of repeated bursts (figure 3.3) whose modulation duty cycle is adjusted according to the PIV acquisition frequency for maintaining a pulse width of 1ms. For this study, the actuator is operated at 5kV peak to peak voltage amplitude, corresponding to a momentum coefficient of  $C_\mu = 1.6 \times 10^{-4}$  (see section 2.1.3).

#### 4.2.2. DATA ACQUISITION

The flow field is investigated with two different time-resolved PIV configurations, planar and tomographic (see section 2.1.2). Planar PIV is used for determining the overall bubble features and dynamics on the  $x - y$  plane. In contrast, to investigate three-dimensional flow characteristics, tomographic PIV focuses on the reattachment region of the bubble. For both configurations, illumination is provided by a *Quantronix Darwin Duo* laser system which delivers green light (532nm) with 45mJ energy per pulse at 1kHz operating frequency. The illuminated region is captured by *Photron SA1.1* cameras equipped with a  $1024 \times 1024$  pixels sensor. Seeding particles are provided by a *SAFEX* smoke generator, that produces  $1\mu\text{m}$  diameter droplets of water-glycol mixture. Image recording and vector field processing are performed with *LaVision DaVis 8.3*.

Details of the planar PIV configuration are found in section 3.2.3. For the tomographic configuration, four cameras are used, each equipped with a 105mm *Nikon* macro objective set at an aperture of  $f/11$ . The cameras are placed in a rectangular arrangement above the flat plate, at an inclination of approximately  $20^\circ$  with respect to the wall-normal axis. In order to adjust the focal plane alignment on the camera sensor, the objectives are mounted on the cameras via Scheimpflug adapters. The volume of interest is illuminated using the multi-pass light amplification technique [50]. The laser beam is collimated with a set of spherical lenses and is subsequently reflected multiple times across the volume by means of two opposing mirrors. Light attenuation effects at the volume boundaries are alleviated with

knife edges. Volume calibration is performed with the self-calibration technique [177], for which residual disparity of less than 0.1 pixels is achieved. Image pairs ( $\Delta \tilde{t} = 140 \mu\text{s}$ ) are recorded at acquisition frequencies of  $\tilde{f}_a = 125\text{Hz}$  and  $2000\text{Hz}$ . The acquisition time over 6236 cropped image pairs is, therefore, 49.9s and 3.1s for each acquisition frequency respectively. The volume reconstruction from the acquired images is obtained by executing the Simultaneous Implementation of Multiplicative Algebraic Reconstruction Techniques (SMART) operation [4]. Particle displacement calculation in the interrogation volume is performed in multiple window steps, from an initial of  $72 \times 72 \times 20$  voxels to a final of  $48 \times 48 \times 11$  voxels, with 75% overlap. This results in a vector volume of  $36 \times 68 \times 31$  vectors ( $49.9 \times 95.6 \times 7.1\text{mm}^3$ ) along the  $x$ ,  $z$  and  $y$  directions, respectively. The corresponding vector pitch in the three directions is 1.42mm, 1.42mm and 0.24mm.

Errors in the estimated velocity fields are highest at the shear layer and reattachment regions. Estimation of the instantaneous uncertainty is based on the correlation statistics method described by Wieneke [178]. According to the latter, the velocity error is derived by assessing the contribution of each individual pixel to the correlation peak shape. In addition, uncertainty on average fields is determined through the linear error propagation technique [152]. Therefore, for the complete datasets, the maximum uncertainty on the planar configuration average field is  $\varepsilon_u \approx 0.2\%$  and  $\varepsilon_v \approx 0.7\%$ . Uncertainty for the tomographic configuration is higher, with values of  $\varepsilon_u \approx 1\%$ ,  $\varepsilon_v \approx 5\%$  and  $\varepsilon_w \approx 5\%$ .

An analogue to digital module is used to monitor the actuator voltage, the laser pulse and camera shutter signals. The moment of actuation is selected as reference time  $\tilde{t}_0 = 0\text{s}$ , thus, the rest of the signals are used for determining the time of the first measurement with an accuracy of  $1 \mu\text{s}$ .

## 4.3. BASELINE LSB

### 4.3.1. STEADY STATE FEATURES

In this section, the features of the naturally developing, unforced bubble are investigated. Time-averaged velocity fields from planar and tomographic PIV configurations are shown in figure 4.2. A closed recirculation region forms in the time-averaged sense as the boundary layer separates and reattaches. The mean dividing streamline is estimated on the planar data and outlines the separation bubble (figure 4.2a). Based on this streamline, the mean separation and reattachment points are estimated at  $\bar{x}_s = 6.3$  and  $\bar{x}_r = 47.5$  respectively, therefore, the length of the LSB is  $\bar{l}_b = 41.2$ . The bubble height is defined by the maximum wall-normal distance of the dividing streamline from the wall. This is evaluated to be  $\bar{h} = 0.73$ , occurring at  $\bar{x}_h = 41.7$ . The maximum amplitude of the reverse flow encountered within the LSB is of the order of 2% of the local freestream velocity. Hence, as suggested by previous studies [2, 48, 140], convective instabilities dominate in the separated shear layer.

The volume captured by the tomographic configuration with respect to the separation bubble is indicated by a grey rectangle in figure 4.2a. Due to experimental limitations, no tomographic data have been acquired below  $y = 0.39$ . Figure 4.2b depicts a three-dimensional outline of the separation bubble as well as several slices

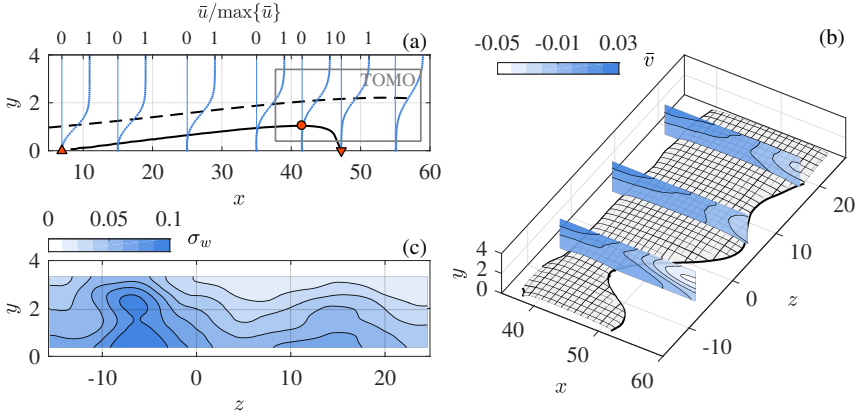


FIGURE 4.2: (a) Planar PIV time-averaged streamwise velocity profiles. *Solid line*: dividing streamline ( $\psi = 0$ ). *Dashed line*: displacement thickness.  $\Delta$ : separation point,  $\nabla$ : reattachment point,  $\circ$ : maximum height. The box indicates the tomographic PIV measurement volume projection. (b) Tomographic PIV time-averaged velocity field. The iso-surface marks the dividing streamline. Slices depict wall-normal velocity. (c) Fluctuation of spanwise velocity component,  $\sigma_w$ , at  $x = 50$ .

of wall-normal velocity. The results show minimal spanwise variation in the dividing streamline within the fore portion of the bubble, confirming the two-dimensional nature of the time-averaged incoming flow. In contrast, the time-averaged topology in the reattachment region shows distinct spanwise non-uniformity manifested by spatially periodic peaks and valleys. A similar trend persists in the fluctuation of the spanwise velocity component (figure 4.2c).

This topology has been observed in some of the previous numerical and experimental studies. For example, Rist & Augustin [139] induced such a peak-valley distribution in their DNS by imposing oblique disturbances in the boundary layer upstream a flat plate separation bubble. In their experiments, Kurelek *et al.* [83] note significant spanwise variation in coherent structures within a separation bubble developing on a symmetric aerofoil. For the current experiment, the characteristic wavelength of the spanwise variation seen in the time-averaged results (figure 4.2) is approximately  $\lambda_r = 18.6$ .

Figure 4.3 compares average and standard deviation of velocity obtained from planar and tomographic PIV at several streamwise locations within the overlap region (figure 4.2a). Overall, the agreement is good and discrepancies are associated with higher uncertainty of the tomographic configuration in the wall-normal direction, in the shear region, and in the aft portion of the bubble where velocity fluctuations are elevated. Fluctuations of the velocity field, expressed through standard deviation ( $\sigma$ ), are present due to shear layer flapping and vortex shedding mechanisms. Flapping is mostly prominent in the  $\sigma_u$  component, as a minor displacement of the shear layer results in strong changes in streamwise velocity at a fixed point. In the downstream part of the field of view where vortex shedding and turbulent breakdown manifest, both  $\sigma_u$  and  $\sigma_v$  attain elevated values.

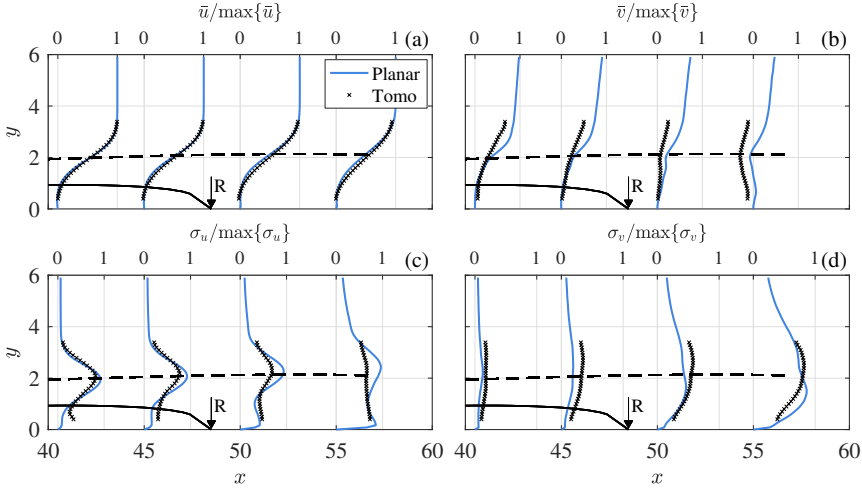


FIGURE 4.3: Comparison between time-averaged planar and tomographic PIV measurements at several  $x$ -stations. *Dashed line*: displacement thickness calculated on the planar data. (a) Streamwise velocity, (b) wall-normal velocity, (c) streamwise velocity standard deviation, (d) wall-normal velocity standard deviation.

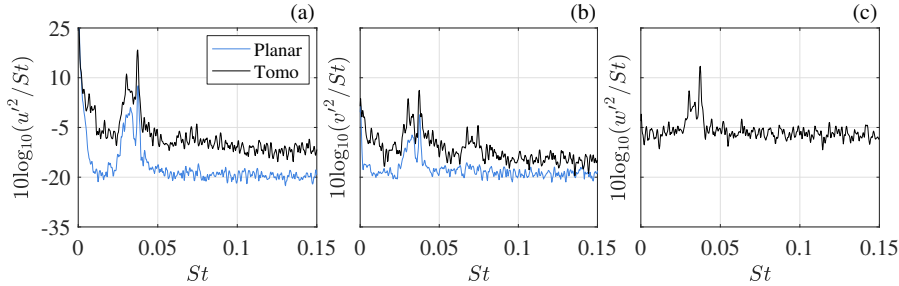


FIGURE 4.4: Power spectral density of the unforced LSB from both configurations estimated at  $x = \bar{x}_h$ ,  $y = \delta^*(\bar{x}_h)$  and  $z = 0$ . (a) Streamwise component fluctuation,  $u'$ , (b) wall-normal component fluctuation,  $v'$  and (c) spanwise component fluctuation,  $w'$ .

### 4.3.2. SPATIO-TEMPORAL CHARACTERISTICS

The steady state features described earlier are directly related to the dynamic behaviour of the laminar separation bubble. First, the spectral content of velocity fluctuations is examined in figure 4.4. The spectra of the fluctuating velocity components  $u'$ ,  $v'$ , and  $w'$  are computed with the Welch method [175] at a frequency resolution of  $St = 2.7 \times 10^{-4}$  (0.98Hz). The required temporal signals are extracted at the mean maximum height streamwise location and the displacement thickness wall-normal distance. A dominant broadband peak is observed in the spectra of all velocity components, located between  $St = 0.022$  (80Hz) and  $St = 0.047$  (170Hz). The most prominent frequency corresponds to  $St_0 = 0.038$  ( $\tilde{f}_0 = 136\text{Hz}$ ) which is confirmed to relate to the frequency of the most unstable mode (section 4.4.2).

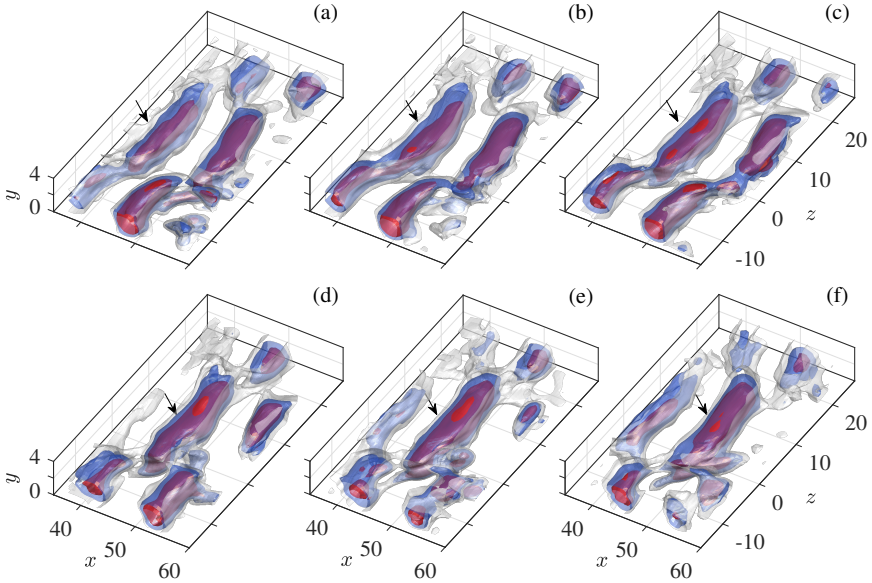


FIGURE 4.5: Unforced bubble instantaneous  $Q$ -criterion series, separated by  $\Delta\tau = 0.14$ . Grey, blue and red iso-surfaces correspond to  $Q = 0, 0.002$  and  $0.006$ , respectively. Arrows mark the same vortex convecting through the snapshots.

Hence, it is referred to as the fundamental frequency ( $St_0$ ). When expressed in terms of dimensionless frequency,  $\omega^* = 0.25\delta_w(2\pi f)/\bar{U}$  [59], based on vorticity thickness ( $\delta_w$ ) and the average velocity of the shear bounding limits ( $\bar{U}$ ), the fundamental frequency is  $\omega_0^* = 0.21$ . This value is within the expected range for Kelvin-Helmholtz instability in free shear layers ( $0.21 < \omega^* < 0.222$  [59]) and agrees well with relevant studies on LSBs [e.g. 128, 159, 173].

The tomographic configuration and vortex identification criteria allow exploration of the three-dimensional coherent structures in the LSB. Instantaneous snapshots of the unforced LSB are shown in figure 4.5, where the structures are identified using iso-surfaces of  $Q$ -criterion [61]. In the aft portion of the bubble, vortical structures exhibit strong spanwise deformation, with notable staggering in the  $x - z$  plane. Similar vortex distribution is observed in the DNS results of Marxen & Henningson [103] where the separation bubble is asymmetrically forced with oblique waves, and in the experiments of Burgmann & Schröder [20] and Nati *et al.* [123].

An additional feature of the flowfield is the presence of vortex filaments connecting the staggered vortex cores, indicated by arrows in figure 4.6a. Similar topological features persist through the shedding cycles, as illustrated in figure 4.5. The results suggest that the locations of dominant deformation do not shift significantly in the spanwise direction from cycle to cycle, resulting in distinct peaks and valleys in the time-averaged outline of the aft part of the LSB (figure 4.2b).

Given the limited spanwise extent of the field of view relative to the wavelength of spanwise deformation, determination of the characteristic streamwise ( $\lambda_x$ ) and

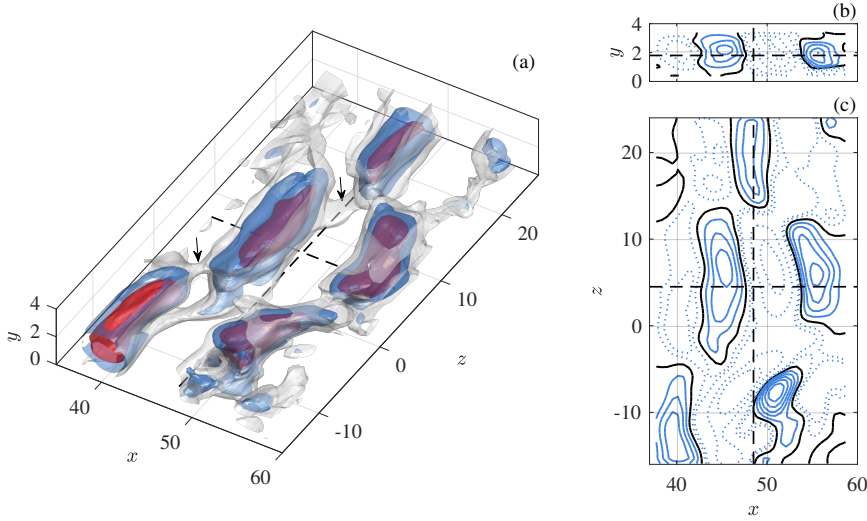


FIGURE 4.6: Unforced bubble instantaneous  $Q$ -criterion snapshot. (a) Grey, blue and red iso-surfaces correspond to  $Q = 0, 0.002$  and  $0.006$ , respectively. (b)  $x - y$  plane at  $z = 4.5$ , (c)  $x - z$  plane at  $x = 48.5$ . *Dashed lines*: measurement volume centre,  $x = 48.5, y = 1.8$  and  $z = 4.5$ , *solid lines*:  $Q \geq 0$ , *dash-dot lines*:  $Q < 0$ .

spanwise ( $\lambda_z$ ) wavelengths is performed through wavelet analysis. More specifically, at each recorded time instant, the total  $Q$ -criterion value is computed along the dashed streamwise and spanwise *monitor* lines indicated in figure 4.6. The two lines intersect at the centre of the measurement volume ( $x = 48.5, y = 1.8, z = 4.5$ ). Exemplary instantaneous spatial distributions of  $Q$  in streamwise and spanwise directions are shown in figures 4.7a and 4.7b, along with their respective wavelet coefficients (figures 4.7c, 4.7d). The dominant wavelength is then estimated based on the maximum of the wavelet coefficients at each time instant. This procedure is repeated for all instantaneous snapshots, and the results are presented in figures 4.7e and 4.7f as probability distributions.

It can be seen that both  $\lambda_x$  and  $\lambda_z$  are distributed about central values corresponding to  $\bar{\lambda}_x = 9.4$  and  $\bar{\lambda}_z = 18.2$ , with standard deviation of  $\sigma_{\lambda_x} = 1.1$  and  $\sigma_{\lambda_z} = 6.7$ , respectively. The average spanwise wavelength is in excellent agreement with the wavelength of spanwise deformation determined from the time-averaged outline of the aft portion of the LSB ( $\lambda_r = 18.6$ , figure 4.2). The ratio of the average spanwise to streamwise wavelengths,  $\bar{\lambda}_z/\bar{\lambda}_x$ , is equal to 1.94, yielding an obliqueness angle of  $27^\circ$ . This is comparable to the results of Rist & Augustin [139], Marxen & Henningson [103], and Kurelek *et al.* [83] who report wavelength ratios of 1.92, 2.4 and 2.5, respectively.

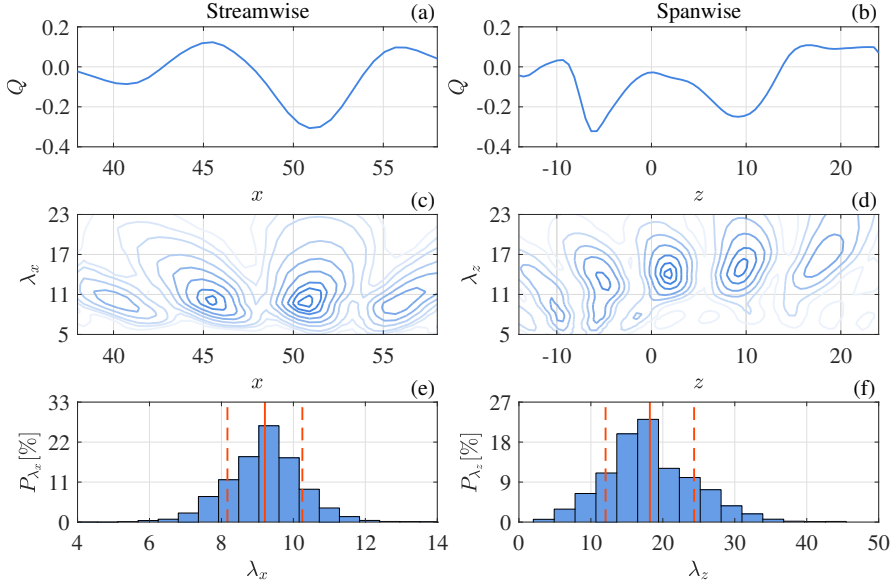


FIGURE 4.7: Columns represent streamwise and spanwise quantities, respectively. *First row:*  $Q$ -criterion at the centre of the volume axes (figure 4.6). *Second row:* corresponding wavelet coefficients. *Third row:* wavelength probability distributions. The vertical dashed lines indicate the standard deviation with respect to the mean value.

## 4.4. ORIGIN OF SPANWISE VORTEX DEFORMATION

### 4.4.1. BOUNDARY LAYER UPSTREAM OF THE LSB

In order to shed light on the mechanism responsible for the observed spanwise topology of vortical structures, it is instructive to examine the stability characteristics of the incoming boundary layer and the fore portion of the LSB. Given the experimental field of view and resolution limitations, characterisation of the incoming boundary layer velocity is performed by numerical solution of the laminar boundary layer equations [150] using an implicit solver. The imposed streamwise pressure gradient is determined by the measured pressure distribution (figure 3.2a). The solution is marched from the location of the most upstream pressure tap, where the boundary layer profile is approximated with a Falkner Skan analytical solution. The subsequent marching is carried out until the expected failure of the numerical solution, upstream of separation. This occurs at  $x = 1.6$ , which is approximately 1% of the plate length upstream of the experimentally determined separation location ( $x_s = 6.3$ ).

The results of the computations are validated through a direct comparison with measured data at  $x = 1.6$  (figure 4.8). The agreement between the results is remarkable, with the only noteworthy deviation observed in the second wall-normal derivative in the proximity of the wall ( $y < 0.5$ , figure 4.8c). In addition, the corresponding integral boundary layer parameters for the computation and the PIV measurements compare as  $\delta^* = 0.88$  and 0.87, and  $H = 3.54$  and 3.41, respectively.

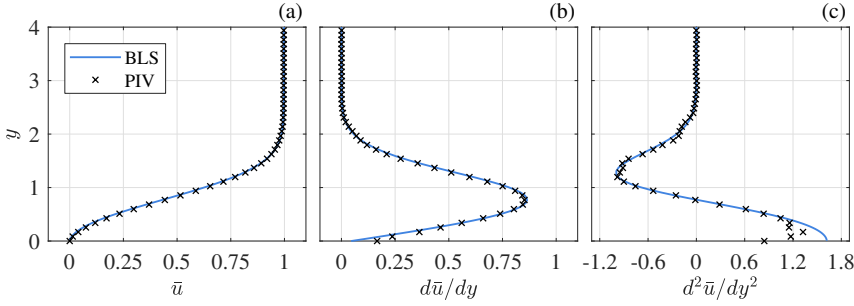


FIGURE 4.8: Comparison between boundary layer solver and PIV measurements, at  $x = 1.6$ . (a) Streamwise velocity profile, (b) first derivative and (c) second derivative of streamwise velocity along the wall-normal direction.

#### 4.4.2. LINEAR STABILITY ANALYSIS

In order to investigate the stability characteristics of the described flow, linear stability theory calculations are performed on the composite flow field consisting of the numerically determined laminar boundary layer in the region  $-140.4 \leq x \leq 1.6$  and the PIV measured flow field in the region  $1.6 \leq x \leq 56.9$ . The primary goal is to investigate the existence and growth of oblique modes upstream of separation that may give rise to spanwise deformation of vortex filaments in the LSB and, thus, lead to the staggered pattern shown in figure 4.6. More specifically, the focus is on the relative amplification of oblique modes with respect to streamwise modes. The typical assumptions of locally parallel, spanwise-uniform flow and small amplitude perturbations are invoked. Consequently, the spanwise growth rate,  $\beta_i$ , and the spanwise velocity component,  $\bar{w}$ , are set to zero in the Orr-Sommerfeld equation (equation 2.8).

The stability diagram for  $\beta_r = 0$ , calculated on the combination of numerical and experimental results, is shown in figure 4.9. A continuous stability spectrum between the attached and separated flow regions is observed, confirming the earlier conjectures of inherent interrelation between the stability characteristics of the boundary layer and the LSB [35, 114], with similar features also observed in recent results of Marxen *et al.* [104] and Yarusevych & Kotsonis [183]. The critical point is located in the adverse pressure gradient region (figure 3.2a) at  $x_c = -47$ , approximately one bubble length upstream of  $x_s$ . The frequency corresponding to the most unstable growth rate, marked by the dashed line, decreases towards the separation location. Past the separation point, the maximum growth rate increases significantly, and the associated frequency begins to increase. The maximum amplification factor is achieved in the vicinity of the mean maximum height and is  $N = 7.2$ . The corresponding frequency effectively matches the fundamental frequency  $St_0 = 0.038$  (136Hz) estimated from the velocity spectra (figure 4.4).

The streamwise growth rate,  $\alpha_i$ , with respect to the spanwise wavenumber and wavelength at the mean maximum height is shown in figure 4.10a. It is noted that an increase in  $\beta_r$  (or a decrease in  $\lambda_z$ ) results in the reduction of the most unstable wave frequency. The critical spanwise wavenumber at which disturbances become

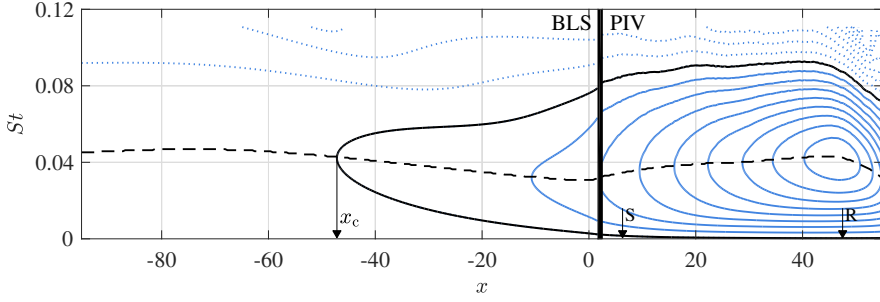


FIGURE 4.9: Iso-contours of streamwise growth rates for  $\beta_r = 0$  as estimated through the boundary layer solver (left) and through the planar PIV measurements (right), in steps of 0.05. *Solid lines*:  $\alpha_i \leq 0$ , *dotted lines*:  $\alpha_i > 0$ , *dashed line*: minimum  $\alpha_i$ .  $x_c$  marks the critical streamwise position where disturbances first become unstable. S and R mark separation and reattachment, respectively.

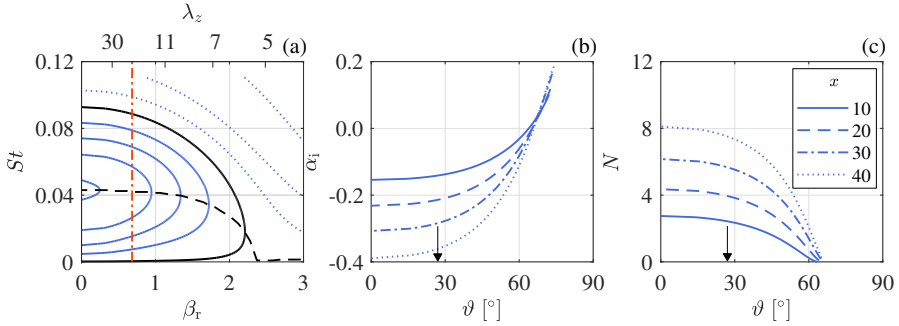


FIGURE 4.10: (a) Streamwise growth rate,  $\alpha_i$  with respect to spanwise wavenumber and wavelength at  $\bar{x}_h$ , in steps of 0.1. *Solid lines*:  $\alpha_i \leq 0$ , *dotted lines*:  $\alpha_i > 0$ , *dashed line*: minimum  $\alpha_i$ , *dash-dot line*:  $\lambda_{z_0} = 18.2$  ( $\beta_{r_0} = 0.68$ ). (b) Streamwise growth rate and (c) amplification factor with respect to wave angle at several streamwise stations and  $St_0$ . The arrows indicate the wave angle estimated from the experimentally observed wavelengths,  $\vartheta = 27^\circ$ .

unstable is  $\beta_{rc} = 2.2$  ( $\lambda_{zc} = 5.7$ ). In addition, for spanwise wavenumbers lower than approximately  $\beta_r < 0.8$  ( $\lambda_z > 15$ ), the frequency of the predicted unstable waves remains largely invariant up to  $\beta_r = 0$ . The maximum growth rate also increases as  $\beta_r$  decreases to zero, suggesting that, at this stage, the most unstable modes are normal TS waves that undergo convective amplification. The same conclusion can be drawn by tracing the streamwise growth rate and amplification factor with respect to the wave angle,  $\vartheta = \tan^{-1}(\beta_r/\alpha_r)$ , shown in figures 4.10b and 4.10c, respectively, for  $St_0$  at several streamwise stations within the bubble. Once again, the most unstable conditions correspond to  $\vartheta = 0^\circ$ , i.e. to mode (1,0).

The stability of oblique disturbances in the boundary layer upstream of separation is assessed by examining the behaviour of the streamwise growth rate with respect to the wave angle,  $\vartheta = \tan^{-1}(\beta_r/\alpha_r)$ . The growth rates corresponding to the most unstable frequency are shown in figure 4.11a at several streamwise locations upstream of the critical point. Their positive value indicates disturbances are damped upstream

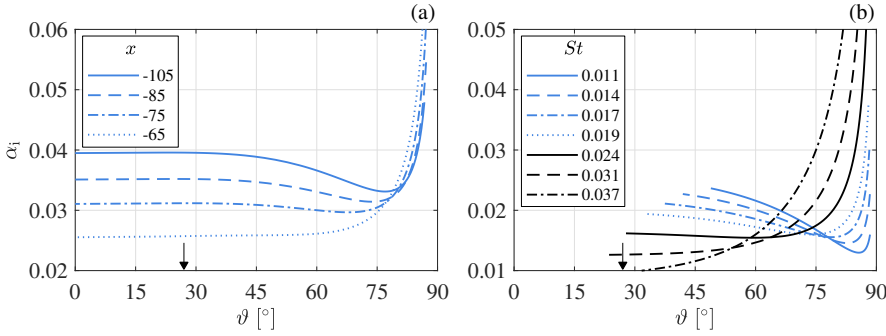


FIGURE 4.11: Streamwise growth rates with respect to wave angle,  $\vartheta = \tan^{-1}(\beta_r/\alpha_r)$ . (a) Selected streamwise positions at  $St_0 = 0.038$  (136Hz) and (b) selected frequencies at  $x_c = -47$ . The arrows indicate the wave angle estimated from the experimentally observed wavelengths,  $\vartheta = 27^\circ$ .

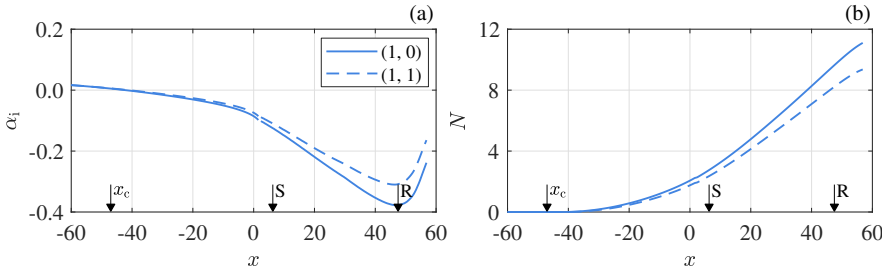


FIGURE 4.12: (a) Streamwise amplification rate and (b) amplification factor for modes (1, 0) and (1, 1), calculated on the composite flow field.  $(h, k)$  denotes integer multiples of the fundamental frequency and spanwise wavenumber, respectively

of the critical location, regardless of the wave angle, however, normal modes are less damped than oblique modes at higher wave angles. The work of Mack [101] demonstrated the same behaviour for a Blasius boundary layer (refer to their figure 6.6), albeit in their case oblique waves are unstable. In further agreement with the findings of Mack [101], is the variation of the growth rate of the oblique waves with frequency, shown in figure 4.11b, at the critical streamwise location,  $x_c$ . It can be seen that when two-dimensional disturbances begin to amplify, i.e. at  $x_c$ , oblique disturbances can be present, having growth rates comparable to or higher than that of the normal perturbations of the same frequency.

It is instructive to compare the stability characteristics of the most amplified normal mode (1,0) and that of the oblique mode (1,1) associated with the same frequency and the spanwise wavenumber corresponding to the dominant spanwise wavelength observed in the experimental data (figure 4.7). Figures 4.12a and 4.12b compare the streamwise variation of the growth rates and amplification factors, respectively, for these two modes. As expected, both modes are amplified downstream of  $x_c$  and experience comparable amplification rates up to the location of separation. The same observation has been made by Rist [138] and Rist & Augustin [139] for

oblique angles lower than  $30^\circ$ . Once the separation point is approached, growth of disturbances is enhanced. While the normal mode  $(1, 0)$  experiences stronger growth than the oblique mode, the latter demonstrates growth rates of the same order. In conjunction with the foregoing discussion, the implication here is that the oblique mode  $(1, 1)$  can attain comparable magnitudes in the vicinity of the separation location, and its superposition with the more amplified normal mode can lead to the vortex deformation observed in the present study (figure 4.5) and previous investigations [e.g. 83, 123].

#### 4.4.3. TWO-DIMENSIONAL IMPULSIVE FORCING

In view of the uncertainty regarding the formation of oblique modes, the boundary layer is impulsively forced in a two-dimensional manner by means of the plasma actuator described in section 3.2.2. The goal is to condition the boundary layer and thus promote the normal mode  $(1, 0)$  via a controlled two-dimensional impulse. As a consequence, the normal mode is expected to reach much higher amplitudes within the separation bubble relative to unforced oblique modes, thereby diminishing the significance of the latter.

Figure 4.13 depicts  $Q$ -criterion surfaces at several instants, for forcing amplitude of  $C_\mu = 1.6 \times 10^{-4}$ . At  $\tau = 0$ , flow in the measurement volume is unperturbed, hence, strong spanwise deformation of the roll-up vortices is observed similar to the results shown in figure 4.5. The impulsively excited wave packet reaches the measurement volume in figure 4.13b, and the evolution of the associated vortical structures is captured in figures 4.13b-f. The vortex evolving directly from the impulse is marked by arrows in the images, and is followed by another strong induced structure, similar to the results of impulsive forcing discussed in chapter 3. The streamwise wavelength of these vortices is consistent with that of the natural shedding and the linear stability predictions, which were confirmed by wavelet analysis at the centre of the volume. In contrast to the natural shedding, the rollers evolving from the impulse are strongly coherent along the span and experience minimal spanwise deformation within the measurement volume. Evidently, two-dimensional impulsive forcing is successful in suppressing spanwise deformations through the promotion of the fundamental normal instability mode  $(1, 0)$ .

Following the passage of the wave packet excited by the impulse over the reattachment region, the bubble undergoes a rapid contraction followed by bursting, as discussed in detail in section 3.5.1. Consequently, no clear evidence of shear layer roll-up is seen in figure 4.13g. As the bubble contracts back to its unperturbed state, weak spanwise structures re-emerge in figure 4.13h, and quasi-steady natural shedding with pronounced spanwise deformations resumes (figure 4.13i).

#### 4.4.4. MECHANISM OF INITIAL SPANWISE VORTEX DEFORMATION

The identified differences in the development of shear layer vortices in the aft portion of the bubble between natural and impulsively forced cases, combined with the results of the linear stability analysis, point to the following mechanism responsible for spanwise vortex deformation in LSBs. Linear stability theory analysis shows that normal and oblique modes of comparable growth rates may be present in the flow

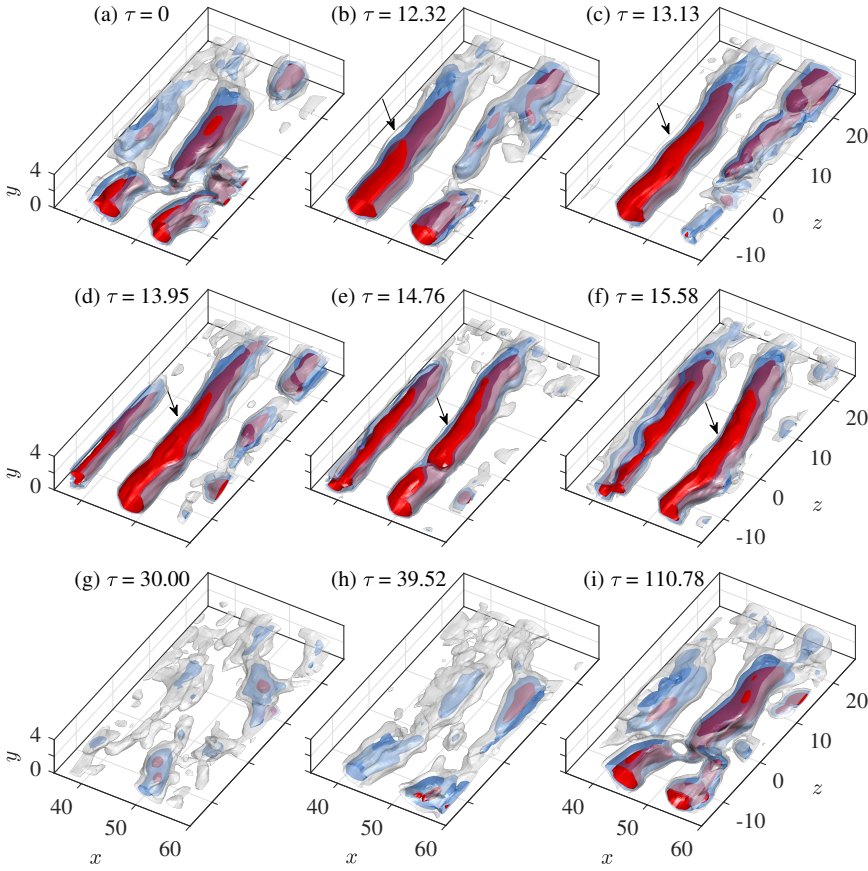


FIGURE 4.13: Instantaneous  $Q$ -criterion at several phases within a forcing cycle at an amplitude of  $C_\mu = 1.6 \times 10^{-4}$ . Grey, blue and red iso-surfaces correspond to  $Q = 0, 0.002$  and  $0.006$ , respectively. Arrows mark the main wave packet vortex associated with the forcing.

upstream of separation (figure 4.11), undergoing convective amplification downstream of the critical point (figure 4.12). The normal modes are the most amplified, their amplification at the fundamental frequency leading to the shear layer roll-up and shedding seen in the aft portion of the bubble. However, a superposition of oblique and normal modes upstream of separation, would lead to spanwise undulations of the resulting perturbations that manifest in the observed spanwise deformations of vortices (figure 4.6). A similar interaction of instability modes is known to occur in attached boundary layer transition, leading to different scenarios such as K-type, H-type or oblique transition [e.g. 10, 56, 72, 76].

A simplified model of superposition of the fundamental normal mode  $(1, 0)$  with the oblique mode  $(1, 1)$  and its mirrored counterpart  $(1, -1)$  is considered in figure 4.14. These modes are labelled as  $n$ ,  $b_1$ , and  $b_2$  in figures 4.14a-c, respectively. It should be noted that the occurrence of the oblique mode  $(1, 1)$  will be accompanied

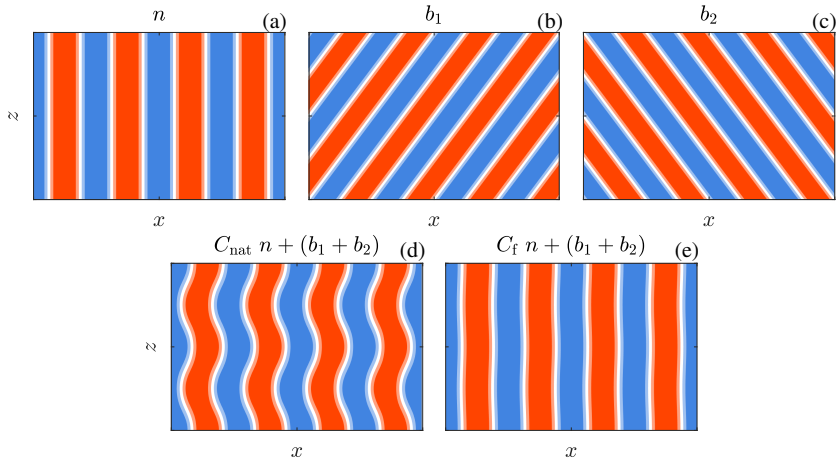


FIGURE 4.14: Waveforms of (a) mode (1, 0), (b) mode (1, 1), (c) mode (1, -1), and their superposition in (d) natural and (e) forced conditions.

by its mirrored counterpart in a two-dimensional flow [101]. For simplicity, the modes are modelled as sinusoidal waves whose salient characteristics are determined based on the analysis of experimental data and stability calculations. First, the superposition of these waves is considered for the unforced flow, namely, in the naturally developing LSB. For a given mode, the amplitude at a given streamwise location is expressed by  $A = A_0 e^N$ , where  $A_0$  is the initial amplitude,  $A_0 = A(x_c)$ , and  $N$  is the amplification factor. Assuming that the initial amplitudes of the normal and oblique waves are comparable, the ratio of their amplitudes at a given streamwise location is given by

$$\frac{A_n}{A_b} = e^{N_n - N_b}, \quad (4.1)$$

where the subscripts  $n$  and  $b$  identify the normal and oblique modes, respectively. For the oblique angle that matches the average ratio of streamwise and spanwise wavelengths determined experimentally ( $\vartheta = 27^\circ$ , figure 4.7), the corresponding  $N$  factors can be obtained from figure 4.12. At  $x = 40$ , located within the tomographic field of view,  $N_n = 8.3$  and  $N_b = 7.1$ , leading to  $C_{\text{nat}} = A_n/A_b = 3.3$ . The superposition of the normal and oblique modes with this amplitude ratio is depicted in figure 4.14d. The results show distinct spanwise deformations similar to those observed in the vortex filaments developing in the natural bubble (figure 4.5). It should be emphasised that similar results can be obtained using oblique modes associated with other obliqueness angles, with the most amplified modes corresponding to oblique angles below  $30^\circ$  (figure 4.10a), and that variations in the relative phase between the modes can change the position of the spanwise crests and valleys.

A similar superposition can be carried out for the case of an impulsively forced wave packet since flow stability characteristics do not change appreciably until the induced perturbations reach the mean reattachment location (see section 3.5.3). Here, the impulse effectively changes the initial amplitude of the normal mode, significantly

increasing its amplitude within the LSB relative to that of the oblique modes. The amplitude of perturbations in the forced and unforced cases can be represented by

$$A_f = A_{n_f} + A_b, \quad (4.2)$$

$$A_{\text{nat}} = A_{n_{\text{nat}}} + A_b, \quad (4.3)$$

respectively, where the forced and natural conditions are defined by the subscripts  $f$  and  $\text{nat}$ , respectively. Equation 4.2 assumes that the development of oblique waves is not affected substantially by the actuator due to its two-dimensional geometry. The amplitude ratio for the forced normal and oblique waves,  $C_f = A_{n_f}/A_b$ , can be obtained by considering the ratio of equations 4.2 and 4.3, and then utilising equation 4.1, leading to

$$\frac{A_{n_f}}{A_b} = \frac{A_f}{A_{\text{nat}}} \left[ e^{(N_n - N_b)} + 1 \right] - 1. \quad (4.4)$$

The ratio  $A_f/A_{\text{nat}}$  can be estimated from measured velocity fluctuations, which gives  $A_f/A_{\text{nat}} \approx 10$  at  $x = 40$ . Substituting this value and the amplification factors corresponding to the same streamwise location, gives  $C_f = A_{n_f}/A_b \approx 40$ . The superposition of the normal and oblique modes with this amplitude ratio is illustrated in figure 4.14e. The outcome demonstrates minimal spanwise deformation, similar to what is observed in the forced vortical structures (figure 4.13).

The presented model agrees with the experimental observations and serves to confirm the proposed relation between vortex deformations and the amplification of oblique perturbations in the fore portion of the separation bubble. Evidently, in naturally developing LSBs, multiple oblique modes are present, and their superposition with the fundamental normal mode produces more complex deformations of the vortex filaments within a range of spanwise wavenumbers. Indeed, the statistical analysis of the experimental data (figures 4.2 and 4.7) shows that spanwise deformation is associated with a range of wavenumbers for a given vortex filament and also varies from cycle to cycle. While a range of unstable modes can be predicted by linear stability theory, the characteristics of the dominant oblique waves will vary for different experimental facilities due to the inevitable minor imperfections in model geometry and the content of the freestream perturbations.

Nonetheless, the present study indicates that oblique modes are unstable upstream of the shear layer roll-up location. Consequently, presence of one or multiple oblique modes will result in spanwise undulations in the dominant shear layer rollers, which has been shown to be a precursor to vortex breakdown in the aft portion of the bubble [83, 106]. It should be emphasised that a superposition of normal and oblique modes occurs upstream of separation and possibly in the fore part of the LSB and serves as an initial spanwise perturbation of the vortices at roll-up, with the subsequent development of spanwise vortex deformation governed by complex vortex dynamics, falling well beyond the purview of linear stability theory. Furthermore, the development of vortices in the aft portion of the bubble involves other, more complex instabilities responsible for vortex splitting and merging (figure 4.5) and the eventual vortex breakdown [106].

The current findings shed light on the underlying physics responsible for the differences in the evolution of roll-up vortices seen in previous studies. For example, for an LSB on a NACA 0018 aerofoil, progressive development of spanwise deformations within a range of spanwise wavenumbers has been reported by Kurelek *et al.* [83] (see their figures 14 and 15), who propose a model linking local vortex breakdown to the development of crests in vortex filaments. Similar progressive spanwise vortex deformations have been observed by Nati *et al.* [123] on an SD 7003 aerofoil. In turn, the results of Burgmann & Schröder [20] and Hain *et al.* [55] show a more pronounced onset of vortex deformations on an SD 7003 profile at comparable Reynolds numbers (see their figures 16 and 25, respectively). The observed differences are attributed to the different relative magnitudes of the dominant normal and oblique modes in the respective studies, which, as discussed earlier, are dependent on both the stability characteristics and specific experimental environment. This is further substantiated by the direct numerical simulations of Jones *et al.* [66]. They observe strongly deformed roll-up in an LSB subjected to three-dimensional forcing (see their figure 11a), i.e., when both normal and oblique modes are promoted. Spanwise coherent vortices form when such forcing is removed (see their figure 11b), thus, similar to the results of the proposed model (figure 4.14), the degree of spanwise deformation of the rollers is related to the relative strength of the fundamental normal and oblique instability modes in a given flow scenario. Furthermore, this provides an explanation for the observed delay in vortex breakdown in studies where the development of the normal mode is promoted via two-dimensional forcing [e.g. 114, 182].

Finally, it has to be emphasised that the discussed model is applicable in flow scenarios with relatively low levels of free-stream turbulence and surface roughness. At higher levels of free-stream or localised perturbations, pronounced streamwise structures can develop in the attached boundary layer [16, 17, 135] and, in the extreme cases, bypass transition can be triggered [64].

## 4.5. CONCLUDING REMARKS

**A**N EXPERIMENTAL investigation is carried out in order to investigate three-dimensional, spatio-temporal flow development in a laminar separation bubble and to elucidate its relation to flow stability. A separation bubble is formed on the flat plate subjected to an adverse pressure gradient. Time-resolved velocity measurements are performed by means of planar and tomographic particle image velocimetry. The measurements are complemented with a numerical solution of the boundary layer equations, which allows for a joint analysis of the flow in the attached and separated flow regions. The stability characteristics of the combined flow field are assessed by means of linear stability theory.

In addition to the natural evolution of the flow within a laminar separation bubble, deterministic, two-dimensional, impulsive forcing via a DBD plasma actuator is employed to assess the effect of forcing the normal instability mode on the bubble dynamics. The results show that a strong amplification of disturbances in the LSB leads to shear layer roll-up and shedding of spanwise oriented vortices in the aft portion of the bubble. However, these structures are shown to develop distinct spanwise deformations followed by complex vortex interactions, involving vortex

splitting, merging, and the development of weaker streamwise vortex connections. Wavelet analysis in spatial formulation demonstrates that the spanwise deformation for a given vortex involves a range of wavelengths, with a statistical mean streamwise to spanwise wavelength ratio of approximately 1:2.

In order to elucidate the mechanism pertinent to the incipient spanwise deformation of the vortices in the LSB, linear stability theory analysis is performed. The results demonstrate that the flow becomes unstable in the adverse pressure region upstream of separation. Upstream of the critical point, oblique modes are less damped compared to the normal modes. However, downstream of the critical point, the normal mode is the most amplified, while the predicted frequency of the most amplified disturbances matches that of the vortex shedding frequency, linking the shear layer roll-up to the amplification of the normal fundamental mode. At the same time, oblique instabilities are also shown to amplify substantially downstream of the critical point, with the highest amplification rates associated with oblique angles below approximately  $30^\circ$ . Moreover, within this range of oblique angles, the growth rate of oblique modes remains virtually invariant to frequency, with the largest growth associated with the fundamental frequency of the most amplified normal mode. Thus, both normal and oblique waves are amplified in the fore portion of the separation bubble, and their superposition produces spanwise undulation in the shed vortices. The degree of such initial undulation is dependent on the relative amplitude of the dominant normal and oblique modes.

Impulsive, two-dimensional forcing results in the emergence of a convectively unstable wave packet whose frequency is determined through selective amplification and matches the fundamental frequency of the unforced case. The results demonstrate that the vortical structures produced by the impulsive perturbation feature strong spanwise coherence, significantly differing from the vortices produced in the naturally developing flow. This is attributed to the promotion of the normal mode through two-dimensional forcing. A simplified linear superposition model is presented to illustrate that the observed differences in vortex topology are attributed to the superposition of normal and oblique instability modes of different amplitude. Utilising the linear stability calculations and measurements, it is shown that a superposition of the fundamental normal and oblique waves of comparable magnitudes leads to substantial spanwise deformation of the most amplified perturbations in the natural separation bubble. In contrast, when two-dimensional forcing is engaged, the relative amplitude of the normal mode is increased by an order of magnitude, leading to a significant increase in the spanwise uniformity of the vortices at formation.

The present study demonstrates that the initial spanwise perturbations of the dominant vortical structures at formation is driven by the superposition of the normal and oblique modes amplified well upstream of separation, and the initial amplitude of such a deformation is dictated by the relative amplitude of the modes. However, further development of the perturbed vortex filaments is governed by the attendant vortex dynamics, and leads to complex vortex interactions and the eventual breakdown of the structures. In practice, the initial amplitude of the spanwise perturbations will vary based on the stability considerations for a given flow, as well as the nature of the experimental conditions such as freestream environment and

geometric imperfections. This explains the differences in vortex dynamics observed in relevant studies [19, 123]. In particular, while distinct deformations of vortex filaments are observed, their severity varies significantly between the studies due to the aforementioned considerations, thereby affecting substantially the flow dynamics in the aft part of the bubble, with implications to the overall flow topology. The current results additionally show that the promotion of the fundamental normal mode can serve to significantly reduce the spanwise deformation of the shear layer vortices, thereby delaying vortex breakdown, as seen in chapter 3. Alternatively, oblique forcing can be used to reduce the spanwise coherence of vortices at roll-up and accelerate their decay, which is of interest, for example, for the control of airfoil trailing edge tonal noise associated with these structures [e.g. 133].

# 5

## SPANWISE STRUCTURES IN AIRFOIL LAMINAR SEPARATION

*This chapter considers the development of a Laminar Separation Bubble on the suction side of a NACA 0018 airfoil, under natural and periodic forcing conditions. The results show that while the time-averaged bubble is strongly two-dimensional, the dominant coherent structures assume three-dimensional organisation in the aft portion of the bubble for both natural and forced conditions.*

---

MICHELIS, T., KOTSONIS. M. & YARUSEVYCH, S. 2017 Spanwise flow development within a laminar separation bubble under natural and forced transition. *Experimental Thermal and Fluid Science* [**Under review**].

MICHELIS, T., KOTSONIS. M. & YARUSEVYCH, S. 2017 Spanwise flow structures within a laminar separation bubble on an airfoil. In *10th International Symposium on Turbulence and Shear Flow Phenomena (TSFP10)*. Chicago, USA.

## 5.1. BACKGROUND

THE phenomenon of Laminar Separation Bubbles (LSB) is common on the suction side of airfoils at low to moderate Reynolds numbers based on chord length ( $Re_c < 500,000$ ). It is relevant for a variety of industrial applications, spanning from unmanned aerial vehicles to gliders and wind turbine blades. Since an LSB is inherently unstable, it may lead to unwanted dynamic effects such as stall, lift reduction, drag increase and tonal noise. Consequently, detailed description of the dynamics of LSBs is essential in order to effectively control them and has been a topic of extensive studies (see section 1.3.1).

It is generally accepted that transition in the separated shear layer is governed by convective amplification of disturbances due to an inviscid Kelvin-Helmholtz instability mechanism [e.g. 13, 106]. The later stages of amplification lead to turbulent breakdown through the development of three-dimensional structures. Many studies that focus on stability of LSBs involve either periodic [65] or impulsive [49] forcing. At the same time, the majority of available experimental investigations are restricted to the two-dimensional description of the bubble topology in the streamwise plane. In comparison, the description of the spanwise evolution of coherent structures in LSBs has been considered only by a limited number of studies [e.g. 18, 179].

The work presented in this chapter focuses on the characterisation of a laminar separation bubble developing on a NACA 0018 airfoil under natural and forced conditions. Repetitive forcing of the LSB by means of a Dielectric Barrier Discharge (DBD) plasma actuator (see section 2.1.3) is applied in order to characterise the effect of natural and forced perturbations in the bubble dynamics. The emphasis is placed on the description of the spanwise flow development, where strong three-dimensional effects are expected in the aft portion of the bubble [106]. The disturbance is introduced locally and in a two-dimensional manner. The resulting spatial and temporal response of the flow field is captured with streamwise and spanwise time-resolved Particle Image Velocimetry (PIV) measurements (see section 2.1.2).

## 5.2. DESCRIPTION OF EXPERIMENTS

EXPERIMENTS are carried out in the closed-loop wind tunnel of the University of Waterloo (see section 2.1.1), bearing a square cross-section of 610mm  $\times$  610mm. A NACA 0018 airfoil of 200mm chord is inserted in the test section (figure 5.1). The airfoil is set at a geometric and aerodynamic angle of attack of  $\alpha = 4^\circ$ , while the pressure side boundary layer is tripped by means of a three-dimensional roughness strip. This is done in order to avoid unsteady effects as well as trailing edge tonal noise emission.

A Cartesian coordinate system is defined with the origin at the leading edge of the airfoil. The  $x$ ,  $y$  and  $z$  axes correspond to streamwise, wall-normal and spanwise directions, respectively. The free stream velocity is set to  $U_\infty = 9.2\text{m/s}$ , resulting in a Reynolds number based on the chord of  $Re_c = 126,000$ . At this speed, the free stream turbulence intensity is approximately 0.1%. For the selected conditions, a laminar separation bubble forms on the suction side, with mean separation and reattachment points located at  $x/c \approx 0.35$  and  $0.53$ , respectively.

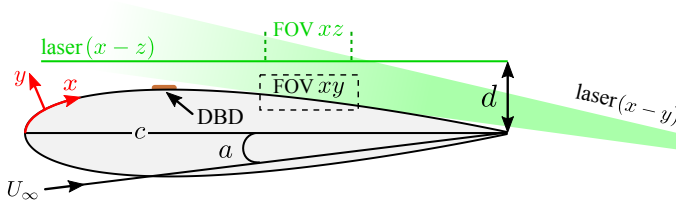


FIGURE 5.1: Experimental arrangement. The green dashed vertical lines denote the streamwise extent of the spanwise field of view (FOV).

The laminar boundary layer is perturbed two-dimensionally by means of an Alternating Current Dielectric Barrier Discharge (AC-DBD) plasma actuator [28, 79]. It consists of two asymmetrically positioned, self-adhesive copper electrodes separated by a *Kapton*<sup>®</sup> dielectric layer (figure 2.3). The electrodes are 10mm wide in the streamwise direction, 30 $\mu$ m thick and 300mm long in the spanwise direction. In turn, the dielectric barrier is 120 $\mu$ m thick. The discharge gap is located at  $x/c = 0.3$ , upstream of the separation point. The forcing signal is comprised of repetitive short pulses that are constructed by modulating a 3.5kV<sub>pp</sub> and 5kHz sinusoidal carrier signal with a square signal of selected frequency (figure 3.3). The modulation duty cycle is adjusted relatively to the pulse frequency, yielding a pulse width of 1ms.

Time-resolved PIV measurements are carried out by employing two *Photron SA4* high-speed cameras with 200mm *Nikkor* macro lenses, set at an aperture of  $f/5.6$ . Illumination is performed by a *Photonic DM20-527* Nd:YLF laser system, whose beam is transformed to an approximately 2mm thick light sheet. A smoke generator uses water-glycol mixture to provide particle seeding.

Two fields of view are captured, both at an acquisition frequency of 2kHz. The first lies in the  $x - y$  plane, at the airfoil midspan ( $z = 0$ ) and is constructed by stitching images from both cameras, covering a total field of view of 65mm  $\times$  22mm. The second view lies on the  $x - z$  plane, parallel to and at a distance of  $d = 21$ mm from the airfoil chord, capturing a field of view of 56mm  $\times$  56mm (figure 5.1). In both cases, the acquired image pairs are processed with the *LaVision DaVis 8.2* software, using the multi-step interrogation window algorithm [147] from an initial window of  $48 \times 48$  pixels to a final of  $16 \times 16$  pixels with 75% overlap. As a result, velocity vector fields of  $473 \times 161$  and  $247 \times 247$  vectors are obtained for  $x - y$  and  $x - z$  views, respectively.

The results are presented on a surface-attached coordinate system (figure 5.1). The  $x$  coordinate runs tangent to the airfoil surface with an origin at the leading edge, while the  $y$  coordinate is normal to the local tangent and is measured from the airfoil surface. The required scaling and geometric transformation of the vector fields (dewarping) is applied to all instantaneous realisation of the measurements on the  $x - y$  plane. For the  $x - z$  plane measurements, no dewarping is applied. The  $z$  coordinate is running parallel to the airfoil leading edge, with an origin at the midspan of the model.

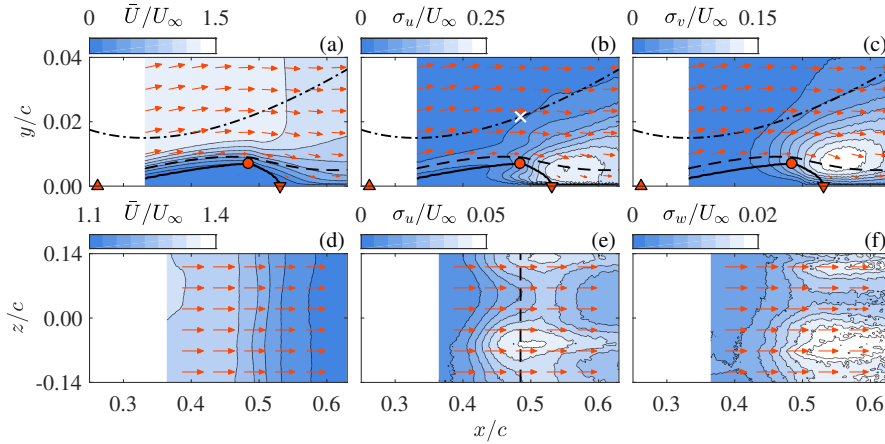


FIGURE 5.2: Time-averaged velocity field of the unforced bubble in the (a)  $x - y$  plane and (d)  $x - z$  plane. Standard deviation of the velocity in the (b-c)  $x - y$  plane and (e-f)  $x - z$  plane.  $\Delta$ ,  $\circ$  and  $\nabla$  indicate mean separation, maximum height and reattachment points, respectively. Thick black line denotes the dividing streamline ( $\psi = 0$ ), while the dashed line the displacement thickness. Black dash-dot line corresponds to the intersection of the  $x - y$  and  $x - z$  planes. White marker and vertical dashed line denote location of velocity probes for the spectral analysis of figure 5.3.

## 5.3. DATA ANALYSIS AND DISCUSSION

ALL RESULTS presented in this section pertain to  $Re_c = 126,000$  and an angle of attack of  $\alpha = 4^\circ$ . All dimensional variables are non-dimensionalised using the airfoil chord ( $c = 0.2\text{m}$ ) and the free stream velocity ( $U_\infty = 9.2\text{m/s}$ ).

### 5.3.1. THE UNFORCED BUBBLE

Figure 5.2 depicts time-averaged velocity and velocity fluctuation fields for the unforced LSB, serving as the baseline for the present study. The velocity field on the streamwise  $x - y$  plane is shown in figure 5.2a along with the time-averaged dividing streamline, indicating the outline of the LSB. The general topology of the bubble follows the well known definition of short laminar separation bubbles by Gaster [47]. The mean separation point is not captured within the measurement domain. This is a necessary compromise for achieving sufficient spatial resolution in the reattachment region of the bubble. Nevertheless, an approximation of the mean separation point can be estimated, capitalising on the nearly linear slope of the dividing streamline in the fore portion of the bubble. Based on the extrapolated estimate of the mean separation point ( $x_s = 0.29$ ) and the mean reattachment point ( $x_r = 0.54$ ), the mean bubble length is  $l = 0.25$ . In turn, the maximum bubble height is  $h = 0.07$  and is located at  $x_h = 0.48$ .

Figures 5.2b and 5.2c demonstrate the standard deviation of streamwise ( $\sigma_u$ ) and wall-normal ( $\sigma_v$ ) fluctuating velocity fields, respectively. Strong spanwise and wall-normal fluctuations in the aft portion of the bubble is attributed to vortex shedding, in line with previous investigations on short separation bubbles [e.g. 183].

In particular, the topological arrangement of streamwise fluctuations (figure 5.2b) reveals two distinct maxima in the vicinity of the maximum bubble height ( $x \approx 0.5$ ). In conjunction with the single maximum in the wall-normal fluctuations located approximately along the mean displacement thickness (figure 5.2c), the overall organisation of the unsteady fluctuating fields in the streamwise plane suggests the existence of coherent vortical shedding in the aft portion of the bubble [55].

Figure 5.2d presents the time-averaged velocity field in the spanwise  $x - z$  plane. As mentioned in section 5.2, the laser sheet on the  $x - z$  plane is placed parallel to the chord of the airfoil. As such, the distance of the spanwise measurement plane from the airfoil surface is not constant along the streamwise direction due to the curvature of the airfoil. In the transformed and projected streamwise plane (dewarped  $x - y$  plane), the measured  $x - z$  plane assumes a curved shape that coincides with the airfoil geometry. The intersection of the measured  $x - z$  plane with the  $x - y$  plane is indicated in figure 5.2 by a dash-dotted line.

The time-averaged flow on the  $x - z$  plane demonstrates a high degree of two-dimensionality along the span (figure 5.2d). The streamwise component of velocity is uniformly decelerating along the  $x$  direction while the spanwise component is near-zero as evident by the quiver plot in figure 5.2d. The overall behaviour of the time-average velocity in the  $x - z$  measurement plane confirms the establishment of spanwise invariant test conditions within the imaged field of view. In contrast, the both streamwise ( $\sigma_u$ ) and spanwise ( $\sigma_w$ ) velocity fluctuations (figures 5.2e and 5.2f) reveal pronounced spanwise modulation. The combination of a highly two dimensional mean flow (figure 5.2d) and pronounced spanwise modulation of the fluctuating field topology in the aft portion of the bubble merits further analysis.

In order to quantify the spectral content of the velocity fluctuations in the aft portion of the bubble, the time-resolved PIV measurements are capitalised. Power Spectral Density (PSD) is computed using Welch's method from temporal signals of velocity components. Figure 5.3a demonstrates the PSD of the fluctuating streamwise velocity measured in the streamwise plane, with the probe location identified by a white marker in figure 5.2b. The frequency resolution is  $St = 0.02$  (0.98Hz). In order to facilitate a comparison between the streamwise and spanwise measurement planes, the streamwise location of the probe corresponds to the location of the maximum bubble height and the wall-normal location corresponds to the intersection of the two planes. The spectrum in figure 5.3a suggests that velocity fluctuations in the aft portion of the bubble are associated with a relatively narrow band of frequencies laying within  $12 < St = fc/U_\infty < 17$ . Additionally, a highly energetic discrete peak appears at  $St \approx 11.8$  corresponding to a physical frequency of 542 Hz.

The presence of a confined frequency band of unsteady fluctuations in the aft-portion of the bubble suggests a selective amplification mechanism attested to the natural stability characteristics of the flow. This can be elucidated with the use of Linear Stability Theory (LST) analysis [101]. The LST analysis is performed through solutions of the Orr-Sommerfeld equation, governing the development of small-amplitude perturbations in a time-invariant parallel flow. It has to be noted here that both assumptions of small perturbation amplitude and parallel flow are challenged by the inherent features of the bubble. Nevertheless, previous studies

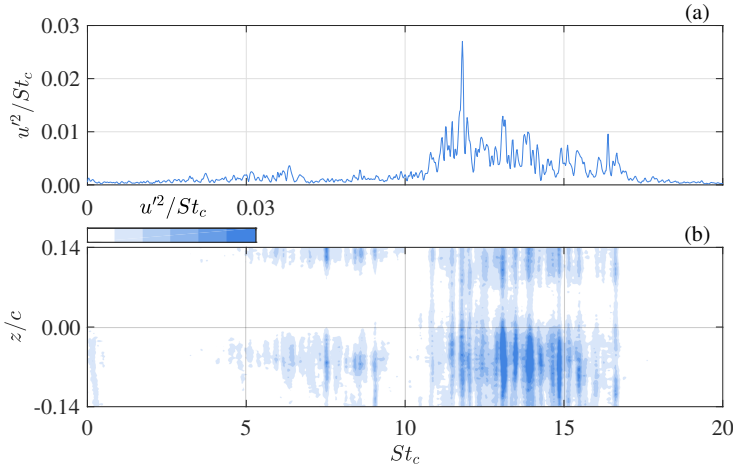


FIGURE 5.3: PSD of  $u'$  in the (a)  $x - y$  plane and (b)  $x - z$  plane for the unforced case. Probe locations are indicated in figure 5.2.

have demonstrated the applicability of LST as a diagnostic tool for accessing the stability of LSBs up to considerably late stages of transition (see section 3.5.3).

In the present study, the experimentally measured time average PIV flow field in the streamwise ( $x - y$ ) measurement plane is used as the mean base flow for the LST analysis. The Orr-Sommerfeld eigenvalue problem is solved in spatial formulation where the real local Reynolds number (i.e. based on the  $x$  location) and frequency are used as known inputs. The eigenvalue is produced in the form of a complex wavenumber ( $\alpha$ ). The imaginary part of the wavenumber corresponds to the non-dimensional local growth rate ( $\alpha_i$ ) associated with a given frequency. Negative values of  $\alpha_i$  denote unstable (i.e. amplifying) modes while positive values of  $\alpha_i$  denote stable (i.e. damping) modes. Neutral modes correspond to zero imaginary wavenumber.

The LST results for the baseline flow are shown in figure 5.4 in the form of a stability curve diagram. The flow is unstable at the upstream boundary of the measured FOV. The band of unstable frequencies spans from  $St_c \approx 0$  to  $St_c \approx 25$  in a streamwise range of  $0.35 < x/c < 0.45$ . The contour levels within the unstable region indicate the local growth rate ( $\alpha_i$ ) and the locus of the most unstable modes is denoted in figure 5.4 by the dashed black line. In the region upstream of the maximum bubble height ( $0.35 < x/c < 0.45$ ) the most unstable frequency remains approximately constant at  $St_c \approx 11$ . This corresponds directly with the spectral peak in figure 5.3, linking the dominant velocity fluctuations in the aft portion of the bubble to the growth of natural instabilities along the incoming boundary layer and the separated shear layer [106].

The respective PSD of streamwise fluctuating velocity components measured in the spanwise ( $x - z$ ) plane is shown in figure 5.3b. The frequency resolution is  $St = 0.04$  (1.9Hz). The corresponding velocity signals were probed along the span (dashed line i figure 5.2b) at the same streamwise location as that used for figure 5.3a.

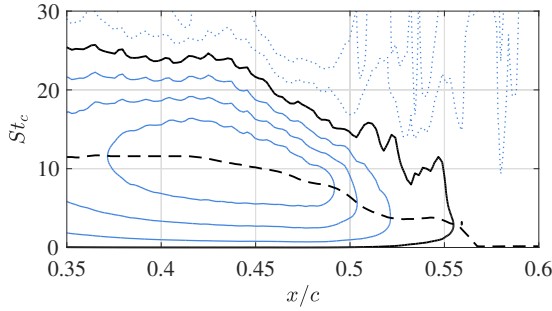


FIGURE 5.4: LST stability contours for the forced case in steps of 0.1. *Solid lines:*  $\alpha_i \leq 0$ , *dotted lines:*  $\alpha_i > 0$ , *black line:* neutral curve ( $\alpha_i = 0$ ), *dashed line:* locus of most unstable modes.

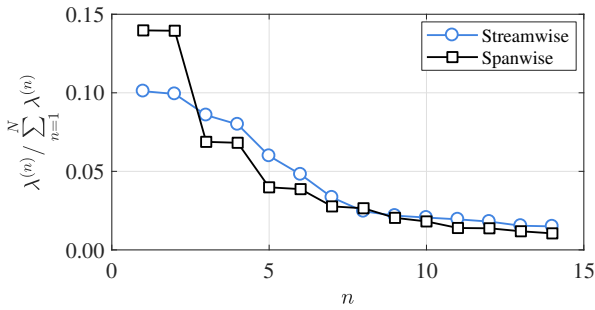


FIGURE 5.5: Relative POD eigenvalues of the forced case.

These are indicated with the vertical dashed line in figure 5.2d. The results indicate that the power of fluctuations along the  $z$  direction is modulated in accordance with the topological distribution of fluctuating velocity fields noted earlier in figures 5.2e and 5.2f. Nevertheless, despite the apparent modulation of the fluctuation power, the corresponding frequency band and centre frequency appear largely invariant along  $z$ , closely following the respective band in the  $x - y$  plane (figure 5.3a) and the LST predictions (figure 5.4). The results in figure 5.3 suggest that while there is strong three-dimensionality in the spatial topology of the fluctuating velocity field in the breakdown region of the bubble (figures 5.2e-5.2f), the dominant velocity fluctuations are associated with a common frequency band, evident in both streamwise and spanwise measurement planes. This implies that vortical structures shed in the aft portion of the bubble develop a consistent spanwise modulation.

Proper Orthogonal Decomposition (POD) is utilised to reveal the presence and topology of the dominant coherent structures in the LSB. For the present study, the snapshot method originally proposed by Sirovich [161] is employed using the ensemble of instantaneous snapshots acquired by PIV. Figure 5.5 shows the relative energy ( $\lambda$ ) of the fourteen most energetic spatial modes in both streamwise and spanwise measurement planes. For both planes, the energy cascade reveals two pairs of modes dominating the fluctuating velocity field. The cumulative energy

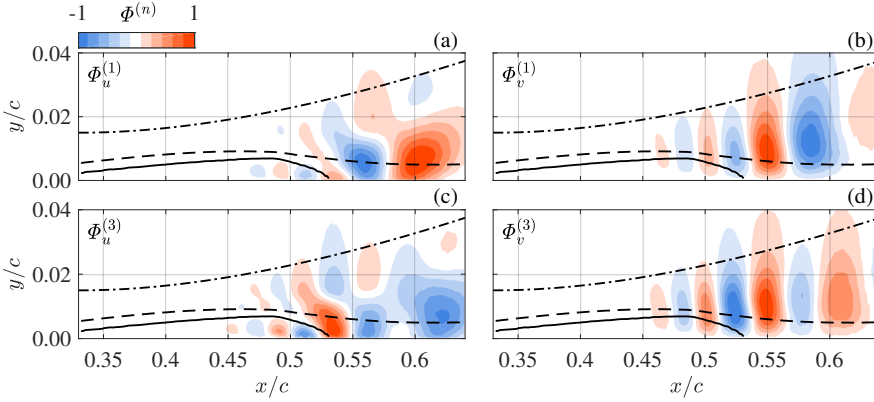


FIGURE 5.6: Normalised POD eigenfunctions in the  $x-y$  plane for the unforced case. Same notation as figure 5.2.

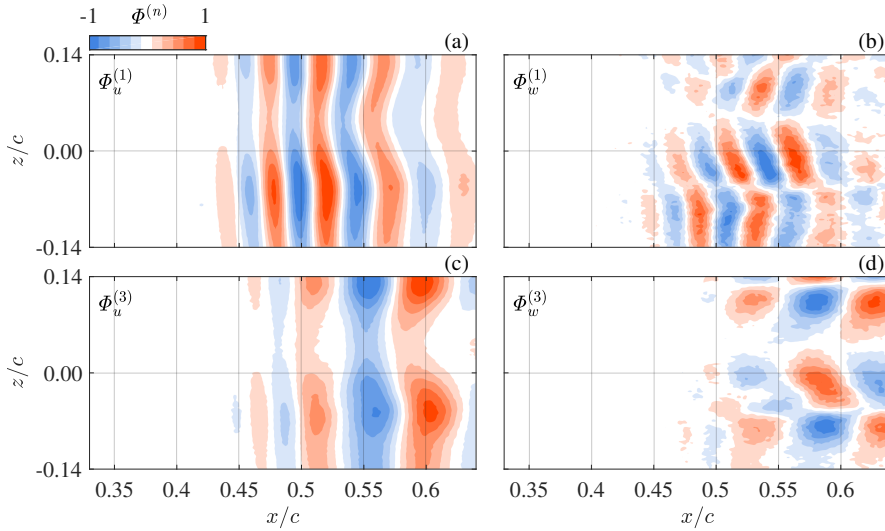


FIGURE 5.7: Normalised POD eigenfunctions in the  $x-z$  plane for the unforced case.

of these first four modes is 37% of the total fluctuating energy for the streamwise plane and 42% for the spanwise plane. A careful inspection of the respective POD eigenfunctions reveals that the four most energetic modes for each measurement plane represent pairs of harmonically coupled modes. The harmonic coupling manifests in the form of a  $\pi/2$  phase shift between the POD modes of each pair, a necessary condition for convective structures. As such, the following analysis will focus on one spatial mode per harmonic mode pair, i.e. the first and third most energetic POD mode per measurement plane. Figures 5.6 and 5.7 show the spatial modes in the streamwise and spanwise plane, respectively. An important note to be made here is

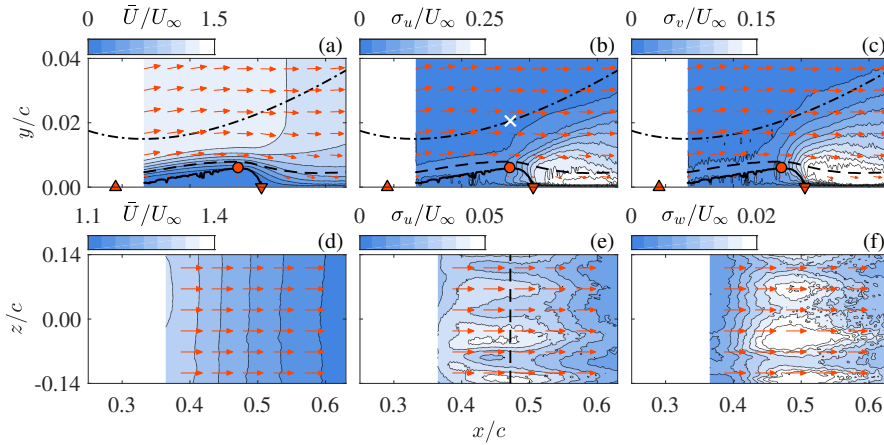


FIGURE 5.8: Statistic quantities of the forced LSB. Same notation as in figure 5.2.

that the measurements and subsequent POD analysis between the two measurement planes are uncorrelated. As such, there is no direct correspondence between POD modes in the  $x - y$  plane and POD modes in the  $x - z$  plane other than their energy sorting. Subsequent analysis will treat the two planes independently. To be noted that all spatial POD modes are normalised to their respective maximum.

The structure of the spatial POD modes  $\Phi^{(1)}$  and  $\Phi^{(3)}$  shown in figure 5.6 corroborate the topology of the velocity fluctuations (figures 5.2b and 5.2c) and confirm the existence of coherent shedding in the aft portion of the bubble. This is further elucidated in figure 5.7 which shows the spatial arrangement of modes  $\Phi^{(1)}$  and  $\Phi^{(3)}$  in the spanwise plane. As previously conjectured, the POD modes confirm the existence of spanwise oriented vortical structures which undergo three-dimensional modulation in the streamwise direction. This is evident from distinct spanwise modulations in the streamwise component of the spatial modes (figures 5.7a and 5.7c) as well as the existence of a distinct spanwise organisation in the spanwise component (figures 5.7b and 5.7d). Additionally, it is striking to note the differences in the characteristic wavelengths between the first ( $\Phi^{(1)}$ ) and the second ( $\Phi^{(3)}$ ) mode pairs. This suggests the existence of multiple modes active in this region, supporting the previously discussed spectral measurements (figure 3.7).

### 5.3.2. THE FORCED BUBBLE

In order to investigate the origin of distinct spanwise deformations of dominant coherent structures, the bubble is conditioned using deterministic impulsive forcing by means of the installed plasma actuator. The frequency of successive pulses is chosen to be within the band of unstable modes predicted by the LST analysis (figure 5.4) at  $St = 13$  ( $f = 600\text{Hz}$ ). The time average velocity and velocity fluctuation fields for the forced bubble are shown in figure 5.8. In comparison to the baseline case (figure 5.2), forcing evidently results in the reduction of the bubble length to approximately 80% and the reduction of the maximum height to approximately 85%

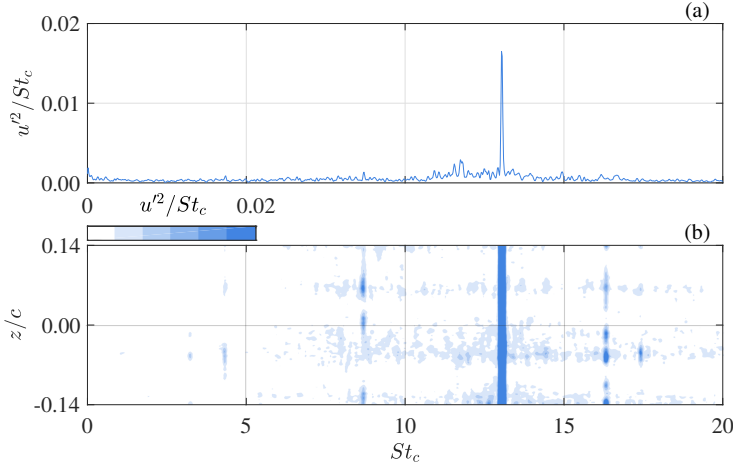


FIGURE 5.9: PSD of  $u'$  in the (a)  $x-y$  plane and (b)  $x-z$  plane for the forced case. Probe locations are indicated in figure 5.8.

of the respective unforced values. This attributed to enhanced levels of velocity fluctuations in both streamwise (figures 5.8b, 5.8c) and spanwise (figures 5.8e, 5.8f) planes, indicating higher amplitude of perturbations and earlier transition. An inspection of the spanwise plane measurements reveals the sustainment of the strongly two dimensional mean flow. However, as for the baseline flow, the  $x-z$  topology of  $\sigma_u$  reveals strong spanwise modulation for both streamwise and spanwise components (figures 5.8e and 5.8f).

The spectral analysis for the forced case has been applied in a similar fashion as for the unforced bubble. The PSD of the streamwise velocity fluctuations in the streamwise plane is shown in figure 5.9a. While the previously identified frequency band (figure 5.3a) is still visible, it is apparent that the majority of fluctuating power is now highly concentrated within a narrow band centred at  $St_c = 13$ , directly corresponding to the forcing frequency. This indicates the locking of the dominant velocity fluctuations on the actuation event. The spanwise spectral power distribution (figure 5.9b), further confirms the strong individuation concentration of the fluctuating energy along the span at the forcing frequency. Nevertheless, distinct spanwise modulation in the spectral content can be seen in figure 5.9b, similar to those observed for the baseline case (figure 5.3c).

The selection of a single coherent fluctuating mode in the spanwise plane due to the plasma forcing is further identified by the cascade of POD modal energy shown in figure 5.10. The first two POD modes in the spanwise plane are responsible for approximately 63% of the total fluctuating energy compared to 28% for the same modes in the unforced bubble. In contrast, the energy cascade in the streamwise plane appears to be weakly affected by the forcing.

Further analysis of the spatial topology of the first and third POD modes for the streamwise and spanwise measurement planes is enabled by figures 5.11 and 5.12, respectively. As suggested by the energy cascade, minor differences can be

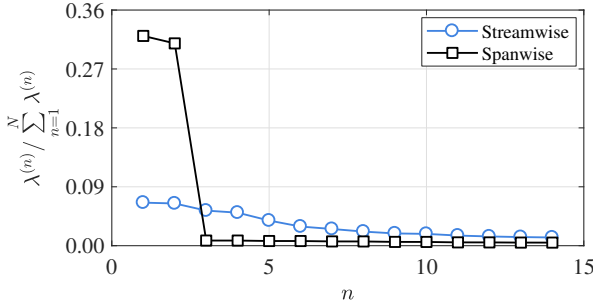
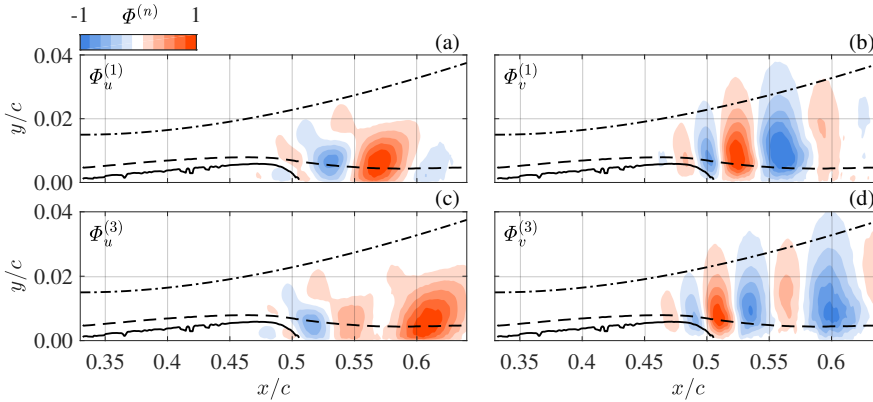


FIGURE 5.10: Relative POD eigenvalues of the forced case.

FIGURE 5.11: Normalised POD eigenfunctions in the  $x-y$  plane for the forced case. Same notation as in figure 5.2.

observed between the forced (figure 5.11) and unforced (figure 5.6) cases in the streamwise plane. In contrast, the topological effect of forcing on the POD modes in the spanwise plane is drastic. More specifically, in the  $x-z$  plane, amplitude modulation is evident in both streamwise (figure 5.11a) and spanwise (figure 5.12b) vector components of the dominating mode,  $\Phi^{(1)}$ . Strong modulation is also apparent for  $\Phi^{(3)}$ , although it should be noted that the fluctuating energy content of this mode is only 0.8% of the total turbulent kinetic energy. The characteristic spanwise wavelength of the observed modulations decreased compared to that seen for the baseline case, likely due to the change in the streamwise wavenumber.

## 5.4. CONCLUDING REMARKS

THE PRESENT STUDY investigated the spatial organisation of shedding structures in the aft portion of a Laminar Separation Bubble. Statistical analysis reveals a rapid growth of velocity fluctuations, suggesting rigorous shedding and eventual transition. Spectral analysis confirms predictions of LST in identifying a band of

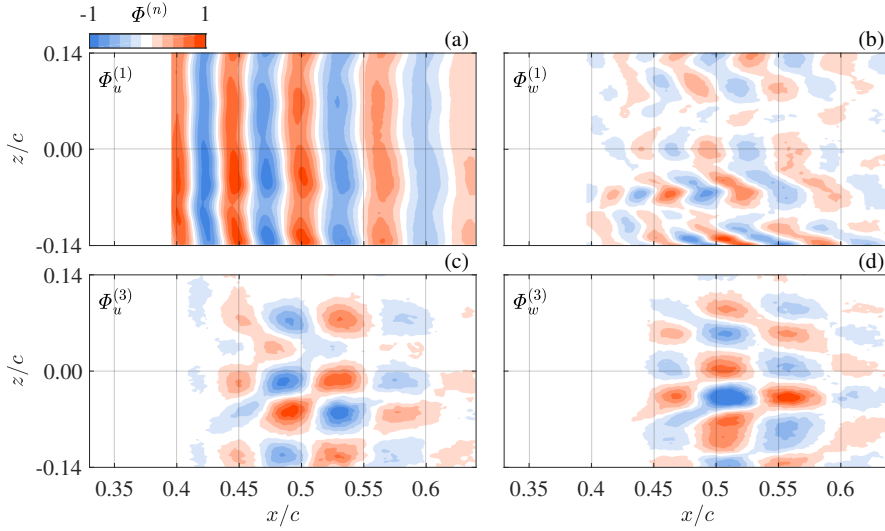


FIGURE 5.12: Normalised POD eigenfunctions in the  $x - z$  plane for the forced case.

unstable frequencies pertinent to the features of the baseline flow. POD analysis in the streamwise plane confirms the manifestation of vortex shedding in the aft portion of the bubble. POD analysis in the spanwise plane shows that, while the dominant modes are coherent and monochromatic, they develop a three dimensional amplitude and shape modulation in the spanwise direction. This occurs under natural unforced conditions within an otherwise strongly two-dimensional baseline flow.

The LSB was further conditioned by two dimensional forcing applied upstream of mean separation using a plasma actuator near the most amplified frequency. Under forcing, vortex shedding locks to a single mode, while the coherency in the spanwise plane increases considerably. Nevertheless, distinct spanwise deformation of the dominant structures persists in the forced case. The aforementioned effect provides insight into the origin of three-dimensional breakdown in LSBs. More specifically, while related to the development of disturbances upstream of separation, spanwise deformation of dominant rollers developing in the separated shear layer is linked to the characteristics of these structures, persisting in both natural and forced bubbles.

# 6

## BLUFF BODY SEPARATION CONTROL WITH A CYLINDER

*The present chapter combines the problem of elongated bluff bodies with the problem of wall-bounded cylinders. More specifically, a cylinder is placed in proximity of a bluff body leading edge and the corresponding flow dynamics are compared with the aforementioned canonical cases. The inclusion of the cylinder imposes a local pressure gradient which changes the topology of the separated region. This global mean flow distortion affects the dynamic features of the shedding processes of both the cylinder and the separated shear layer at the bluff body leading edge.*

---

MICHELIS, T. & KOTSONIS, M. 2015 Interaction of an off-surface cylinder with separated flow from a bluff body leading edge. *Experimental Thermal and Fluid Science* **63**, 91-105.

MICHELIS, T. & KOTSONIS, M. 2014 Cylinder in the vicinity of a bluff body leading edge. *44th AIAA Fluid Dynamics Conference*.

## 6.1. BACKGROUND

AERODYNAMICS of bluff bodies play an important role in many engineering applications and often involves the introduction of ancillary passive control elements in proximity to the main surface [165]. Flow phenomena that occur in these configurations may be complex and are usually dominated by unsteady separation, vortex shedding and wake-boundary layer interaction [36, 163]. This chapter concentrates on the problem of a cylinder placed in proximity to the leading edge of an elongated bluff body. An approach towards understanding the underlying physics involves the deconstruction of the problem at hand into a subset of canonical cases. These are: flow around an elongated bluff body and flow around a wall-bounded cylinder, introduced in sections 1.3.2 and 1.3.3, respectively.

Elongated and symmetric bluff bodies are distinguished by both leading and trailing edge separation above a critical Reynolds number. If the bluff body is of sufficient length, flow reattaches before separating again at the trailing edge, forming a closed recirculation bubble. The overall bubble dynamics are dependent on factors such as free stream turbulence intensity, leading edge curvature and bluff body length [60, 169]. Apart from regular vortex roll-up and shedding, the separation bubble exhibits a low-frequency, large-scale fluctuation termed *flapping* [23, 74, 181].

Considering the case of wall-bounded cylinders, according to Price *et al.* [132], four distinct regions can be identified relative to the gap to diameter ratio ( $G/D$ ). The first region corresponds to  $G/D \leq 0.125$ . It is characterised by weak or no gap flow, separation of the wall boundary layer both upstream and downstream of the cylinder and periodicity at the cylinder's upper shear layer without regular vortex shedding. The second region lies between  $0.125 \leq G/D \leq 0.5$ . It is similar to the first region but involves strong interaction between the lower shear layer and the wall boundary layer. The third region is found in the range  $0.5 \leq G/D \leq 0.75$ , for which vortex shedding from the cylinder sets in and the size of the wall separation upstream of the cylinder is reduced. Finally, for  $G/D > 1$ , no separation is observed on the wall boundary layer either upstream or downstream with respect to the cylinder. The flow field resembles that of an isolated cylinder.

A critical gap to diameter ratio exists below which regular vortex shedding is suppressed. The value of  $G/D_{\text{crit}}$  is typically in the range  $0.2 < G/D_{\text{crit}} < 0.5$  and is greatly dependent on the character and thickness of the wall boundary layer in the absence of the cylinder. Some studies have associated shedding suppression with the cancellation between the vorticity of the lower cylinder shear layer and opposite vorticity of wall boundary layer [52, 168]. Nonetheless, when periodic shedding is established, the Strouhal number based on the cylinder diameter and the free stream velocity ( $St = fD/U_\infty$ ) is independent from  $G/D$  for  $Re_D > 5 \times 10^3$ . Instead, for Reynolds numbers below this value,  $St_D$  increases as  $G/D$  decreases. This increase has not been observed in studies where wall boundary layer growth is eliminated by means of a moving wall. Periodicities present for  $G/D$  ratios below critical are associated with the upper shear layer of the cylinder and not with regular vortex shedding. In addition, there is general agreement that  $St_D$  is not affected by the boundary layer thickness for a fixed  $Re_D$ .

The present chapter attempts the combination of the problem of elongated bluff

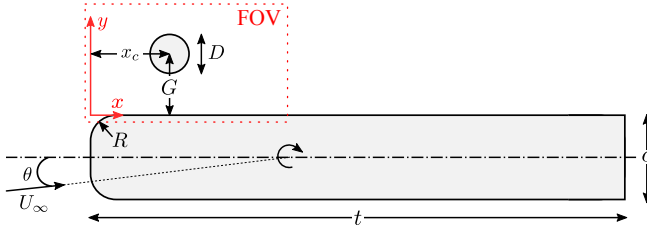


FIGURE 6.1: Dimensions of the model (not to scale).  $D = 20\text{mm}$ ,  $R = 0.75D$ ,  $t = 2.5D$ ,  $c = 15.75D$ ,  $\theta = -5^\circ, 0^\circ, 5^\circ$ ,  $G = 0.25D, 0.75D, 1.25D$ . The dashed box indicates the measurement field of view.

bodies with the problem of wall-bounded cylinders. More specifically, a cylinder is placed at different locations in the vicinity of a bluff body leading edge and the corresponding flow dynamics are compared with the aforementioned canonical cases. The inclusion of the cylinder imposes a local pressure gradient which changes the topology of the separated region. This global mean flow distortion causes a change in the dynamic features of the shedding processes of both the cylinder and the separated shear layer at the bluff body leading edge. Conclusions on this interaction are useful for applications such as the side view mirrors of transport trucks, proximity of buildings and cooling pipes running along edges.

## 6.2. DESCRIPTION OF EXPERIMENTS

### 6.2.1. FLOW AND MODEL CONFIGURATION

Experiments are performed in the W-tunnel (see section 2.1.1), with square cross-section of  $0.4\text{m} \times 0.4\text{m}$ . The model consists of two elements, a cylinder and an elongated bluff body with rounded leading edge, dimensions of which may be found in figure 6.1. A Cartesian coordinate system is used throughout the current study for which  $x = 0$  coincides with the bluff body leading edge,  $y = 0$  with its top surface and  $z = 0$  with its midspan. The bluff body is characterised by leading edge radius to thickness ratio of,  $\eta = R/t = 0.3$ . This value is selected such that the separation bubble height and reattachment length are of comparable size to the cylinder diameter [85]. Both elements are attached on transparent rotating windows, located at the sides of the test section. The windows facilitate setting the angle of attack ( $\theta$ ) and provide optical access. The total blockage is 12.5%. Due to the primary interest of this study towards topological and dynamic features of the flow rather than aerodynamic force measurements, no blockage correction is performed.

Three angles of attack are chosen,  $-5^\circ$ ,  $0^\circ$  and  $5^\circ$  for assessing the topological dependence with respect to the inflow angle. For each angle of attack, six positions of the cylinder relative to the bluff body are selected. With reference to figure 6.1, for  $x_c/D$  of 0 and 1, the gaps applied are  $0.25D$ ,  $0.75D$  and  $1.25D$ . The free stream velocity ( $U_\infty = 20\text{m/s}$ ) is set such that the cylinder is in the subcritical regime. Therefore, the Reynolds number based on cylinder diameter is  $Re_D = 2.6 \times 10^4$ . The turbulence intensity of the wind tunnel at this speed is 0.5%. The analysis of experimental data did not demonstrate significant variations for the angles of attack

selected, hence, the focus of the discussion in this chapter is limited to  $\theta = 0^\circ$ . For the rest of this chapter, lengths are scaled with the cylinder diameter.

### 6.2.2. DATA ACQUISITION

A time-resolved, two-component PIV system (see section 2.1.2) is employed in order to investigate the two dimensional structure of the flow field at the midspan of the bluff body. Illumination is performed by a *Quantronix Darwin-Duo* laser system, emitting green light ( $\lambda = 527\text{nm}$ ). The laser beam is transformed to a sheet of 1mm approximate thickness via a set of spherical and cylindrical lenses. Two *Photron FAST CAM SAI.1* cameras with a  $1024 \times 1024$  pixels CMOS sensor are used to image the illuminated region. The cameras are equipped with a *Nikon* objective of 105mm focal length, set at an aperture of  $f/5.6$ . For reducing pixel locking bias, the focal plane is slightly offset from the illuminated plane, spreading the particle diffracted light to approximately 3 pixels span. The cylinder and bluff body models are matte painted in order to reduce reflections. Particle seeding is provided by a *SAFEX* smoke generator, placed in the plenum of the tunnel, that produces  $1\mu\text{m}$  diameter droplets of vaporised water-glycol mixture.

The imaged fields of view (FOV) from the two cameras are placed as to cover adjacent regions with 10mm overlap, resulting in a combined FOV of  $66\text{mm} \times 122\text{mm}$  and magnification  $M = 0.31$ . Image pair recordings with  $\Delta t = 40\mu\text{s}$  pulse separation time are performed at an acquisition frequency of 2500Hz for an integration time of 1s, for a total of 2500 frames. Images are then processed using *LaVision DaVis 8.1*, applying the multi-step interrogation algorithm [147], from an initial window of  $24 \times 24$  pixels to a final of  $12 \times 12$  pixels, with 50% overlap between windows. The resulting vector field grid comprises of  $310 \times 169$  vectors, with vector spacing of 0.39mm in both  $x$  and  $y$  directions. Errors are calculated based on the description provided in section 2.3. The maximum error for both velocity components at each measurement realisation is of the order of 1%. This value is reduced to 0.02% for time-averaged fields.

## 6.3. DATA ANALYSIS AND DISCUSSION

### 6.3.1. BASELINE FLOW

Two-dimensionality and spanwise uniformity of the flow has been assessed by aligning the PIV illumination sheet with the  $x - z$  plane at a distance of  $y = 0.5$  from the surface of the body, for  $\theta = 0^\circ$ . Ratios of spanwise to streamwise standard deviation ( $\sigma_w/\sigma_u$ ) for the isolated bluff body and for the cylinder placed at  $x_c = 1$ ,  $G = 0.75$  are shown in figure 6.2 for a few streamwise positions. Evidently, the profiles at the leading edge ( $x = 0$ ) are not uniform, most likely due to a minor yaw misalignment of the bluff body with respect to the incoming flow. The remaining profiles are uniform, particularly when the cylinder is introduced for which case a strong jet develops in the gap. Three-dimensional effects become more prominent progressing further downstream due to transition and turbulent breakdown [60, 85]. Consequently, the respective standard deviation profiles increase in magnitude. Thus, the time-averaged flow is regarded sufficiently two-dimensional for the purpose of this study, retaining

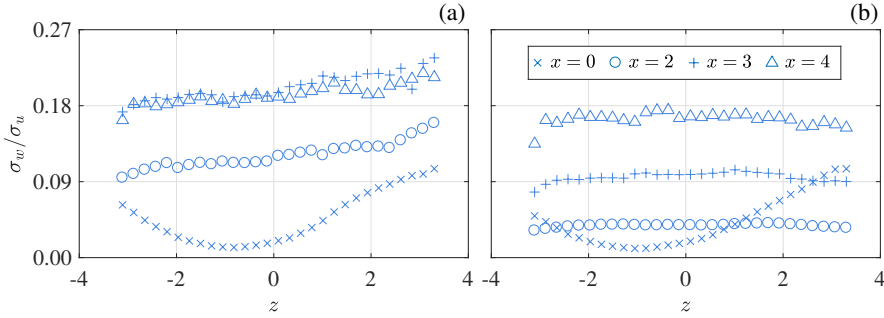


FIGURE 6.2: Ratio of spanwise to streamwise standard deviation ( $\sigma_w/\sigma_u$ ) for  $\theta = 0^\circ$ , measured at  $y = 0.5$  and  $x = 0, 2, 3$  and  $4$ . (a) Isolated bluff body and (b) Cylinder at  $x_c = 1$ ,  $G = 0.75$ .

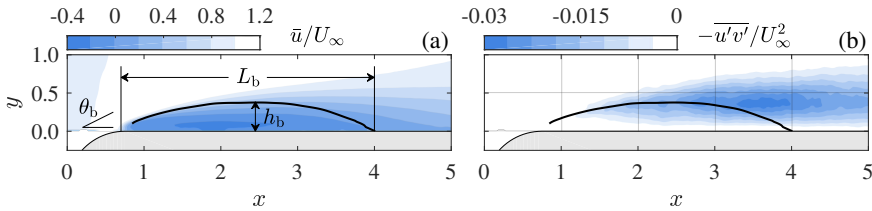


FIGURE 6.3: Baseline flow for  $\theta = 0^\circ$ . (a) Streamwise velocity component and metric parameters.  $\theta_b$ : leading edge separation angle,  $h_b$ : bubble height and  $L_b$ : reattachment length. (b) Reynolds stress. Solid line: dividing streamline ( $\psi = 0$ ).

the relevant flow characteristics on the  $x - y$  plane.

Elongated bluff bodies are characterised by leading edge separation and flow reattachment before the trailing edge [23]. Several metric parameters can be defined in order to characterise the separation bubble, quantified on the time-averaged velocity field. These are the leading edge separation angle ( $\theta_b$ ), the height of the bubble ( $h_b$ ) and the reattachment length ( $L_b$ ), shown in figure 6.3a. The boundary of the bubble is defined by the dividing streamline ( $\psi = 0$ ). The aforementioned quantities are known to be significantly dependent on free stream turbulence [57] and leading edge curvature [86] which, for this study, remain invariant.

Transition to turbulence of the separation shear is responsible for increase of wall-normal momentum exchange, leading to reattachment. As seen in the Reynolds stress field (figure 6.3b) the mixing process begins soon after separation, at approximately  $x = 1.5$  for  $\theta = 0^\circ$  and Reynolds number based on the body thickness,  $Re_t = 6.4 \times 10^4$ . The resulting reattachment length, is estimated to be  $L_b/t = 1.24 \pm 0.02$  ( $L_b/D = 3.1 \pm 0.06$ ). The corresponding separation angle is  $\theta_b = 28^\circ$  while the bubble height is  $h_b/t = 0.14 \pm 0.002$ . These values are in good agreement with the experiments of Taylor *et al.* [169] who obtained  $\theta_{30^\circ}$ ,  $h_b/t = 0.10$  and  $L_b/t = 0.94$  for a bluff body with  $\eta = 0.5$  at  $Re_t = 3 \times 10^4$ . Differences are attributed to stronger curvature and higher Reynolds number for the current experiment which result in a more adverse pressure gradient at the leading edge.

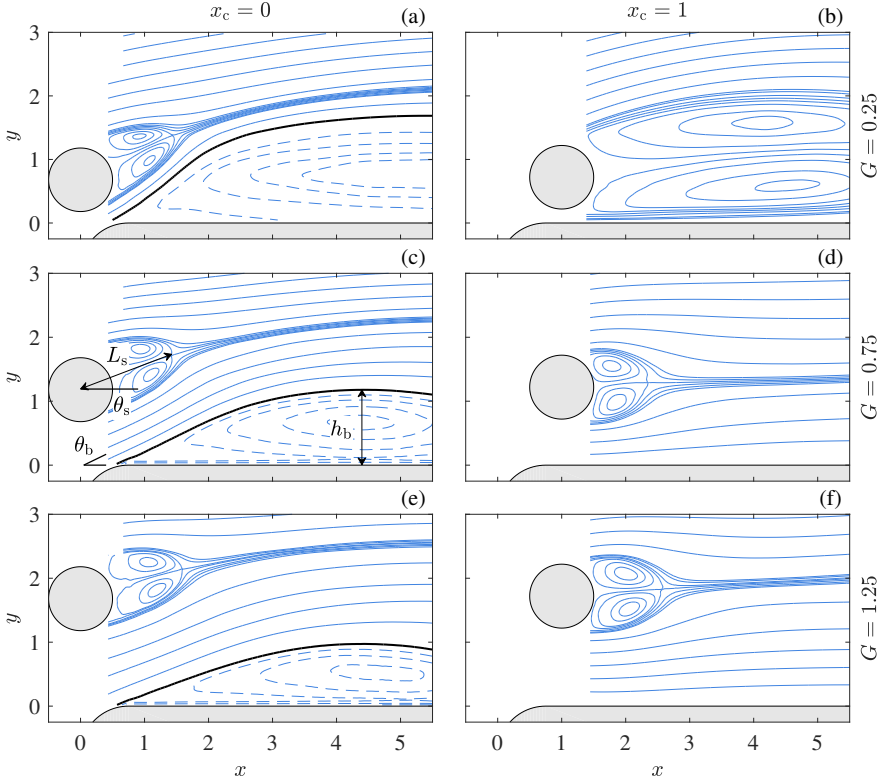


FIGURE 6.4: Selected streamlines at  $\theta = 0^\circ$  for all cylinder configurations.

### 6.3.2. STEADY STATE FEATURES

When a cylinder is placed in proximity to the leading edge of the bluff body, two scenarios are studied. In the first case, half of the cylinder is located upstream of the bluff body leading edge ( $x_c = 0$ ). In the second case, the whole cylinder is downstream of the bluff body leading edge ( $x_c = 1$ ). The shift of cylinder streamwise location causes dramatic changes in the flow field (figure 6.4). The main difference between the two cases concerns the bluff body leading edge separation bubble which is eliminated when the cylinder is placed at its most downstream position. This behaviour is observed for all the tested gaps and at all angles of attack. Hence, the analysis mainly focuses at a bluff body angle of attack of  $\theta = 0^\circ$ .

Evaluation of this topology and the distinctive differences between upstream and downstream positioning of the cylinder requires consideration of the pressure gradient field for each described configuration. In time-averaged terms, pressure gradient is estimated using the incompressible Reynolds Averaged Navier-Stokes momentum equation (see section 1.2.1), that reads

$$\frac{\partial \bar{u}_i}{\partial t} + \bar{u}_j \frac{\partial u_i}{\partial x_j} = F_i - \frac{\partial \bar{p}}{\partial x_i} + \nu \frac{\partial^2 \bar{u}_i}{\partial x_j \partial x_j} - \frac{\partial \overline{u'_i u'_j}}{\partial x_j}. \quad (6.1)$$

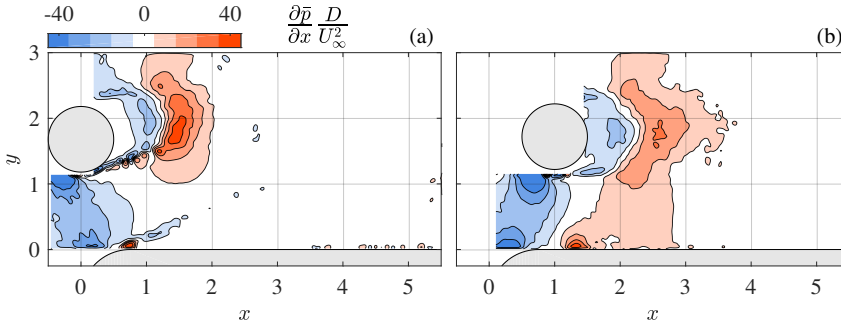


FIGURE 6.5: Streamwise pressure gradient with the cylinder at a distance  $G = 1.25$  from the wall. (a)  $x_c = 0$ ; (b)  $x_c = 1$ .

Assuming steady state due to time-averaging and no external body force action, the terms  $\partial \bar{u}_i / \partial t$  and  $F_i$  can be disregarded. In addition, the diffusion term,  $\nu \partial^2 \bar{u}_i / \partial x_j^2$  is negligible. Therefore, the time-averaged pressure gradient along the  $x$  and  $y$  axes is provided by the following reduced equation,

$$\frac{\partial \bar{p}}{\partial x_i} = -\bar{u}_j \frac{\partial u_i}{\partial x_j} - \frac{\overline{\partial u'_i u'_j}}{\partial x_j}. \quad (6.2)$$

The calculated pressure gradient along the  $x$  axis for two streamwise positions is shown in figure 6.5. Favourable and adverse pressure gradients are represented by  $\partial \bar{p} / \partial x < 0$  and  $\partial \bar{p} / \partial x > 0$ , respectively. Two main favourable pressure gradient regions are present. The first is associated with the upstream stagnation point of the cylinder while the second is located at the leading edge of the bluff body, where flow is accelerated. The displacement of the cylinder from  $x_c = 0$  to  $x_c = 1$  causes the relative position of the cylinder favourable pressure gradient region to shift from upstream to downstream with respect to the bluff body favourable pressure gradient region. This global shift of pressure gradients is responsible for the elimination of the large separation bubble on the main body. Consequently, significant alterations on the dynamics of the wake flow of the cylinder are enforced, as shown in later in this chapter.

A more detailed review of the salient features between the two topological cases is essential. Several metric parameters can be defined in order to quantify and compare the flow topology between the two configurations (figure 6.4c). When a separation bubble is present,  $h_b$  and  $\theta_b$  represent the bubble height and separation angle, respectively. In turn,  $L_s$  is the length of the cylinder recirculation area, defined as the distance between the centre of the cylinder and the recirculation saddle point.  $\theta_s$  is, in turn, the angle between the  $L_s$  line and the horizontal axis.

The values of the aforementioned metric parameters with respect to the gap are plotted in figure 6.6. By decreasing  $G$ , the stagnation point of the cylinder moves towards the bluff body. As a result, the pressure gradient on the bluff body becomes more adverse, forcing the bubble to deflect upwards, increasing its separation angle and height (figures 6.6a, 6.6b). In all cases, the bubble is larger than the baseline

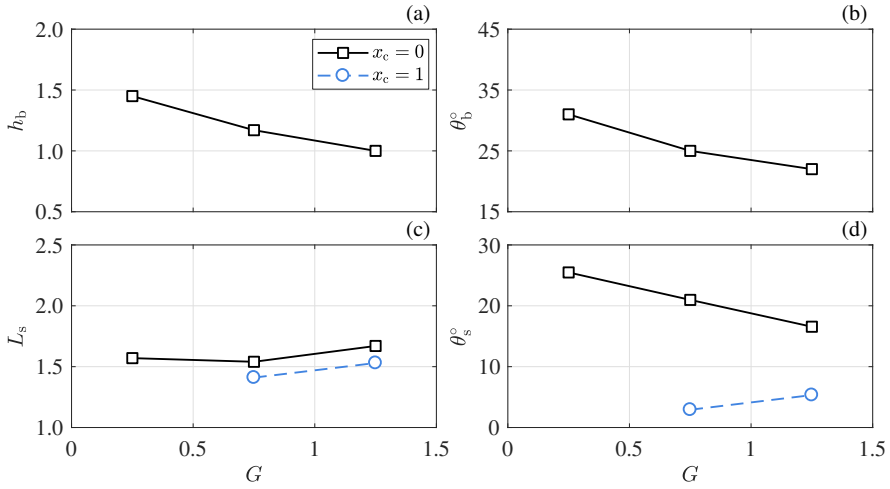


FIGURE 6.6: Metric quantities at different configurations. Uncertainty is of the order of 1%.

case. An effect is, thus, apparent where the cylinder acts as a deflector for the high velocity gap jet formed between the cylinder and the bluff body. This has strong implications not only on the bubble overall size but also on its dynamic behaviour.

The length of the cylinder recirculation area is highly dependent on the presence of the bluff body separation bubble. More specifically,  $L_s$  remains largely invariant under the influence of the bubble ( $x_c = 0$ ). The same applies, when the separation bubble is eliminated ( $x_c = 1$ ), with the exception of  $G = 0.25$  (figure 6.6d). In this case, the cylinder shear layers significantly elongate and extend outside the imaged field of view. Consequently no values of  $L_s$  and  $\theta_s$  are provided for this configuration. Since the bubble diminishes when the cylinder is positioned at  $x_c = 1$ ,  $\theta_s$  decreases for decreasing  $G$ . It is apparent that in the case of  $x_c = 1$ , very small gaps locate the lower separation shear layer of the cylinder in close proximity to the impermeable wall. The inhibition of vertical velocities due to the wall presence mitigates the mixing process in the wake of the cylinder, considerably prolonging the wake recovery.

Turbulent mixing is also dependent on the streamwise position of the cylinder as seen in the Reynolds stress fields (figure 6.7). When the cylinder is located at  $x_c = 0$ , the mixing process does not intensify as close to the cylinder as when  $x_c = 1$ . Elimination of the bubble implies that the gap jet does not fill the cylinder wake and the spreading of the mixing region is not prevented. Hence, with the exception of a very small gap, mixing downstream of the cylinder is stronger for  $x_c = 1$ .

### 6.3.3. SPECTRAL ANALYSIS

Time-resolved analysis on the baseline case reveals, apart from the shear layer shedding, a low frequency fluctuation of the whole bubble, often termed as *flapping*. This fluctuation has been observed in both experimental [23, 39, 75] and numerical

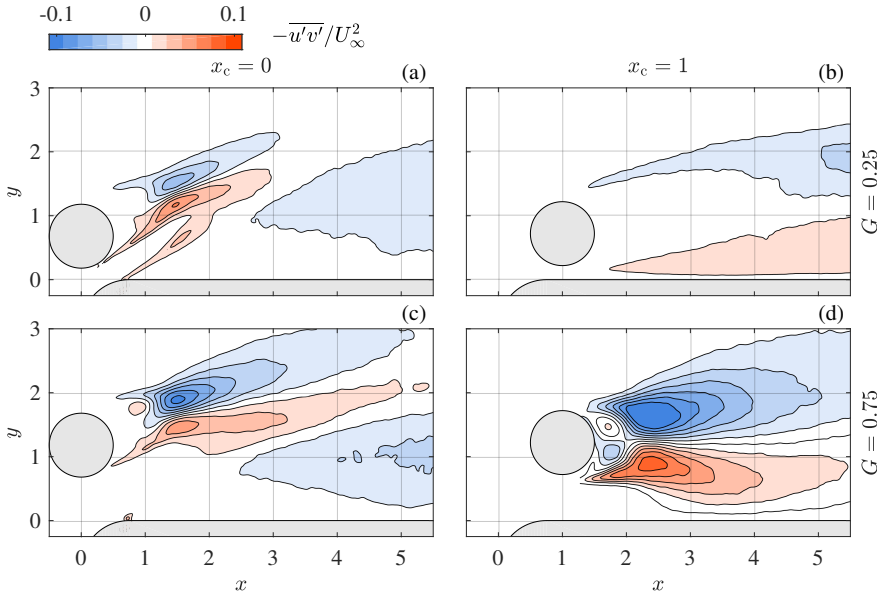


FIGURE 6.7: Reynolds stress fields for representative cylinder configurations.

studies [166, 181]. The effect of the fluctuation is more significant close to the separation point and causes deflection of the shear layer [23].

Figure 6.8a shows typical frequency spectra of the resultant fluctuating component ( $U'^2 = u'^2 + v'^2$ ) for the baseline case as well as when the cylinder is placed at  $x_c = 0$  and  $G = 0.75$ . The temporal signal,  $U(t)$ , is registered at  $x = 1.4$  and  $y = 0.7$  for both configurations. Power spectral density is estimated via the Welch method [175] by dividing the corresponding temporal signal into 4 windows with 75% overlap. The resulting frequency resolution is 2.4Hz. Frequencies are provided in terms of the Strouhal number based on the cylinder diameter ( $St_D$ ) as well as on the bubble reattachment length ( $St_{L_b}$ ) for better comparison to literature.

In the case of the isolated bluff body, low frequency flapping is observed below  $St_D < 0.03$  ( $St_{L_b} < 0.08$ ) while the bubble shedding in the range  $0.07 < St_D < 0.09$  ( $0.21 < St_{L_b} < 0.26$ ). These values are in good agreement with the flat plate leading edge separation experiments of Cherry *et al.* [23] ( $St_{L_b}^{fl} < 0.125$ ,  $St_{L_b}^{sh} = 0.7$ ) and Kiyama & Sasaki [75] ( $St_{L_b}^{fl} < 0.12$ ,  $St_{L_b}^{sh} = 0.6$ ). The differences are accredited to the leading edge curvature and turbulence intensity differences, both of which are known to affect the reattachment length.

By introducing the cylinder, a clear peak in the spectrum becomes evident. The central frequency of this peak is used in order to estimate the Strouhal number of the cylinder for all different configurations. The results are shown in figure 6.8b, along with values from literature. The cylinder  $St_D$  number is found to be higher when  $x_c = 0$  than when  $x_c = 1$ . This is attributed to the increase of blockage due to the extensive bluff body separation at  $x_c = 0$ . The increased blockage deflects

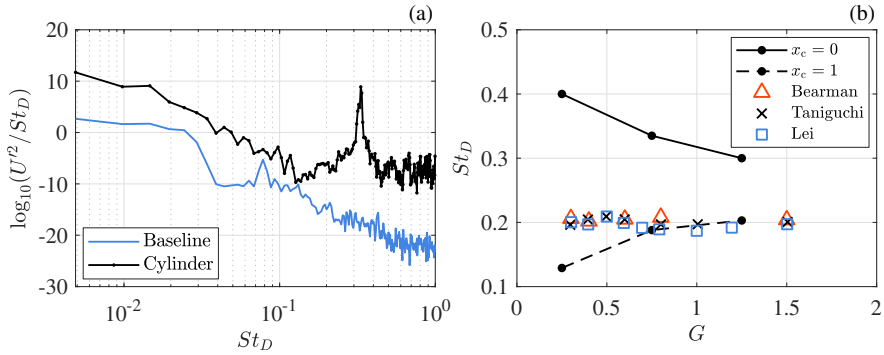


FIGURE 6.8: (a) Frequency spectrum for the isolated bluff body and for the cylinder placed at  $x_c = 0$  and  $G = 0.75$ . (b) Cylinder Strouhal number estimates for all configurations and comparison with the results of Bearman & Zdravkovich [7], Taniguchi & Miyakoshi [168] and Lei *et al.* [93].

and forces flow to fill the recirculation region behind the cylinder. Consequently, considering the definition of the Strouhal number ( $St_D = fD/U_\infty$ ), the blockage increase results in a reduction of the cylinder “effective diameter”, thus, an increase of  $St_D$  number.

For  $x_c = 1$ , the  $St_D$  number reduces below the literature reported values for  $G$  less than critical. This difference is caused by the absence of a wall upstream of the cylinder. Consequently, the pressure gradient topology is distinctively different and, at the same time, there is no boundary layer growth. As the gap increases above the critical value, there is good agreement with literature and  $St_D$  converges to the Strouhal number of an isolated cylinder in the subcritical regime ( $St_D = 0.21$ ) [43].

#### 6.3.4. PROPER ORTHOGONAL DECOMPOSITION

Large coherent structures in the flow field are identified with the *snapshot* POD method (see section 2.2.2). Each POD eigenvalue reflects the relative kinetic energy associated with the corresponding mode, hence, the most energetic modes represent the most dominant flow structures.

Figure 6.9 depicts the first 7 POD eigenvalues of all measured configurations. Corresponding spatial eigenfunctions are provided in figure 6.10. In the majority of cases, two out of three modes have similar eigenvalue. In general, these coupled modes are a characteristic of convective events such as periodic vortex shedding [34, 126]. Considering the baseline body, coupled and single eigenvalues correspond to bubble shedding and flapping, respectively. In turn, when the cylinder is in position, coupled eigenvalues correspond to phase-locked cylinder-bubble shedding. Higher order modes contain harmonics of low order modes, fluctuations related to small scale random turbulence and PIV noise.

In the presence of a separation bubble ( $x_c = 0$ ) vortex shedding from both the cylinder and the bubble manifest. At the cylinder’s lowest position (figure 6.10b), the flapping mode has the highest eigenvalue, thus, dominates the flow field. Modes  $\Phi^{(2)}$  and  $\Phi^{(3)}$  reveal that the bubble shedding is phase-locked to the cylinder shedding.

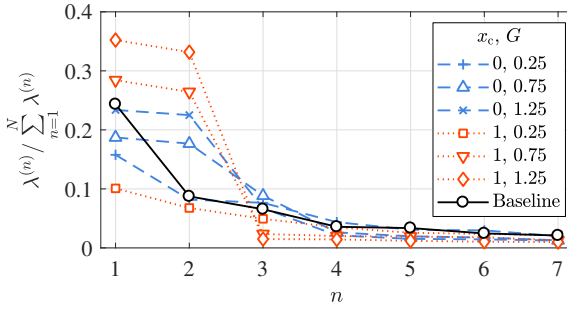


FIGURE 6.9: First 7 normalised POD eigenvalues for each configuration.

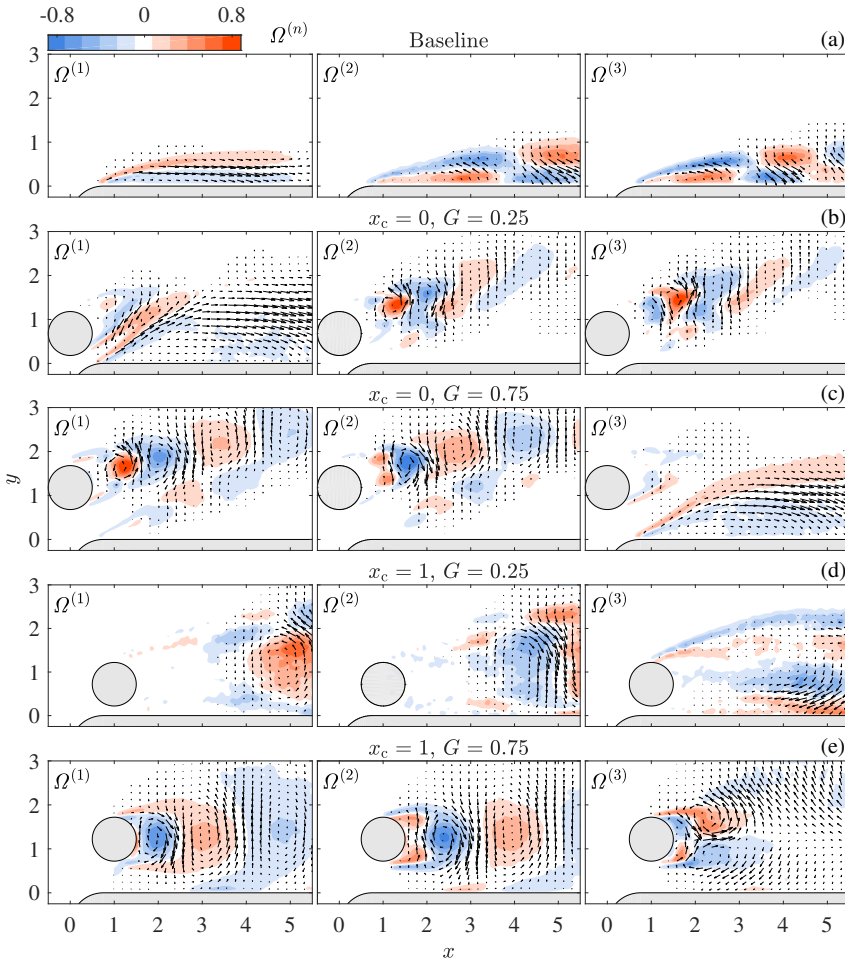


FIGURE 6.10: Curl between the streamwise and wall-normal component of the first three POD eigenfunctions,  $\Omega^{(n)} = \nabla \times [\Phi_u^{(n)} \Phi_v^{(n)}]$ .

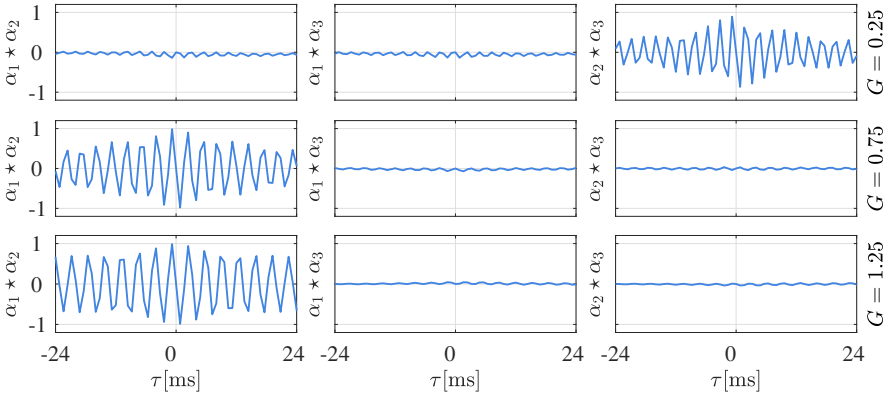


FIGURE 6.11: Cross-correlation ( $\alpha_n \star \alpha_m = \overline{\alpha_n \alpha_m} / \sigma_n \sigma_m$ ) of POD temporal coefficients corresponding to the first three POD modes of  $x_c = 0$ .

The occurrence of phase-locking is also evident from the calculation of the  $St_D$  number, for which only one peak, other than flapping, is present in the frequency spectra (figure 6.8a). Moving the cylinder further away from the wall at  $G = 0.75$  (figure 6.10c), the relative dominance of the modes is reversed, with the shedding modes becoming stronger than flapping. Phase-locking still takes place, however, in contrast to the previous case, bubble shedding is less prominent. Moreover, the wavelength of the fluctuations increases, implying a decrease in  $St_D$ , in accord to figure 6.8b. The same features were observed for  $G = 1.25$ .

When the cylinder is placed at  $x_c = 1$ , the bluff body bubble is eliminated, thus, only cylinder shedding manifests. At the lowest cylinder position (figure 6.10d), although the gap is below critical, weak cylinder shedding is still observed in  $\Phi^{(1)}$  and  $\Phi^{(2)}$ . This takes place at the downstream edge of the imaged field of view, as the recirculation zone is significantly elongated. It is important to note that since  $\Phi^{(1)}$  and  $\Phi^{(2)}$  are not fully captured within the field of view, their eigenvalue may be underestimated. Moving the cylinder away from the wall at  $G = 0.75$  (figure 6.10e), shedding becomes stronger and the wavelength decreases, suggesting an increase of  $St_D$ , concurring figure 6.8b. In both cases,  $\Phi^{(3)}$  has very low eigenvalue, hence, it is not considered to represent any relevant flow feature.

The POD temporal coefficients may be used in order to assess the periodicity of the observed phenomena by means of cross-correlation. Figure 6.11 shows the cross-correlation estimate between the most dominant modes in the presence of a bubble ( $x_c = 0$ ). The modes that were previously shown to represent periodic shedding are coupled, thus, are highly correlated in time. The correlation value as a function of correlation shift ( $|\tau|$ ) decreases for decreasing  $G$ . This is due to increased intermittency for gap ratios below critical as the feedback between the cylinder shear layers is interrupted [132].

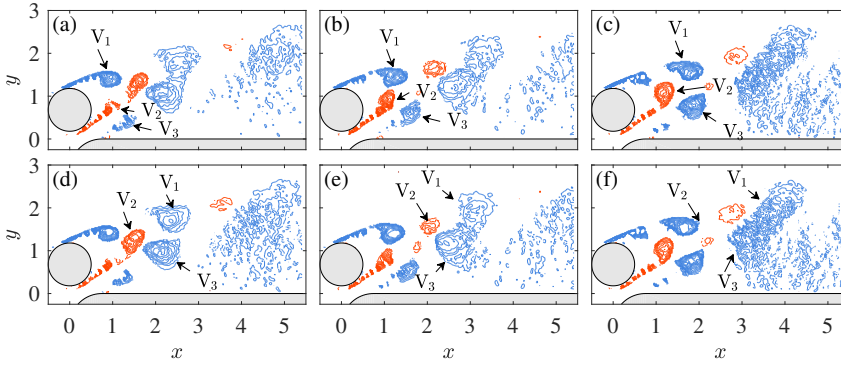


FIGURE 6.12: Temporal sequence ( $\Delta t = 4 \times 10^{-4}$ s) of  $Q_\omega$  for  $x_c = 0$  and  $G = 0.25$ . *Blue*: clockwise rotation, *red*: anti-clockwise rotation.

### 6.3.5. WAKE AND VORTEX DYNAMICS

The three most dominant POD modes identified in the previous section are used for reconstructing the instantaneous flow field. Subsequently, large scale vortical structures are identified by means of the  $Q$ -criterion [61, 78]. The formulation used here reads

$$Q = -\frac{1}{2} \left[ \left( \frac{\partial u}{\partial x} \right)^2 + 2 \frac{\partial u}{\partial y} \frac{\partial v}{\partial x} + \left( \frac{\partial v}{\partial y} \right)^2 \right]. \quad (6.3)$$

This criterion is modified in order to identify the rotation direction for facilitating tracking of individual vortices and their interactions. First, the vorticity,  $\omega$ , of the flow field is calculated. Its sign is subsequently applied on the rotation regions that are detected by  $Q$ , expressed as  $Q_\omega = Q\omega/|\omega|$ . This separates clockwise ( $Q_\omega < 0$ ) from anti-clockwise ( $Q_\omega > 0$ ) rotating vortices.

Figure 6.12 shows consecutive timesteps ( $\Delta t = 4 \times 10^{-4}$ s) for the case of  $x_c = 0$  and  $G = 0.25$ . Vortex  $V_1$  is released from the upper shear layer of the cylinder, followed by the release of two counter rotating vortices,  $V_2$  and  $V_3$ . The latter are simultaneously released from the lower side of the cylinder and the bluff body leading edge separation, respectively. As these three vortices propagate downstream, their close proximity forces them to reposition, with  $V_2$  taking place behind  $V_1$ . At this point, the co-rotating vortices  $V_1$  and  $V_3$  approach each other and, as a result, merge into a larger but weaker vortex. Large structures as such are believed to affect the bubble flapping process as has been suggested by Yang & Voke [181]. Indeed, for this case, the bubble flapping POD mode dominates over the cylinder shedding as can be seen in figures 6.9 and 6.10b.

Moving the cylinder at  $G = 0.75$  (figure 6.13), it is observed that the initial vortex dynamics remain the same as in the previous case.  $V_1$  is released and is followed by the simultaneous release of  $V_2$  and  $V_3$ . However, since the distance between the latter vortices is larger, they do not merge, at least within the imaged field of view. The same behaviour is observed when  $x_c = 0$  and  $G = 1.25$ .

The time series of figure 6.14 ( $\Delta t = 4 \times 10^{-4}$ s) corresponds to the case of  $x_c = 1$

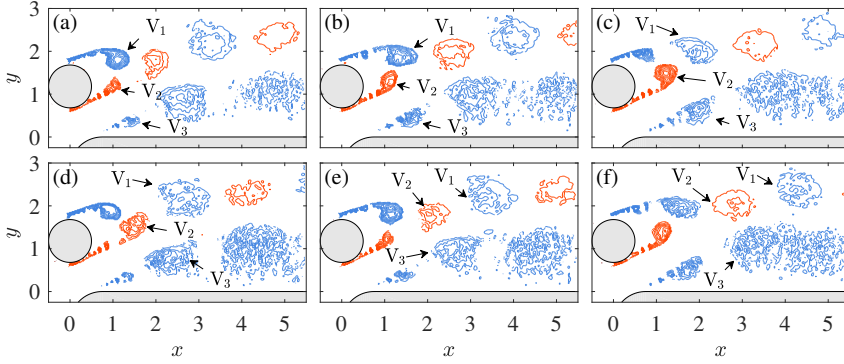


FIGURE 6.13: Temporal sequence ( $\Delta t = 4 \times 10^{-4}$ s) of  $Q_\omega$  for  $x_c = 0$  and  $G = 0.75$ . *Blue*: clockwise rotation, *red*: anti-clockwise rotation.

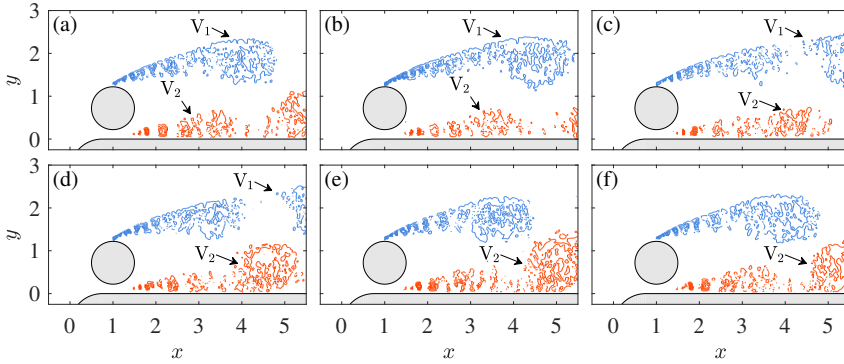


FIGURE 6.14: Temporal sequence ( $\Delta t = 8 \times 10^{-4}$ s) of  $Q_\omega$  for  $x_c = 1$  and  $G = 0.25$ . *Blue*: clockwise rotation, *red*: anti-clockwise rotation.

and  $G = 0.25$ , where no separation bubble develops. In this configuration, the feedback between cylinder separation shear layers is reduced [132] and vortices  $V_1$  and  $V_2$  become weaker. This is a consequence of the dominating instability turning from absolute to convective [125]. Further from the wall, at  $G = 0.75$  (figure 6.15) vortex shedding typical of an isolated cylinder instates.

## 6.4. CONCLUDING REMARKS

**A**N EXPERIMENTAL investigation is carried out for assessing leading edge separation control of an elongated and symmetric bluff body by means of a cylinder at  $Re_D = 2.6 \times 10^4$ . A range of gap to diameter ratios between the cylinder and the bluff body wall ( $0.25 < G < 1.25$ ) are explored for two streamwise positions of the cylinder, upstream and downstream with respect to the bluff body leading edge. The developing flow field is captured with time-resolved particle image velocimetry.

Flow around the isolated bluff body separates and reattaches with a mean

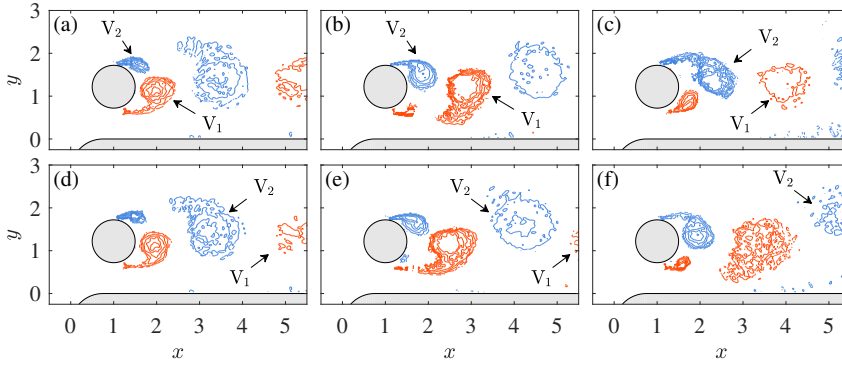


FIGURE 6.15: Temporal sequence ( $\Delta t = 8 \times 10^{-4}$ s) of  $Q_\omega$  for  $x_c = 1$  and  $G = 0.75$ . *Blue*: clockwise rotation, *red*: anti-clockwise rotation.

reattachment length of  $L_b/t = 1.24 \pm 0.02$ . When the cylinder is placed in proximity to the bluff body leading edge, two cases can be identified from the time-averaged velocity field. The bluff body separation bubble is present when the cylinder's leading edge is placed upstream of the bluff body leading edge. Instead, when the cylinder is shifted downstream, the bubble is eliminated. This behaviour is related to the variation of the pressure gradient field for the two cases. By moving the cylinder downstream, the relative position of the cylinder favourable pressure gradient region shifts from upstream to downstream with respect to the bluff body favourable pressure gradient region. As a consequence, the adverse pressure gradient on the bluff body is mitigated and the development of the separation bubble is prevented. This global change of topology has significant impact on the dynamic behaviour of the flow, particularly on the shedding process of both the cylinder and the bubble.

The separation bubble size increases as  $G$  decreases. This is due to the fact that as the two bodies move closer to each other their stagnation points converge towards the same location driven by the pressure gradient. This results in a more adverse pressure gradient in the aft part of the cylinder, deflecting upwards the gap jet, thus, promoting the growth of the bubble. The cylinder recirculation region length remains invariant while the bubble is present for all gaps. However, when the bubble is eliminated, significant elongation of the recirculation is observed for the smallest gap. This behaviour is ascribed to the retarded mixing process that reduces momentum exchange in the wake.

Time resolved analysis on the isolated bluff body captures both vortex shedding and flapping of the separation bubble. By introducing the cylinder where the formation of the bubble is promoted, flapping is preserved. At the same time, bubble shedding locks to the cylinder shedding, hence, both shedding phenomena appear as one peak in the velocity spectra. This behaviour is exposed through POD analysis, where fluctuations from the cylinder shedding and the separation bubble shear layer are staggered in space.

The cylinder  $St_D$  number varies significantly depending on the streamwise position

of the cylinder. In particular, for every case where the bubble is present, the  $St_D$  number is higher than the respective case in the absence of a bubble. The separation creates blockage, forcing the gap flow jet to fill the recirculation region behind the cylinder. As a result, the effective diameter of the cylinder is reduced. Since the gap size affects the bubble dimensions which, in turn, define the cylinder effective diameter,  $St_D$  is also dependent on  $G$ . More specifically, for smaller gaps, the bubble is larger, hence,  $St_D$  rises. In the absence of a bubble,  $St_D$  for  $G$  below critical, is significantly lower than previously reported values in the same order of  $Re_D$ . This difference is caused by the inflow conditions upstream of the cylinder, where, in contrast to previous work, there is no wall, hence no surface on which an upstream separation bubble can develop or a boundary layer can grow. Nonetheless, as  $G$  increases,  $St_D$  converges to the  $St_D$  number of an isolated cylinder in the subcritical regime.

POD modes with similar eigenvalues are treated as periodic vortex shedding. In the presence of a bubble, the analysis reveals two modes for the cylinder-bubble shedding and one mode for bubble flapping. The flapping mode dominates over the cylinder-bubble shedding modes at  $G = 0.25$ , while the opposite holds true for larger gaps. This domination can be explained by observing the vortices that are shed from the upper side of the cylinder and the separation bubble. Vortices that emanate from these points are co-rotating and, when  $G$  is sufficiently small, they are close enough to merge, which is not the case for larger gaps. The merging of vortices creates a larger structure that is able to strengthen low frequency flapping. When the cylinder is at its downstream position, the only two modes correspond to periodic shedding from the cylinder. At  $G = 0.25$ , the mixing process is substantially hindered and, hence, reduced feedback between upper and lower cylinder shear layers causes vortices to form significantly further downstream with respect to the other configurations.

To conclude, it has been shown that pressure gradient changes imposed by the cylinder on the flow field in proximity to an elongated bluff body leading edge can significantly affect the mean flow topology of the separated region, which also implies changes in the vortex shedding dynamics of both bodies. The topological variations and the flow response to changes of pressure gradient as a function of cylinder positioning demonstrate that the two canonical cases cannot be treated separately but should be combined into one non-linear problem.

# 7

## HYBRID SEPARATION CONTROL ON A TRUCK MIRROR

*In this chapter, an experimental study is discussed, aimed at investigating a hybrid flow control concept. The wake of a full-scale transport truck side mirror is reduced by means of a passive guide vane and an active AC-DBD plasma actuator. The work presented is part of the CONVENIENT project, funded by the European Commission under FP7-TRANSPORT and carried out in cooperation with DAF Trucks B.V.*

---

MICHELIS, T. & KOTSONIS, M. 2015 Flow control on a transport truck side mirror using plasma actuators. *Journal of Fluids Engineering, Transactions of the ASME* **137** (11).

MICHELIS, T. & KOTSONIS, M. 2014 Hybrid flow control of a transport truck side-mirror using AC-DBD plasma actuated guide vane. *APS Division of Fluid Dynamics Meeting Abstracts*.

## 7.1. BACKGROUND

**B**LUFF BODY aerodynamics present high relevance toward improving the efficiency of transport vehicles. The specific case of trailer trucks is of particular interest due to the astounding number of such vehicles being in use. Part of their emissions can be reduced by careful aerodynamic optimisation. The area of side mirrors is of high importance as the wake emanating from it has significant influence on the downstream evolution of the flow around the vehicle, directly contributing to drag. Practical and legal matters have led, so far, in design methods that are restricted to shaping and positioning of the mirrors. This chapter explores the possibility of using a hybrid configuration consisting of a passive guide vane and an active DBD plasma actuator in order to reduce the size of the mirror wake.

Guide vanes are passive elements that can redirect flow by imposing the appropriate pressure gradient. In essence, they are flow deflectors and are encountered in many flow control applications such as drag reduction [58], vortex shedding cancellation [90], mixing enhancement [95], etc. Since they form channels, they suffer from increased skin friction. However, they are capable of deflecting high-momentum flows. In the transport truck industry, they are commonly seen at the front vertical edges of the cabin [102]. Being passive and fixed elements implies that they can perform favourably only within a limited range of inflow angles of attack before separating at their leading edge.

As discussed in section 2.1.3, AC-DBD plasma actuators have received significant attention for flow control as they do not involve any mechanical parts, respond fast and consume little energy. The body force induced during discharge results in the formation of a weak jet parallel to the surface. However, its momentum is low, hence, AC-DBD plasma actuators are more suitable for leading edge separation control as they can exploit the receptivity of transitional boundary and shear layers through unsteady forcing.

The concept behind the hybrid control proposed is to couple the advantages of the two control elements. The guide vane prevents early separation on the surface of the mirror and accelerates flow for filling part of the mirror wake. In turn, possible leading edge separation from the guide vane itself is reduced or eliminated by the AC-DBD plasma actuator. The primary interest is not reducing the absolute value of the mirror drag but to condition its wake width. This is expected to have significant impact on the whole truck drag, given the length of the trailer on which the mirror wake expands. A reduced wake size improves flow conditions for any additional controlling devices located further downstream such as boat tails, side skirts, etc [24, 26, 117].

## 7.2. DESCRIPTION OF EXPERIMENTS

**E**XPERIMENTS are carried out in the Open Jet Facility (see section 2.1.1). The model consists of two bodies, an L-shaped cabin model with a circular leading edge and a full-scale *DAF-XF* production mirror. Dimensions of the setup are provided in figures 7.1 and 7.2. The total blockage including the mirror is 15.2%. Since no force measurements are performed, no blockage correction is applied during

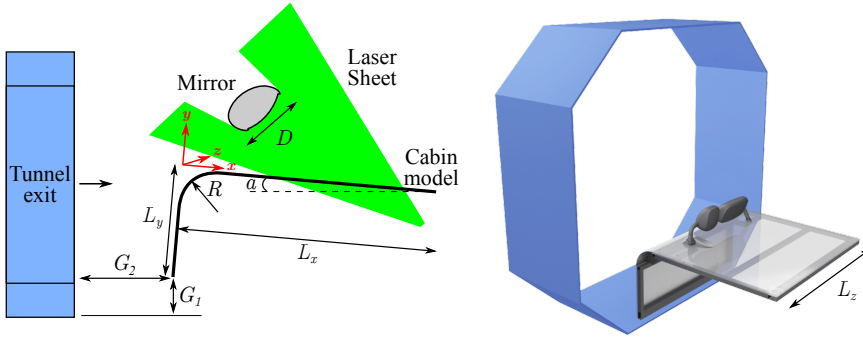


FIGURE 7.1: Schematic of model configuration (right to scale). Coordinate axes are parallel and normal to the cabin wall.  $D = 20\text{cm}$ ,  $R = 20\text{cm}$ ,  $L_x = 148\text{cm}$ ,  $L_{75\text{cm}} = 75\text{cm}$ ,  $L_z = 150\text{cm}$ ,  $G_1 = 15\text{cm}$ ,  $G_2 = 5\text{cm}$  and  $\alpha = -5^\circ, 0^\circ, 5^\circ$ .

the analysis. The model is completely submerged in the open jet, leaving 15cm gap with the lower wall of the wind tunnel for bleeding the incoming boundary layer. The stagnation location of the front face is then checked by means of smoke visualisation. Once the appropriate bleeding is established, results are insensitive to the positioning of the model with respect to the tunnel exit. A Cartesian coordinate system is defined such that  $x = 0$  lies on the leading edge,  $y = 0$  on the surface and  $z = 0$  at the midspan of the cabin model (figure 7.1). The  $x$ -axis is parallel to the cabin surface and the  $y$ -axis normal to it, while the  $z$ -axis is perpendicular to the  $x - y$  plane. A yaw of  $7.5^\circ$  is applied with respect to the free stream, simulating windscreens angle.

A combination of passive and active elements is introduced in order to reduce the mirror wake (figure 7.2a). A passive guide vane prevents separation to develop on the mirror surface and at the same time creates a jet that fills the mirror wake. In turn, flow at its leading edge may separate, an effect that is reduced or eliminated by means of an AC-DBD plasma actuator. The guide vane has a chord length of  $c = 6\text{cm}$  and a thickness of  $t = 0.6\text{cm}$ . It is fully 3D printed and has a slit that houses the ground electrode of the plasma actuator. Both electrodes consist of copper and are 0.1mm thick. The guide vane material (PA2200) also constitutes the dielectric barrier for the plasma actuator. The latter is driven by a 35kV peak-to-peak amplitude voltage signal at a carrier frequency of 6kHz. The signal is modulated at 200Hz frequency and 25% duty cycle, thus forming 1.25ms pulses.

Three angles of attack are chosen,  $\alpha = -5^\circ, 0^\circ$  and  $5^\circ$  in order to represent windward, frontal and leeward conditions, respectively. For each angle, measurements on the  $x - y$  plane are taken at several stations along the  $z$ -axis. In addition, the flow parallel to the plate ( $x - z$  plane) is assessed at  $y$ -axis stations: below, in the middle and above the mirror. The relative positions of all measurement planes is shown in figure 7.2b. Since, in practice, only the orientation of the reflective surfaces is adapted, no study is hereby performed assessing position and geometry of the mirror

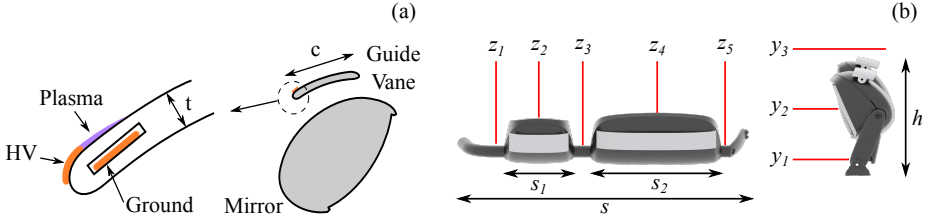


FIGURE 7.2: (a) Schematic of controlling elements (not to scale).  $c = 60\text{mm}$  and  $t = 5\text{mm}$ . (b) Measurement planes along the  $x-z$  and  $x-y$  planes. Note two mirror elements and the corresponding guide vanes placed atop.  $s = 90\text{cm}$ ,  $s_1 = 22\text{cm}$ ,  $s_2 = 41\text{cm}$  and  $h = 32\text{cm}$ .

body. The latter are prescribed by the industrial partner, considering European legislation regarding pedestrian safety and operator field of view blockage. The free stream velocity is set at  $U_\infty = 15\text{m/s}$ ,  $20\text{m/s}$  and the typical cruising speed of  $25\text{m/s}$ . Thus, the Reynolds numbers based on the mirror diameter range from  $Re_D = 1.9 \times 10^5$  to  $Re_D = 3.2 \times 10^5$ .

A two-component low-speed planar PIV system is employed for investigating the two-dimensional structure of the flow field (see section 2.1.2). Illumination is performed by a *Quantel EverGreen* laser system emitting green light ( $\lambda = 532\text{nm}$ ) at  $200\text{mJ}$  average energy per pulse. The beam is transformed to a sheet of approximate thickness of  $1\text{mm}$ . A *LaVision Imager Pro LX* camera with a 12-bit CCD sensor of  $4870 \times 3246$  pixels is used to image the illuminated region. The camera is equipped with a *Nikon* objective of  $135\text{mm}$  focal length, set at an aperture of  $f/5.6$ . Seeding is provided by a *SAFEX* smoke generator that produces vaporised water-glycol droplets of  $1\mu\text{m}$  diameter. Five hundred image pairs are recorded ( $\Delta t = 60\mu\text{s}$ ) and processed with the *LaVision DaVis 8.1* software package. The multi-step interrogation algorithm [147] is applied, from an initial window of  $48 \times 48$  pixels to a final of  $32 \times 32$  pixels, with 50% overlap between windows. The resulting vector spacing is  $1.5\text{mm}$  in both measurement plane directions. Velocity errors are calculated based on the description provided in section 2.1.2. The maximum error for both velocity components at each measurement realisation is of the order of 1%, which is reduced to 0.05% after time averaging.

## 7.3. DATA ANALYSIS AND DISCUSSION

### 7.3.1. BASELINE FLOW

The baseline flow is determined by time-averaging the processed images at each measurement plane shown in figure 7.2b, without the introduction of any control elements. Figures 7.3 and 7.4 depict the resulting flow fields at  $\alpha = 0^\circ$  and  $U_\infty = 25\text{m/s}$ . Masked regions correspond to locations where no velocity vectors are obtained due to shadowing or insufficient illumination.

Focusing on the  $x-y$  plane (figure 7.3), the following topological features are observed for both mirror elements. Two separation shear layers associated with flow separation are present, one above and one below each mirror. Separation at the

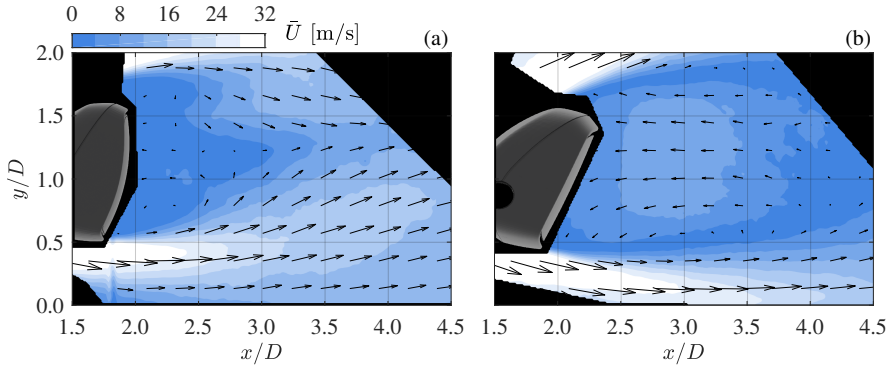


FIGURE 7.3: Baseline flow parallel to the  $x - y$  plane for  $\alpha = 0^\circ$  and  $U_\infty = 25\text{m/s}$ . Measurement planes: (a)  $z_2$  and (b)  $z_4$  (see figure 7.2b).

uppermost side of the mirror initiates before the flow reaches the end of the curved surface. In contrast, separation at the lower side is fixed at the end of the contour. The two separated shear layers contribute to the formation of a large wake behind each mirror, affecting the drag force and the downstream moving flow. Note that significant backflow is present in the wake of the large mirror element.

A strong jet forms in the gap between each mirror and the wall, whose velocity is of the order of  $30\text{m/s}$ . It contains significant momentum and, thus, ensures that the flow on the wall surface remains attached, at least within the imaged field of view. The strength of the jet and the derived pressure gradient at the lower shear layer regions lead to selecting the top surface of the mirror for positioning the control elements (figure 7.2).

The velocity field on the  $x - z$  plane (figure 7.4) demonstrates notable side effects, particularly on the  $y_1$  and  $y_2$  measurement planes. This is due to the presence of the supporting pillar that is mounted on the wall. Combined with the mirror elements, the geometry of the setup promotes three-dimensional effect. One of the outcomes is the kink observed in the top region of the small element wake (figure 7.3a). Due to the small element's narrow span, the mixing process and the consequent momentum recovery in the recirculation region is faster relative to the large element.

### 7.3.2. CONTROLLED FLOW

Flow control focuses on reducing the upper separation angle. The boundary layer on the mirror surface is turbulent and of variable thickness depending on the angle of attack, hence, may prove difficult to control solely by a plasma actuator. The introduction of a passive guide vane imposes a strong favourable pressure gradient that results in the formation of a jet. The latter delays boundary layer separation until the end of each mirror element curved surface. The disadvantage of the guide vane is that, above a certain angle of attack, flow separates from its leading edge. Since the boundary layer on the guide vane itself is laminar and thin prior to separation, it is possible to utilise the AC-DBD plasma actuator for altering the

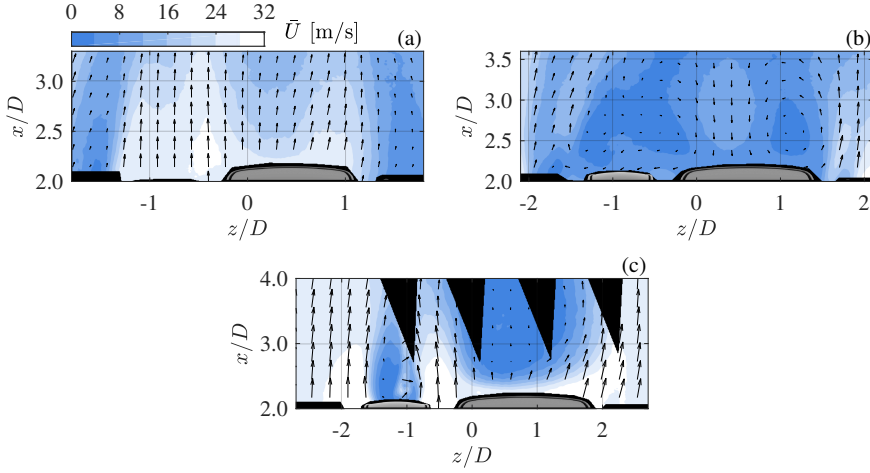


FIGURE 7.4: Baseline flow parallel to the  $x - z$  plane for  $\alpha = 0^\circ$  and  $U_\infty = 25\text{m/s}$ . Measurement planes: (a)  $y_1$ , (b)  $y_2$  and (c)  $y_3$  (see figure 7.2b).

transition characteristics of the separated shear layer by exploiting receptivity.

A preliminary study was carried out for determining the appropriate actuation frequency. It is widely acknowledged that the range of effective actuating dimensionless frequencies for flow control is of the order of unity [153]. The dimensionless frequency, or reduced frequency  $F^+$ , is defined as

$$F^+ = \frac{fL_s}{U_\infty}, \quad (7.1)$$

where  $f$  is the actuation frequency and  $L_s$  is the separation region length. A sweep of actuation frequencies demonstrates that the maximum wake reduction is obtained at  $f = 200\text{Hz}$ . The guide vane and the mirror form a single feedback system, thus, the performance of pulsed actuation cannot be directly compared with conventional cases such as airfoils [3]. This is due to the strong flow deflection and the large wake given the bluntness of the mirror. As a consequence, there is no straightforward definition of the separation length, hence,  $F^+$  is estimated based on the guide vane chord, yielding  $F^+ = 0.5$ .

This work aims at a proof of concept, hence, the analysis of the controlled flow focuses only on the large mirror element, on plane  $z_4$ . Time-averaged flow fields of the controlled cases obtained for all angles at  $U_\infty = 25\text{m/s}$  are provided in figure 7.5. The introduction of the guide vane and the operation of the plasma actuator change the separation angle and the magnitude of the backflow in the mirror wake. The jet formation and separation from the guide vane are evident in leeward conditions, marked by a circle in figure 7.5b.

Since no direct drag force measurements are performed, assessment and quantification of the controlling configuration are carried out by means of momentum

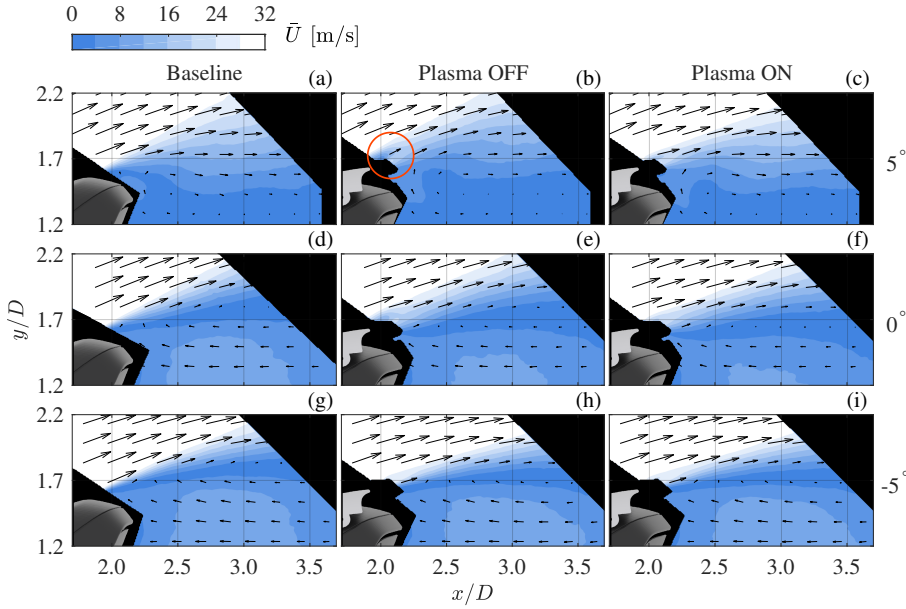


FIGURE 7.5: Time-averaged velocity fields for  $U_\infty = 25\text{m/s}$  at the  $z_4$  measurement plane. Top row:  $\alpha = 5^\circ$  (leeward), middle row:  $\alpha = 0^\circ$  and bottom row:  $\alpha = -5^\circ$  (windward). Columns from left to right: baseline conditions, guide vane only and hybrid control, respectively.

calculations. In general, momentum flux along a curve is given by

$$\dot{M}_c = \int_c \mathbf{U} \rho (\mathbf{U} \cdot \hat{n}) dS, \quad (7.2)$$

where  $\mathbf{U}$  is the velocity vector,  $\rho$  is the fluid density and  $\hat{n}$  the unit vector normal to  $\mathbf{U}$ . When the momentum across the  $y$ -axis is investigated, the above equation reduces to

$$\dot{M}_y = \int_{y_1}^{y_2} u \rho (u \cdot \hat{n}) dy. \quad (7.3)$$

For the experimental data at hand, profiles are selected at  $x/D = 2.6$ , between  $y_1/D = 1$  and  $y_2/D = 2.35$ . It is important to note that a complete momentum deficit study for a strongly three-dimensional flow, such as the one presented, would require volumetric velocity or balance measurements. This was not possible to perform due experimental limitations, thus, the two-dimensional momentum deficit estimations are used as an indicator of the performance of different configurations.

The percentile momentum difference between the baseline flow and the controlled flow is provided in table 7.1 for all experimental cases. The introduction of the guide vane (plasma OFF) is found to be favourable in all cases other than leeward inflow conditions ( $\alpha = 5^\circ$ ), where excessive separation occurs. This disadvantage may be reduced by careful shaping of the guide vane. Nonetheless, by switching on

TABLE 7.1: Percentile momentum and deflection angle change with respect to the baseline on plane  $z_4$ . Momentum is estimated at  $x/D = 2.6$  and  $1 < y/D < 2.35$ . Deflection angle is obtained at  $x/D = 2.8$  and  $y/D = 2.3$

$\alpha$ [°]	$U_\infty$ [m/s]	Plasma OFF $\Delta M_y$ [%]	Plasma ON $\Delta M_y$ [%]	Plasma OFF $\Delta \alpha_d$ [°]	Plasma ON $\Delta \alpha_d$ [°]
5	15	-17.6	24.1	-0.2	-3.3
	20	-15.8	15.6	-1.3	-3.2
	25	-19.5	6.2	-1.0	-2.7
0	15	34.3	67.2	-3.8	-5.4
	20	27.1	45.1	-2.5	-3.7
	25	7.1	28.8	-1.7	-3.0
-5	15	26.6	29.8	-3.4	-3.4
	20	23.9	23.5	-2.8	-2.6
	25	17.4	16.8	-2.0	-2.1

the plasma actuator, momentum recovery is observed, especially at lower speeds. For the specific case of windward conditions ( $\alpha = -5^\circ$ ), actuation does not result in any noticeable improvement as the favourable pressure gradient effect is preventing separation on the guide vane. Similar conclusions are drawn from the change in deflection angle,  $\alpha_d$  (table 7.1). The latter has been estimated at a downstream location outside the separation region ( $x/D = 2.8$  and  $y/D = 2.3$ ) and is defined as the angle of the velocity vector with respect to the  $x$ -axis. The deflection angle is reduced by the introduction of the guide vane for all cases, even for leeward conditions. Similar to momentum, at windward conditions, no considerable change in deflection angle is observed.

Considering that a truck has two side mirrors, the above imply that only the leeward side plasma actuator needs to be operational above a certain angle of attack, reducing the required energy investment. In addition, both leeward and windward momentum changes must be taken into account for estimating the total effect. Hence, for  $U_\infty = 25\text{m/s}$  and  $5^\circ$  absolute angle of attack, a total of 23% increase of momentum is achieved in the wake of the large mirror element (measurement plane  $z_4$ ). The reduction of the deflection angle and the resulting momentum recovery suggests that the inflow to any controlling elements placed downstream of the mirror may operate more efficiently, thus, impacting the total drag coefficient.

The effect of the actuator on the mixing process becomes prevalent in the Reynolds stress fields shown in figure 7.6. In the absence of any control device (figure 7.6a) evidence of mixing begins at a distance from the mirror surface, marked by a cross at approximately  $x/D = 2.25$ . and  $y/D = 1.75$ . In contrast, for both of the controlled cases, mixing processes begin much earlier, already on the guide vane. For the actuated case, pulsing at 200Hz causes earlier transition of the separated shear layer and, thus, substantial mixing is visible at the trailing edge of the guide vane. As a consequence, momentum redistribution initiates earlier, minimising the wake of the mirror.

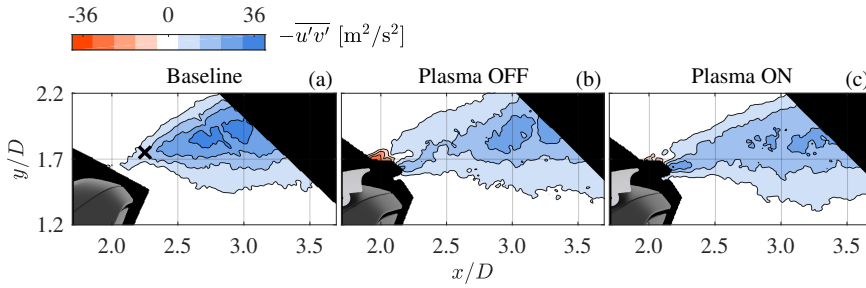


FIGURE 7.6: Reynolds stress fields for baseline and controlled configurations at  $\alpha = 0^\circ$  and  $U_\infty = 25\text{m/s}$  on measurement plane  $z_4$ .

### 7.3.3. POWER CONSIDERATIONS

Assessment of the energy consumption of the AC-DBD plasma actuator is performed by monitoring voltage and current signals by means of an oscilloscope. The average power is estimated based on equation 2.6. Calculation over a 1s time interval yields an average power of 7.7W in continuous operation for an actuator of 30cm length (25.7W/m). This suggests that for a complete set of plasma actuators for both mirrors and mirror elements ( $2 \times (30 + 15)\text{cm}$ ), the power required is of the order of 25W for continuous discharge. In turn, at 25% duty cycle modulation, the power consumption drops to approximately 6W. This is a very low requirement that can be met by the low-voltage circuit of transport trucks. Note that the total power consumption of the actuator system is dependent on the high voltage amplification circuitry. Therefore, for a transport truck cruising at a speed of 25m/s, drag reduction of less than 1N would be sufficient to balance the power requirement of the actuators operating in a modulated fashion at 200Hz. Any drag reduction above this value would constitute net gain.

## 7.4. CONCLUDING REMARKS

IN THIS CHAPTER, an experimental study is discussed, aimed at investigating a hybrid flow control concept. The wake of a full-scale transport truck side mirror is reduced by means of a passive guide vane and an active AC-DBD plasma actuator. Velocity data are acquired by means of low-speed PIV for different free stream velocities and angles of attack. A comparison case is made between the reference flow field and two controlling configurations: guide vane only and guide vane with plasma actuation.

The time-averaged baseline flow fields indicate the strong three-dimensional nature of the flow around the mirror. Nonetheless, a two-dimensional analysis on the PIV planes is sufficient for evaluating the performance of the different configurations. The analysis performed on the time-averaged velocity fields of the controlled flow demonstrates that by using the guide vane only, improvement is possible at lower free stream velocities. The introduction of the plasma actuator eliminates any adverse effects of the guide vane at leeward conditions, at least within the range of angles tested. Careful shaping of the guide vane can be performed for increasing the range

of angles of attack as well as for increasing the effectiveness of the AC-DBD.

At windward conditions, the pressure gradient imposed by the flow on the guide vane is sufficient to eliminate any flow separation. Consequently, no significant change is observed with the operation of the plasma actuator. Hence, the activation of the windward plasma actuator is not necessary, reducing the total power requirement for a given angle of attack.

The comparison to the baseline flow of the two control configurations on the large mirror element (plane  $z_4$ ) yields a momentum increase of the order of 17% and a deflection angle reduction of  $2^\circ$  at  $U_\infty = 25\text{m/s}$  and windward conditions ( $\alpha = -5^\circ$ ). In contrast, at leeward conditions ( $\alpha = 5^\circ$ ), the guide vane reduces momentum by 20% and deflection angle by 1 deg. However, with the application of the AC-DBD, a momentum increase of approximately 6% is achieved with a reduction of 2.7 deg of the deflection angle. Due to the strong three-dimensional nature of the flow, the aforementioned quantities serve as an indication of the overall performance of the control system.

The deflection angle reduction and the consequent momentum recovery are expected to have an impact on the total drag of the truck. This is due to the expansion of the wake along the length of the trailer which, if reduced, inflow conditions for any ancillary control devices that are located downstream the mirror are improved. Since it is not practical to measure the drag forces of a full truck in a wind tunnel and confidence in such computations varies, a field test with the controlling configurations is necessary for concluding on fuel consumption savings.

# 8

## CONCLUSIONS AND RECOMMENDATIONS

*A selection of the most important findings are hereby provided, along with a few recommendations for future work.*

## 8.1. ON LAMINAR SEPARATION BUBBLES

IN AN EFFORT to provide insight into both flapping and bursting mechanisms of a short, flat plate laminar separation bubble, the boundary layer is impulsively forced by means of a spanwise uniform AC-DBD plasma actuator (see chapter 3 and Michelis *et al.* [114]). The impulsive disturbance undergoes selective amplification, forming a convectively unstable wave packet that assumes the frequency of the primary Kelvin-Helmholtz instability of the separated shear layer.

An important observation is that the bubble begins to shrink once the disturbance interacts with the reattachment region. The percentile size reduction of the separation bubble is dependent on the disturbance amplitude. However, this is not the case for the bubble relaxation time to its unforced state, which is shown to remain invariant regardless of the disturbance input. Bursting is identified as an elongation of the bubble between the disturbance convection and relaxation, and is associated with stabilisation of the bubble.

Quasi-steady linear stability analysis demonstrates that the growth rate and the frequency of the most unstable mode decrease for increasing disturbance amplitude. The same behaviour is observed for the boundary layer integral parameters. Consequently, a linear relation is found between growth rate and shape factor. In addition, in line with direct observations on the bubble size, stability changes ensue only when disturbances interact with reattachment. This is evident from direct measurements as well as from linear stability analysis.

The above confirm that both flapping and bursting mechanisms are due to the same feedback loop. Disturbances interacting with reattachment cause variation of the mean flow and, thus, of the stability characteristics of the shear layer. This causes the transition location to shift, affecting the amplification of following disturbances, thus, closing the loop.

Investigation of the natural bubble with three-dimensional measurements demonstrates that the shear layer rollup process consists of spanwise-staggered vortex cores (see chapter 4 and Michelis *et al.* [116]). This spanwise topology does not significantly vary throughout the measurement intervals. Consequently, a consistent streamwise to spanwise wavelength ratio is established, approximately 1:2. Linear stability analysis suggests that normal and oblique modes in the boundary layer upstream of the separation bubble develop with comparable amplification. The observed pattern is, therefore, associated with the superposition between normal and oblique modes prior to separation. The ensuing dynamics are, thus, dependent on the relative amplitude of these modes. This is confirmed by two-dimensional forcing of the boundary layer with which the normal mode is promoted and spanwise uniformity is increased.

Similar conclusions are drawn from studying the laminar separation bubble on a NACA 0018 airfoil under natural conditions and continuous two-dimensional forcing (see chapter 5 and Michelis *et al.* [115]). In the unforced case, though dominant modes are monochromatic, spanwise modulation is evident. When periodically forcing, the shedding process locks to a single mode that coincides with the forcing frequency while the bubble size decreases. Strikingly, spanwise deformation of dominant structures persists.

The aforementioned considerations point out that the answer to the observed three-dimensional topology in the aft portion of laminar separation bubbles lies in the receptivity of the boundary layer. It is expected that the interaction of modes in this region is then amplified by the separated shear layer, however, the measurements performed were not suitable for such investigations.

Further expanding our understanding of transition phenomena such as oblique transition and subharmonic resonance and how they interact with shear layers is necessary. Given the small scale of relevant disturbance amplitudes, direct measurements are cumbersome, therefore, the possibility of a combined numerical and experimental approach should be explored. Within this framework, it is suggested that a study regarding the positioning and type of forcing (i.e. streamwise location and spanwise modulation) can give conclusions related to the possibility of manipulation of spanwise wavelengths in separation bubbles.

Although laminar separation bubbles on flat plates exhibit similar characteristics to the ones on airfoils, there is no dedicated study treating their differences. More specifically, given the demonstrated sensitivity of the bubble stability to incoming flow conditions, it is expected that shedding in the trailing edge of airfoils and the consequent fluctuation of the leading edge stagnation point conditions the primary KH mode characteristics. In addition, flat plate LSBs do not account for the influence of curvature variations.

In general it has been shown that plasma actuators are a suitable diagnostic tool due to their flexibility, response and accuracy when it comes to temporal specifications of forcing. With the emergence of new techniques for their manufacture, such as printing on the dielectric, forcing may be applied in fashions superiorly exotic in comparison to the simple two-dimensional forcing presented in this work. More specifically, tailored spatial distribution in both streamwise and spanwise directions can be a great aid in elucidating physical mechanisms of not only separation bubbles but transitional phenomena as a whole, thus expanding the boundaries of efficient and effective flow control.

A few recommendations may be suggested regarding data acquisition. Particle Image Velocimetry has been proven successful for the investigation of laminar separation bubbles on both flat plates and airfoils. However, time-resolved PIV measurements suffer from spatial resolution, particularly when linear stability analysis in spatial formulation and tomographic measurements are considered. In conjunction with preliminary experiments carried out that are not presented in this thesis, low-speed PIV is deemed more appropriate in order to boost both spatial resolution, illumination intensity and, uncorrelated in time, measurement realisations for statistics. In cases where impulsive forcing is employed, measurements may be carried out by phase-locking the PIV system with respect to the pulse.

## 8.2. ON BLUFF BODY PASSIVE SEPARATION CONTROL

**I**NTRODUCING a static cylinder in the vicinity of leading edge separation from a bluff body significantly affects the flow topology, in both statistical and dynamic terms (see chapter 6 and Michelis & Kotsonis [113]). Shifting the cylinder with respect to the leading edge of the bluff body results in variation of the pressure

gradient field. Two cases are identified depending on whether the cylinder front is located upstream or downstream with respect to the bluff body leading edge.

In the first case, separation is promoted with the gap jet being deflected towards the cylinder. As the distance of the cylinder from the wall decreases, the bubble size increases creating blockage and, thus, resulting in higher cylinder Strouhal number. In addition, vortex shedding from the separation bubble becomes phase-locked with the cylinder shedding. Moreover, it is demonstrated that the bubble flapping mode dominates over shedding modes when the cylinder is located close to the surface at this streamwise position. This is a direct consequence of vortex merging of vortices shed from the bubble and the cylinder's lower shear layer, an interaction that is not observed at larger distances of the cylinder from the wall.

In turn, when the cylinder is placed downstream of the bluff body leading edge, its favourable pressure gradient eliminates separation. At this streamwise position, reduction of the distance between the cylinder and the wall results in lower Strouhal number in comparison to the ones reported in studies of wall-bounded cylinders. This behaviour is attested to the absence of an adequately thick boundary layer. In addition, for small gaps, the primary instability in the aft part of the cylinder transforms from absolute to convective. Consequently, the decreased feedback reduces the mixing strength, thus elongating the cylinder wake.

An important parameter that was not sufficiently explored in the presented study is the feedback effect of the bluff body trailing edge shedding. It is well assessed that the latter is dependent on the bluff body thickness and length. Given the strong pressure gradients present in bluff body flows, it is likely that the dynamics of the separation bubble are influenced, forming an absolutely unstable system. In the presence of a cylinder, an additional factor is introduced which consists of the trace from the cylinder shedding reaching the bluff body trailing edge. In order to examine such phenomena, synchronised measurements in both the leading and trailing edges are required.

### 8.3. ON HYBRID SEPARATION CONTROL

THE COMBINATION of a passive guide vane and an active AC-DBD plasma actuator is proven to be a successful scheme for reducing the wake of a full-scale transport truck side view mirror (see chapter 7 and Michelis & Kotsonis [112]). In essence, with this solution, the problem of separation from the mirror's unreceptive turbulent boundary layer is shifted to the receptive laminar boundary layer of the guide vane. The transition characteristics of the latter can be exploited by the plasma actuator in order to promote momentum recovery in the wake. In order to properly assess the effectiveness of the proposed hybrid control system, road tests are necessary. However, contemporary full scale tests are restricted to total vehicle fuel consumption, thus, the effect of a single device is within measurement uncertainty limits. Development of adequate techniques of on-site aerodynamic performance assessment is, therefore, required. Finally, the proposed solution is not restricted to the side view mirror problem. Instead it may be expanded to any application where extensive leading edge separation occurs, such as the case of gusts in wind turbines.

# BIBLIOGRAPHY

- [1] ADRIAN, R.J. & WESTERWEEL, J. 2011 *Particle Image Velocimetry*. Cambridge University Press.
- [2] ALAM, M. & SANDHAM, N.D. 2000 Direct numerical simulation of “short” laminar separation bubble with turbulent reattachment. *Journal of Fluid Mechanics* **410**, 1–28.
- [3] AMITAY, M., SMITH, D.R., KIBENS, V., PAREKH, D.E. & GLEZER, A. 2001 Aerodynamic flow control over an unconventional airfoil using synthetic jet actuators. *AIAA Journal* **39** (3), 361–370.
- [4] ATKINSON, C. & SORIA, J. 2009 An efficient simultaneous reconstruction technique for tomographic particle image velocimetry. *Experiments in Fluids* **47**, 553–568.
- [5] BAINES, P.G., MAJUMDAR, S.J. & MITSUDERA, H. 1996 The mechanics of Tollmien-Schlichting waves. *Journal of Fluid Mechanics* **312**, 107–124.
- [6] BAKE, S., MEYER, D.G.W. & RIST, U. 2002 Turbulence mechanism in Klebanoff transition: a quantitative comparison of experiment and direct numerical simulation. *Journal of Fluid Mechanics* **459**, 217–243.
- [7] BEARMAN, P.W. & ZDRAVKOVICH, M.M. 1978 Flow around a circular cylinder near a plane boundary. *Journal of Fluid Mechanics* **89**, 33–47.
- [8] BENARD, N. & MOREAU, E. 2014 Electrical and mechanical characteristics of surface AC dielectric barrier discharge plasma actuators applied to airflow control. *Experiments in Fluids* **55** (11).
- [9] BERKOOZ, G., HOLMES, P. & LUMLEY, J.L. 1993 The Proper Orthogonal Decomposition in the Analysis of Turbulent Flows. *Annual Review of Fluid Mechanics* **25**, 539–575.
- [10] BERLIN, S., WIEGEL, M. & HENNINGSON, D.S. 1999 Numerical and experimental investigations of oblique boundary layer transition. *Journal of Fluid Mechanics* **393**, 23–57.
- [11] BIMBATO, A.M., PEREIRA, L.A.A. & HIRATA, M.H. 2013 Suppression of vortex shedding on a bluff body. *Journal of Wind Engineering and Industrial Aerodynamics* **121**, 16–28.
- [12] BOIKO, A.V., GREK, G.R., DOVGAL, A.V. & KOZLOV, V.V. 2002 *The origin of Turbulence in Near-Wall Flows*. Springer.
- [13] BOUTILIER, M.S.H. & YARUSEVYCH, S. 2012 Separated shear layer transition over an airfoil at a low Reynolds number . *Physics of Fluids* **24** (084105).
- [14] BREVDO, L. & BRIDGES, T.J. 1997 Local and global instabilities of spatially developing flows: cautionary examples. *Proceedings of the Royal Society of London A*:

- Mathematical, Physical and Engineering Sciences* **453** (1962), 1345–1364.
- [15] BRIDGES, T.J. & MORRIS, P.J. 1984 Differential eigenvalue problems in which the parameter appears nonlinearly. *Journal of Computational Physics* **55**, 437–460.
- [16] BRINKERHOFF, J. R. & YARAS, M. I. 2011 Interaction of viscous and inviscid instability modes in separation-bubble transition. *Physics of Fluids* **23**, 124102.
- [17] BRINKERHOFF, J. R. & YARAS, M. I. 2015 Numerical investigation of transition in a boundary layer subjected to favourable and adverse streamwise pressure gradients and elevated free stream turbulence. *Journal of Fluid Mechanics* **781**, 52–86.
- [18] BURGMANN, S., BRÜCKER, C. & SCHRÖDER, A. 2006 Scanning PIV measurements of a laminar separation bubble. *Experiments in Fluids* **41**, 319–326.
- [19] BURGMANN, S., DANNEMANN, J. & SCHRÖDER, A. 2008 Time-resolved and volumetric PIV measurements of a transitional separation bubble on an SD7003 airfoil. *Experiments in Fluids* **44**, 609–622.
- [20] BURGMANN, S. & SCHRÖDER, A. 2008 Investigation of the vortex induced unsteadiness of a separation bubble via time-resolved and scanning PIV measurements. *Experiments in Fluids* **45**, 675–691.
- [21] CARMICHAEL, B.H. 1981 Low Reynolds Number Airfoil Survey. *Tech. Rep.* 165803, Vol. I. NASA.
- [22] CARPENTIER, J. 1901 Improvements in enlarging or like cameras. GB Patent No. 1139. Filed 17 January 1901.
- [23] CHERRY, N.J., HILLIER, R. & LATOUR, M.E.M.P. 1984 Unsteady measurements in a separated and reattaching flow. *Journal of Fluid Mechanics* **144**, 13–46.
- [24] CHOI, H., LEE, J. & PARK, H. 2014 Aerodynamics of heavy vehicles. *Annual Review of Fluid Mechanics* **46**, 441–468.
- [25] COHEN, J., BREUER, K.S. & HARITONIDIS, J.S. 1991 On the evolution of a wave packet in a laminar boundary layer. *Journal of Fluid Mechanics* **225**, 575–606.
- [26] COOPER, KEVIN R. & LEUSCHEN, JASON 2005 Model and full-scale wind tunnel tests of second-generation aerodynamic fuel saving devices for tractor-trailers. In *Commercial Vehicle Engineering Congress and Exhibition*. Chicago, IL, United States.
- [27] CORDIER, L. & BERGMANN, M. 2003 Proper Orthogonal Decomposition: an overview. In *Advanced post-processing of experimental and numerical data*. Lecture series, Von Kármán Institute for Fluid Dynamics.
- [28] CORKE, T.C., ENLOE, C.L. & WILKINSON, S.P. 2010 Dielectric barrier discharge plasma actuators for flow control. *Annual Review of Fluid Mechanics* **42**, 505–529.
- [29] CORKE, T.C. & MANGANO, R.A. 1989 Resonant growth of three-dimensional modes in transitioning Blasius boundary layers. *Journal of Fluid Mechanics* **209**, 93–150.
- [30] CORREALE, G., AVALLONE, F. & STARIKOVSKIY, A.Y. 2016 Experimental method to quantify the efficiency of the first two operational stages of nanosecond dielectric barrier discharge plasma actuators. *Journal of Physics D: Applied Physics* **49** (50).

- 
- [31] CORREALE, G., MICHELIS, T., RAGNI, D., KOTSONIS, M. & SCARANO, F. 2014 Nanosecond-pulsed plasma actuation in quiescent air and laminar boundary layer. *Journal of Physics D: Applied Physics* **47** (10), 105201.
- [32] CRAIK, A.D.D. 1971 Non-linear resonant instability in boundary layers. *Journal of Fluid Mechanics* **50**, 393–413.
- [33] DAUBECHIES, I. 1992 *Ten Lectures on Wavelets*, CBMS-NSF Regional Conference Series in Applied Mathematics, vol. 61. SIAM.
- [34] DEANE, A.E., KEVREKIDIS, I.G., KARNIADAKIS, G.E. & ORSZAG, S.A. 1991 Low-dimensional models for complex geometry flows: Application to grooved channels and circular cylinders. *Physics of Fluids A* **3** (10), 2337–2354.
- [35] DIWAN, S.S. & RAMESH, O.N. 2009 On the origin of the inflectional instability of a laminar separation bubble. *Journal of Fluid Mechanics* **629**, 263–298.
- [36] DOLIGALSKI, T.L., SMITH, C.R. & WALKER, J.D.A. 1994 Vortex interactions with walls. *Annual Review of Fluid Mechanics* **26** (1), 573–616.
- [37] DOVGAL, A.V. & BOIKO, A.V. 1994 Effect of harmonic excitation on instability of a laminar separation bubble on an airfoil. In *Laminar-Turbulent Transition* (ed. H.F. Fasel & W.S. Saric), pp. 675–680. Springer.
- [38] DOVGAL, A.V., KOZLOV, V.V. & MICHALKE, A. 1994 Laminar boundary layer separation: Instability and associated phenomena. *Progress in Aerospace Sciences* **30** (1), 61–94.
- [39] EATON, J.K. & JOHNSTON, J.P. 1982 Low frequency unsteadiness of a reattaching turbulent shear layer. In *Turbulent Shear Flows 3*, pp. 162–170. Springer Berlin Heidelberg.
- [40] ELSINGA, G.E., SCARANO, F., WIENEKE, B. & VAN OUDHEUSDEN, B.W. 2006 Tomographic particle image velocimetry. *Experiments in Fluids* **41**, 933–947.
- [41] ELSINGA, G.E., WESTERWEEL, J., SCARANO, F. & NOVARA, M. 2011 On the velocity of ghost particles and the bias errors in Tomographic-PIV. *Experiments in Fluids* **50** (4), 825–838.
- [42] FARGE, M. 1992 Wavelet transforms and their applications to turbulence. *Annual Review of Fluid Mechanics* **24**, 395–457.
- [43] FEY, U., KÖNIG, M. & ECKELMANN, H. 1998 A new Strouhal-Reynolds-number relationship for the circular cylinder in the range  $47 < Re < 2 \times 10^5$ . *Physics of Fluids* **10**, 1547–1549.
- [44] FRIDMAN, A. 2008 *Plasma Chemistry*. Cambridge University Press.
- [45] GAD-EL-HAK, M. 2007 *Flow Control: Passive, Active and Reactive Flow Management*, 1st edn. Cambridge University Press.
- [46] GAD-EL-HAK, M., POLLARD, A. & BONNET, J.-P., ed. 1998 *Flow Control: Fundamentals and Practices*, 1st edn., *Lecture Notes in Physics Monographs*, vol. 53. Springer.
- [47] GASTER, M. 1967 The Structure and Behaviour of Laminar Separation Bubbles. *Tech.*

- Rep. 3595. Aeronautical Research Council Reports and Memoranda.
- [48] GASTER, M. 1992 Stability of velocity profiles with reverse flow. In *Instability, Transition, and Turbulence* (ed. M.Y. Hussaini, A. Kumar & C.L. Streett), *ICASE NASA LaRC*, vol. 1, pp. 212–215. New York: Springer.
- [49] GASTER, M. & GRANT, I. 1975 An experimental investigation of the formation and development of a wave packet in a laminar boundary layer. *Proceedings of the Royal Society of London A: Mathematical, Physical and Engineering Sciences* **347**, 253–269.
- [50] GHAEMI, S. & SCARANO, F. 2010 Multi-pass light amplification for tomographic particle image velocimetry applications. *Measurement Science and Technology* **21** (12), 127002.
- [51] GLEZER, A. & AMITAY, M. 2002 Synthetic jets. *Annual Review of Fluid Mechanics* **34**, 503–529.
- [52] GRASS, A.J., RAVEN, P.W.J., STUART, R.J. & BRAY, J.A. 1984 Influence of boundary layer velocity gradients and bed proximity on vortex shedding from free spanning pipelines. *Journal of Energy Resources Technology, Transactions of the ASME* **106** (1), 70–78.
- [53] GRUNDMANN, S. & TROPEA, C. 2008 Active cancellation of artificially introduced Tollmien-Schlichting waves using plasma actuators. *Experiments in Fluids* **44**, 795–806.
- [54] HÄGGMARK, C.P., HILDINGS, C. & HENNINGSON, D.S. 2001 A numerical and experimental study of a transitional separation bubble. *Aerospace Science and Technology* **5** (5), 317–328.
- [55] HAIN, R., KÄHLER, C.J. & RADESPIEL, R. 2009 Dynamics of laminar separation bubbles at low-Reynolds-number aerofoils. *Journal of Fluid Mechanics* **630**, 129–153.
- [56] HERBERT, T. 1988 Secondary instability of boundary layers. *Annual Review of Fluid Mechanics* **20**, 487–526.
- [57] HILLIER, R. & CHERRY, N.J. 1981 The effects of stream turbulence on separation bubbles. *Journal of Wind Engineering and Industrial Aerodynamics* **8** (1172), 49–58.
- [58] HIRST, T., LI, C., BRANDS, E. & ZHA, G. 2015 Bluff body drag reduction using passive flow control of jet boat tail. *SAE International Journal of Commercial Vehicles* **8** (2), 713–721.
- [59] HO, C.M. & HUERRE, P. 1984 Perturbed free shear layers. *Annual Review of Fluid Mechanics* **16**, 365–424.
- [60] HOURIGAN, K., THOMPSON, M.C. & TAN, B.T. 2001 Self-sustained oscillations in flows around long blunt plates. *Journal of Fluids and Structures* **15** (3174), 387 – 398.
- [61] HUNT, J.C.R., WRAY, A.A. & MOIN, P. 1988 Eddies, Stream, and Convergence Zones in Turbulent Flows. *Tech. Rep. CTR-S88*. Center For Turbulence Research.
- [62] VAN INGEN, J.L. 2008 The  $e^N$  method for transition prediction. Historical review of work at TU Delft. In *38th Fluid Dynamics Conference and Exhibit*. Seattle, WA.
- [63] VAN INGEN, J.L. & KOTSONIS, M. 2011 A two-parameter method for  $e^N$  transition

- prediction. In *6th AIAA Theoretical Fluid Mechanics Conference*. Honolulu, HI.
- [64] JACOBS, R. G. & DURBIN, P. A. 2001 Simulations of bypass transition. *Journal of Fluid Mechanics* **428**, 185–212.
- [65] JONES, L.E., SANDBERG, R.D. & SANDHAM, N.D. 2010 Stability and receptivity characteristics of a laminar separation bubble on an aerofoil. *Journal of Fluid Mechanics* **648**, 257–296.
- [66] JONES, L.E., SANDBERGH, R.D. & SANDHAM, N.D. 2008 Direct numerical simulation of forced and unforced separation bubbles on an airfoil at incidence. *Journal of Fluid Mechanics* **602**, 175–207.
- [67] KACHANOV, Y.S. 2000 Three-dimensional receptivity of boundary layers. *European Journal of Mechanics, B/Fluids* **19** (5), 723–744.
- [68] KACHANOV, Y.S. & LEVCHENKO, V.Y. 1984 The resonant interaction of disturbances at laminar-turbulent transition in a boundary layer. *Journal of Fluid Mechanics* **138**, 209–247.
- [69] KÄHLER, C.J., SCHARNOWSKI, S. & CIERPKA, C. 2012 On the resolution limit of digital particle image velocimetry. *Experiments in Fluids* **52**, 1629–1639.
- [70] KENNEY, K.F. & KEEPING, E.S. 1962 *Mathematics of Statistics part I*, 3rd edn. Van Nostrand.
- [71] VON KERCZEK, C. & DAVIS, S.H. 1974 Linear stability theory of oscillatory stokes layers. *Journal of Fluid Mechanics* **62**, 753–773.
- [72] KING, R.A. & BREUER, K.S. 2002 Oblique transition in a laminar Blasius boundary layer. *Journal of Fluid Mechanics* **453**, 177–200.
- [73] KIRK, T. M. & YARUSEVYCH, S. 2017 Vortex shedding within laminar separation bubbles forming over an airfoil. *Experiments in Fluids* .
- [74] KIYA, M. & SASAKI, K. 1983 Structure of a turbulent separation bubble. *Journal of Fluid Mechanics* **137**, 83–113.
- [75] KIYA, M. & SASAKI, K. 1985 Structure of large-scale vortices and unsteady reverse flow in the reattaching zone of a turbulent separation bubble. *Journal of Fluid Mechanics* **154**, 463–491.
- [76] KLEBANOFF, P.S., TIDSTROM, K.D. & SARGENT, L.M. 1962 The three-dimensional nature of boundary-layer instability. *Journal of Fluid Mechanics* **12**, 1–34.
- [77] KOGELSCHATZ, U. 2002 Filamentary, patterned, and diffuse barrier discharges. *IEEE Transactions on Plasma Science* **30**, 1400–1408.
- [78] KOLÁŘ, V. 2007 Vortex identification: New requirements and limitations. *International Journal of Heat and Fluid Flow* **28** (4), 638–652.
- [79] KOTSONIS, M. 2015 Diagnostics for characterisation of plasma actuators. *Measurement Science and Technology* **26** (9), 092001.
- [80] KOTSONIS, M., GHAEMI, S., VELDHIJUS, L.L.M. & SCARANO, F. 2011 Measurement of the body force field of plasma actuators. *Journal of Physics D: Applied Physics*

- 44** (4), 045204.
- [81] KOTSONIS, M., SHUKLA, R.M. & PRÖBSTING, S. 2015 Control of Natural Tollmien-Schlichting Waves using Dielectric Barrier Discharge Plasma Actuators. *International Journal of Flow Control* **7** (1+2), 37–54.
- [82] KOZLOV, V.V. & RYZHOV, O.S. 1990 Receptivity of boundary layers: asymptotic theory and experiment. *Proceedings of the Royal Society of London A: Mathematical, Physical and Engineering Sciences* **429**, 341–373.
- [83] KURELEK, J.W., LAMBERT, A.R. & YARUSEVYCH, S. 2016 Coherent Structures in the Transition Process of a Laminar Separation Bubble. *AIAA Journal* **54** (8), 2295–2309.
- [84] KURELEK, J.W. & YARUSEVYCH, S. 2016 The effect of acoustic excitation on the later stages of transition in a laminar separation bubble. In *46th AIAA Fluid Dynamics Conference*.
- [85] LAMBALLAIS, E., SILVESTRINI, J. & LAIZET, S. 2008 Direct numerical simulation of a separation bubble on a rounded finite-width leading edge. *International Journal of Heat and Fluid Flow* **29** (3), 612 – 625.
- [86] LAMBALLAIS, E., SILVESTRINI, J. & LAIZET, S. 2010 Direct numerical simulation of flow separation behind a rounded leading edge: Study of curvature effects. *International Journal of Heat and Fluid Flow* **31** (3), 295–306.
- [87] LANG, M., RIST, U. & WAGNER, S. 2004 Investigations on controlled transition development in laminar separation bubble by means of LDA and PIV. *Experiments in Fluids* **36**, 43–52.
- [88] LANGMUIR, I. 1928 Oscillations in Ionized Gases. *Proceedings of the National Academy of Sciences of the United States of America* **14** (8), 627–637.
- [89] LAROUSSE, M., ALEXEFF, I., RICHARDSON, J.P. & DYER, F.F. 2002 The resistive barrier discharge. *IEEE Transactions on Plasma Science* **30** (1 I), 158–159.
- [90] LARSEN, A., ESDAHL, S., ANDERSEN, J.E. & VEJRUM, T. 2000 Storebælt suspension bridge - vortex shedding excitation and mitigation by guide vanes. *Journal of Wind Engineering and Industrial Aerodynamics* **88** (2-3), 283–296.
- [91] LASHERAS, J.C. & CHOI, H. 1988 Three-dimensional instability of a plane free shear layer: an experimental study of the formation and evolution of streamwise vortices. *Journal of Fluid Mechanics* **189**, 53–86.
- [92] LEBLANC, P., BLACKWELDER, R. & LIEBECK, R. 1989 A comparison between boundary layer measurements in a laminar separation bubble flow and linear stability theory calculations. In *Low Reynolds Number Aerodynamics* (ed. T.J. Mueller), *Lecture Notes in Engineering*, vol. 54, pp. 189–205. Berlin, Heidelberg: Springer.
- [93] LEI, C., CHENG, L. & KAVANAGH, K. 1999 Re-examination of the effect of a plane boundary on force and vortex shedding of a circular cylinder. *Journal of Wind Engineering and Industrial Aerodynamics* **80** (3), 263–286.
- [94] LENGANI, D., SIMONI, D., UBALDI, M. & ZUNINO, P. 2014 POD analysis of the unsteady behavior of a laminar separation bubble. *Experimental Thermal and Fluid*

*Science* **58**, 70–79.

- [95] LI, Y.S. & CUMPTSY, N.A. 1991 Mixing in axial flow compressors: Part II - Measurements in a single-stage compressor and a duct. *ASME Journal of Turbomachinery* **113** (2), 166–174.
- [96] LIN, J.C. 2002 Review of research on low-profile vortex generators to control boundary-layer separation. *Progress in Aerospace Sciences* **38**, 389–420.
- [97] LIN, N., REED, H.L. & SARIC, W.S. 1992 Effect of leading-edge geometry on boundary-layer receptivity to freestream sound, Instability, Transition and Turbulence. In *Instability, Transition, and Turbulence* (ed. M.Y. Hussaini, A. Kumar & C.L. Streett), *ICASE NASA LaRC*, vol. 1, pp. 421–440. New York: Springer-Verlag.
- [98] LIN, W.J., LIN, C., HSIEH, S.C. & DEY, S. 2009 Flow characteristics around a circular cylinder placed horizontally above a plane boundary. *Journal of Engineering Mechanics* **135** (7), 697–716.
- [99] LISSAMAN, P.B.S. 1983 Low-Reynolds-Number airfoils. *Annual Review of Fluid Mechanics* **15**, 223–239.
- [100] LITTLE, J., NISHIHARA, M., ADAMOVICH, I. & SAMIMY, M. 2010 High-lift airfoil trailing edge separation control using a single dielectric barrier discharge plasma actuator. *Experiments in Fluids* **48** (3).
- [101] MACK, L.M. 1984 Boundary-layer linear stability theory. *Tech. Rep.* 709. AGARD.
- [102] MARKS, C.H. & BUCKLEY, F.T. 1978 A wind-tunnel study of the effect of turning vanes on the aerodynamic drag of tractor-trailer trucks. *ASME Journal of Fluids Engineering* **100** (4), 439–442.
- [103] MARXEN, O. & HENNINGSON, D.S. 2011 The effect of small-amplitude convective disturbances on the size and bursting of a laminar separation bubble. *Journal of Fluid Mechanics* **671**, 1–33.
- [104] MARXEN, O., KOTAPATI, R.B., MITAL, R. & ZAKI, T. 2015 Stability analysis of separated flows subject to control by zero-net-mass-flux jet. *Physics of Fluids* **27** (2), 024107.
- [105] MARXEN, O., LANG, M. & RIST, U. 2012 Discrete linear local eigenmodes in a separating laminar boundary layer. *Journal of Fluid Mechanics* **711**, 1–26.
- [106] MARXEN, O., LANG, M. & RIST, U. 2013 Vortex formation and vortex breakup in a laminar separation bubble. *Journal of Fluid Mechanics* **728**, 58–90.
- [107] MARXEN, O., LANG, M., RIST, U., LEVIN, O. & HENNINGSON, D.S. 2009 Mechanisms for spatial steady three-dimensional disturbance growth in a non-parallel and separating boundary layer. *Journal of Fluid Mechanics* **634**, 165–189.
- [108] MARXEN, O. & RIST, U. 2010 Mean flow deformation in a laminar separation bubble: Separation and stability characteristics. *Journal of Fluid Mechanics* **660**, 37–54.
- [109] MAUCHER, U., RIST, U. & WAGNER, S. 2000 Secondary disturbance amplification and transition in laminar separation bubbles. In *Laminar-Turbulent Transition: IUTAM Symposium, Sedona/AZ September 13 – 17, 1999* (ed. Hermann F. Fasel & William S.

- Saric), *IUTAM Symposia*, vol. 1, pp. 657–662. Berlin, Heidelberg: Springer-Verlag.
- [110] MEDEIROS, M.A.F. & GASTER, M. 1999 The production of subharmonic waves in the nonlinear evolution of wavepacwave in boundary layers. *Journal of Fluid Mechanics* **399**, 301–318.
- [111] MEHTA, R.D. 1985 Aerodynamics of sports balls. *Annual Review of Fluid Mechanics* **17**, 151–189.
- [112] MICHELIS, T. & KOTSONIS, M. 2015 Flow control on a transport truck side mirror using plasma actuators. *Journal of Fluids Engineering* **137** (11).
- [113] MICHELIS, T. & KOTSONIS, M. 2015 Interaction of an off-surface cylinder with separated flow from a bluff body leading edge. *Experimental Thermal and Fluid Science* **63**, 91–105.
- [114] MICHELIS, T., KOTSONIS, M. & YARUSEVYCH, S. 2017 Response of a laminar separation bubble to impulsive forcing. *Journal of Fluid Mechanics* **820**, 633–666.
- [115] MICHELIS, T., KOTSONIS, M. & YARUSEVYCH, S. 2017 Spanwise flow structures within a laminar separation bubble on an airfoil. In *10th International Symposium on Turbulence and Shear Flow Phenomena (TSFP10)*. Chicago, USA.
- [116] MICHELIS, T., KOTSONIS, M. & YARYSEVYCH, S. 2017 On the origin of spanwise vortex deformations in laminar separation bubbles. *Journal of Fluid Mechanics* [**In review process**].
- [117] MIRALBES, R. & CASTEJON, L. 2012 Aerodynamic analysis of some boat tails for heavy vehicles. *International Journal of Heavy Vehicle Systems* **19** (2), 115–127.
- [118] MOFFAT, R.J. 1988 Describing the uncertainties in experimental results. *Experimental Thermal and Fluid Science* **1**, 3–17.
- [119] MONKEWITZ, P.A. & HUERRE, P. 1982 The influence of the velocity ratio on the spatial instability of mixing layers. *Physics of Fluids* **25**, 1137–1143.
- [120] MOREAU, E. 2007 Airflow control by non-thermal plasma actuators. *Journal of Physics D: Applied Physics* **40** (3), 605–636.
- [121] MORKOVIN, M.E., RESHOTKO, E. & HERBERT, T. 1994 Transition in open flow systems—a reassessment. *Bulletin of American Physical Society* **39** (1882).
- [122] MUELLER, T.J. & DELAURIER, J.D. 2003 Aerodynamics of small vehicles. *Annual Review of Fluid Mechanics* **35** (98).
- [123] NATI, A., DE KAT, R., SCARANO, F. & VAN OUDHEUSDEN, B. W. 2015 Dynamic pitching effect on a laminar separation bubble. *Experiments in Fluids* **56** (9), 172.
- [124] NIEW, T.R. 1993 The stability of the flow in a laminar separation bubble. PhD thesis, Cambridge University.
- [125] NISHINO, T. & ROBERTS, G.T. 2008 Absolute and convective instabilities of two-dimensional bluff body wakes in ground effect. *European Journal of Mechanics, B/Fluids* **27** (5), 539–551.
- [126] VAN OUDHEUSDEN, B.W., SCARANO, F., VAN HINSBERG, N.P. & WATT, D.W. 2005

- Phase-resolved characterization of vortex shedding in the near wake of a square-section cylinder at incidence. *Experiments in Fluids* **39** (1), 86–98.
- [127] OWEN, P.R. & KLANFER, L. 1955 On the laminar boundary layer separation from the leading edge of a thin airfoil. *Tech. Rep. C.P. 220*. Aeronautical Research Council, UK.
- [128] PAULEY, L.L., MOIN, P. & REYNOLDS, W.C. 1990 The structure of two-dimensional separation. *Journal of Fluid Mechanics* **220**, 397–411.
- [129] PEARSON, K. 1901 On lines and planes of closest fit to systems of points in space. *Philosophical Magazine Series 6* **2** (11), 559–572.
- [130] PEREIRA, R., RAGNI, D. & KOTSONIS, M. 2014 Effect of external flow velocity on momentum transfer of dielectric barrier discharge plasma actuators. *Journal of Applied Physics* **116** (10).
- [131] PRANDTL, L. 1904 Über Flüssigkeitsbewegung bei sehr kleiner Reibung. In *Verhandlungen des dritten internationalen Mathematiker-Kongresses in Heidelberg*, pp. 484–491.
- [132] PRICE, S.J., SUMNER, D., SMITH, J.G., LEONG, K. & PAIDOUSSIS, M.P. 2002 Flow visualization around a circular cylinder near to a plane wall. *Journal of Fluids and Structures* **16** (2), 175–191.
- [133] PRÖBSTING, S. & YARUSEVYCH, S. 2015 Laminar separation bubble development on an airfoil emitting tonal noise. *Journal of Fluid Mechanics* **780**, 167–191.
- [134] RAFFEL, M., WILLERT, C.E., WERELEY, S.T. & KOMPENHANS, J. 2007 *Particle image velocimetry - A practical guide*, 2nd edn. New York: Springer.
- [135] RAO, V. N., JEFFERSON-LOVEDAY, R., TUCKER, P. G. & LARDEAU, S. 2014 Large Eddy Simulations in Turbines: Influence of Roughness and Free-Stream Turbulence. *Flow Turbulence and Combustion* **92**, 543–561.
- [136] REED, H.L., SARIC, W.S. & ARNAL, D. 1996 Linear stability theory applied to boundary layers. *Annual Review of Fluid Mechanics* **28**, 389–428.
- [137] REYNOLDS, W.C. & HUSSAIN, A.K.M.F. 1972 The mechanics of an organised wave in turbulent shear flow. part 3. theoretical models and comparisons with experiments. *Journal of Fluid Mechanics* **54**, 263–288.
- [138] RIST, U. 1999 Zur Instabilität und Transition in Laminaren Ablöseblasen. PhD thesis, Universität Stuttgart.
- [139] RIST, U. & AUGUSTIN, K. 2006 Control of laminar separation bubbles using instability waves. *AIAA Journal* **44** (10), 2217–2223.
- [140] RIST, U. & MAUCHER, U. 2002 Investigations of time-growing instabilities in laminar separation bubbles. *European Journal of Mechanics, B/Fluids* **21** (5), 495–509.
- [141] ROSHKO, A., STEINOLFSON, A. & CHATTOORGOON, V. 1975 Flow forces on a cylinder near a wall or near another cylinder. In *2nd U.S. National Conference on Wind Engineering Research*, , vol. IV-15. Colorado State University, Fort Collins.
- [142] SANDHAM, N.D. 2008 Transitional separation bubbles and unsteady aspects of aerofoil

- stall. *The Aeronautical Journal* **112**, 395–404.
- [143] SARIC, W.S., REED, H.L. & KERSCHEN, E.J. 2002 Boundary-layer receptivity to freestream disturbances. *Annual Review of Fluid Mechanics* **32**.
- [144] SARIC, W.S. & WHITE, E. 1998 Influence of high-amplitude noise on boundary-layer transition to turbulence. *AIAA Journal* **98-2645**.
- [145] SARKAR, S. & SARKAR, S. 2010 Vortex dynamics of a cylinder wake in proximity to a wall. *Journal of Fluids and Structures* **26** (1), 19 – 40.
- [146] SCARANO, F. 2012 Tomographic PIV: Principles and practice. *Measurement Science and Technology* **24**.
- [147] SCARANO, F. & RIETHMULLER, M.L. 2000 Advances in iterative multigrid PIV image processing. *Experiments in Fluids* **29** (SUPPL. 1), S51–S60.
- [148] SCHEIMPFLUG, T. 1904 Improved method and apparatus for the systematic alteration or distortion of plane pictures and images by means of lenses and mirrors for photography and for other purposes. GB Patent No. 1196. Filed 16 January 1904.
- [149] SCHIACCHITANO, A., NEAL, D.R., SMITH, B.L., WARNER, S.O., VLACHOS, P.P., WIENEKE, B. & SCARANO, F. 2015 Collaborative framework for PIV uncertainty quantification: Comparative assessment of methods. *Measurement Science and Technology* **26** (7).
- [150] SCHLICHTING, H. & GERSTEN, K. 2000 *Boundary Layer Theory*, 8th edn. Springer.
- [151] SCHRÖDER, A., GEISLER, R., ELSINGA, G.E., SCARANO, F. & DIRKSCHIED, U. 2008 Investigation of a turbulent spot and a tripped turbulent boundary layer flow using time-resolved tomographic PIV. *Experiments in Fluids* **44**, 305–316.
- [152] SCIACCHITANO, A. & WIENEKE, B. 2016 PIV uncertainty propagation. *Measurement Science and Technology* **27** (8), 084006.
- [153] SEIFERT, A., DARABI, A. & WYGNANSKI, I. 1996 Delay of airfoil stall by periodic excitation. *Journal of Aircraft* **33** (4), 691–698.
- [154] SELIG, M.S., MAUGHMER, M.D. & SOMERS, D.M. 1995 Natural-laminar-flow airfoil for general-aviation applications. *Journal of Aircraft* **32**, 710–715.
- [155] SERNA, J. & LÁZARO, B.J. 2014 The final stages of transition and the reattachment region in transitional separation bubbles. *Experiments in Fluids* **55** (4).
- [156] SERNA, J. & LÁZARO, B.J. 2015 On the bursting condition for transitional separation bubbles. *Aerospace Science and Technology* **44**, 43–50.
- [157] SERPIERI, J. & KOTSONIS, M. 2016 Spatio-temporal characteristics of secondary instabilities in swept wing boundary layers. *Journal of Fluid Mechanics* **799**, 200–245.
- [158] SERPIERI, J., VENKATA, S.Y. & KOTSONIS, M. 2017 Towards laminar flow control on swept wings with AC-DBD plasma actuators as active roughness. In *55th AIAA Aerospace Sciences Meeting*.
- [159] SIMONI, D., UBALDI, M., ZUNINO, P. & BERTINI, F. 2012 Transition mechanisms in laminar separation bubbles with and without incoming wakes and synthetic jets.

- Experiments in Fluids* **53**, 173–186.
- [160] SIMONI, D., UBALDI, M., ZUNINO, P., LENGANI, D. & BERTINI, F. 2012 An experimental investigation of the separated-flow transition under high-lift turbine blade pressure gradients. *Flow Turbulence and Combustion* **88**, 45–62.
- [161] SIROVICH, L. 1987 Turbulence and the dynamics of coherent structures. I - Coherent structures. II - Symmetries and transformations. III - Dynamics and scaling. *Quarterly of Applied Mathematics* **45**, 561–571, 573–590.
- [162] SMITH, F.T. & BROWN, S.M., ed. 1986 *Boundary-Layer Separation, Proceedings of the IUTAM Symposium*. London: Springer Berlin Heidelberg.
- [163] SQUIRE, L.C. 1989 Interactions between wakes and boundary-layers. *Progress in Aerospace Sciences* **26** (3), 261 – 288.
- [164] STARIKOVSKIY, A.Y., NIKIPELOV, A.A., NUDNOVA, M.M. & ROUPASSOV, D.V. 2009 SDBD plasma actuator with nanosecond pulse-periodic discharge. *Plasma Sources Science and Technology* **18** (3).
- [165] STRYKOWSKI, P.J. & SREENIVASAN, K.R. 1990 On the formation and suppression of vortex 'shedding' at low reynolds numbers. *Journal of Fluid Mechanics* **218**, 71–107.
- [166] TAFTI, D.K. & VANKA, S.P. 1991 A three-dimensional numerical study of flow separation and reattachment on a blunt plate. *Physics of Fluids A* **3** (12), 2887–2909.
- [167] TANI, I. 1964 Low-speed flows involving bubble separations. *Progress in Aerospace Sciences* **5**, 70–103.
- [168] TANIGUCHI, S. & MIYAKOSHI, K. 1990 Fluctuating fluid forces acting on a circular cylinder and interference with a plane wall - effects of boundary layer thickness. *Experiments in Fluids* **9** (4), 197–204.
- [169] TAYLOR, Z.J., PALOMBI, E., GURKA, R. & KOPP, G. 2011 Features of the turbulent flow around symmetric elongated bluff bodies. *Journal of Fluids and Structures* **27** (2), 250–265.
- [170] THEOFILIS, V. 2011 Global linear instability. *Annual Review of Fluid Mechanics* **43**, 319–352.
- [171] THEOFILIS, V., HEIN, S. & DALLMANN, U. 2000 On the origins of unsteadiness and three-dimensionality in a laminar separation bubble. *Philosophical Transactions of the Royal Society of London A: Mathematical, Physical and Engineering Sciences* **358** (1777), 3229–3246.
- [172] TROPEA, C., YARIN, A.L. & FOSS, J.F., ed. 2007 *Springer Handbook of Experimental Fluid Mechanics, Springer Handbooks*, vol. 1. Springer Science.
- [173] WATMUFF, J.H. 1999 Evolution of a wave packet into vortex loops in a laminar separation bubble. *Journal of Fluid Mechanics* **397**, 119–169.
- [174] WEIDEMAN, J.A. & REDDY, S.C. 2000 A MATLAB differentiation matrix suite. *ACM Transactions on Mathematical Software* **26**, 465–519.
- [175] WELCH, P. 1967 The use of fast Fourier transform for the estimation of power spectra: A method based on time averaging over short, modified periodograms. *IEEE*

- Transactions on Audio and Electroacoustics* **15**, 70–73.
- [176] WHITE, F.M. 2005 *Viscous Fluid Flow*, 3rd edn. McGraw-Hill Education.
- [177] WIENEKE, B. 2008 Volume self-calibration for 3D particle image velocimetry. *Experiments in Fluids* **45**, 549–556.
- [178] WIENEKE, B. 2015 PIV uncertainty quantification from correlation statistics. *Measurement Science and Technology* **26** (7).
- [179] WOLF, E., KÄHLER, C.J., TROOLING, D.R., KYKAL, C. & LAI, W. 2011 Time-resolved volumetric particle tracking velocimetry of large-scale vortex structures from the reattachment region of a laminar separation bubble to the wake. *Experiments in Fluids* **50**, 977–988.
- [180] YAMAMOTO, T. & OKUBO, M. 2007 Nonthermal plasma technology. In *Advanced Physicochemical Treatment Technologies* (ed. K.W. Lawrence, Y.-T. Hung & K.S. Nazih), *Handbook of Environmental Engineering*, vol. 5, pp. 135–293. Humana Press.
- [181] YANG, Z. & VOKE, P.R. 2001 Large-eddy simulation of boundary-layer separation and transition at a change of surface curvature. *Journal of Fluid Mechanics* **439**, 305–333.
- [182] YARUSEVYCH, S. & KOTSONIS, M. 2017 Effect of Local DBD Plasma Actuation on Transition in a Laminar Separation Bubble. *Flow, Turbulence and Combustion* pp. 1–22.
- [183] YARUSEVYCH, S. & KOTSONIS, M. 2017 Steady and transient response of a laminar separation bubble to controlled disturbances. *Journal of Fluid Mechanics* **813**, 955–990.
- [184] YARUSEVYCH, S., SULLIVAN, P.E. & KAWALL, J.G. 2007 Effect of acoustic excitation amplitude on airfoil boundary layer and wake development. *AIAA Journal* **45** (4), 760–771.
- [185] YARUSEVYCH, S., SULLIVAN, P.E. & KAWALL, J.G. 2009 On vortex shedding from and airfoil in low-reynolds-number flows. *Journal of Fluid Mechanics* **632**, 245–271.
- [186] ZAMAN, K.B.M.Q., MCKINZIE, D.J. & RUMSEY, C.L. 1989 Natural low-frequency oscillation of the flow over an airfoil near stalling conditions. *Journal of Fluid Mechanics* **202**, 403–442.
- [187] ZELMAN, M.B. & MASLENNIKOVA, I.I. 1993 Tollmien-Schlichting-wave resonant mechanism for subharmonic-type transition. *Journal of Fluid Mechanics* **252**, 447–478.

# SCIENTIFIC CONTRIBUTIONS

## JOURNAL PUBLICATIONS

6. MICHELIS, T., KOTSONIS. M. & YARUSEVYCH, S. 2017 Spanwise flow development within a laminar separation bubble under natural and forced transition. *Experimental Thermal and Fluid Science* [**Under review**].
5. MICHELIS, T., KOTSONIS. M. & YARUSEVYCH, S. 2017 On the origin of spanwise vortex deformations in laminar separation bubbles. *Journal of Fluid Mechanics* [**Under revision**].
4. MICHELIS, T., KOTSONIS. M. & YARUSEVYCH, S. 2017 Response of a laminar separation bubble to impulsive forcing. *Journal of Fluid Mechanics* **820**, 633-666.
3. MICHELIS, T. & KOTSONIS. M. 2015 Flow control on a transport truck side mirror using plasma actuators. *Journal of Fluids Engineering, Transactions of the ASME* **137** (11).
2. MICHELIS, T. & KOTSONIS. M. 2015 Interaction of an off-surface cylinder with separated flow from a bluff body leading edge. *Experimental Thermal and Fluid Science* **63**, 91-105.
1. CORREALE, G., MICHELIS, T., RAGNI, D. KOTSONIS, M. & SCARANO, F. 2014 Nanosecond-pulsed plasma actuation in quiescent air and laminar boundary layer. *Journal of Physics D: Applied Physics* **47** (10).

## CONFERENCE PROCEEDINGS

5. MICHELIS, T., KOTSONIS. M. & YARUSEVYCH, S. 2017 Spanwise flow structures within a laminar separation bubble on an airfoil. In *10th International Symposium on Turbulence and Shear Flow Phenomena (TSFP10)*. Chicago, USA.
4. MICHELIS, T. & KOTSONIS. M. 2016 Spatio-temporal response of a laminar separation bubble under impulsive forcing. *46th AIAA Fluid Dynamics Conference*.
3. MICHELIS, T. & KOTSONIS. M. 2014 Cylinder in the vicinity of a bluff body leading edge. *44th AIAA Fluid Dynamics Conference*.
2. CORREALE, G., MICHELIS, T. & KOTSONIS. M. 2014 NS-DBD plasma actuation on a backward facing step. *52nd AIAA Aerospace Sciences Meeting - AIAA Science and Technology Forum and Exposition, SciTech 2014*.

1. MICHELIS, T., CORREALE, G., POPOV, I. B., KOTSONIS, M., RAGNI, D., HULSHOFF, S. J. K. & VELDHUIS, L. L. M. 2013 Disturbance introduced into a laminar boundary layer by a NS-DBD plasma actuator *1st AIAA Aerospace Sciences Meeting including the New Horizons Forum and Aerospace Exposition*.

## CONFERENCE ABSTRACTS

2. MICHELIS, T. & KOTSONIS, M. 2016 Three dimensional breakdown of an impulsively forced laminar separation bubble. *APS Division of Fluid Dynamics Meeting Abstracts*.
1. MICHELIS, T. & KOTSONIS, M. 2014 Hybrid flow control of a transport truck side-mirror using AC-DBD plasma actuated guide vane. *APS Division of Fluid Dynamics Meeting Abstracts*.

# BIOGRAPHICAL NOTE



Theodoros Michelis (Θεόδωρος Μιχελής) was born in Athens, Greece, on an early May Saturday morning. From an early age he showed interest in incinerating various objects and in disassembling anything that had screws on it, preferably expensive. His passion towards science persisted through the years, thus he followed the scientific track in high school. Eventually, he decided to study Mechanical Engineering, obtaining his BEng degree from University College London in 2010, with a project on computational modelling of blood flow in artificial heart valves. His interest in fluid mechanics lead him to pursue an MSc degree in aerodynamics at Delft University of Technology, completed in 2012. The topic of his thesis regarded experimen-

tal investigation on fundamental aspects of nanosecond plasma actuators. During his MSc years, he was also involved in the university's Formula Student team, designing the brakes system and developing and manufacturing the battery packs of the DUT11 car, winner in both competitions at which it took part. In 2013, he began his PhD in the same aerodynamics department, a venture that ended in 2017 with the composing of this document. In his free time, Theo enjoys reading, music, photography, catering for plants, cooking and savouring alcoholic beverages. However, he draws ultimate pleasure from travelling and socialising with people of any possible background, a passion he gradually discovered by living in a few different countries.







  
**TU Delft**

ISBN 978-94-92516-82-4